Doctoral Thesis

Mechatronic Implementations of Wearable Robots for Physical Interaction: From Rigid to Soft Robotics

Suin Kim

Department of Mechanical Engineering

Graduate School of UNIST

Spring, 2019

Mechatronic Implementations of Wearable Robots for Physical Interaction: From Rigid to Soft Robotics

A dissertation
submitted to the Graduate School of UNIST
in partial fulfillment of the
requirements for the degree of
Doctor of Philosophy

Suin Kim

11. 12. 2018 of submission
Approved by

_____

Advisor
Joonbum Bae

Mechatronic Implementations of Wearable Robots for Physical Interaction: From Rigid to Soft Robotics

Suin Kim

This certifies that the dissertation of Suin Kim is approved.

11/12/2018 of submission

_____

Advisor: Joonbum Bae

_____

Hungsun Son

_____

Hooneui Jeong

_____

Jeongmin Baik

_____

Hyunhyub Ko

Abstract

Mechatronic Implementations of Wearable Robots for Physical Interaction:
From Rigid to Soft Robotics
by
Suin Kim
Doctor of Philosophy in Engineering – Mechanical Engineering
Ulsan National Institute of Science and Technology (UNIST)
Professor Joonbum Bae, Chair

Wearable robots for physical interaction, which measure the movement of the body parts and apply physical force to the body, have gained great attention for the purposes of power augmentation, rehabilitation, and interfaces for virtual reality or tele-operation. To implement wearable systems more practically, various mechatronic technologies have been studied. However, the exoskeleton-type systems cannot be easily found in our daily lives, because there still remain unsolved issues in interactive control with human. Also, the uncomfortable, heavy and complex structure prohibit wide-spread application of exoskeleton systems, which leads us to replace the rigid robotic components with soft, flexible, and stretchable materials.

In this dissertation, several mechatronic considerations of wearable robots for physical interaction are discussed from the point of view from rigid to soft robotics. First, a rigid wearable robot, called an exoskeleton system, was developed with series elastic actuators, and controlled by robust control algorithms to deliver the interaction force delivered to the user accurately even with the presence of the uncertain and unknown interactions from the user. Second, to operate the exoskeleton system based on the user's muscular forces, the muscular forces were estimated by fusion of wearable sensors and biomechanics-based algorithms. Last, novel manufacturing methods for soft sensor systems were developed, based on direct writing of a conduct liquid metal on soft materials, to overcome the fundamental wearable issues of the wearable robots. The research contents in this dissertation are series of efforts towards practical implement of the wearable robots: development of a low-level controller (simple and robust force control algorithms), a high-level controller (determining desired forces based on estimated muscular forces), and novel manufacturing methods for soft sensors (endowing high wearability to the wearable system). Based on the research outcomes of this dissertation, wearable systems will be found around our daily lives with practical forms to improve the quality of human life.

Acknowledgement

In my life, it has been my great pleasure to be a member of Bio-robotics and Control (BiRC) laboratory. All my experiences in this place were wonderful for me, from beautiful natural landscape in the campus to interesting research contents in our laboratory. I was dreaming of being an engineer in a certain area, and here was a good start point for me.

First of all, I want to express my appreciation to my advisor Joonbum Bae, who I respect most not only as a researcher, but also as a considerate person. He always gave me lots of intuitions, indications, and advise willingly, when I got lost in the middle of my study or even my life. In addition, it has always been a great pleasure for me to discuss research topics with him. These greatly encouraged me to carry on my work, despite there were many difficulties the way. So, I would like to say a very big thank him.

All the work in this dissertation could be done thanks to great passion and efforts of my colleagues, including members and internship students in BiRC laboratory, Kyoungkwan Ro, Wookeun Park, Jinkhyuk Oh, Dahee Jeong, Jeongsoon Hong, Heeyeop Kim, Eunji Kwon, Jihye Oh, Kyungtaek Kim, Kunhee Kim, and Soyoung Choi, I really appreciate them. Of course, the other members in our laboratory, Inseong Jo, Yeongtae Jung, Jihhoon Kim, Younkyu Park, Jeongsoo Lee, Sungman Park, Bokeon Kwak, Hoyeon Yeom, Minhyuk Lee, Junsoo Kim, Kyutaek Han, Dongyoung Lee, Sungmin Seo, and Hyeonjun Kim, also encouraged me to continue my work, sharing our interests in studies with each other. I also want to thank to Jinsik Kim and Jinhoe Hur, in UNIST research assistance center, who helped me solve several technical issues in my research.

I would like to thank the global Ph.D fellowship (GPF) from the Korean Government for their generous support during my Ph.D study.

Especially, I want to thank Sohyun Han, who is my best friend and a good mentor. For me, she always has shown pure passion and sincere attitudes for research as well as her life. It has greatly helped me overcome many difficulties during my doctoral course. I want to thank Seolyoung Ahn for many great memories in Ulsan, which act as valuable emotional support. Lastly, I'd like to express my special gratitude for huge support from my mother, Hyunhee Han, who is my wisest counselor. She always encouraged me to keep learning many interesting things in the world with a happy heart. I'd like to take this opportunity to thank all my people for their sincere support.

Contents

List of Figures

List of Tables

Chapter 1

Introduction

1.1 Realization of Internet of Things (IoT): Wearable Devices

In recent years, the concept of internet of things (IoT) has gained much attention to improve the quality of our lives, with a strong potential economic impact [35]. The very first step for realizing IoT is to build a block of IoT through embedded systems, which are connected to the internet to collect data around us, deliver feedback to the users, or both [198]. Nowadays, familiar embedded systems have been around in various forms, such as smart phones, smart home appliances, and service robots. Wearable devices are the best example of IoT realization, e.g. smart watches, smart glasses, or health monitoring systems, due to their capability of sensing, computing, and communication [66].

Except for the wearable devices we are familiar with, such as smart watches and glasses, wearable robots for physical interaction have attracted attention also, which measure the movement exerted in the human body, deliver physical force to the body, or both [142]. As shown in Figure 1.1, the wearable robots have been implemented as a form of exoskeletons to augment human power [80, 81], apply physical therapeutic intervention to the patients [34], and provide an intuitive interface for virtual reality [139]. To physically interact with the human, various scope of studies have been conducted: design of exoskeleton structures with considerations of the human body [79], development of an actuator or a control algorithm with considerations of interaction with the human [184], analysis on efficacy of assistance from the exoskeleton [145], and estimation of human motion intension to activate the exoskeleton [170].

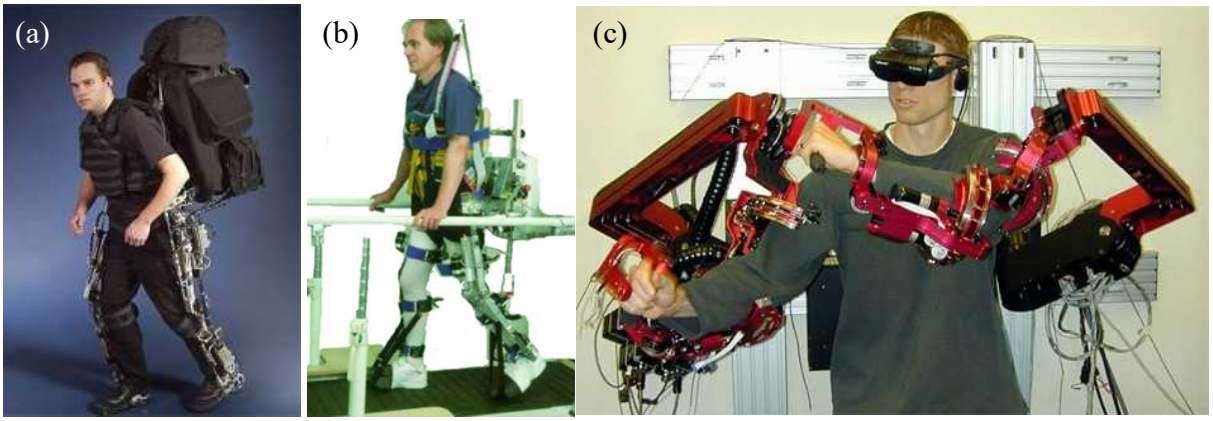

Figure 1.1: Exoskeleton systems: (a) Berkeley lower extremity exoskeleton (BLEEX) for human power augmentation [81], (b) driven gait orthosis (DGO) for gait rehabilitation [34], (c) a upper extremity exoskeleton as an interface to virtual reality [139].

1.2 Issues on Control Systems for Wearable Robots

For appropriate operation of the exoskeletons, a control system should be applied, which consists of a high-level and a low-level controller as shown in Figure 1.2. The role of the high-level controller is determining a desired torque trajectory based on the status of the user and a predetermined task, such as assisting user's motion or applying therapeutic intervention to a patient [80, 81, 34]. An ideal high-level controller may operate according to the user's intention of movements to assist the movement appropriately. Because the movements in the human body are exerted from the muscular forces, estimation of the muscular actions might be a solution for the high-level controller. However, estimation of muscular forces have remained as a challenging task, because an invasive method, direct installation of a force transducer to the muscles, is inevitable to measure muscular forces accurately [190]. Surface electromyography (sEMG) is the most widely used as an non-invasive method, but it provides only qualitative activation level of muscles and requires complex and frequent calibration processes due to the high noise/signal ratio, differences among individuals, and surrounding conditions [39]. Thus, it is necessary to find a simpler and more quantitative clue for the muscular forces to be implemented as a high-level controller for the wearable robots.

Another requirement is accurate control of the interaction force delivered to the user, which is a role of a low-level controller [182, 54, 24, 9, 10]. For some applications, the accuracy of the interaction forces is emphasized, such as an exoskeleton used as a rehabilitation device

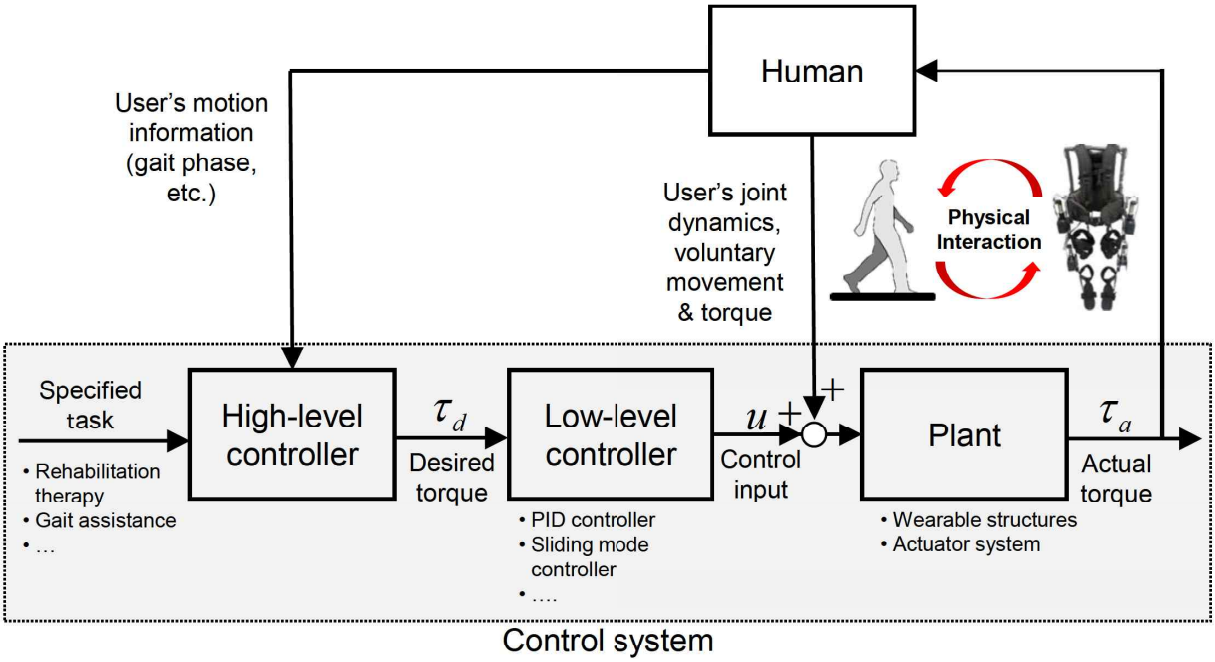

Figure 1.2: Block diagram of a control system in a wearable robot.

copying the interaction force that the therapist applies to the patient and a haptic device providing delicate haptic feedback [182, 54, 24, 9, 10]. However, it has been a challenging task for the wearable robots to control the interaction force accurately, because interactions with the user generate uncertainties in the system and act as an external disturbances, which are hardly predictable in real-time [143, 188, 182, 183, 184, 10]. These uncertainties can degrade the performance of the robust controllers, because such controllers usually require accurate information of the plant and the environment to ensure performance. Thus, for satisfactory performance of wearable robots, there still remains a need for a robust control algorithm, which can realizes high fidelity force control performance even in these uncertain environments.

1.3 Transition from Rigid Robotics to Soft Robotics in the Field of Wearable Robots

Although rapid technological advance has been achieved with the exoskeleton systems, technical barriers have been discussed continuously, such as discomfort caused by rigid compo-

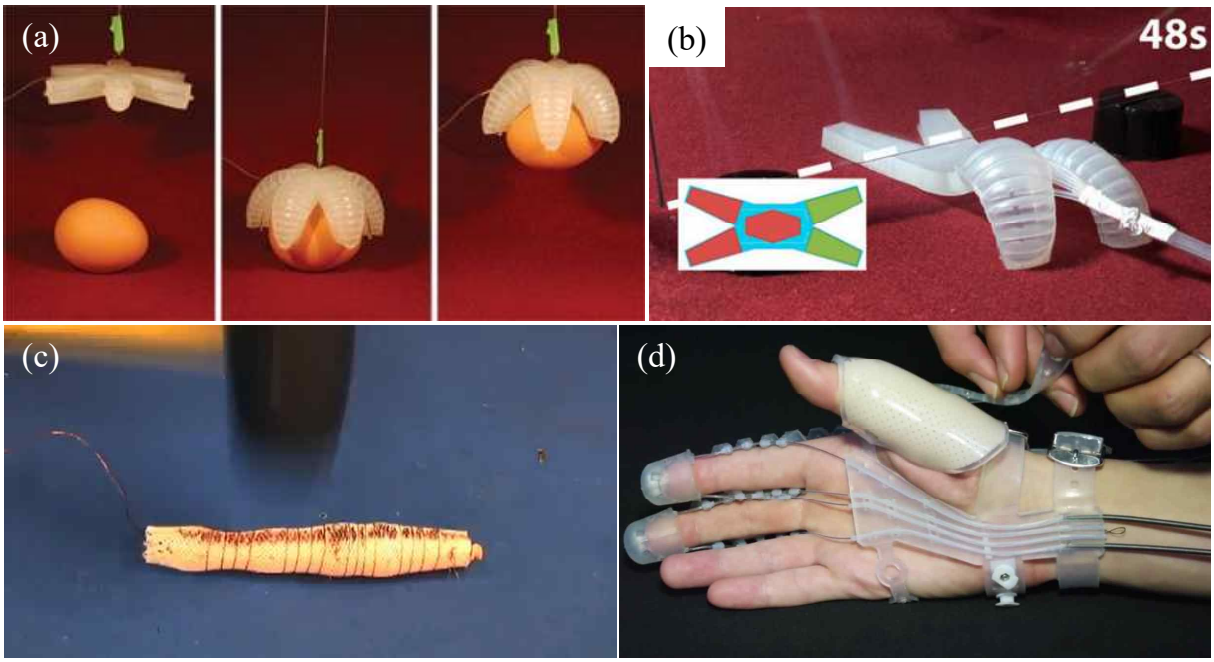

Figure 1.3: Soft robots: (a) soft gripper [72], (b) multi-gait soft robot [159], (c) Meshworm [157], and (d) Exo-Glove Poly [73].

nents in the system [133, 73, 117]. The robotic system with predetermined axes or heavy component cannot cover the soft and multi-degrees of freedom human body without incurring the discomfort: three-dimensional movements of the thumb or the wrist [130, 186]. To overcome the limitation, a new possibility has been proposed recently, so-called soft and stretchable electronics [87, 111, 151]. As shown in Figure 1.3, soft and stretchable electronics consist of only elastomer (usually soft and stretchable like the human skin) embedded functional materials to generate mechanical strain or bending to the elastomer body (acting as a soft actuator) or just measure the mechanical deformation of it (acting as a soft sensor) rather than using the conventional sensor or actuator modules with rigid linkages to form rotational or translational axes. Due to its inherent compliance, such a functional elastomeric body can passively adapt to the human body or the external environment without losing its original functions.

Many interesting examples of soft robots have been suggested as follows. Soft grippers can grasp even fragile objects such as eggs without a precise control of the actuator motion, because it automatically adapts to the shape of the object while deforming its soft body (Figure 1.3 (a) [72]). Soft robots can pass though a narrow gap, which cannot be easily

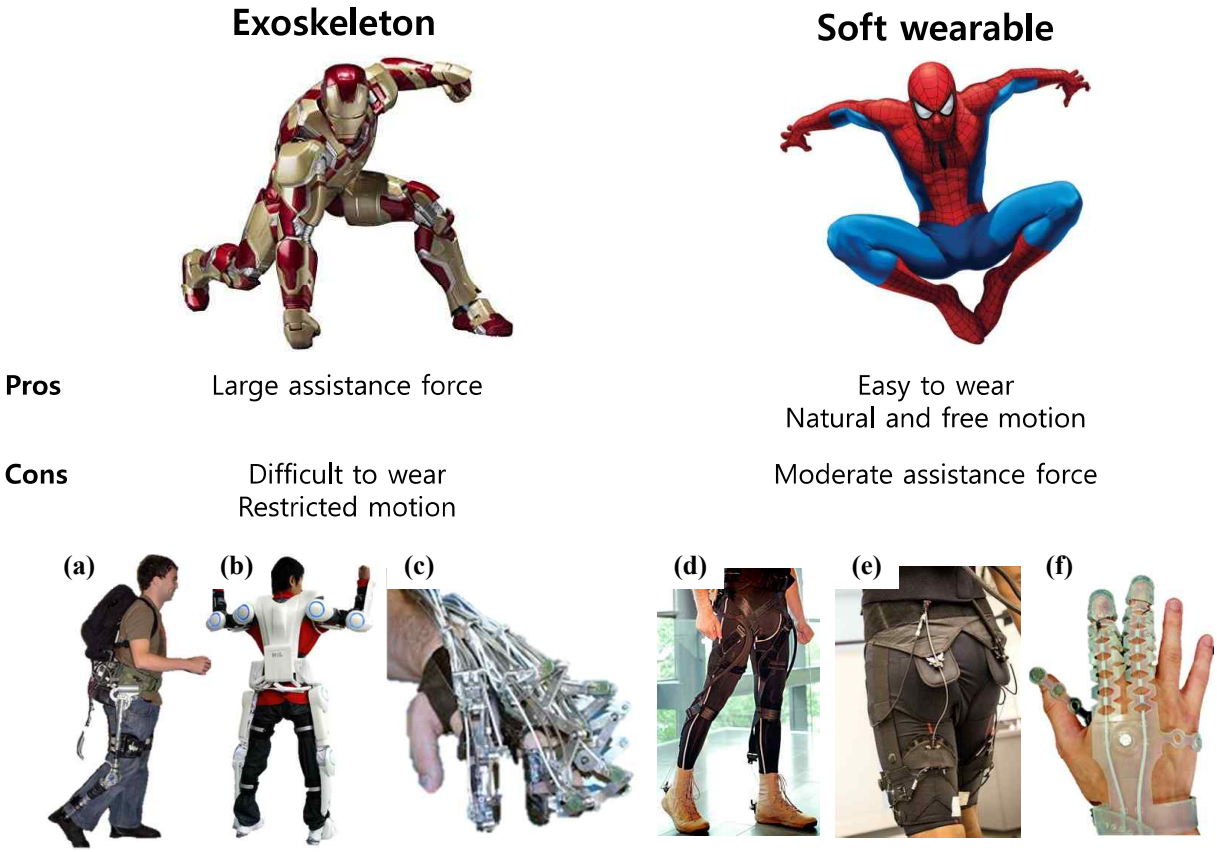

Figure 1.4: Comparison between exoskeleton-type systems and soft wearable systems with examples of exoskeleton-type systems: (a) leg exoskeleton [187], (b) hybrid assistive limb (HAL) exoskeleton [170], (c) hand exoskeleton [192] and examples of soft wearable systems: (d) soft exosuit for the ankle joint [193], (e) soft exosuit for the hip joint [45], (f) exo-glove [73].

accessed by the conventional robotic systems (Figure 1.3 (b) [159]). Soft robots possess higher mechanical durability; they maintained their original function even after hit by a hammer (Figure 1.3 (c) [157]). Rigid linkages in the hand exoskeleton can be replaced with elastomer bodies and cable-driven systems, not impeding the natural movement of the users (Figure 1.3 (d) [73]). In these examples, the inherent compliance of the material can provide a novel and simple solution to each engineering problem.

The pros and cons of the rigid and soft wearable robots can be summarized as shown in Figure 1.4. The rigid wearable robots such as exoskeletons are able to generate large assistance force, while inevitably accompanying a certain level of discomfort. In contrary, the soft wearable robots can be worn more easily, allowing natural motion of the user, while

generating moderate magnitude of the assistance force.

1.3.1 Liquid Metal as a Functional Material for Stretchable Electronics

To implement the technologies in the field of soft robotics more functionally, stretchable electronics are necessary to replace the conventional electronic components [111]. The primary requisite of stretchable electronics is highly stretchable conductive path, maintaining the conductivity even with mechanical strain. For this application, liquid metal, known as eutectic Gallium-Indium (eGaIn), has attracted much attention due to its metallic conductivity and extreme stretchability [43]. The micro-scale channels have been constructed and filled with eGaIn to form conductive pathes, which have been used as conductive path for stretchable electric circuit [127] or soft sensors [3]. The simplest application of stretchable electronics is the soft sensors; resistance changes in a conductive pathes under mechanical strain can be directly used as a strain gauge [134].

Due to attractive properties of eGaIn, the soft sensors have been developed in various forms as shown in Figure 1.5. A highly stretchable soft sensor, able to measure both planar strain and axial pressure, was developed with multilayered microchannels (Figure 1.5 (a) [131]). Curvature sensor was fabricated by modifying the structure of the microchannel (Figure 1.5 (b) [113]). With multiple force posts aligned and embedded in the elastomeric body, a three axes axial forces were measured by the soft sensor (Figure 1.5 (c) [94]). Due to highly stretchability and softness, the eGaIn-based soft sensors have been frequently attached on the human body as an artificial skin to measure applied pressure on the skin, acting as a skin-mountable touch pad (Figure 1.5 (d) [100]), and movement of the wrist (Figure 1.5 (e) [186]), fingers (Figure 1.5 (f) and (g) [60, 130]), and the legs (Figure 1.5 (h) [117]). Without complex linkages or structures, the soft sensors successfully measures body motions without causing discomfort to the users. Without doubt, the application of such an attractive technology can be widen and highlighted greatly, if a fabrication technique is properly advanced with high productivity, programmability, scalability, low process cost, low barrier-to-entry, allowing facile production [181, 3].

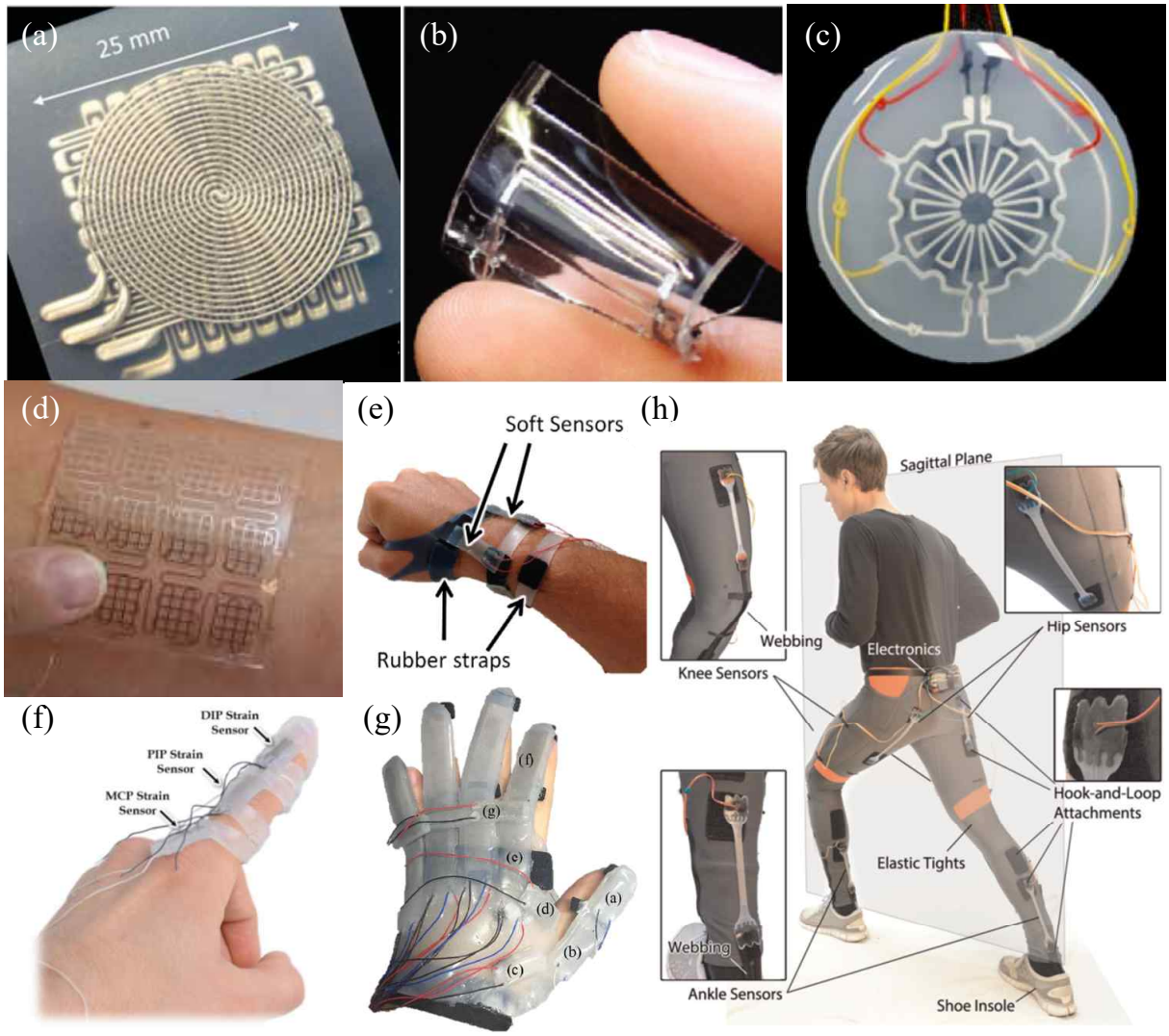

Figure 1.5: Liquid metal-based soft sensors: (a) multi-layered 3-axis strain gauge [131], (b) curvature sensor [113], (c) 3-axes force sensor [94], (d) touch pad [100], (e) wrist motion sensor [186], (f) finger motion and fingertip pressure sensor [60], (g) 3D finger motion sensor [130], (h) sensing suit for the lower extremity [117].

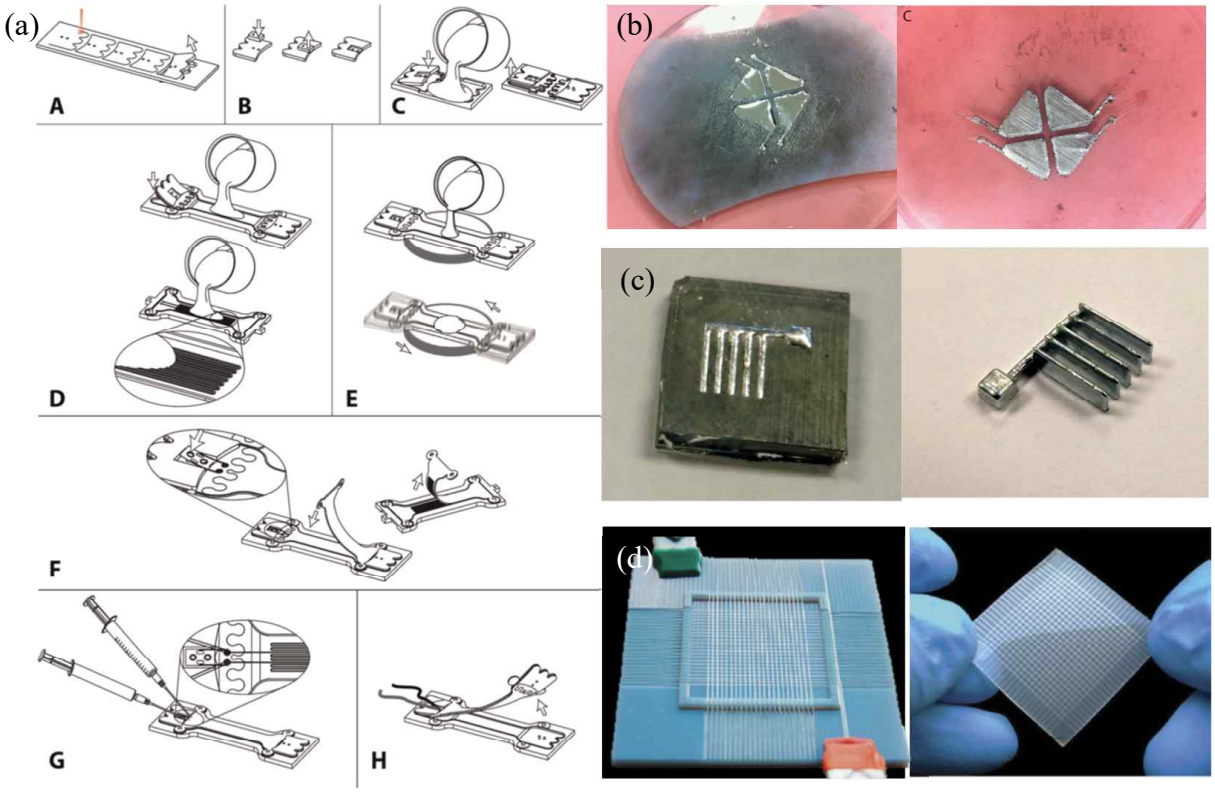

Figure 1.6: Fabrication methods for liquid metal-based soft sensors: (a) molding, bonding, and injection [117], (b) mask deposition [148], (c) freeze casting [52], and (d) direct filament casting [105, 104].

1.3.2 Fabrication Techniques for Liquid Metal-based Stretchable Electronics

According to the needs for a fabrication technique for liquid metal-based conductive pathes, various fabrication methods have been suggested [84]. The most common is casting with a mold, followed by bonding and injection (Figure 1.6 (a) [117]), which have been applied to various types of soft sensors [44, 131, 185, 113, 169, 197, 31, 117, 203, 130, 29, 135, 161]. Others include mask deposition (Figure 1.6 (b) [148]), freeze casting (Figure 1.6 (c) [52]), and direct filament casting (Figure 1.6 (d) [105, 104]). In most fabrication methods, the design of the microchannel cannot be modified readily, because a customized mold or mask is required for a specific design of the microchannel. In addition, the fabrication steps require high dexterity of the hand, resulting in low production rate and high cost for fabrication;

which might be cause of practical difficulties for developing various types of soft electronics based on the liquid metal [30].

Recently, novel fabrication techniques with high programmability for these stretchable liquid metal traces have been proposed: selective wetting (Figure 4.6 (a) [106]) and direct ink writing (DIW) (Figures 4.6 (b)-(d) [102, 55, 17]. As reported recently, the unique fabrication techniques are attributed to the unique mechanical and rheological behaviors of the liquid metal [44, 199, 102, 106]. In case of the selective wetting, however, a fabrication step, such as sputtering nanoparticles, is necessary, which results in high fabrication costs [106, 127]. In contrast, in case of DIW, liquid metal traces with any configurations can be directly written by a motorized syringe, without special mechanical or chemical treatment of the raw materials, which can allow high programmability and a lower barrier-to-entry of fabrication as well as low production cost [16, 55, 17, 102, 176]. In the field of material science, although the interesting behaviors of the liquid metal have been reported vigorously, including the direct writable property, little investigation has been conducted on apply the characteristics of the liquid metal to highly productive and programmable fabrication technique for stretchable conductive paths with various applications. Therefore, practical realization of such a technology might be a chance to bring the liquid metal-based electronics into a real market (our daily lives).

1.4 Thesis Overview

In the transition from the rigid robotics to the soft robotics, several technologies for practical considerations for the wearable devices are suggested and verified in this thesis. The remainder of this thesis is organized as follows.

[Chapter 2: Implementation of a Rigid Exoskeleton with a High Fidelity Force Control]

To understand the issues in the field of the exoskeleton, a typical lower extremity exoskeleton is introduced and implemented with a robust control algorithm. For the exoskeleton, it is important to assist the user properly and not impede motion of the user. To satisfy the requirements, a precise force control system is necessary. However, in case of the exoskeleton, it is difficult to maintain the performance of a control system, because the control environments are usually very uncertain due to the interaction with the user (acting as an

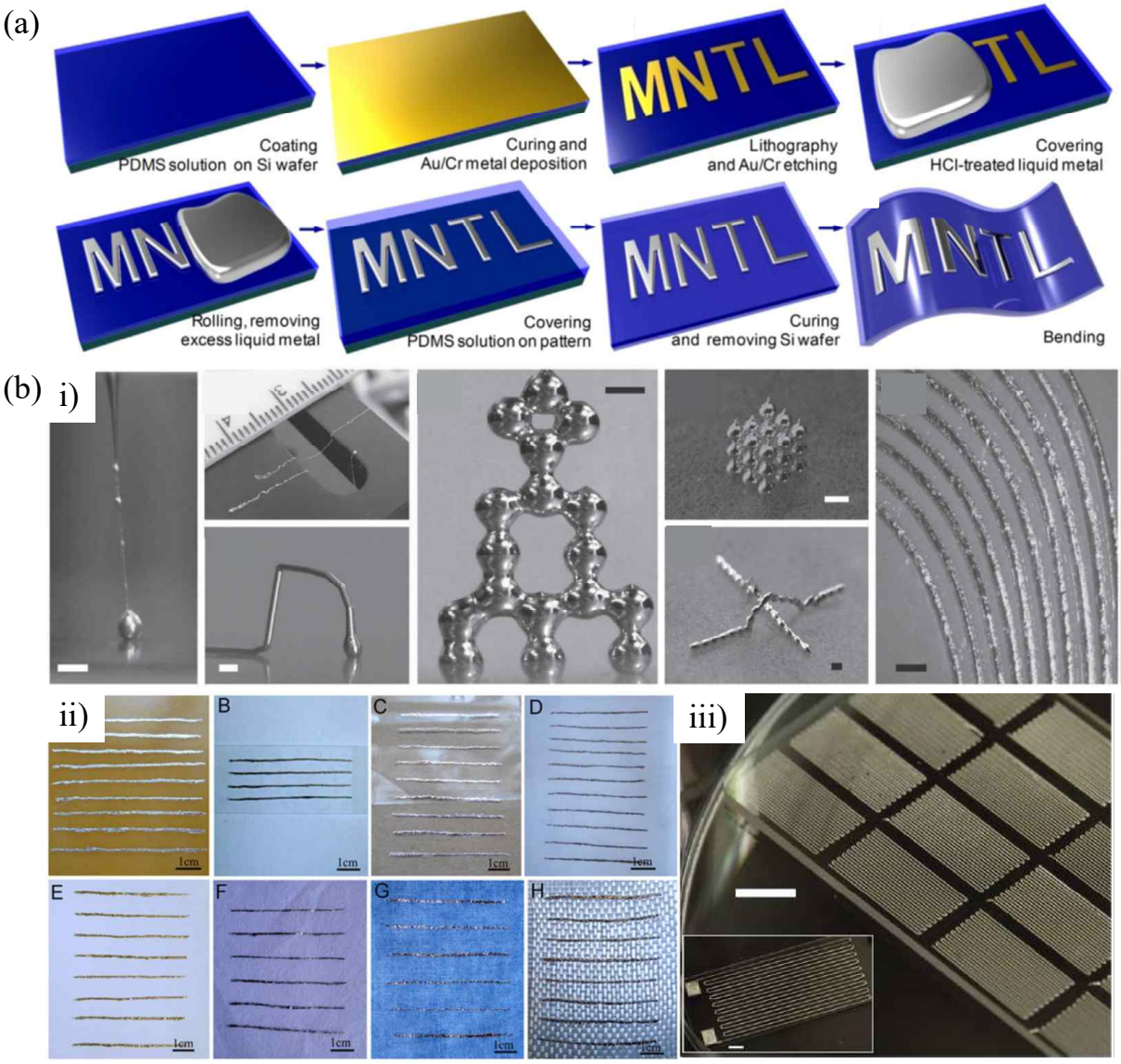

Figure 1.7: Highly programmable fabrication methods for liquid metal-based conductive pathes: (a) selective wetting [106] and (b) direct ink writing (DIW): i) 2D and 3D structures written directly by liquid metal [102], ii) liquid metal written on various substrates [55], and iii) strain gauges based on DIW [17].

external disturbance). To deal with the problem, series elastic actuator (SEA) modules are used with an augmented time delay control (TDC) strategy to control the interaction force between the exoskeleton and the user robustly without modeling the control environment. The implemented exoskeleton can be used as an accurate force-controlled platform.

[**Chapter 3: Estimation of Muscular Forces for Determining a Desired Force Trajectory**]

Ideally, the exoskeleton can help the user most beneficially, if it can apply assistant force to the user with the proper magnitude and timing. To activate the exoskeleton properly, it is necessary to identify the user's motion intention in real-time. In this chapter, estimation of individual muscular forces is investigated to utilize the force information as a clue for the user's motion intention. To estimate the muscular forces in the lower extremity, inverse dynamics-based static optimization is implemented with the wearable sensor system composed with four inertial measurement units (IMUs) and a shoe-type sensor. As another application of the algorithm, a hand exoskeleton is introduced and combined with the algorithm to estimate individual muscular forces of the fingers.

[**Chapter 4: Direct Writing of Liquid Metal for Soft Sensors**]

This chapter covers development of a fabrication technique for soft sensors based on direct writing of the liquid metal. First, the conventional mold-based fabrication method is applied to fabricate soft sensors, and the necessity of a new fabrication technique is discussed based on the experimental results of the sensors. Secondly, a direct writing-based fabrication technique is proposed, with quantitative verification of its stability, consistency, and reproducibility. The following contents describes application of the fabrication technique to sensing gloves. The final part covers the verification of the electrical connection between the liquid metal and the metal electrode, considering electrical stability, and mechanical and thermal durability.

Chapter 2

Development and Implementation of a Rigid Exoskeleton*

2.1 Introduction

To implement the physical human-robot interaction (pHRI) system, such as an exoskeleton, it is an important issue to provide appropriate assistant force with proper timing. In other words, the aim of the control systems in the exoskeleton is to provide interactions according to a target task, and the interactions are usually implemented as impedance delivered to the user [25, 85, 196, 149, 77, 177, 180, 59, 188, 182]. The impedance controller usually consists of a desired impedance model and a low-level force controller [78, 18, 182, 24, 9]. However, in some of applications, an open-loop impedance control was used without a force feedback to control the exoskeleton performing a certain task [25, 85, 177, 59, 188]. The open-loop impedance control can be simply implemented based on a closed-loop position control, and augmented further with a feedforward term. However, the strategy has a limitation in the accuracy of the realized impedance and the feed-forward augmentation is susceptible to modeling error [24].

For some applications, the accuracy of the impedance should be emphasized, such as an exoskeleton used as a rehabilitation device copying the interaction force that the therapist applies to the patient and a haptic device providing delicate haptic feedback [182, 54, 24, 9, 10]. To improve the impedance accuracy, a requirement of a force feedback was argued and the impedance control with a force feedback was applied to the exoskeleton systems [24,

*The contents in this chapter is based on the published work of the author [89].

196, 149, 77, 180, 9]. In addition, the need of a high fidelity force source for the exoskeleton has been suggested and a series elastic mechanism has been studied actively as an one of the solutions [143, 188, 182, 183, 184, 97, 9, 10].

Even though the force control with the series elastic actuator (SEA) can improve the impedance accuracy, it was unavoidable to generate undesired interaction forces caused by uncertainties in dynamics of the exoskeleton and the human body, because it is difficult to identify the uncertainties accurately [143, 188, 182, 183, 184, 10]. To compensate for the uncertainties, a disturbance observer was introduced with a feedforward controller, and the controlled SEA showed very low impedance and precise force control performance while interacting with a human [97]. However, the design of such a controller required accurate prior information of the plant itself and the performance and stability of the controller was dependent on the accuracy of the information [97].

On the other hand, a time-delay control (TDC) has been suggested as another novel robust control algorithm [206]. The key feature of such a controller is direct cancellation of the system uncertainties and unknown disturbances by modifying the control actions based on past observations of system response and control inputs; that is the source of robustness of TDC [205, 69]. With such a feature, TDC maintains the desired performance even in the presence of uncertainties, although the method requires no estimates of the system parameters or uncertainties and does not require varying the controller gain. To ensure the performance of TDC, an assumption is required that the sampling frequency of the control system could cover the frequency range of possible uncertainties. Since the possible range of the sampling rate become faster due to advance technology in the control hardware, a range of application of TDC become wider than before. In addition, implementation of the control action is a simple task, with about four lines of C code [205]. These advantages have been clearly demonstrated in the successful applications of TDC to a robot manipulator [205, 63, 204].

In the case of a pHRI system such as an exoskeleton, the advantages of TDC are especially attractive. Therefore, in this research, the law of TDC was applied to control the SEA module to develop an ideal force-mode controller and to fill the requirements of the accurate low-level controller for the exoskeleton To apply TDC to the given system, it was very important to choose a nominal value of control distribution matrix, because it determined intensity of the control law. However, a specified way to determine the parameter has not been discussed yet [206, 205, 69, 63, 204]; thus, this paper presents how to choose the parameter and verifies the discussion experimentally.

After proper value of the parameter was selected, the successful application of TDC realized the designed model dynamics. However, the delay between the desired position and the model dynamics was observed, which degraded performance of force-mode control of the SEA. The problem has not been dealt with before, because the previous applications of TDC have been focused on realization of a model dynamics [205, 63, 204]. To minimize the delay in position control, the speed of the model dynamics was increased, but the performance was limited by saturated control input which resulted in severe chattering to the system. Thus, in this paper, a new reference position was introduced, calculated by the inverse of model dynamics; this proposed method was named 'model-inverse time delay control' (MiTDC). The proposed controller showed better performance than a fast TDC without causing saturation in control effort, and it significantly improved force control performance of the SEA. The improved performance was demonstrated with free oscillation of a pendulum connected to the SEA module and the operation of SEA module in the exoskeleton during walking.

The remainder of this chapter is organized as follows. Section 2.2 describes the configuration of the lower extremity exoskeleton system and derivation of the analytic model of the SEA to emphasize the difficulties for force-mode control in the SEA due to uncertain parameters. Fundamental theories and a discussion about the implementation of TDC are introduced in Section 2.3 with experimental verifications. In Section 2.4, the concept of MiTDC is derived, and performance of it was verified experimentally.

2.2 Lower Extremity Exoskeleton System

2.2.1 System Configuration

Figure 2.1 shows the components of the lower extremity exoskeleton system developed in our previous work [88]. The exoskeleton system consists of four rotary-series elastic actuator (SEA) modules to assist flexion and extension of the hip and knee joints in the sagittal plane. The total weight of the system is 14.2 kg, including a $10,000\,mAh$ lithium polymer (LiPo) battery, which lasts for about 2 h of operation. Each SEA module is able to generate 17.472 Nm continuous torque. For the control device, a National Instruments (NI) single-board real-time operating system (sbRIO-9632) was selected with a NI LabVIEW programming.

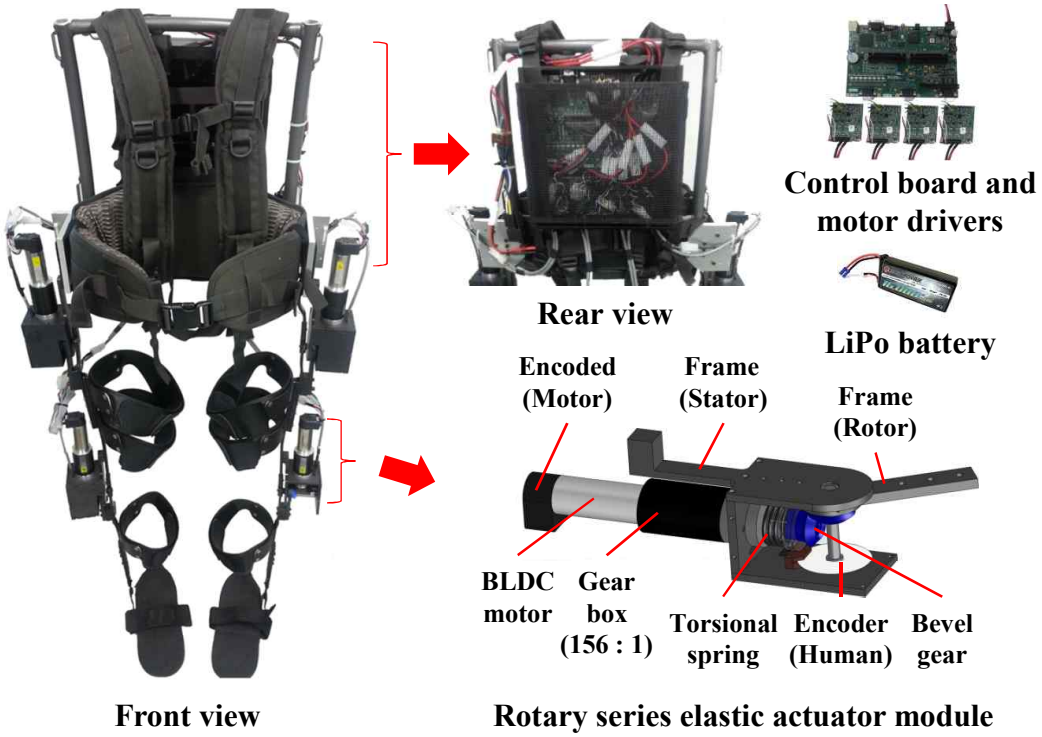

Figure 2.1: Lower extremity exoskeleton system with the four rotary series elastic actuator (SEA) modules.

2.2.2 Modeling of a Rotary Series Elastic Actuator (SEA)

The series elastic mechanism has many benefits in force control, including high force fidelity, low impedance, low friction, and good force control bandwidth [143]. In particular, the SEA mechanism is capable of converting force control into position control using a compliant component between the external load and the actuator output. The output force is controlled by manipulating the deflection of the compliant component. Figure 2.2 shows a schematic diagram of the SEA mechanism in the exoskeleton. To generate the desired torque, τ_d, the reference position for the motor r is calculated as follows:

$$r = \theta_H + \frac{\tau_d}{k} \tag{2.1}$$

where θ_H is the angular position of the human-side, τ_d is the desired torque, and k is the spring constant.

The ultimate goal of the controller is to manipulate the motor position θ_M by adjusting τ_M in the presence of interactions with the user, θ_H and τ_H. To describe the dynamics of

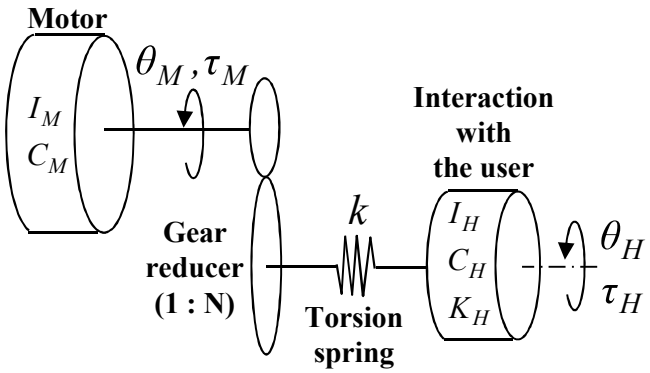

Figure 2.2: Schematic diagram of the rotary series elastic actuator module interacting with the human (I, C, and K: inertial, damping, and spring parameters respectively, θ: angular position, and τ: torque where subscript M and H are motor and human respectively).

the motor and the human-side, the following governing equations were derived:

$$(N^2 I_M s^2 + N^2 C_M s + k)\frac{\theta_M}{N} - k\theta_H = N\tau_M \tag{2.2}$$

$$(I_H s^2 + C_H s + K_H + k)\theta_H - k\frac{\theta_M}{N} = \tau_H \tag{2.3}$$

where I, C, and K are the inertial, damping, and spring coefficients, respectively, in which subscripts M and H refer to the motor and the human, and N is the reduction ratio of the gear box. Removing the human motion term θ_H by substituting (3) into (2), the resulting motor position θ_M was determined by two inputs: the motor torque τ_M and the torque generated by the human τ_H.

$$\begin{aligned}\theta_M = &\frac{1}{(I_M s^2 + C_M s) + \frac{k}{N^2}\left(\frac{I_H s^2 + C_H s + K_H}{I_H s^2 + C_H s + K_H + k}\right)}\tau_M \\ &+ \frac{\frac{k}{N}\left(\frac{1}{I_H s^2 + C_H s + K_H + k}\right)}{(I_M s^2 + C_M s) + \frac{k}{N^2}\left(\frac{I_H s^2 + C_H s + K_H}{I_H s^2 + C_H s + K_H + k}\right)}\tau_H\end{aligned} \tag{2.4}$$

Note that human factors, such as I_H, C_H, and K_H, are included in the governing equation, and τ_H acts as external disturbances. To design a model-based robust controller, it was necessary to identify the system parameters accurately. In actual situations, however, it may be impossible to identify the exact values of I_H, C_H, and K_H, and they could be varied by the interaction with the user [97]. Thus, to apply the model-referenced controller, a nominal model of the system, excluding the unknown parameters, was selected in the previous

studies, and the effects of the unknown parameters were considered as uncertainties [96, 97]. Considering the complexity in modeling the SEA module, simple implementation of a control algorithm is a strong advantage of TDC that requires only simple information on the system, specifically, the nominal value of the control distribution matrix.

2.3 Application of Time Delay Control (TDC)

2.3.1 Implementation of TDC

The key idea of TDC is to estimate the effect of uncertain terms at the present time t as the value in the past $(t - L)$ close to that time, with a small time delay L. To regulate position of a motor, the law of the TDC was derived as follows [206]:

$$\begin{aligned} u(t) &= u(t-L) \\ &\quad + \frac{1}{\hat{b}}[-\dot{z}_2(t-L) + \omega_n^2(r - z_1) - 2\zeta\omega_n z_2] \end{aligned} \tag{2.5}$$

where $\hat{b}$ is a nominal value of the control distribution coefficient, z_1 and z_2 are position and velocity estimated by the state observer, and ω_n and ζ are natural frequency and damping ratio of model dynamics to be realized by the control law. Detailed information on TDC, including the derivation of control law, meaning of each term, design of a state observer, and stability issues are well-explained in [206, 26].

As in (2.5), $\hat{b}$ determines the intensity scale of the control law, and it was important to select an appropriate value of $\hat{b}$ to realize satisfactory performance of the TDC. However, it was difficult to acquire $\hat{b}$ by identifying the plant dynamics because of unmodeled dynamics in the identification procedure. In addition, due to the inherent characteristics of the control law in (2.5), the sampling rate of the control system affected the intensity of the control input, because the additive terms accumulated more quickly with a faster sampling rate; as a result, the proper value of $\hat{b}$ varied with different sampling rates.

Due to that reason, it was suitable to determine $\hat{b}$ experimentally. In detail, the corresponding control input calculated using (2.5) was observed with $\hat{b} = 1$ and $r = 1\ rad$ (step response), while the designed model dynamics were entered into the control system without inserting the control input into the actual system. Depending on the range of the observed control input, $\hat{b}$ was selected such that the required control input was within the available range of u. After $\hat{b}$ was roughly determined, it was specified further by observing the resulting tracking performance.

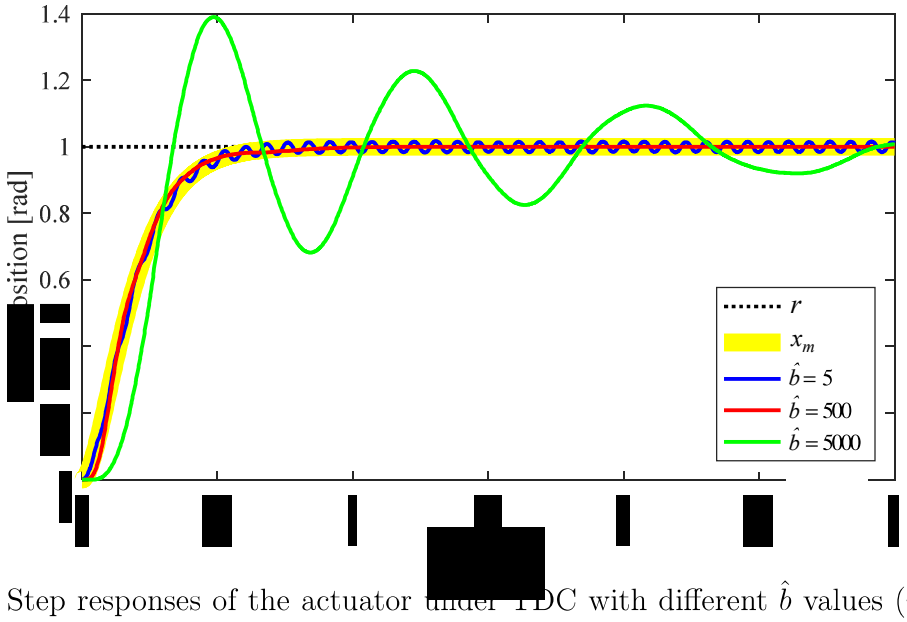

Figure 2.3: Step responses of the actuator under TDC with different $\hat{b}$ values (r: reference position and x_m: simulated position of the model dynamics).

As shown in Figure 2.3, the three cases with different values of $\hat{b}$ showed different patterns of response, although all the cases converged to the desired response x_m. If $\hat{b}$ was underestimated ($\hat{b} = 5$), the control input was calculated to be too strong. The overestimated control command enabled the fast response, but severe chattering was accompanied. In contrast, if $\hat{b}$ was overestimated ($\hat{b} = 5000$), then the response was too slow with the underestimated control command. With an appropriate value ($\hat{b} = 500$), acceptable tracking performance was observed. Note that the shorter the loop time, the larger $\hat{b}$ required for the same performance.

2.3.2 Experimental Verification of TDC

To prove successful operation of TDC, the step response of the controlled plant, the observer, and the model dynamics were compared as shown in Figure 2.4 (a). The results show that the observer successfully estimated position and the controlled system satisfied the model dynamics; the tracking error ($x_m - x$) converged quickly without steady state error. Another proof was discovered as a result of sinusoidal sweeping, as shown in Figure 2.4 (b). Recording the output position of the motor, a sinusoidal reference was given to the actuator, the frequency of which ranged from $0.5\,rad/sec$ to $50\,rad/sec$. The data set in the frequency domain, using the least-squares method, were fitted with a general second-order

system, $G(s) = \omega_n^2/[s^2 + 2\zeta\omega_n s + \omega_n^2]$. As a result, the identified natural frequency ω_n and the damping ratio ζ were $10.1931\,rad/sec$ and 1.0115 in the controlled system $G_c(s)$, almost identical to the model dynamics $G_m(s)$ in which the natural frequency and damping ratio were $10\,rad/sec$ and 1.

To verify performance of TDC against external disturbance, the responses with and without disturbances were compared in Figure 2.5 (a). The reference position r was given as a sine wave, and the motor followed the reference, with some delay due to the model dynamics. Under the same experimental conditions, an external disturbance was additionally given to the motor: the shaft of the motor was clenched by hand during the experiments. Despite the disturbances, no significant discrepancies were observed in the output positions, x_{wod} and x_{wd}, because additional control commands compensated for the external disturbances as shown in Figure 2.5 (b). The tracking error became larger in the presence of the disturbance, but the difference was not significant (Figure 2.5 (c)).

2.4 Model-inverse Time Delay Control (MiTDC)

2.4.1 Derivation of MiTDC

In the previous section, TDC performance was validated experimentally; the results indicated that the controlled plant followed the model dynamics. However, the controlled plant experienced intrinsic delays when it tracked the given reference position (Figure 2.5), resulting in undesirable torque output in the SEA module. The deflection of the spring in the SEA module generated output torque; the torque output can be calculated by Hooke's law, as follows: $\tau = k(\theta_M - \theta_H)$.

To reduce the delays in position tracking, the speed of the model dynamics could be increased by selecting a higher value of ω_n. However, as in (2.5), the higher value of ω_n leads large control effort due to $\omega_n^2(r - z_1)$, amplifying the position error, and it can be restricted by limit of the given system; in our system, the saturation condition was set as $3V$ for safety. To overcome the limited performance, in the proposed strategy, the delay was compensated by a predicted reference position using the inverse of the model dynamics in TDC. If the plant followed the virtual reference while satisfying the model dynamics, the resultant response of the plant could consequentially match up with the original reference without causing saturation in control input.

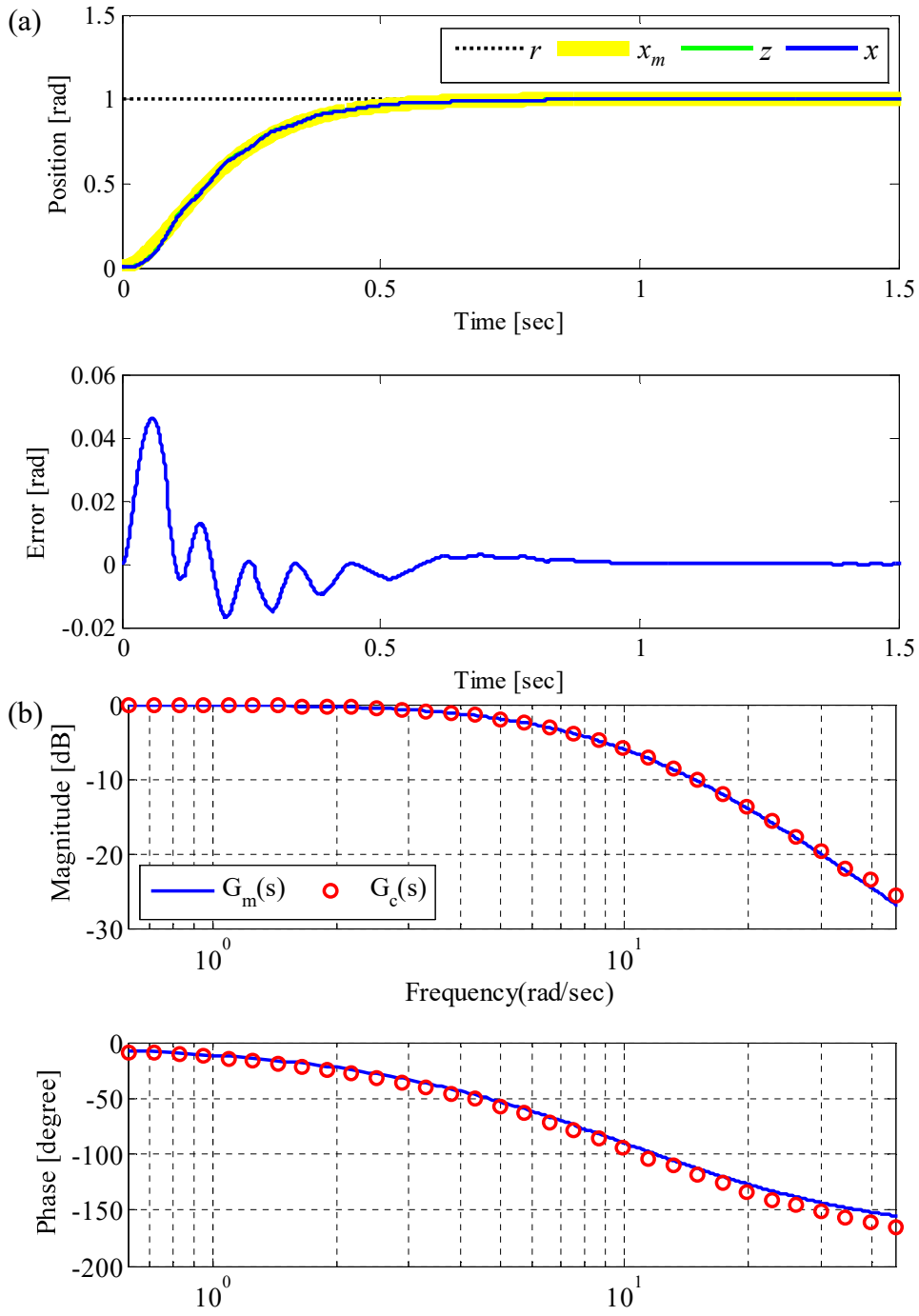

Figure 2.4: Experimental verification of TDC: (a) step response (r: reference position ($1rad$), x: position of the plant, z: position estimated by the state observer, x_m: position estimated by the model dynamics, and $Error = (x_m - x)$)), (b) frequency response acquired by a sinusoidal sweeping ($G_c(s) = 104.9/[s^2+20.6s+104.9]$: identified dynamics of the controlled system and $G_m(s) = 100/[s^2 + 20s + 100]$: designed model dynamics).

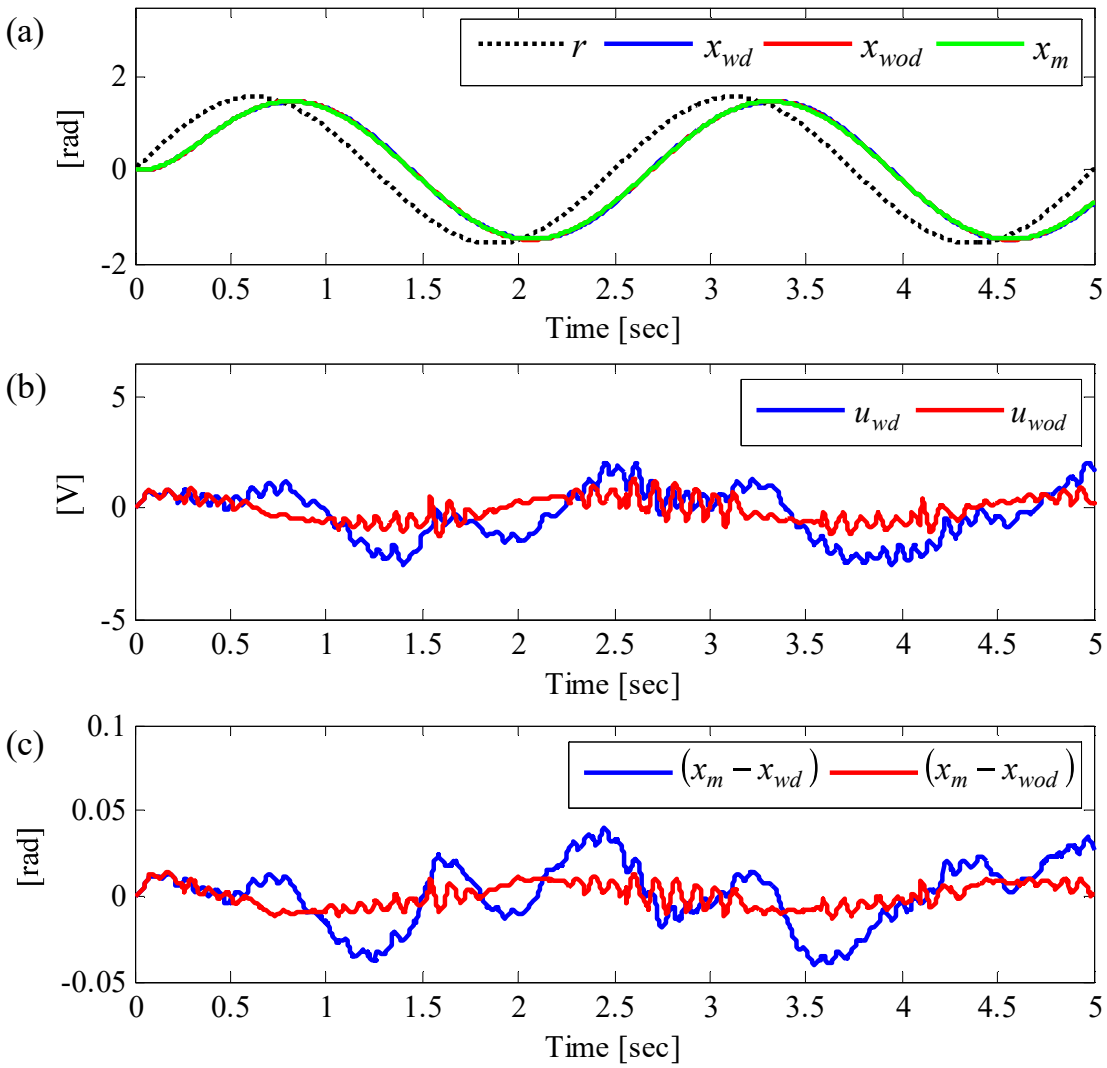

Figure 2.5: Position regulation under TDC with and without external disturbances: (a) position, (b) control input, and (c) tracking error (x_{wd} and x_{wod}: position of the plant with and without disturbance, x_m: position calculated by the model dynamics, u_{wd} and u_{wod}: control input with and without disturbance).

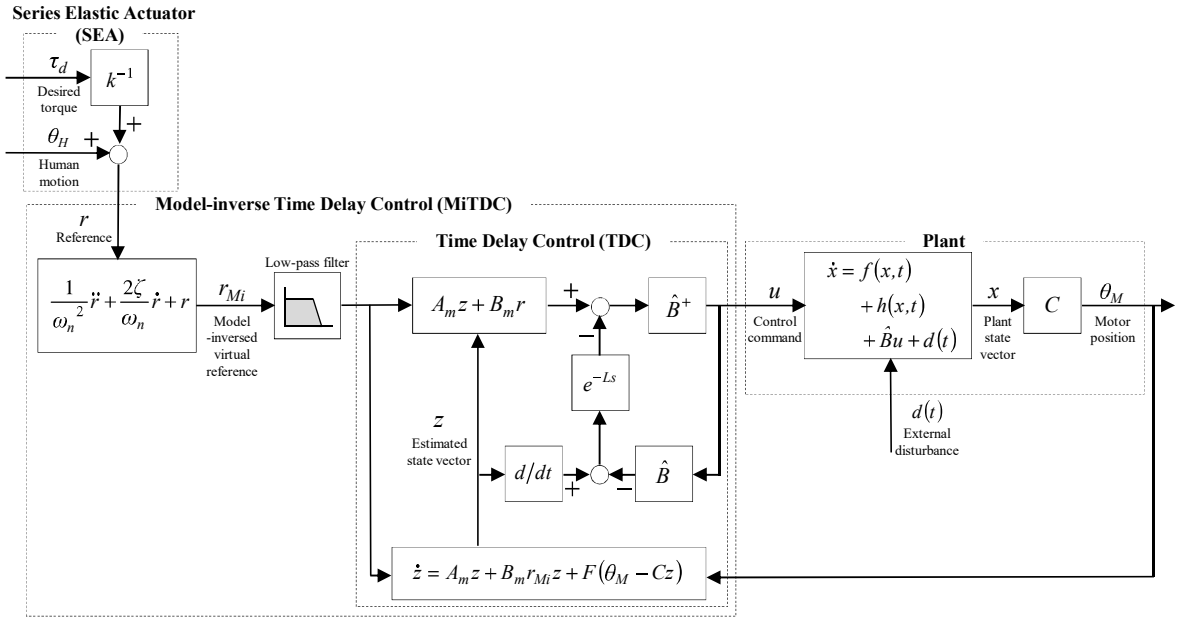

Figure 2.6: Block diagram of model-inverse time delay control (MiTDC) in the SEA module.

The virtual reference was calculated, as follows:

$$r_{Mi} = \frac{1}{\omega_n^2}\ddot{r} + 2\frac{\zeta}{\omega_n}\dot{r} + r \tag{2.6}$$

where the calculation of (2.6) was implemented by backward differentiation. Due to amplification of sensory noises from double differentiation, the calculated r_{Mi} included noisy signals. However, the noise had little effect on the response, because the model dynamics with a natural frequency $\omega_n = 10\, rad/sec$ acted as a low pass filter (Figure 2.4 (b)). Although the model dynamics may reject the high frequency noises, an additional low pass filter was applied.

To realize satisfactory performance of MiTDC, it is necessary to determine a speed of the model dynamics appropriately. For example, if the model dynamics is very slow, its inverse will be very fast and the resultant virtual reference will consist of very high frequency signals. Since the high frequency signals cannot be separated from the sensor noise, the important signals can be rejected by the low pass filter. In addition, it will be very challenging for the slow TDC loop to follow up the fast reference. Contrary, if the model dynamics is very fast, the effectiveness of the virtual reference will be negligible, and the entire control system will act like the conventional TDC. Therefore, it was important to select a moderate speed of the model dynamics to divide severity caused by the required fast response.

Also, note that the resultant performance of the controller may be severely affected by a discontinuous r due to differentiation process. However, the reference would hardly be given as a discontinuous form, because it scarcely occurs that the desired force feedback to the user or the movement of the user varies discontinuously in a physical human-robot interaction system.

The block diagram illustrated in Figure 2.6 describes the entire control system with the SEA module. Based on the desired torque trajectory and measured human motion, the reference position was determined. After that, using the inverse of model dynamics, the original reference position r was transformed as a new reference position r_{Mi} which was ahead of r as much as the model dynamics. Since the controlled system under TDC satisfied the linear and certain model dynamics in a robust manner, the controlled system under MiTDC consequently satisfied very fast tracking performance, following up r almost perfectly. That is the fundamentals of MiTDC to realize position tracking with minimal delay and accurate force-mode control in the SEA module.

For the application of TDC, the sampling rate was set as $1\,kHz$ in all experiments. It covered the frequency range of uncertainties caused by motor dynamics and movement of the user; the frequency response of the identified motor dynamics over $10\,Hz$ was negligible (below $-60\,dB$), and the angular velocity of the joints in the lower extremity hardly exceeds $10\,Hz$ [194]. The introduction of the virtual reference r_{Mi} in the MiTDC does not affect stability of the system, because the inverse of the model dynamics does not change the closed loop characteristic equation of the entire system. Therefore, the stability of the proposed control system was guaranteed by the criterion of TDC analytically proved in [26].

2.4.2 Experimental Verification of MiTDC

To check torque-mode control performance with an external disturbance, the experimental setup in Figure 2.7 (a) was prepared. The input motor on the right provided external movement to the output side of the SEA module, acting as human motions, and the controlled motor was under a control law to generate the desired torque by adjusting the deflection of the spring. The output position of each motor was measured by an encoder embedded in the motor, and a rotary torque transducer was used to identify the spring constant and to measure the output torque of the SEA module as a reference value.

Figure 2.7 (b) shows the experimental results that the controlled system tried to adjust the torque output of the SEA module to be zero in the presence of sinusoidal movements

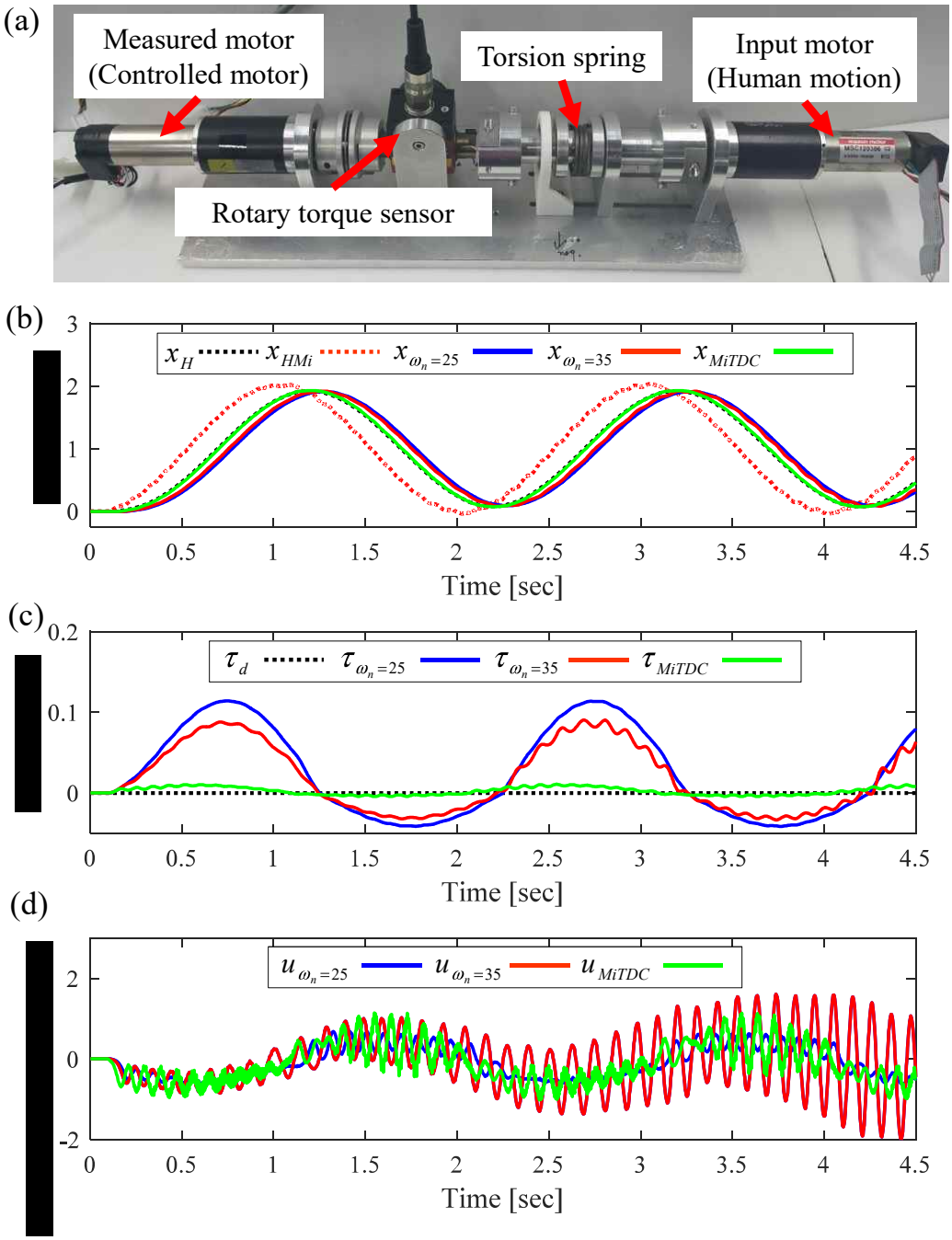

Figure 2.7: Experimental verification of MiTDC (a) experimental setup, (b) zero-torque regulation in the SEA module (x_H: position of the human-side motor, x_{HMi}: virtual reference calculated by the inverse model dynamics, x: position of the controlled motor, τ_d: desired torque, τ: actual output torque, and u: control input).

generated by the input motor. In an ideal case, the position of the actuator x_{MiTDC} should be matched with the human-side position of the SEA module x_H for no deflection in the spring. However, the controlled system under TDC law, $x_{\omega_n=25\,rad/sec}$ and $x_{\omega_n=35\,rad/sec}$, showed delays between x_H and x, even the speed of the model dynamics was increased up to $35\,rad/sec$. Due to the delay in position tracking, the undesirable torques were generated as shown in $\tau_{\omega_n=25\,rad/sec}$ and $\tau_{\omega_n=35\,rad/sec}$. Experimental results with a model dynamics faster than $\omega_n = 35\,rad/sec$ were not included in the result because of saturated control input and much deteriorated tracking performance. In other words, the performance of TDC was limited by the saturated control input.

In case of MiTDC, the virtual reference x_{HMi} was calculated by substituting the reference position x_H into (2.6), which corresponded to the predicted reference by solving the differential equation. The output position of the actuator, x, closely pursued the external movement of the output shaft, x_H, decreasing the torque error significantly as shown in τ_{MiTDC}. Some remaining torque error was due to the discrepancy between the realized model dynamics and the compensated model dynamics; the performance could be improved by adjusting $\hat{b}$ in (2.5). Even with smaller control input, MiTDC showed better performance than TDC.

In the experiment, the controlled system under TDC with $\tau_{\omega_n=35\,rad/sec}$ showed chattering behavior even the control input was not saturated, which cannot be prevented by adjusting $\hat{b}$. The chattering might originate from the nature of TDC which satisfies a model dynamics very strictly by accumulating the uncertainties with respect to time as in (2.5). To overcome the performance limitation, some of required rapidity was shifted into a feedforward term in the proposed strategy, which improved the resultant performance significantly. In other words, the fast response was realized by alleviating the required rapidity within the TDC loop.

To test the back-drivability of the SEA module, the velocity of the input motor in the experimental setup in Figure 2.7 (a) was controlled, ranging from $-20\,rad/sec$ to $20\,rad/sec$, while the controlled motor regulated the output torque of the SEA module to be zero. Figure 2.8 shows the experimental results in the cases in which no control, TDC, or MiTDC were applied. In the uncompensated case, the resistive torque within the motor dynamics was measured; the measurement results showed bias, stiction, and Coulomb friction. Additionally, the asymmetric response in the uncontrolled case was mainly caused by asymmetry of the torsional spring. In the case in which the conventional TDC was applied, the bias and stiction were removed; however, resistive torque was generated, proportional to the velocity of the input motor, due to the delay caused by the model dynamics. The proposed control

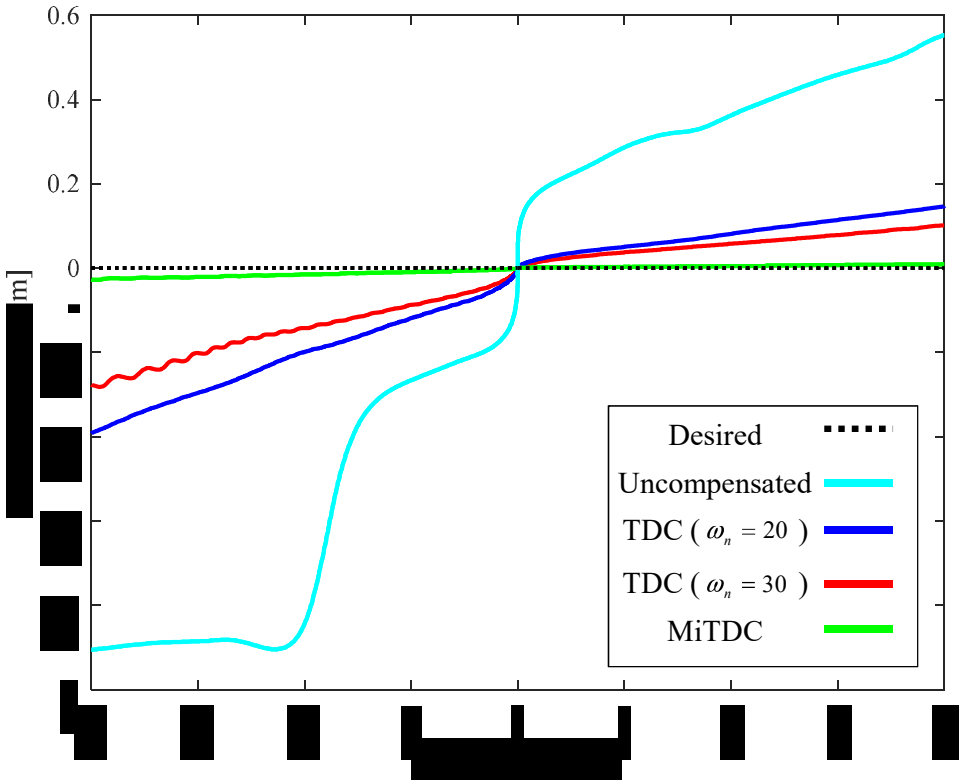

Figure 2.8: Experimental results of back-drivability test in the SEA module.

strategy, MiTDC, completely compensated for all resistive torque, realizing back-drivability of the SEA module.

2.4.3 Application of MiTDC to free oscillation of a pendulum

For further verification of zero impedance control, the free oscillation of a pendulum connected to the SEA module was demonstrated. The experimental equipment was prepared as shown in Figure 2.9 (a). The pendulum was released with initial angle of 60 degrees, and the motor was under MiTDC law to follow up the movement of the pendulum measured by the optical encoder to realize zero impedance in the output of the SEA module. As shown in Figure 2.9 (b), the experimental result was compared with the case without the spring, which represented the ideal free oscillation only affected by bearing friction. Experimental result indicates that free oscillation of the pendulum was demonstrated, even it was connected to the SEA module, which refers that MiTDC realized zero impedance in the SEA module successfully.

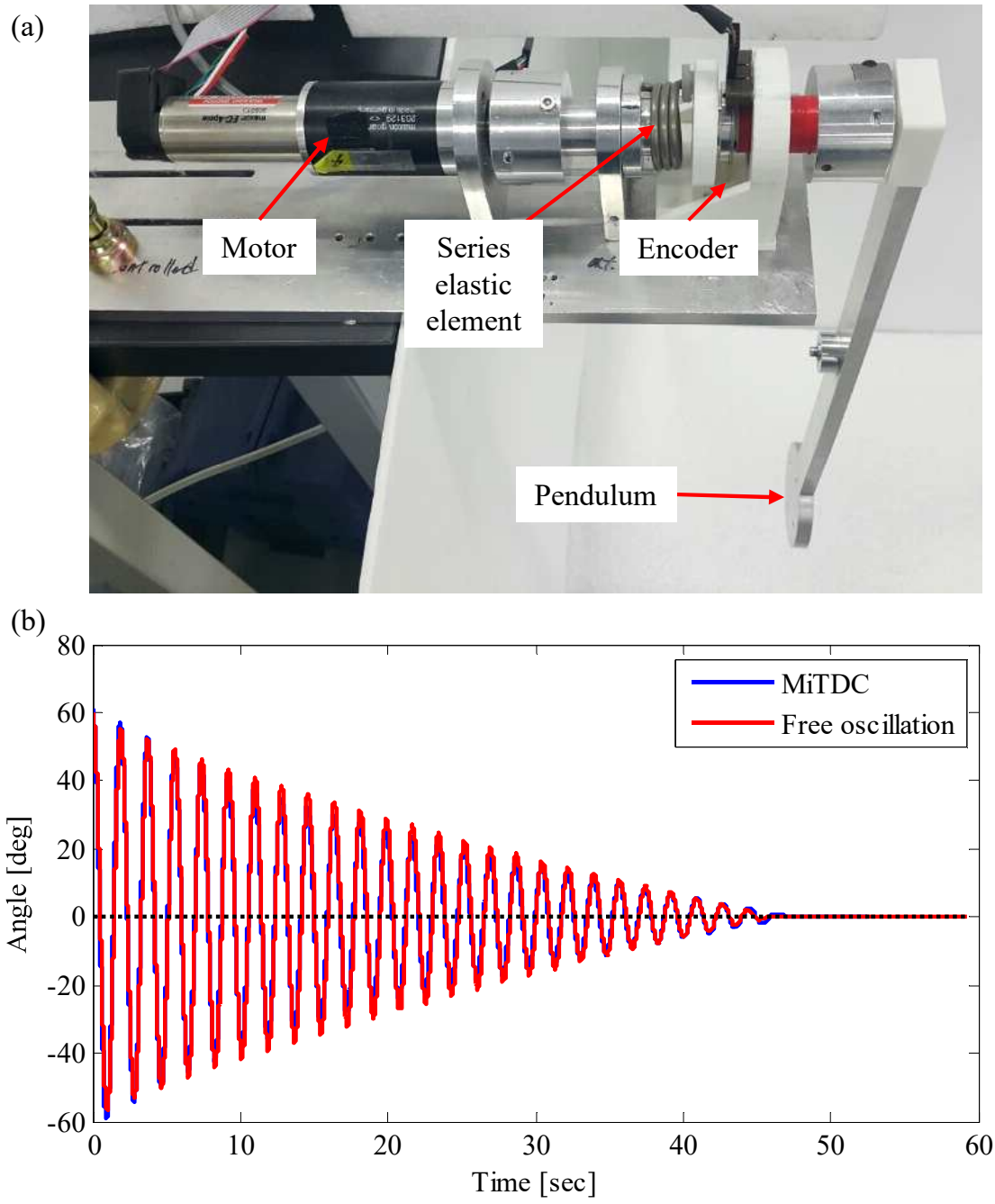

Figure 2.9: Free oscillation of the pendulum connected to the SEA module under MiTDC: (a) experimental setup, (c) experimental results.

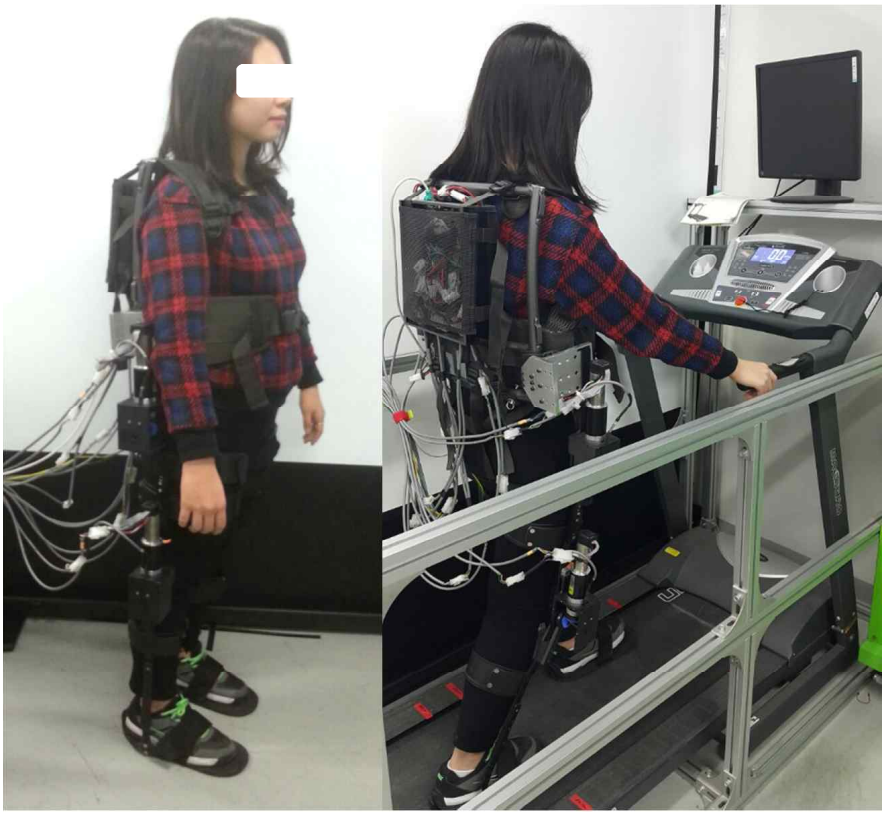

Figure 2.10: Experimental setup: the lower extremity exoskeleton worn by the subject.

2.4.4 Application of MiTDC to a Lower Extremity Exoskeleton

A lower extremity exoskeleton was worn by a female subject (Figure 2.10), whose weight was 53 kg and height was 163 cm. The subject walked on the treadmill at a rate of 2 km/h while the actuator modules generated the assistant torque as a sinusoidal pattern at the knee joint. Figure 2.11 shows the experimental results during a gait cycle. The black dashed line x_H in Figure 2.11 (a) shows the knee joint angle measured by the encoder installed in the exoskeleton structure, and x_d refers to the desired position of the motor, calculated by substituting the desired torque τ_d and x_H into (2.1) (Figure 2.11 (b)). As shown in the results, the motor position x followed x_d well, even in the presence of human motion x_H, satisfying $\tau \cong \tau_d$; the root-mean-square (RMS) of the torque error was 0.1297 Nm (Figure 2.11 (c)). For the exoskeleton system, it is an important task to determine the torque pattern of each actuator according to the user's motion. Since the aim of this research was to validate accurate torque control in the SEA interacting with the human, the sinusoidal torque pattern

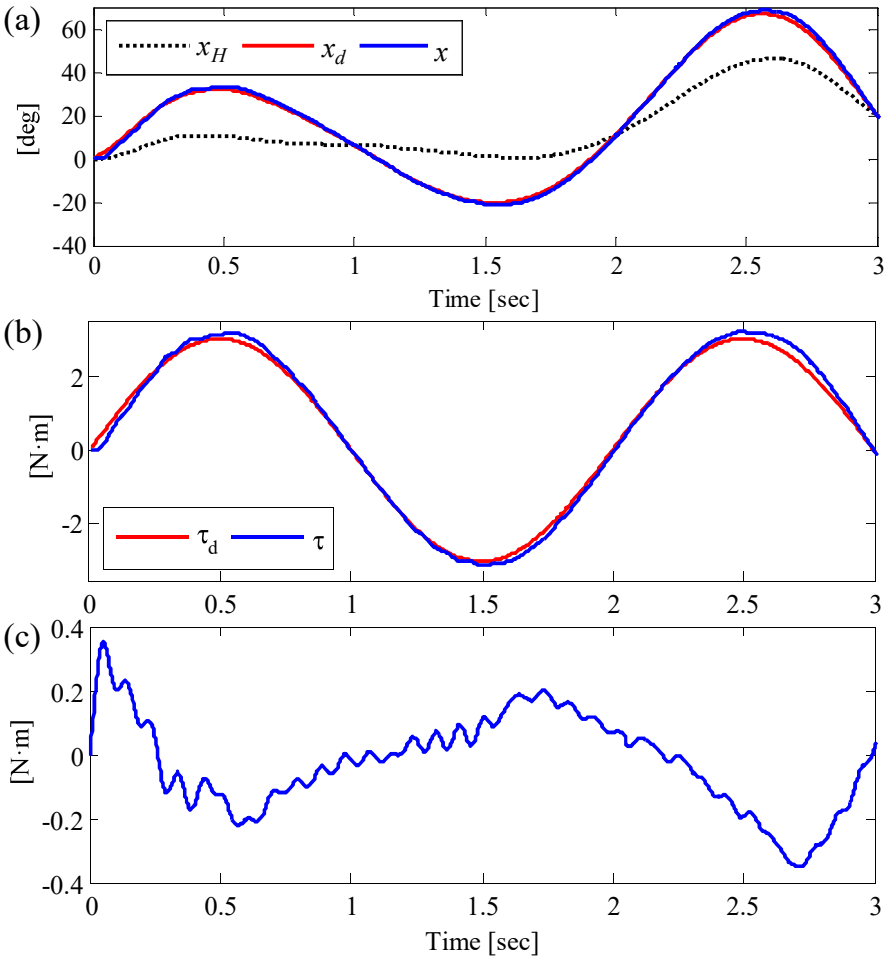

Figure 2.11: Experimental results of torque regulation using MiTDC to assist the knee joint during walking: (a) position, (b) torque, and (c) torque error (x_H: position of the human-side motor, x_m: position of the model dynamics, and x: position of the controlled motor, τ_d: desired torque and τ: actual output torque, and torque error$(= \tau_d - \tau)$).

with an actuator module was enough to demonstrate it.

2.5 Summary

In this chapter, a rigid exoskeleton for the lower extremity was developed. To control the interaction force between the exoskeleton and the user, series elastic actuator modules were implemented with a time delay control (TDC). Robust performance can be achieved by the TDC without accurate information of control systems, which is suitable for the exoskeleton usually undergoing uncertain interactions with the user. The performance of the controller was further improved by introducing a feedforward term, which was a main idea of model-inverse time delay control (MiTDC) proposed in this study. As verified with the experimental results, the suggested actuator modules and the controller can be used as a robust force-mode control platform for exoskeletons.

Chapter 3

Estimation of Muscular Forces for Determining a Desired Force Trajectory*

3.1 Introduction

For an exoskeleton system, it will be the most beneficial to activate it according to the intention of the user. Because the motions of the human is exerted by muscles, muscular forces can be a direct clue for the motion intention. As well as the purpose, many studies have been conducted to estimate muscular forces for 1) fundamental and quantitative analysis of human motion [207], 2) design of systemic training and analysis of injury mechanisms in the field of sports science [76], 3) diagnosis of abnormal muscular functions and evaluation of the therapeutic effects of rehabilitation [173], and 4) design and development of prosthetic and orthotic [65] and human-robot interaction systems such as an exoskeleton [6, 132, 193].

In spite of the many potential applications, however, estimation of muscular forces have remained as a challenging task. Among them, the most simple is to connect a force transducer directly to a muscle [190]. However, it cannot be applied to the human because it requires surgery to the body. Surface electromyography (sEMG) is the most widely accepted non-invasive method to measure the activation level of a muscle [39]. However, it requires complex and frequent calibration processes due to the high noise/signal ratio, differences among individuals, and surrounding conditions. Additionally, only superficial muscles can

*The contents in this chapter is based on the published work of the author [91].

be measured and it is difficult to block interference from neighboring muscles. Moreover, the true relationship between EMG signals and muscular forces is not yet fully understood. Other researchers have attempted to measure muscle hardness using ultrasound waves and muscle volume using strain sensors, but these have similar drawbacks to EMG [36, 2].

Recently, computational simulation programs, such as OpenSim [40], were developed to analyze motor tasks. They provide a model-based estimation method, which enables to build a musculoskeletal model and analyze movements and muscle functions conveniently. The fundamental algorithm within the simulation is 'computed muscle control' (CMC), which aims to find the optimal muscle activation according to given kinematic data of the body, such as joint angles, velocities, and accelerations [174]. The algorithm demands relatively high computational costs due to the intrinsic calculation processes including both optimization and forward dynamics.

The inverse dynamics-based static optimization is one of model-based estimation methods, which requires little computation cost, because it does not include a forward dynamic process. In addition, unlike the other model-based estimation methods, it is possible to be implemented in real-time, since the inverse dynamics-based static optimization does not demand the full set of motion data in advance. The inverse dynamics-based static optimization has been applied to various motor tasks: walking [32, 38, 37, 56, 136, 137, 150, 156], spinal compression [154, 13, 71, 99, 125, 22], finger [21], wrist [138], elbow [146, 141], arm, and shoulder [70, 108, 50] movements.

More specifically, the first step in the inverse dynamics-based static optimization is to capture the motions and external forces applied to the body. In previous research, the body movements were usually measured by a camera-based motion capture system, and external forces were measured by a force plate. Because the measurement systems have inherent limitations in terms of mobility, this is only available within a laboratory environment and natural movement may be restricted by use of a fixed force plate. In addition, it is not easy to equip the experimental instruments because of spatial and cost limitations.

Therefore, in this study, wearable systems were developed to capture motion information during movements to estimate individual muscular forces based on the inverse dynamics-based static optimization, which cannot implemented with limited sensor systems. Specifically, to augment mobility of the conventional motion capture system, a wearable sensor system for the lower extremity was developed, measuring joint angles of the lower extremity and ground reaction force (GRF). In addition, a wearable hand exoskeleton system was developed to measure joint angles of the fingers and external force applied at the finger tips,

which cannot be accomplished by the conventional measurement system. As a result, the individual muscular forces were successfully estimated, during walking and during extension of the fingers, respectively.

The remainder of this chapter is organized as follows. In Section 3.2, the wearable sensor system for the lower extremity is described with experimental verification of it. In Section 3.3, application of the inverse dynamics-based static optimization is described. In Section 3.4, the experimental results to estimate the individual muscular forces of the lower extremity are presented. Correspondingly, the hand exoskeleton and related experimental results are presented in the following three sections (Section 3.5-3.7).

3.2 A Lower Extremity Wearable Sensor System

The wearable sensor system consisted of a wearable structure, four IMUs and a manually-developed insole-type GRF sensor (Figure 3.1). The objective of the sensor system was to measure the rotational angles of the hip, knee, and ankle joint, and two-dimensional pelvic acceleration and GRF, not restraining the motion of the user. For that purpose, the IMU was better than a conventional rotary sensor, such as an encoder, which was required to be aligned with the articular axis. Furthermore, the GRF sensor was fabricated with silicone tubes attached on the insole, which made it lighter and softer than typical force transducers.

3.2.1 Inertial Measurement Unit (IMU)

To measure joint angles, the four commercially available 9 DOFs IMUs were adopted, which provide Euler angles [195]. Since the Euler angles were given with respect to the absolute coordinate system (i.e., the earth), the reference frame was defined to measure joint angles by attaching an IMU on the trunk. Therefore, the postures of each segment were calculated as a unit vector with respect to the reference coordinate. For example, the following provides the detailed steps for calculating knee joint angle (Figure 3.2). The roll axes of the two IMUs attached on the thigh and shank were aligned with the longitudinal axes of each segment (Figure 3.2(a)), setting the approaching vectors along the longitudinal axis of each IMU:

$$v_s^s = [(1, 0, 0)^T]^s \tag{3.1}$$

Figure 3.1: Configuration of the wearable sensor system.

where the superscript indicates which reference coordinate the vector is expressed in and the subscript corresponds to whose approaching vector is under consideration out of the thigh, shank, and foot. Consequently, a rotational matrix of the IMU was given as follows:

$$R = \begin{bmatrix} c\gamma c\beta & c\gamma s\beta s\alpha - s\gamma c\alpha & c\gamma s\beta c\alpha + s\gamma s\alpha \\ s\gamma c\beta & s\gamma s\beta s\alpha + c\gamma c\alpha & s\gamma s\beta c\alpha - c\gamma s\alpha \\ -s\beta & c\beta s\alpha & c\beta c\alpha \end{bmatrix} \tag{3.2}$$

where c and s; cosine and sine, α, β, and γ; roll, pitch, and yaw angles respectively. Then, the longitudinal direction of the segment was expressed with respect to the earth by multiplying

(3.2) to (3.1) (Figure 3.2(b)):

$$v_s^e = \begin{bmatrix} c\gamma c\beta \\ s\gamma c\beta \\ -s\beta \end{bmatrix} \tag{3.3}$$

where the superscript e and the subscript s refers to the earth and the segment.

Next, the approaching vectors of the segments can be expressed with respect to the reference coordinate of the IMU on the trunk by multiplying the inverse of (3.2) on the trunk (Figure 3.2 (c)):

$$v_s^{tr} = \begin{bmatrix} \begin{pmatrix} c\beta_1 c\beta_2 c(\gamma_1 - \gamma_2) \\ +s\beta_1 s\beta_2 \end{pmatrix} \\ \begin{pmatrix} -c\beta_1 s\beta_2 s\alpha_1 \\ +c\beta_2(c(\gamma_1 - \gamma_2)s\beta_1 s\alpha_1 \\ -c\alpha_1 s(\gamma_1 - \gamma_2)) \end{pmatrix} \\ \begin{pmatrix} -c\beta_1 c\alpha_1 s\beta_2 \\ +c\beta_2(c\gamma_1 c(\gamma_1 - \gamma_2)s\beta_1 \\ +s\alpha_1 s(\gamma_1 - \gamma_2)) \end{pmatrix} \end{bmatrix} \tag{3.4}$$

where the subscript '1' refers to the angles of the IMU on the target segment, and '2' represents the reference frame on the trunk.

Finally, the direction vectors of the thigh and shank were projected onto the sagittal plane, so that angle of the segments with respect to the body reference frame was calculated using simple trigonometrical functions (Figure 3.2 (d)):

$$\theta_i = -sgn(a)\arccos(\tfrac{a}{\sqrt{a^2+c^2}}) \quad (i = 1, 2, 3) \tag{3.5}$$

where θ is the angle of the segment with respect to the coordinate of the IMU on the trunk, and a and c are the first and third components of (3.4) respectively. The knee joint angle θ_k was calculated as $\theta_1 - \theta_2$.

An important issue was to align the IMU carefully along the longitudinal direction of the segment; xz plane of each IMU (Figure 3.2) was set to be parallel to the sagittal plane of the corresponding segment. To align each IMU, the subject was asked to stand still, and the IMUs were attached on the each segment maintaining the condition that the direction of gravity measured by the IMU was on xz plane. If the condition was satisfied, the xz plane

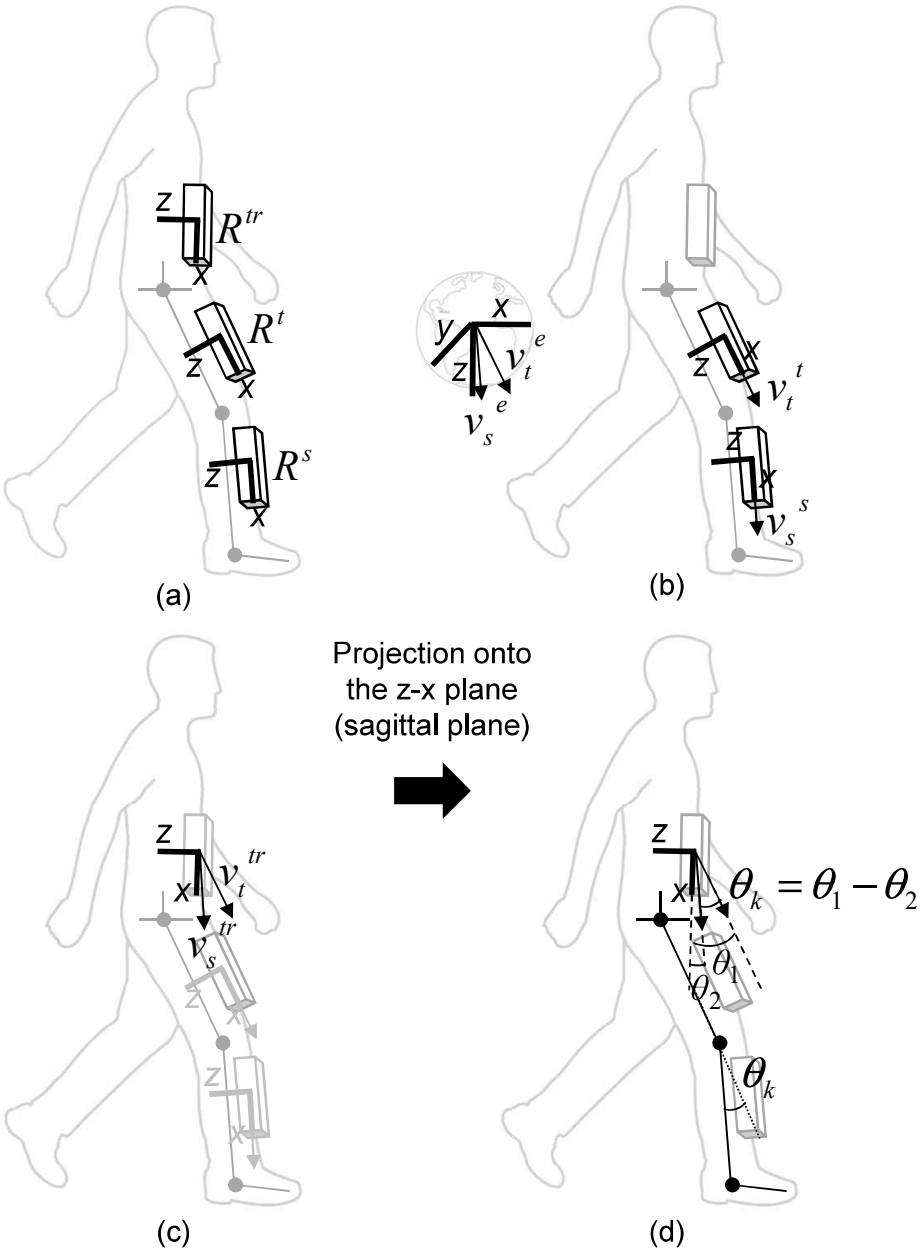

Figure 3.2: Procedures for converting the Euler angles from the IMUs to the knee joint angle: (a) extracting the rotation matrices from each IMU, (b) calculating the directional vector of each segment, (c) transforming the reference coordinate from the earth to the trunk, and (d) projecting the vectors into the sagittal plane and calculating the joint angle.

and the sagittal plane could be considered parallel. The IMUs were attached to the wearable structure which was made of straps and rubber bands. The wearable structure hold the IMUs tightly in place to ensure that alignment of IMUs was unchanged during experiments. The initial angles were set to zero before the start of an experiment, by asking the subject to stand and make the leg be straightened. All the same procedures were applied to calculate the joint angles at the hip and ankle.

3.2.2 Ground Reaction Force (GRF) Sensor

The proposed GRF sensor was a modified version of Smart shoes whose performance was validated in the previous studies [12, 11]. Figure 3.3 describes its configuration and the weight of the entire insole sensor was $125g$. The GRF sensor only measured force along the vertical axis from the ground by measuring pressure changes within the air bladders. The tangential GRF was assumed to be negligible, because the magnitude of the vertical force is about 20 times more than both the lateral shear force and progressional shear force during walking [140, 107]. From the force distribution of the four air bladders, the center of pressure (COP) of the GRF was also calculated with respect to the position of the ankle joint.

It was necessary to determine the relationship between the pressure changes within the air bladder and external force applied to it. For the calibration process, during the air bladder was pressurized, the corresponding external force was measured using a force transducer while simultaneously measuring the air pressure within the air bladder. Before the calibration process, to remove hysteresis effect caused by the viscoelastic properties of the silicone tubes, dynamic compensator was applied to compensate dynamic effect of the air bladders. The performance of the dynamic compensator was verified in the previous research [8, 98]. After the dynamic compensator was applied, the calibration procedures were conducted. The collected results were fitted with a line, as shown in Figure 3.4, to make a linear model, the slope of which was associated with the amount of air inside and the geometry of the bladder. The coefficient of determination, R^2, was also calculated, which indicated how the acquired data fit a linear model. On the assumption that the slope remained unchanged, it was necessary to initialize the signal to zero for accurate measurements.

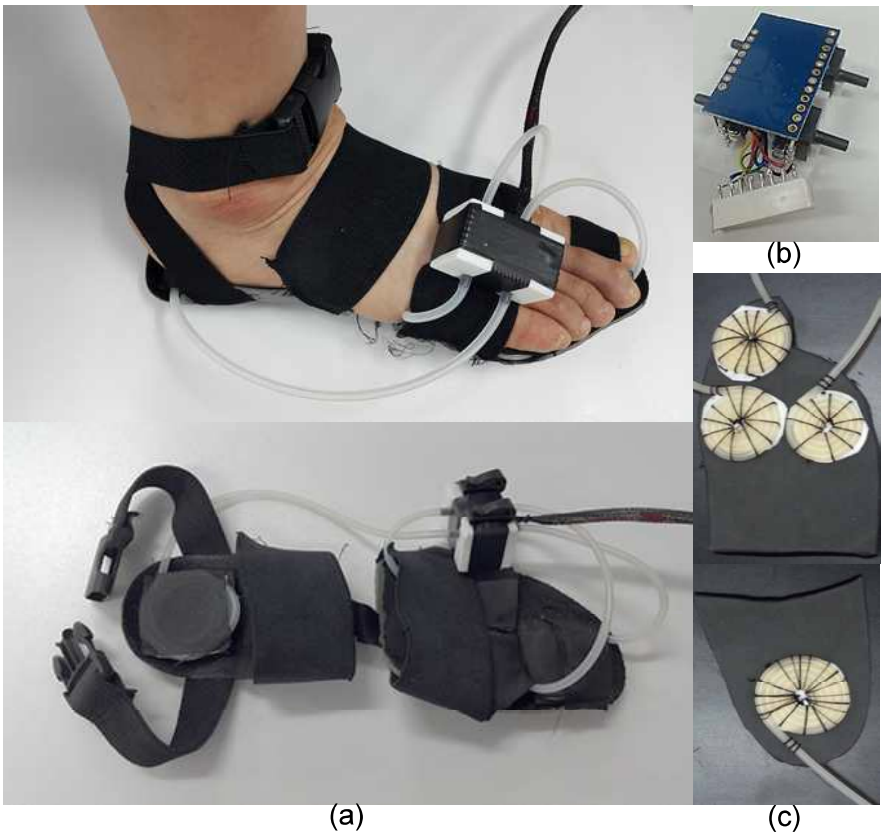

Figure 3.3: Manually-developed GRF sensor with four air bladders: (a) entire view, (b) pressure sensor module, and (c) air bladders attached to the insole.

3.2.3 Verification of the Wearable Sensor System

To verify the proposed wearable sensor system, joint angles and ground reactions were measured during normal walking by the proposed sensor system and camera-based motion capture system (Motion Analysis Corp.) with a force plate (Kistler) simultaneously [118, 95]. A subject (male, 178 cm, 70 kg) with no musculoskeletal disease walked at a speed of 3 km/h. As shown in Figure 3.5, the joint angles were successfully measured by the proposed sensor system. In addition, preparation time was less than a minute for attachment of the IMUs and initialization of joint angles, which was much faster than the camera-based motion capture system. Ground reactions and its center of pressure were also successfully measured by the proposed sensor system (Figure 3.6).

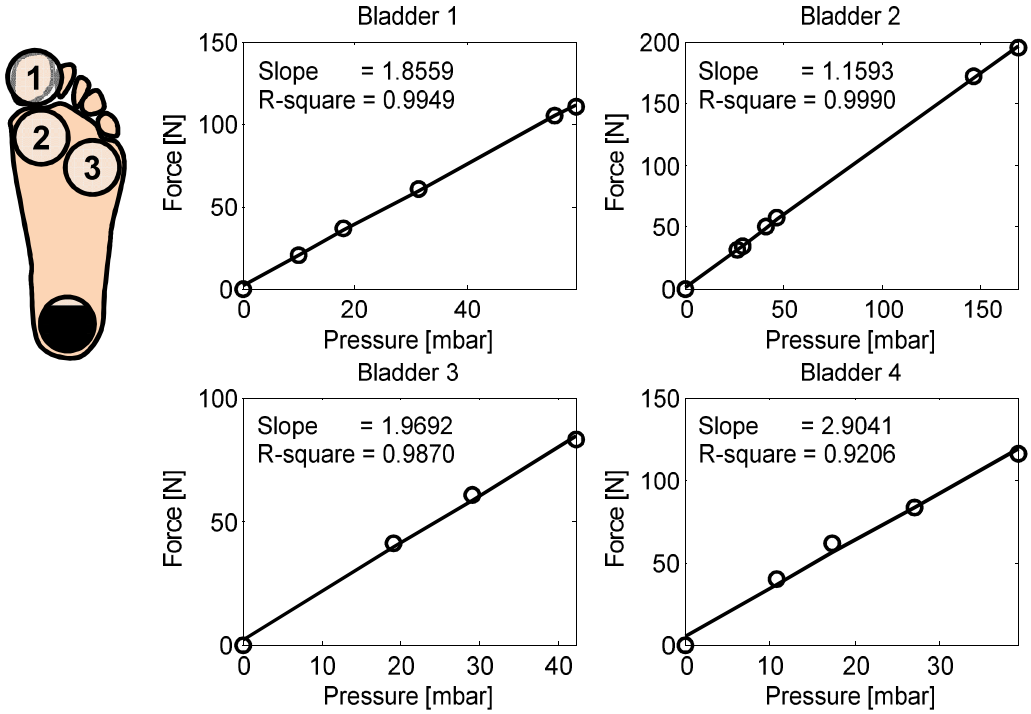

Figure 3.4: Calibration results with the slope and R^2 value.

3.3 Inverse Dynamics-based Static Optimization: Lower Extremity

Individual muscular forces of the lower limb were estimated by applying inverse dynamics-based static optimization through a series of procedures (Figure 3.7). The lower extremity was modeled as a two-dimensional musculoskeletal system in the sagittal plane that includes three segments (thigh, shank, and foot), three joints (hip, knee, and ankle), and nine muscle groups. The model includes information on body segment parameters to solve the inverse dynamics problem, and moment arms and the physiological cross-sectional area of each muscle for defining the static optimization problem. Based on the musculoskeletal model, a set of motion data were measured, the motion data were substituted into the inverse dynamic equations to estimate joint moments, and the individual muscular forces were estimated by solving the static optimization based on the joint moments.

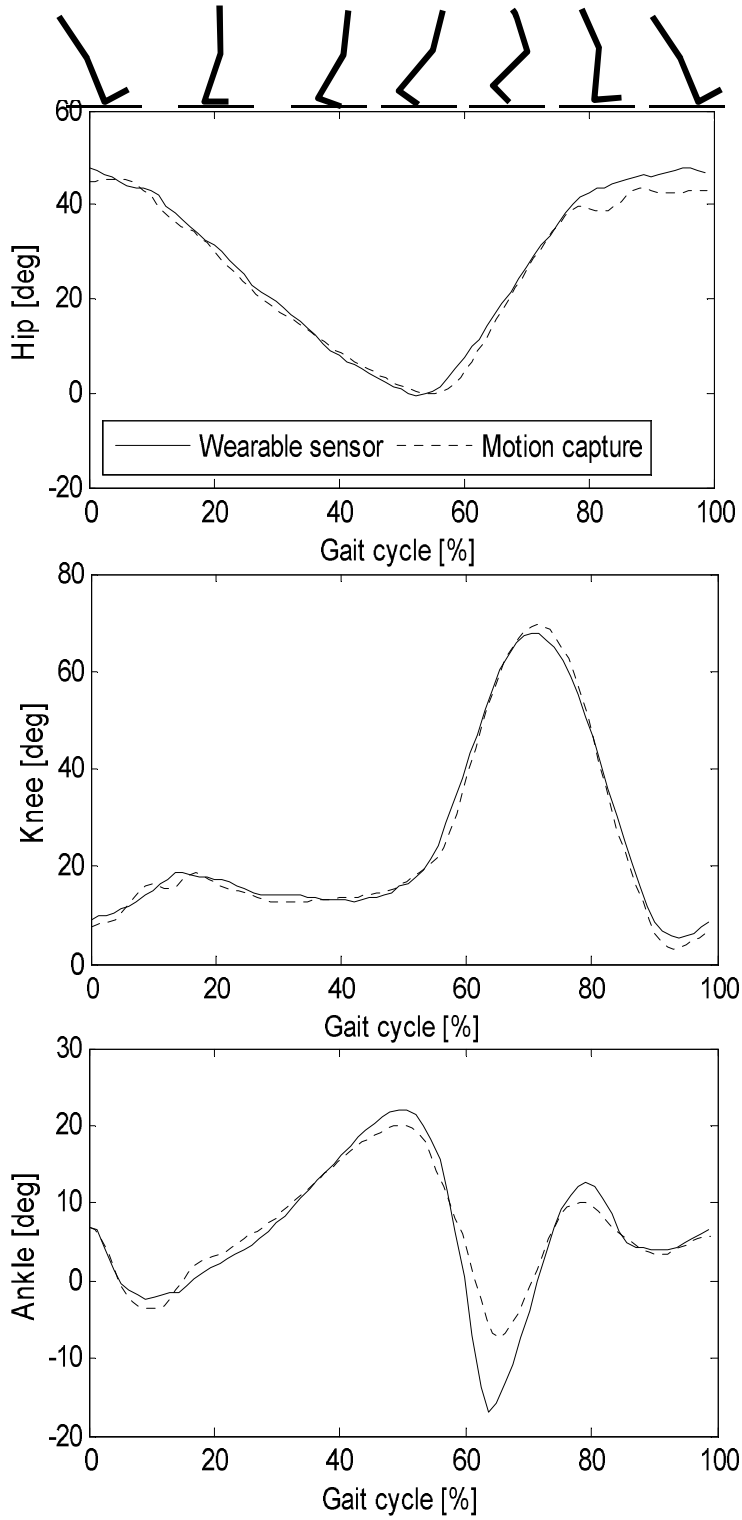

Figure 3.5: Joint angles during normal gait.

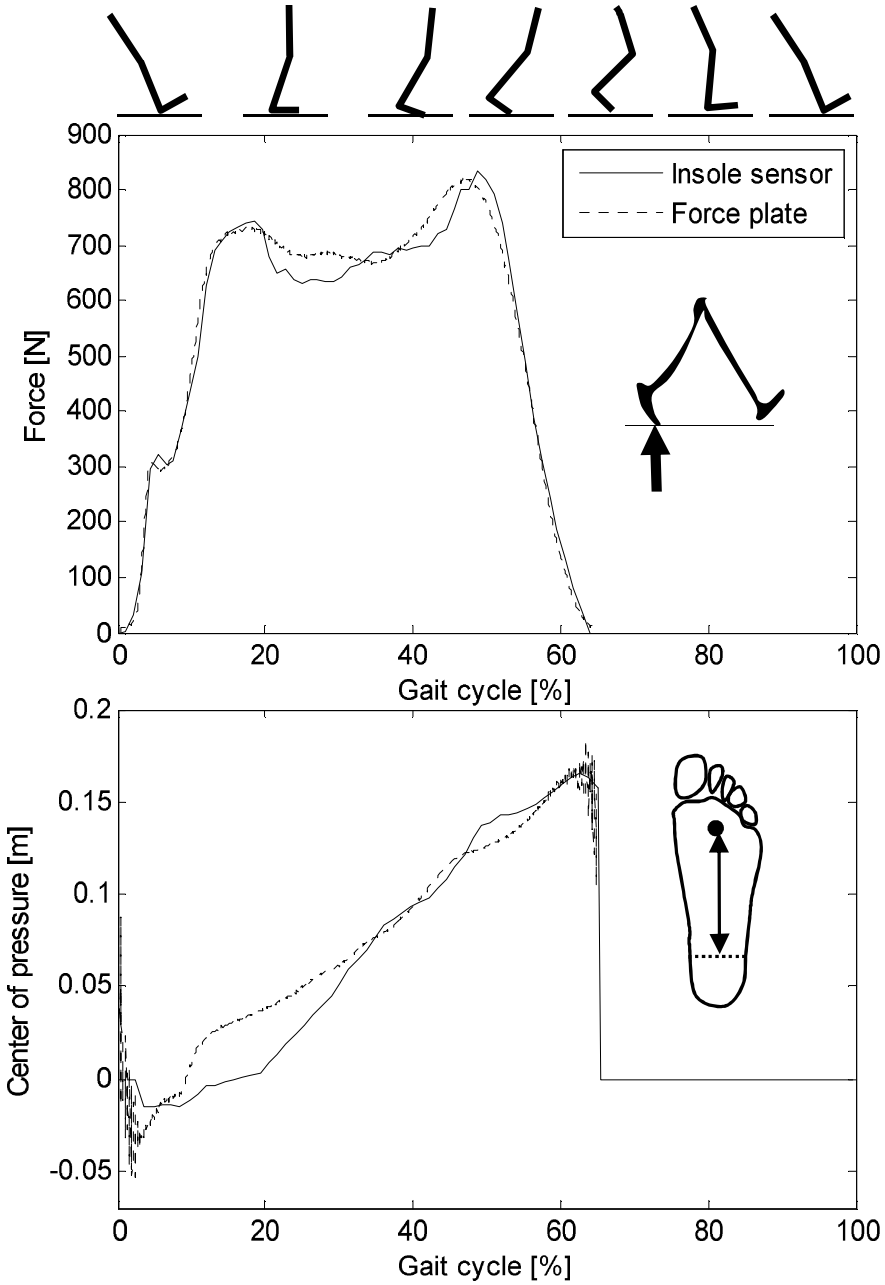

Figure 3.6: Ground reactions and center of pressure position with respect to the ankle position during normal gait.

Procedures	Musculoskeletal model	Diagram
Measurement of movements	• Joint-segment model	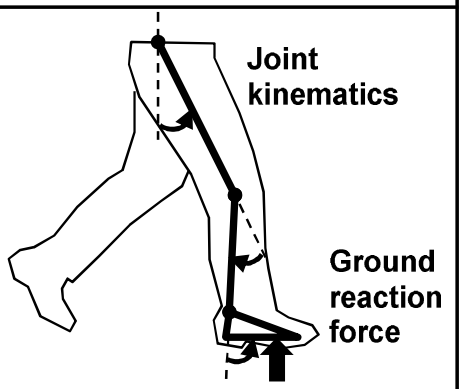
Inverse dynamics	• Body segment parameters (mass, length center of mass moment of inertia)	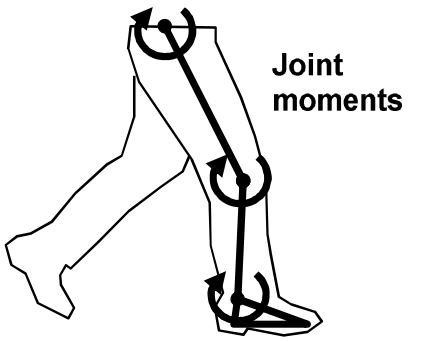
Static optimization	• Muscle groups • Moment arms • Physiological cross sectional area (PCSA)	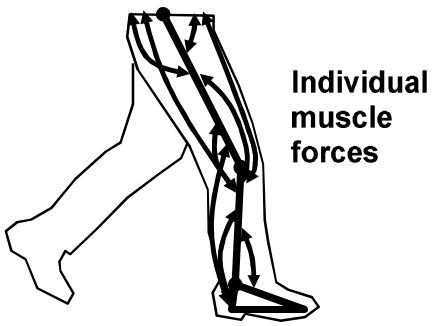

Figure 3.7: Detailed procedures of inverse dynamics-based static optimization.

3.3.1 Inverse Dynamics

The lower extremity was described as a mechanical system in dynamic equilibrium under the actions of gravity, inertia, ground reactions, and muscular forces, which generate appropriate moments at the joints. Figure 3.8 shows a free body diagram of the lower extremity in the sagittal plane, considering only flexion/extension motion of the three joints; because most of the movements and forces in the lower limb during walking occur in the plane [20]. The two dimensional model involves five degrees of freedom, including three joint angles and the planar motion of the pelvis. Using Lagrange mechanics, the inverse dynamic equations were derived with respect to the absolute angle of the three segments:

$$\begin{aligned} M_A = &- F_{GRF} r \sin\theta_3 + J_f \ddot{\theta}_3 + g \sin\theta_3 \\ &+ d_f m_f(-l_t \dot{\theta}_1^2 \sin(\theta_1 - \theta_3) + l_s \dot{\theta}_2^2 \sin(\theta_2 + \theta_3) \\ &+ l_t \ddot{\theta}_1^2 \cos(\theta_1 - \theta_3) + l_s \ddot{\theta}_2 \cos(\theta_2 + \theta_3) \\ &+ d_f \ddot{\theta}_3 + \ddot{x}_p \cos\theta_3 + \ddot{y}_p \sin\theta_3) \end{aligned} \tag{3.6}$$

$$\begin{aligned} M_H = &M_K - l_t F_{GRF} \sin\theta_2 + J_t \ddot{\theta}_1 \\ &+ g(l_t(m_f + m_s) + d_t m_t) sin\theta_1 \\ &+ l_t(l_s m_f + d_s m_s)\dot{\theta}_2^2 \sin(\theta_1 + \theta_2) \\ &+ d_f l_t m_f \dot{\theta}_3^2 \sin(\theta_1 - \theta_3) \\ &- l_s l_t m_f \ddot{\theta}_2 \cos(\theta_1 + \theta_2) \\ &+ (l_t^2(m_f + m_s) + d_t^2 m_t)\ddot{\theta}_1 \\ &- d_s l_t m_s \ddot{\theta}_2 \cos(\theta_1 + \theta_2) \\ &+ d_f l_t m_f \ddot{\theta}_3 \cos(\theta_1 - \theta_3) \\ &+ (l_t(m_f + m_s) + d_t m_t)\ddot{x}_p \cos\theta_1 \\ &+ (l_t(m_f + m_s) + d_t m_t)\ddot{y}_p \sin\theta_1 \end{aligned} \tag{3.7}$$

$$
\begin{aligned}
M_H =& M_K - l_t F_{GRF} \sin\theta_2 + J_t \ddot{\theta}_1 \\
&+ g(l_t(m_f + m_s) + d_t m_t) sin\theta_1 \\
&+ l_t(l_s m_f + d_s m_s)\dot{\theta}_2^2 \sin(\theta_1 + \theta_2) \\
&+ d_f l_t m_f \dot{\theta}_3^2 \sin(\theta_1 - \theta_3) \\
&- l_s l_t m_f \ddot{\theta}_2 \cos(\theta_1 + \theta_2) \\
&+ (l_t^2(m_f + m_s) + d_t^2 m_t)\ddot{\theta}_1 \\
&- d_s l_t m_s \ddot{\theta}_2 \cos(\theta_1 + \theta_2) \\
&+ d_f l_t m_f \ddot{\theta}_3 \cos(\theta_1 - \theta_3) \\
&+ (l_t(m_f + m_s) + d_t m_t)\ddot{x}_p \cos\theta_1 \\
&+ (l_t(m_f + m_s) + d_t m_t)\ddot{y}_p \sin\theta_1
\end{aligned}
\tag{3.8}
$$

where the capital subscripts indicate the relevant joint, hip, knee, and ankle, and the small letters represent the segment: pelvis, thigh, shank, and foot. M is the joint moment generated by the muscles, d is the center of mass positions from the proximal joints, θ_1, θ_2 and θ_3 are the absolute angles of the thigh, shank, and foot, x and y are the center of mass position of each segment, F_{GRF} is the ground reaction, and r is the application point of the ground reaction from the ankle.

Except for the measured motion data, there exists some required parameters to solve the dynamic equations such as segment length, mass, center of mass position, and mass moment of inertia. However, they are not directly measurable, except for the segment length, thus the other parameters should be estimated using the formulas found in cadaveric experiments [194]:

$$
\begin{aligned}
m &= P \cdot (body\, mass) \\
c &= R \cdot (segment\, length) \\
I &= m \cdot K \cdot (segment\, length)^2
\end{aligned}
\tag{3.9}
$$

where m, c, and I are the mass, the center of mass position, the mass moment of inertia. The coefficients, P, R and K, of each segment are listed in Table 4.1 [42, 41].

3.3.2 Musculoskeletal Model and Static Optimization

Individual muscular forces were determined by the static optimization based on the moment equilibrium equations between net joint moment produced by the muscles and the joint moments calculated from the inverse dynamics. Because the number of muscles are usually

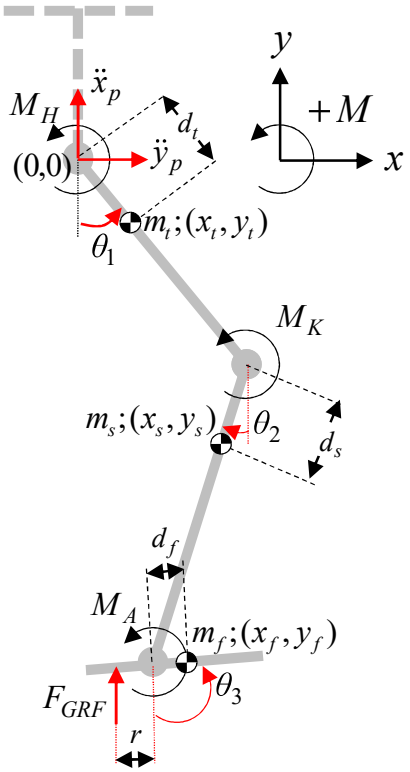

Figure 3.8: Two dimensional free body diagram of the lower limb (M_i: joint moment ($i = H$: hip, K: knee, A: ankle), θ_j: absolute angle of the joints ($j = 1$: thigh, 2: shank, 3: foot), (x_k, y_k): center of mass position of each segment ($k = t$: thigh, s: shank, f: foot), F_{GRF}: ground reaction, and r: center of pressure of F_{GRF}

larger than that of equilibrium equations, an optimization process is required. The detailed discussion on applying the static optimization is described in this section, including selecting the muscles of interest, calculating moments arms of each muscle, and choosing an optimization criterion. The optimization problem was solved by a sequential quadratic programming (SQP) algorithm.

Muscle Groups

As shown in Figure 3.9, the musculoskeletal model included all of the muscle groups which are functionally independent: 1) the iliacus (IL) for the hip flexor, 2) the hamstrings (HA) for the hip extensor and knee flexor simultaneously, 3) the rectus femoris (RF) for the hip flexor and knee extensor, 4) the gastrocnemius (GA) for the knee flexor and plantar flexor, 5) the biceps femoris short head (BF) for the knee flexor, 6) the vastus (VA) for the knee

Table 3.1: Coefficients for the body segment parameters

	P	R_p	R_d	K_{CG}	K_p	K_d
Foot	0.0145	0.500	0.500	0.475	0.690	0.690
Leg	0.0465	0.433	0.567	0.302	0.528	0.643
Thigh	0.1000	0.433	0.567	0.323	0.540	0.653

The subscript means the origin point where the resultant parameter is referring to; d refers to the distal joint, p refers to the proximal joint, and CG refers to the center of gravity [42, 41].

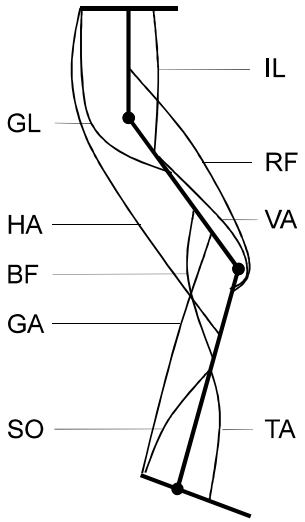

Figure 3.9: Muscle groups in the sagittal plane(IL: iliacus, HA: hamstrings, RF: rectus femoris, GA: gastrocnemius, BF biceps femoris short head, VA: vastus, TA: tibialis anterior, SO: soleus, GL: gluteus maximus)

extensor, 7) the tibialis anterior (TA) for the dorsiflexor, 8) the soleus (SO) for the plantar flexor, and 9) the gluteus maximus (GL) for the hip extensor. The muscles have significant force capabilities and moment arms, such that their contributions to the joint torque are also more significant than the excluded muscles [64, 51].

Moment Arms

Even though a muscle exerts only a tensile force, it produces torsional force with respect to the joint due to its attachment to the bones. This means that how the muscle generates torque about a joint depends on both muscle tendon force and the musculoskeletal geometry.

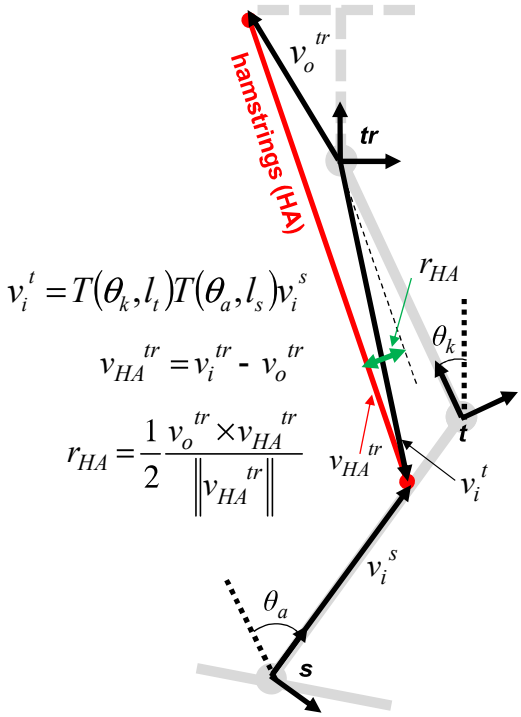

Figure 3.10: Vector operation for calculating moment arm of the hamstring; the subscript identifies the vector (o, i: origin and insertion), the superscript indicates which reference frame the vector is referring to (tr: trunk, t: thigh, s: shank), θ: is rotational angle, l is segment length, and T is homogeneous transformation matrix as a function of θ and l.

Moment arms of the muscle groups were calculated using the vector operations based on the coordinate data of the muscle origin and insertion with respect to a corresponding reference frame [68, 19]. For example, Figure 3.10 illustrates the vector operation to calculate the moment arm of the hamstring, where v_o^{tr} and v_i^s are the origin and insertion coordinates with respect to reference coordinate, tr; trunk, s; shank, respectively given in reference [19]. Using the same strategy, moment arms of the muscles arms were expressed as a function of joint angles.

Optimization Criterion

To solve the individual muscular forces without reducing the number of muscle groups, an optimization process is required. It is important to adopt the proper optimization criteria, and various types have been suggested to simulate the actual body functions for recruiting the muscles: minimizing 1) muscle force[136], 2) joint moment [32], 3) ligament force, 4)

joint contact force, 5) instantaneous muscle power [150], and 6) muscle stress [38]. Among them, the criterion of maximum endurance is the most widely accepted recently, because it was demonstrated to be the most biologically meaningful. The cost function to be minimized is as follows:

$$J = \sqrt[n]{\sum (f_i/A_i)^n} \tag{3.10}$$

where f_i is the muscular force and A_i is the physiological cross-sectional area (PCSA) of the muscle. The PCSA is defined as the total area of the cross-section perpendicular with respect to the muscle fiber [115], and it is also calculated as the volume of the muscle divided by the optimal fiber length [5]. An appropriate value of the power n in (3.10) cannot be determined exactly due to differences in individuals and muscles. In addition, to specify the value, it is necessary to measure the muscular forces accurately, which would not be available. Accordingly, the average value in literature reports, $n = 3$, has been adopted as the most appropriate value [37].

The optimization problem was specified to minimize the cost function in (3.10) satisfying the following constraints:

$$0 \leq f_i \leq (f_i)_{max} \tag{3.11}$$

$$AX = B \tag{3.12}$$

where f_i is the exerted muscular force, $(f_i)_{max}$ is the maximum isometric force.

The equality constraint (3.21) in static optimization was specified as follows:

$$X = \begin{bmatrix} f_{IL} \\ f_{HA} \\ f_{RF} \\ f_{GA} \\ f_{BF} \\ f_{VA} \\ f_{TA} \\ f_{SO} \\ f_{GL} \end{bmatrix} \tag{3.13}$$

$$A = \begin{bmatrix} 0 & 0 & r_{IL} \\ 0 & -r_{HA,k} & -r_{HA,h} \\ 0 & r_{RF,k} & r_{RF,h} \\ -r_{GA,a} & -r_{GA,k} & 0 \\ 0 & -r_{BF} & 0 \\ 0 & r_{VA} & 0 \\ r_{TA} & 0 & 0 \\ -r_{SO} & 0 & 0 \\ 0 & 0 & -r_{GL} \end{bmatrix}^T \tag{3.14}$$

$$B = \begin{bmatrix} M_a & M_k & M_h \end{bmatrix}^T \tag{3.15}$$

where X refers to a vector of muscular forces, r means the moment arm of the muscle with respect to the corresponding joint in the subscript; a, k, and h means the ankle, knee, and hip joints respectively, M in is the joint moment calculated by the inverse dynamics.

The first constraint in (3.20) represents the force capability of each muscle, and the maximum isometric force $(f_i)_{max}$ is determined by multiplying the PCSA and the specific tension, 61 N/cm^2, of the muscle fiber, which is the maximum stress the fiber can endure. The values of the PCSA in the reference [5] were used. The other constraint in (3.21) is moment equilibrium between the joint moment from the inverse dynamics and the resulting moment exerted by the muscles.

3.4 Individual Muscular Forces During Walking

Based on the motion data shown in Figs. 3.5 and 3.6, the joint moments were estimated by solving the inverse dynamics, and the solution of the optimization problem produced instantaneous values of muscular forces in the nine muscle groups at each instant. To interpret the estimated muscular efforts, the experimental results organized according to the four important functions of a gait cycle (Figure 3.11); each phase of gait cycle was identified by the ground reaction patterns in Figure 3.6.

Heel rocker occurs during the phase of initial contact and the loading response phase, which is required to bear the large flexion torque of the hip joint due to a significant vertical vector (60% body weight) that is anterior to the hip joint. Thus, in the estimated result, a

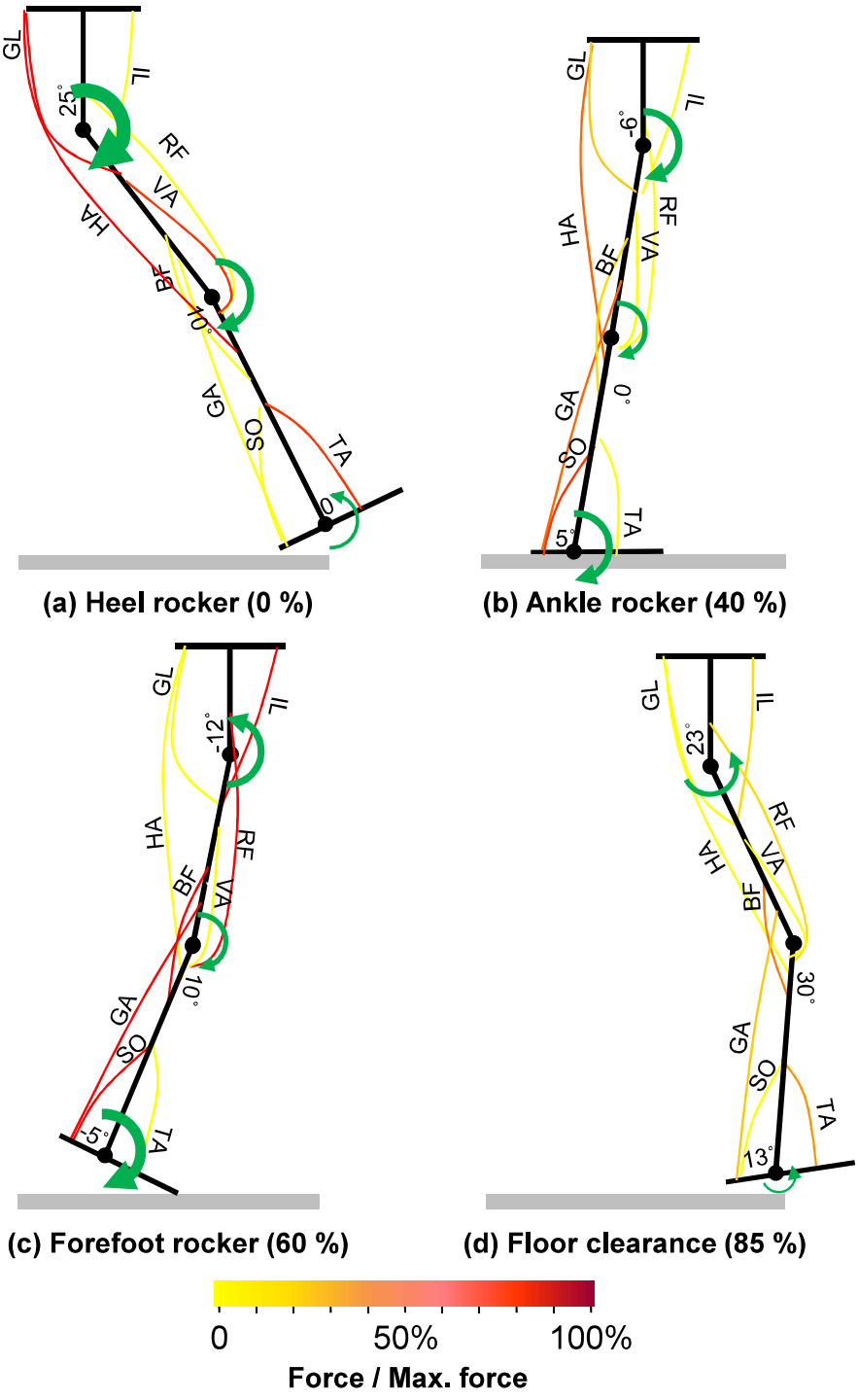

Figure 3.11: Visualized experimental results at the four important gait functions; the posture of the segments were based on the measured joint angles, the green arrows represent directions and relative magnitudes of joint torques estimated by the inverse dynamics, and intensity of the red color represents the usage of each muscle determined by the static optimization.

large extension torque was generated by the hip extensors (HA and GL). Similarly, flexion torque at the knee joint is necessary to endure the vertical ground reaction force. Due to the two-jointed muscle, HA, a large flexion torque was also produced at the knee joint, and it was released by the knee extensor, VA. In the case of the ankle joint, the dorsiflexor TA was excited to endure ground reactions placed behind the ankle. In accordance with the actions of muscles, the shank made its advance (Figure 3.11(a)).

Ankle rocker occurs during the mid-stance to continue progression of the body (Figure 3.11(b)). As the limb rolls forward over the supporting foot, the directions of the joint torques were identically downwards. All of the muscles placed on the posterior side of the limb, such as the GL, HA, BF, GA, and SO, were involved in the motion. The SO muscle, assisted by the GA, was excited to maintain stance stability of the limb. Due to the secured stability gained by the action of the SO and GA muscle, further demand on the quadriceps, including the VA and RF muscle, was minimized.

Forefoot rocker takes place during the terminal stance (Figure 3.11(c)). The heel rolled over the anchor of the forefoot with the ankle virtually locked by the SO and GA, continuing advancement of the shank. Maximal plantar flexion torque was required because the vertical ground reactions, combined with falling body weight, were applied at the toe. The heel rise posture demanded strong SO and GA action, approximately three times more than in mid stance. As the knee began to flex by the end of the terminal stance, the BF muscle was involved in this phase. While the hip was fully extended, the body rolls forward over the forefoot rocker, and the IL and RF muscles were activated as hip flexors to restrain the rate and extent of hip extension.

The limb accomplishes foot clearance in the phase of the initial swing and the mid swing (Figure 3.11(d)). As the shank became vertical, the ankle joint supported the downward force of the foot weight. Thus, the TA muscle was activated at that instant. Because momentum produced by the hip flexion compensated for the pull of gravity on the shank, joint torque at the knee reached a balance. Additionally, hip flexion of the swing phase was generated by the passive gravitational force of the limb, such that the intervention of the hip and knee muscles were not significant.

The experimental results of individual muscular forces during a normal stride are presented in Figure 3.12(a). To validate the experimental result, the estimated muscular forces were compared with the another experimental result (Figure 3.12(b)); muscular forces were estimated by using a model-based estimation algorithm, a camera-based motion capture system and a force plate were used to measure motion information, and EMG signals were also

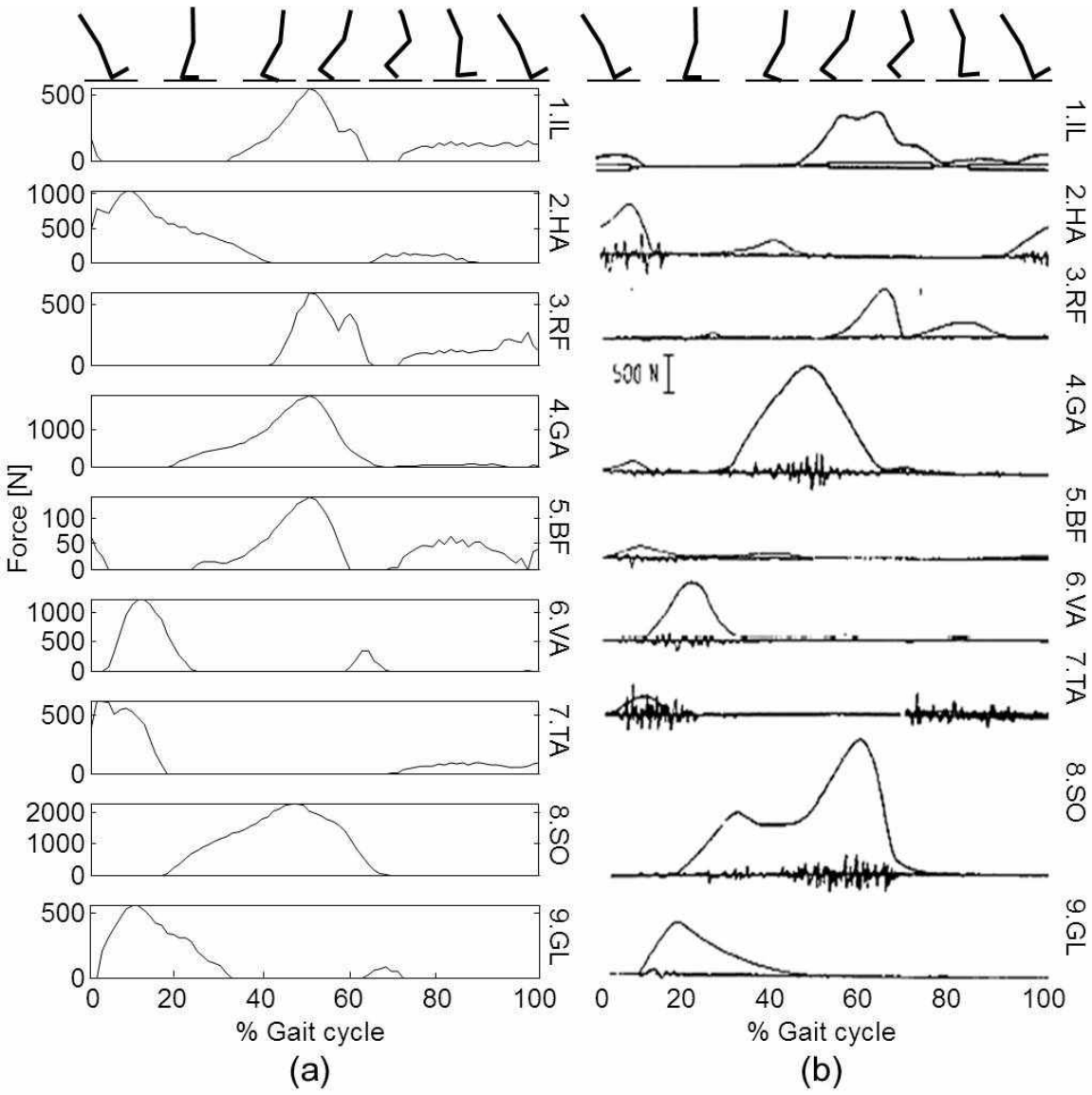

Figure 3.12: Comparison of the estimated muscular forces: (a) proposed method (b) model-based estimation with camera-based motion capture system and a force plate.

recorded for validation [51]. The estimated muscular forces shows similar patterns and magnitudes, and the results in this study coincides with EMG patterns also. Because it is very difficult to measure true muscular forces of a human, it is not easy to validate the estimated muscular forces quantitatively. However, the activation pattern of muscles during normal walking was evidenced by well-documented experimental results with EMG signals [32, 38, 37, 137, 150, 140, 23]. Comparing the estimated muscular forces with the electromyography patterns in the previous studies, it was possible to check feasibility of the estimated results.

3.5 Application to Fingers[†]

In this subchapter, the inverse dynamics-based static optimization is applied to the fingers with a hand exoskeleton system. The aim of this work is to estimate muscular efforts related to the fingers during the fingers being extended by the hand exoskeleton, which can be a clue for rigidity of the fingers, frequently observed by patients with motor function injuries.

3.5.1 A Hand Exoskeleton System

The hand exoskeleton system was developed to apply the pulling force at five fingertips and measure the applied force and joint angles simultaneously. Due to the complex and small structure of the finger, it was not easy to deliver the pulling force to the finger tip in the full range of finger motion. In the proposed hand exoskeleton, a cable-driven mechanism was designed with four-bar linkage structures, and the loadcells were embedded in the connectors which deliver the pulling force of the cable to the fingertips to measure the applied force. The joint angles were measured by the rotary potentiometer installed in the four-bar linkages using the geometric information of the linkages.

Measurement of the Finger Joint Angles

To measure joint angles of the fingers, the multiple sensors should be installed in the limited space of the finger. If the sensors are attached on the side of the fingers, the sensors may interfere their movements. Therefore, the sensors should be attached on the fingers, and the simplest kinematic structure, four-bar linkage, was adopted to measure joint angles indirectly [210]. As shown in Figure 3.13, the lengthes of the three linkages, a_1, a_2, and

[†]The contents in this chapter is based on the published work of the author [90].

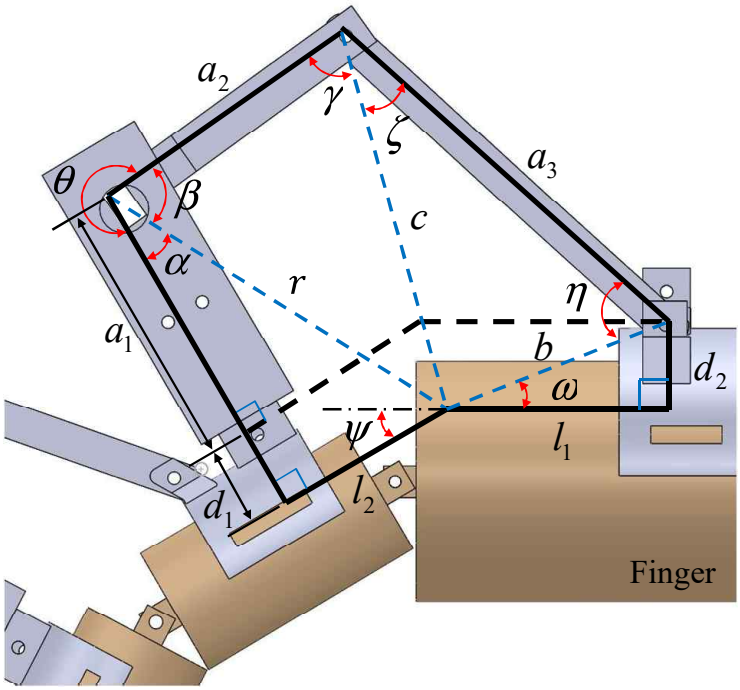

Figure 3.13: The four-bar linkage for measuring the joint angle

a_3, were design parameters of the four-bar linkage, which were determined according to the kinematic simulation using Matlab. Ranging from 0° and 90° of the finger joints, the four-bar linkages covered the range of motion with given length of the phalanges from both of the big and small hands.

Provided that the lengthes of the linkages such as a_1, a_2, a_3, d_1, d_2, l_1 and l_2 were determined, the finger joint angle ψ was calculated as follows:

$$\psi = \theta - 90^\circ - \gamma - \zeta - \eta + \omega \tag{3.16}$$

where

$$\begin{gathered} \alpha = tan^{-1}(\frac{l_2}{a_1+d_1}),\ r = \sqrt{(a_1+d_1)^2+l_2^2},\ \beta = 360^\circ - \theta - \alpha \\ c = \sqrt{a_2^2+r^2-2ra_2cos\beta},\ b = \sqrt{d_2^2+l_1^2},\ \gamma = cos^{-1}(\frac{a2_2+c^2-r^2}{2a_2c}) \\ \zeta = cos^{-1}(\frac{c^2+a_3^2-b^2}{2a_3c}),\ \eta = cos^{-1}(\frac{a_3^2+b^2-c^2}{2a_3b}),\ \omega = tan^{-1}(\frac{d_2}{l_1}) \end{gathered} \tag{3.17}$$

Note that θ was the only parameter required to calculate the joint angle ψ; therefore, a rotary potentiometer was embedded in the linkage to measure it. The same structure was

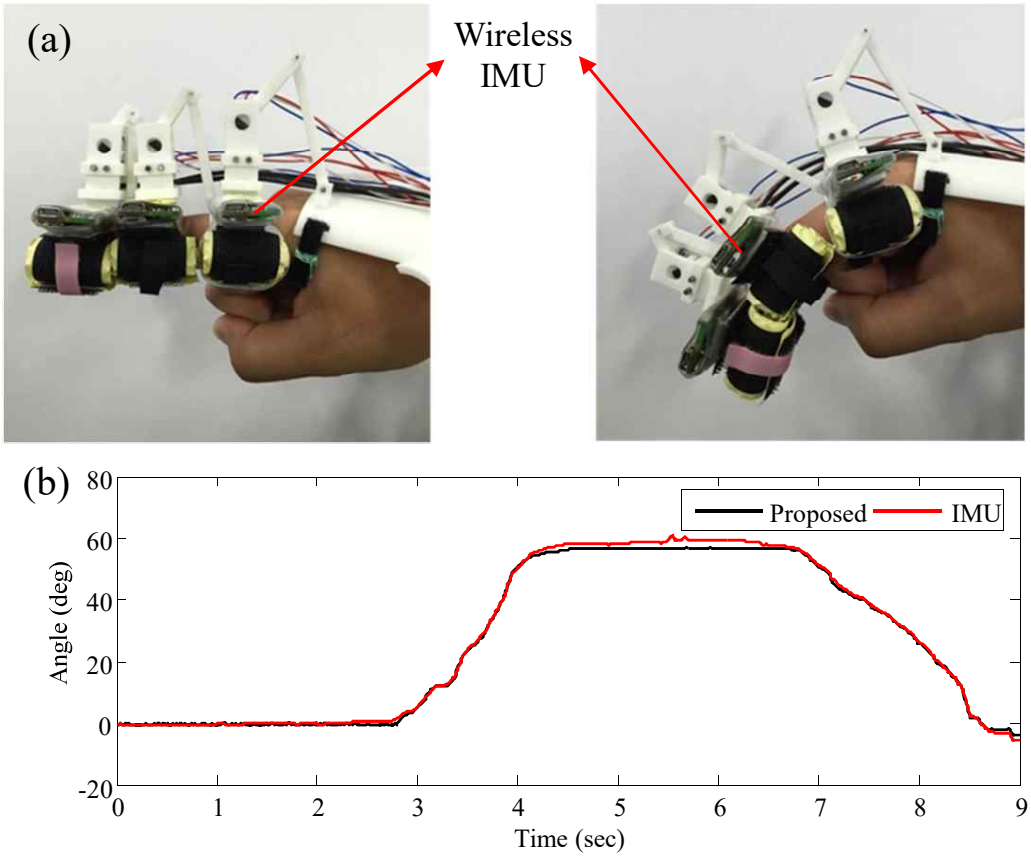

Figure 3.14: Verification of the four-bar linkage structures for measuring finger joint angles: (a) experimental setup, (b) joint angles estimated by the proposed method and the IMU

duplicated for 14 joints of all fingers (two for the thumb, three for rest four fingers) to measure each joint angle.

To verify the performance of the proposed method, the experimental setup was prepared as shown in Figure 3.14 (a); the inertial measurement units (IMU) were attached on each phalanx. Using the proposed system and the IMU, the MCP joint angles were measured and compared as shown in Figure 3.14 (b). The experimental result indicates that the proposed structure measured the joint angle accurately with little root-mean-square (RMS) error, 1.1642°.

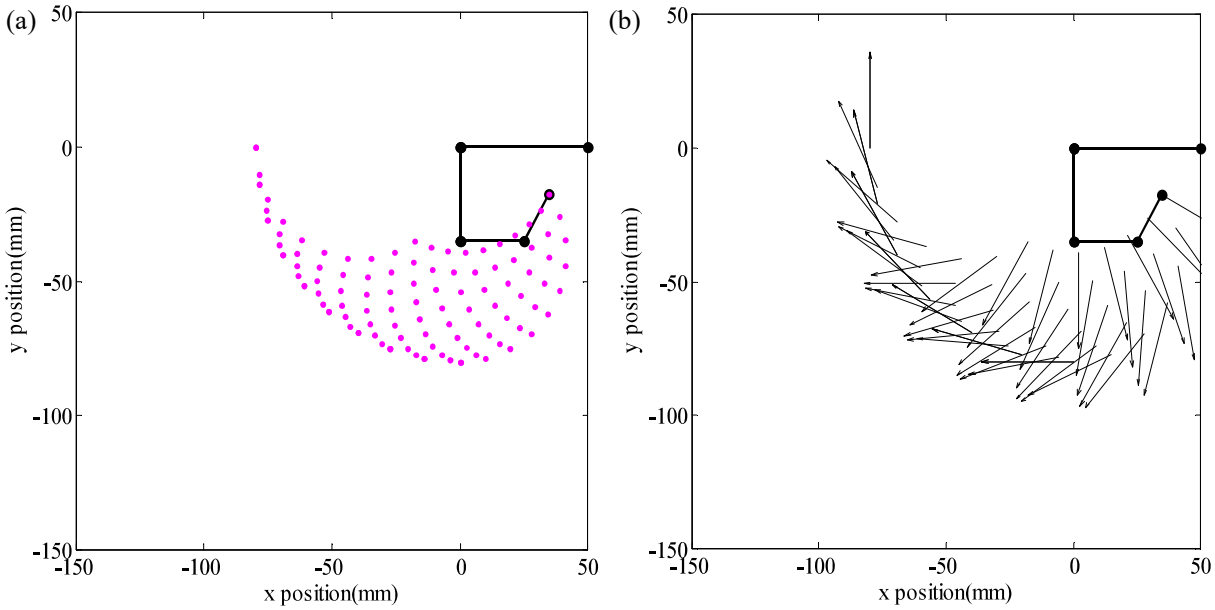

Figure 3.15: Verification of the four-bar linkage structure with its range of motion

Application/measurement of the Pulling Force

To extend the clenched fingers, an actuation system was required to pull the fingertips in the upward normal direction. However, it was not an easy task because of the wide motion range of the finger. As shown in Figure 3.15(a), the fingertip positions were tracked in the simulation during the angles of the MCP and PIP joints were changed from 0° to 90° simultaneously and DIP joint angle was set to 2/3 of PIP joint angle. Moreover, the normal direction also varied significantly in the given motion range as shown in Figure 3.15(b). As the finger was fully extended, the direction headed for 90° and changed to −45° with the fingers fully flexed. In the previous research, several design candidates were considered to apply the normal force in the whole range of motion [103].

In this research, the cable-driven actuation system was selected, which consisted of the cable guide made by the flexible carbon strip. As shown in Figure 3.16, the flexible strip slid through the exoskeleton structure as the finger moved, providing the guidance to the cable. A motor was installed on the back of the hand to pull the cable whose other end was connected to the lower plate which slid along the exoskeleton structure as shown in Figure3.17. As the cable pulled the lower plate upwards, the loadcell was pressurized by the upper plate fixed to the exoskeleton structure. Using the proposed mechanism, the exoskeleton enabled to

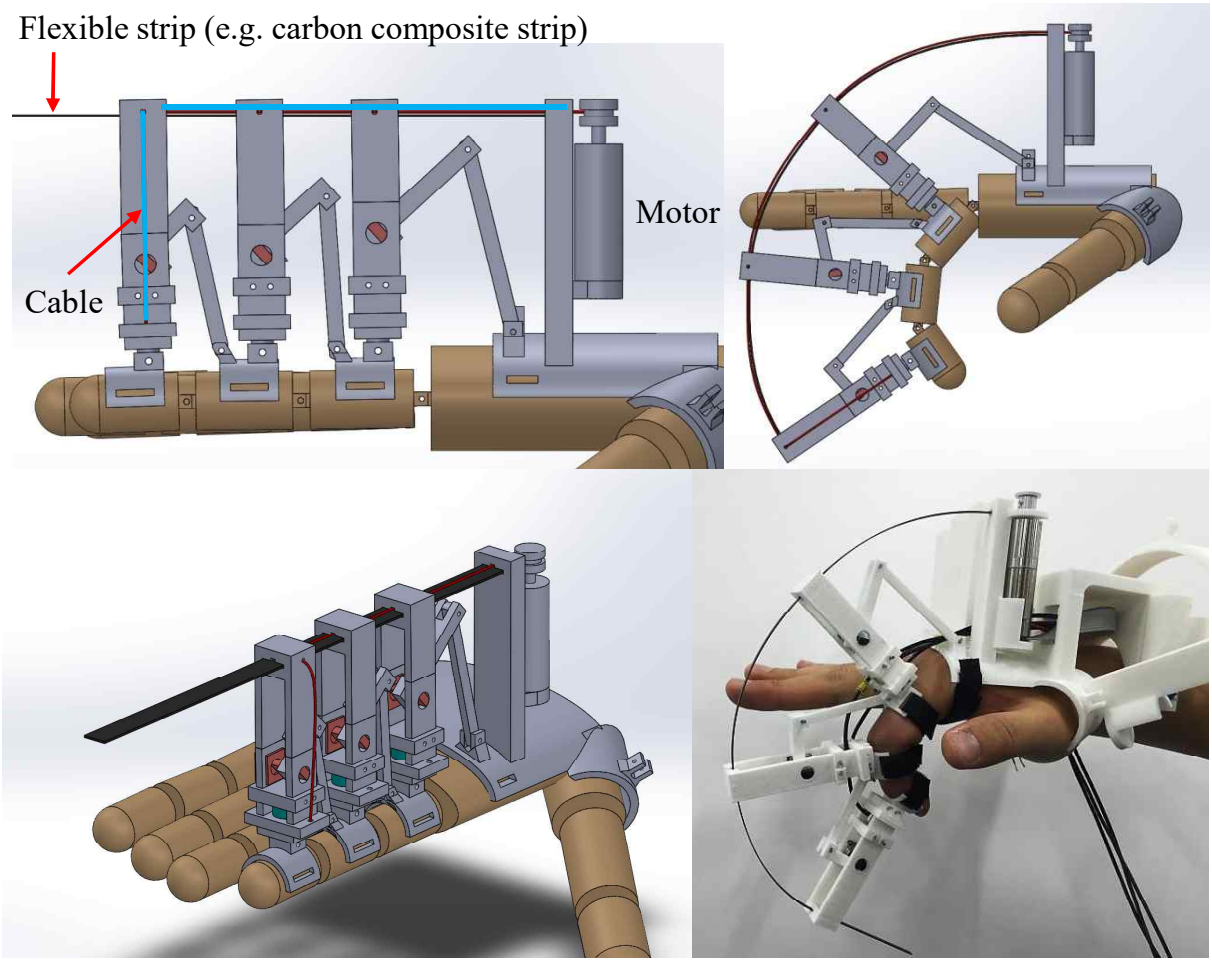

Figure 3.16: Final design and the prototype for the hand exoskeleton system

deliver the drawing force of the cable to the distal phalanx, simultaneously measuring the applied force.

To control the drawing force of the cable, it was important to calculate a proper cable length with respect to the joint angles, because the length of the cable was increased as the finger flexed. Therefore, the motor was commanded to increase or decrease the cable length according to the measured joint angles not to retrain the movement of the user. In the case that the fingertip needed to be pulled, the motor wound the cable at a speed predetermined in the program. All motors were controlled by PID control whose gains were determined heuristically.

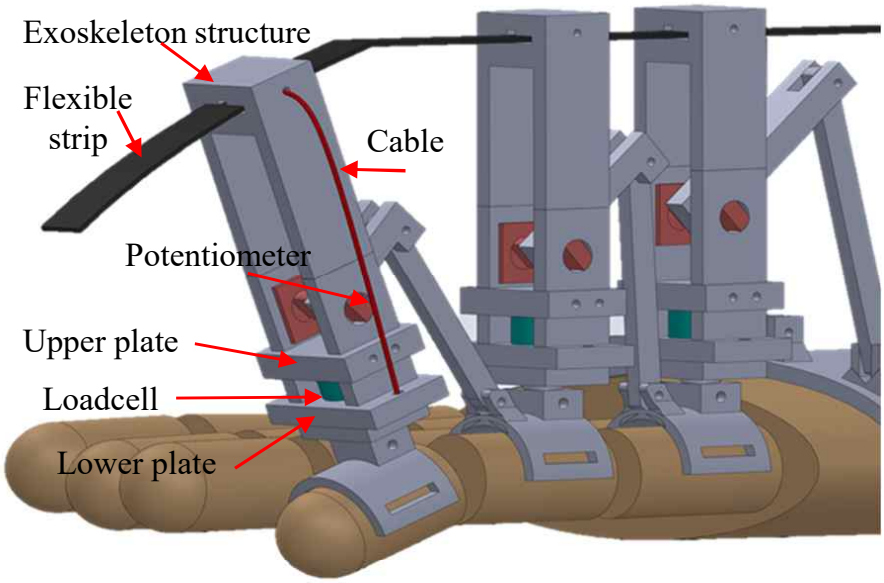

Figure 3.17: A loadcell embedded between the two plates for measuring the pulling force at the fingertip

Figure 3.18: The prototype of the proposed hand exoskeleton

Implementation of the Hand Exoskeleton

The final product of the hand exoskeleton system was developed as shown in Fig. 3.18. Each of hand exoskeleton was equipped with 14 potentiometers (produced by Panasonic [128]) for measuring finger joint angles (two for the thumb, three for the rest four fingers), 14 loadcells for measuring pulling force applied to the phalanx, and 5 motors (produced by Maxon [116]) for pulling the cable connected to the phalanx. Although the cables were connected to the fingertips only, the loadcells were installed on every phalanx for potential use of them. The components of the exoskeleton were manufactured by 3D printers and CNC machining, and a National Instrument (NI) device was used as a main controller and a data acquisition board [120]. Using NI LabVIEW, a graphical user interface (GUI) was constructed to control the exoskeleton systems and acquire motion and force data.

3.5.2 Inverse Dynamics-based Static Optimization: Fingers

The inverse dynamics-based static optimization was applied to the fingers as shown in Figure 3.19. The inverse dynamic equation was derived to calculate joint torques from the joint kinematics and the external forces measured by the hand exoskeleton. To determine the force applied by a single muscle, the muscular force sharing problem, so called static optimization, was solved for each instant. The optimization process is necessary because the human body has inherent redundancy with larger number of muscles than the degrees of freedom in the skeletal system [33].

Inverse Dynamics

In this study, flexion/extension motion was considered, because the spastic hand usually involves excessive intervention of the flexors. In such a case, the two dimensional movements are more critical than the abduction/adduction of the metacarpophalangeal (MCP) joint. Therefore, a two dimensional free body diagram was defined to describe motion of the fingers and external forces applied to the fingers, which included the four links and three joints (Figure 3.20). The four links consisted of the proximal, middle, and distal phalanges, and metacarpals, which were connected with revolute joints, and the metacarpals were fixed to the ground. The three joints were MCP, proximal interphalangeal (PIP), and distal interphalangeal (DIP) joints. The thumb only had two joints: the MCP and interphalangeal (IP) joint. Specifically, M_m, M_p, and M_d represent the joint moments at the MCP, PIP and

Procedures	Musculoskeletal model	Diagram
Measurement of movements	• Joint-segment model	Joint kinematics 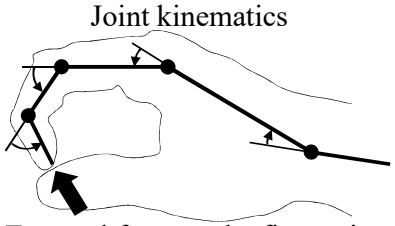 External force at the finger tip
Inverse dynamics	• Body segment parameters (mass, length, center of mass, moment of inertia)	Joint moment 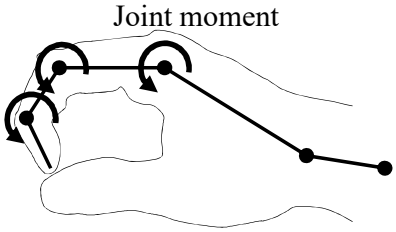
Static optimization	• Muscle groups • Moment arms • Physiological cross sectional area (PCSA)	Individual muscular forces 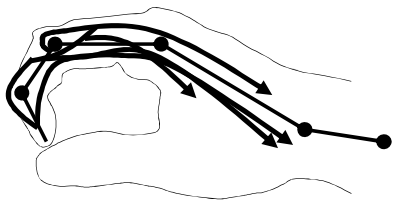

Figure 3.19: Inverse dynamics-based static optimization procedure to evaluate muscular forces of the fingers.

DIP joints, and c_1, c_2, and c_3 are the distance between the center of mass of each link and the adjacent proximal joint of the proximal, middle, and distal phalanges. In this study, it was assumed that the hand exoskeleton system pulled the finger tip with force F perpendicular to the distal phalanx, and the downward reaction force, $F/2$, was applied to the center of the middle and proximal phalanges due to the structure of the hand exoskeleton. ϕ_1, ϕ_2, and ϕ_3 represent the absolute angle of each phalange.

The inverse dynamic equations were derived using Lagrange mechanics, and the dynamic equations of the fingers were totally same with that of the lower extremity well-organized in [23]. The equations expressed the joint moments as a function of motion, external forces, and the body segment parameters including mass, the center of mass, the mass moment of inertia, and the segment length. Except for the length, the segment parameters cannot

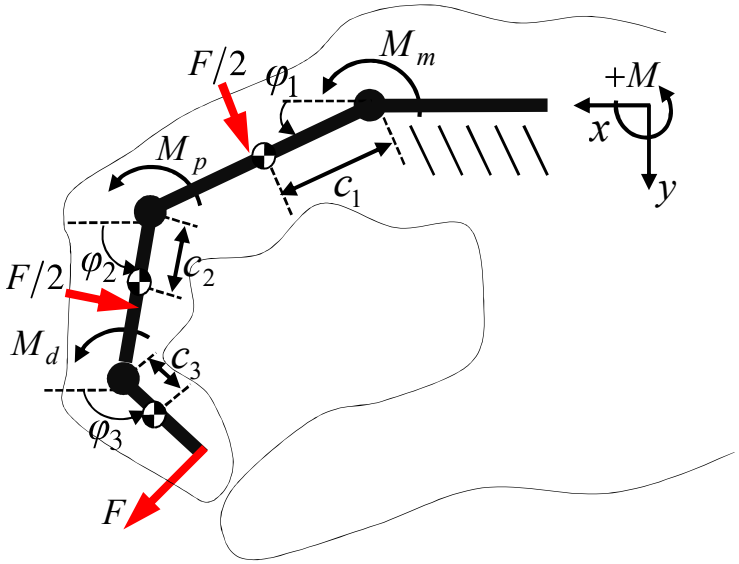

Figure 3.20: Two dimensional free body diagram of the index fingers.

be measured directly, so the parameters were estimated using the predefined relations from the experimentation on cadavers [42, 41]; the unknown segment parameters were calculated using segment length and body weight, both of which were measured directly.

Musculoskeletal Model

A musculoskeletal model was defined that included the target muscles with their architectural properties such as the tendon balance, moment arms, and the physiological cross-sectional area (PCSA) which were used to solve static optimization. Owing to the small and complex structures of the finger, an intricate tendon net exists and transmits the muscular forces to the bones as shown in Figure 3.21(a) and (b) [21]. The net includes the terminal extensor (TE), extensor slip (ES), long extensor (LE), flexor digitorum profundus (FDP), flexor digitorum superficialis (FDS), lumbrical (LU), radial band (RB), ulnar band (UB), radial interossei (RI), and ulnar interossei (UI) and satisfies the force equilibrium conditions as follows [27]:

$$\begin{aligned} f_{TE} &= f_{RB} + f_{UB} \\ f_{RB} &= \frac{2}{3} f_{LU} + \frac{1}{6} f_{LE} \\ f_{UB} &= \frac{1}{3} f_{UI} + \frac{1}{6} f_{LE} \\ f_{ES} &= \frac{1}{3} f_{LU} + \frac{1}{6} f_{LE} + \frac{1}{3} f_{RI} + \frac{1}{3} f_{UI} \end{aligned} \tag{3.18}$$

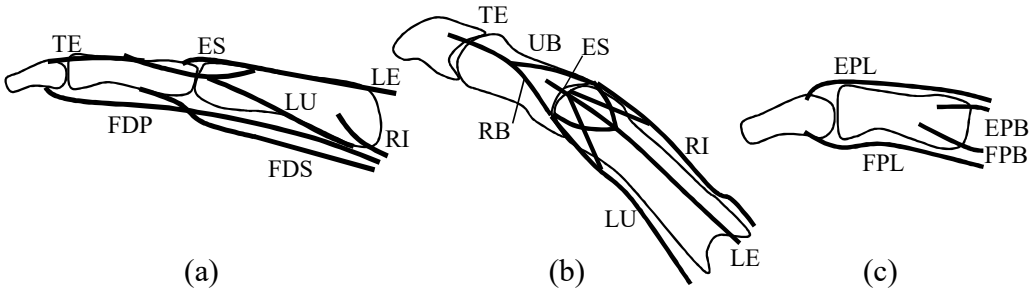

Figure 3.21: Muscle-tendon structure of the index finger [21]: (a) lateral view of the index, middle ring, little fingers, (b) dorsal view of the index, middle ring, little fingers, (c) lateral view of the thumb.

where f represents the muscle-tendon forces. Unlike the four fingers, the thumb has the four muscles with no complex tendon net, including the flexor pollicis brevis (FPB), flexor pollicis longus (FPL), extensor pollicis brevis (EPB), and the extensor pollicis longus (EPL) as shown in Figure 3.21(c).

To determine muscular forces from the joint moments, the moment arms of the muscles were specified. The tendon moment arms were measured for the joints that they transverse by direct measurement in fresh-frozen cadaver dissections, or calculated by simple vector operations based on the origins and insertion positions of the muscles obtained from cadaver investigation [82, 68, 4]. In this work, both methods were used in the model; if origin and insertion data were available, the vector operation was used; otherwise, the directly measured constant value was used. Additionally, the values of PCSA from cadavers were used, which determined the force capability of the muscle [75, 110, 57, 144, 67]. The PCSA is defined as the total area of the cross-section perpendicular to the muscle fiber [115].

Static Optimization

The number of unknowns in the musculoskeletal model exceeds the number of known variables, because there are more muscles than equilibrium equations. Therefore, a static optimization method was used to solve this problem, which calculated the instantaneous muscular force without considering the contraction dynamics of the muscles. The criterion of maximum endurance was applied, which has been accepted as the most physiologically meaningful solution [37]. The optimization problem determined the individual muscular forces by minimizing

$$J = \sqrt[3]{\sum (f_i/A_i)^3} \tag{3.19}$$

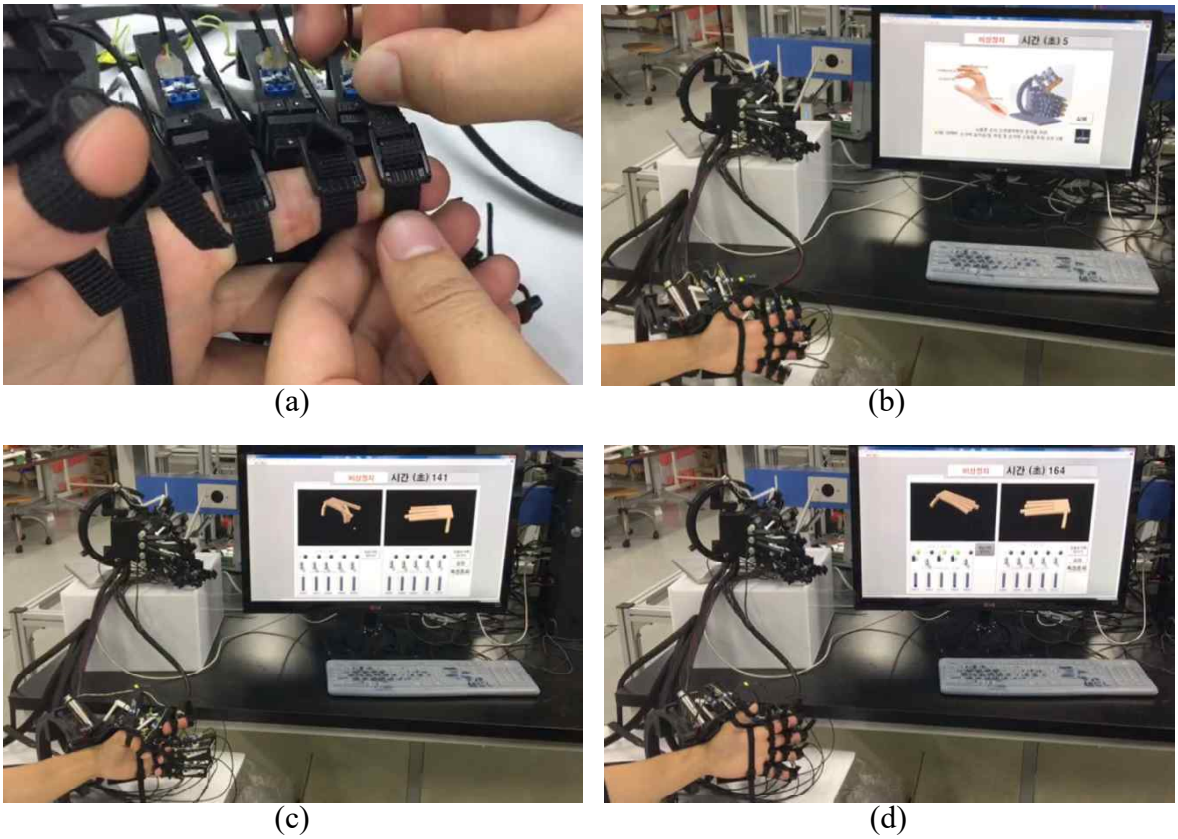

Figure 3.22: Experimental protocols: finger extension using the hand exoskeleton

while satisfying the following constraints:

$$0 \leq f_i \leq (f_i)_{max} \tag{3.20}$$

$$AX = B \tag{3.21}$$

where the inequality (3.20) indicates that the muscle only contracts and generates a force less than its maximal capability, which is the product of a specific tension (30 N/cm^2 [1]) and the PCSA. The constraint in (3.21) refers to the moment equilibrium equation, the matrix A describes the moment arms and tendon balances, X is the vector of muscular forces, and B is the joint moment vector. The vectors and matrix are specified in the Appendix. The optimization problem was solved by using a Matlab command 'fmincon' with the sequential quadratic programming (SQP) algorithm.

3.5.3 Individual Muscular Forces During Extension of Fingers

Experimental Protocols

Since the aim of this study was to investigate muscular efforts in the fingers during the flexed fingers were extended by the hand exoskeleton system, the following experimental protocol was conducted: 1) the exoskeleton structure were fixed with the phalanges by fastening the strap (Figure 3.22(a)), 2) the joint angles were initialized in the program with the fingers fully-extended (Figure 3.22(b)), 3) let the subject move their fingers freely to check whether the device allowed natural movement of the user and the joint angles were measured appropriately (Figure 3.22(c)), 4) before the measurement began, the subject flexed the fingers, and 5) the pulling was applied to specified fingers while the joint angles and the applied forces were recorded in the program (Figure 3.22(d)).

Experimental Results

A male subject with no history of musculoskeletal disease participated in the experiment. The subject was informed about the experimental procedures by IRB proved documents (UNISTIRB-15-26-C). Figure 3.23 shows the measured flexion angles of the five fingers. Although the fingers were flexed at the start of the experiment, the DIP joints were rarely flexed as the initial flexion angles were not large enough. Also, it was observed that the MCP joint was started to be extended earlier than the PIP joint due to the subject was asked to extend fingers naturally. If the PIP joint was extended faster than the MCP joint, the extensor and flexor muscles were activated simultaneously due to the anatomical structure of the fingers. Figure 3.24 shows the pulling force applied to each fingertip and measured by the loadcells. The forces were gradually increased by the cable-driven actuation system during the fingers were extended.

The inverse dynamic equations were solved using the measured motion information to calculate the joint moments shown in Figure 3.25. The estimated joint moments indicate that the moment was greater at the joint on the proximal side, particularly when the fingers were fully extended, as the pulling force was applied to the fingertip. Based on the joint moments, the static optimization was applied to estimate the individual muscular forces as shown in Figure 3.26. As shown in the results, the long extensor (LE) muscle was not involved in the motion, primarily due to the experimental protocol in which the finger flexors resisted against the pulling force while the fingers were extended. The FDS muscle was not

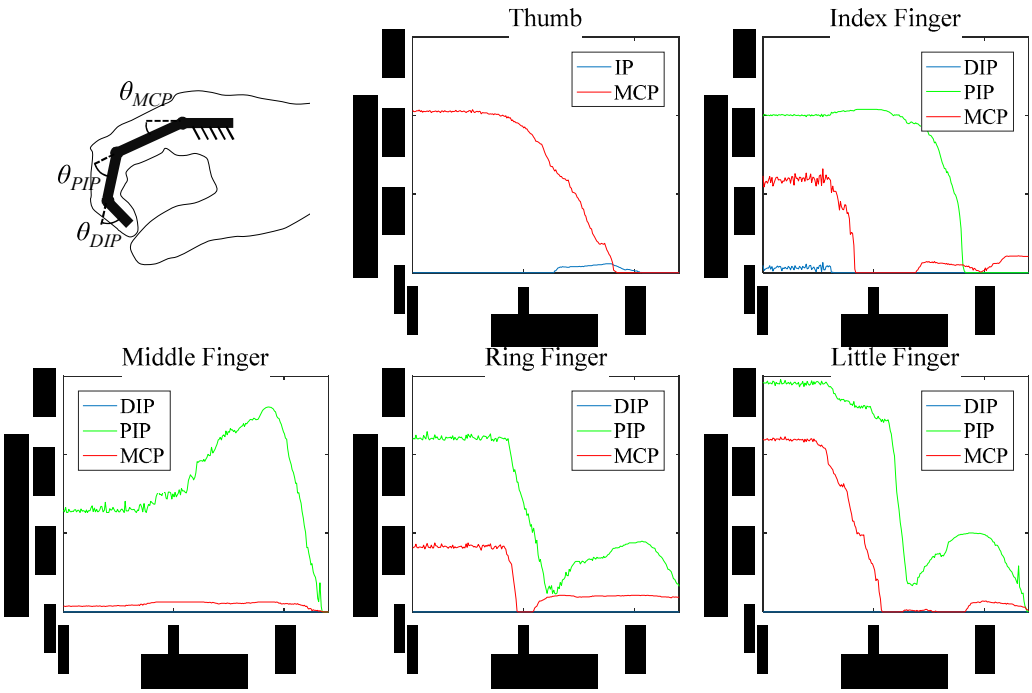

Figure 3.23: Joint angles measured by the hand exoskeleton.

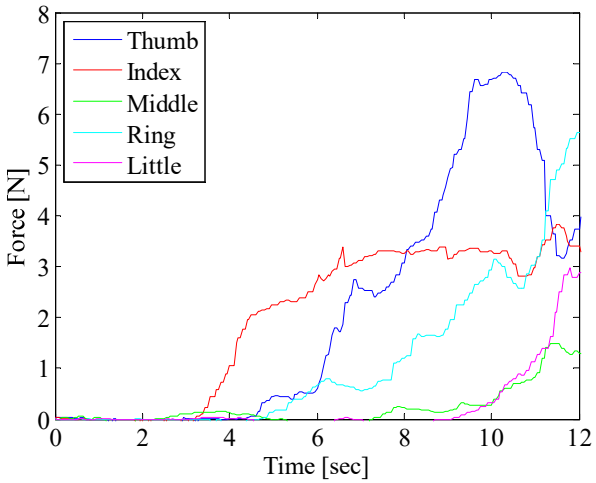

Figure 3.24: The force delivered to each fingertip from the cable-driven actuation system

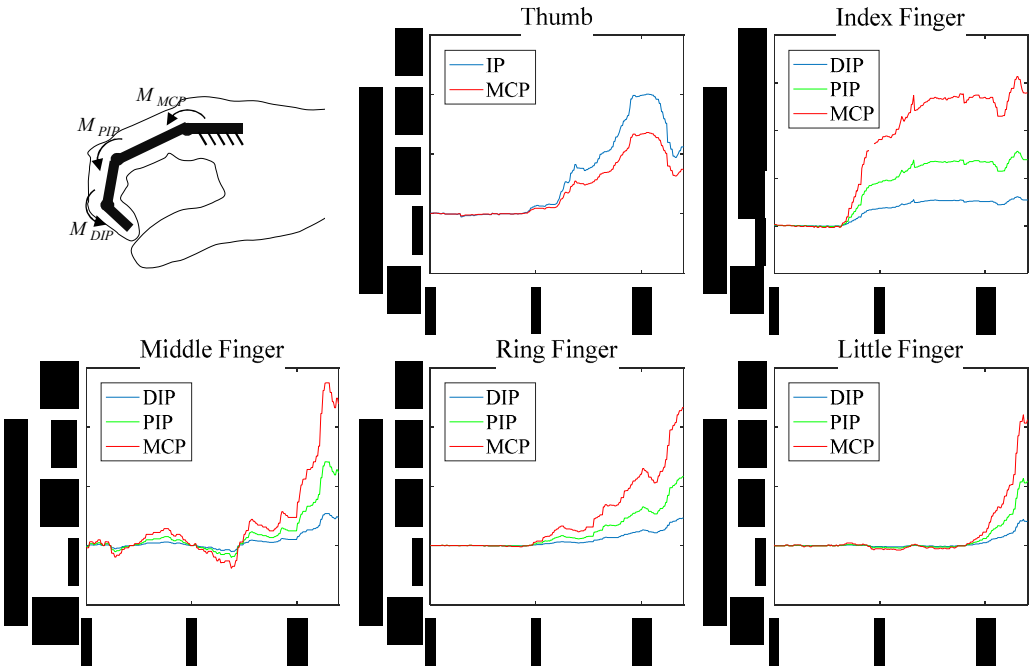

Figure 3.25: Joint moments estimated by the inverse dynamic equations.

activated, because activation of the FDP muscle was more physiologically efficient, because all the three joints were flexed by the FDP muscle. More complex loading conditions and movements could introduce activation of the FDS muscle.

3.6 Summary

In this chapter, the inverse dynamics-based static optimization was applied to the lower extremity and the fingers to estimate individual muscular forces. To collect motion information such as joint angles and external forces, the wearable sensor system and the hand exoskeleton were developed, respectively. The estimated individual muscular forces of the lower extremity and the fingers were able to explain the physical movements properly during walking and during extension of the fingers, respectively. The results can be combined with the low-level control platform suggested in Chapter 2, as a high level algorithm to activate the exoskeleton system according to the motion intention of the user.

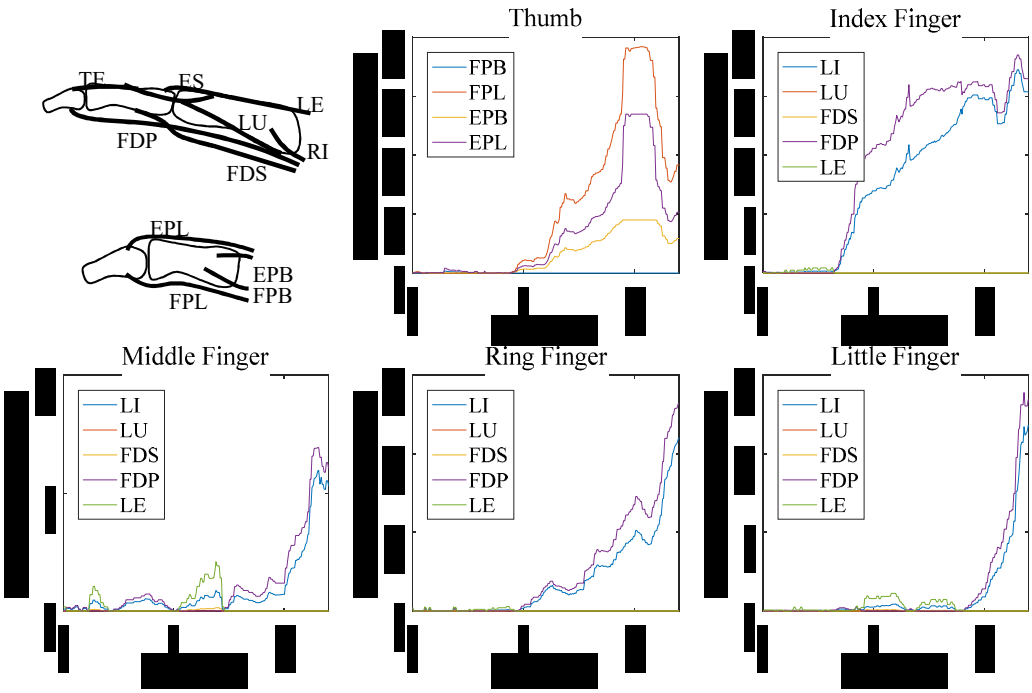

Figure 3.26: Individual muscular forces estimated by static optimization.

Chapter 4

Direct Writing of Liquid Metal for Soft Sensors*

4.1 Introduction

In the previous chapters, technical issues in the field of rigid robotics, specifically exoskeletons, are dealt with. By combining the exoskeleton system with the accurate force-mode controller (described in Chapter 2) with the estimation algorithm for the muscular forces (described in Chapter 3), the exoskeleton can be operated to assist the user. The mechanical structures of the exoskeleton, however, may be too uncomfortable and heavy to provide meaningful assistance to the user. Thus, we decided to find a way to develop a more helpful wearable system with soft robotics, because the practical applications with rigid exoskeletal structures are limited by the inherent characteristics such as heavy weight, rigid material, and uncomfortable wearable structures. Soft robotic systems are very attractive for wearable systems, because they usually consist of soft and stretchable materials without rigid mechanical components. Specifically, the soft elements in soft wearable systems should have tensile modulus lower than 1 MPa not to disturb natural motion of the users, considering the modulus of the human flesh is about hundreds of kPa (Figure 4.1).

In this study, we first tried to develop soft sensor systems, as an application of soft robotics to wearable systems. Soft sensors can be simply realized by forming stretchable conductive path inside an elastomeric body, which is a crucial ground technology for stretchable electronics. Specifically, soft sensors usually consist of thin sheets of silicone elastomer with

*The contents in this chapter is based on the published work of the author [93, 92].

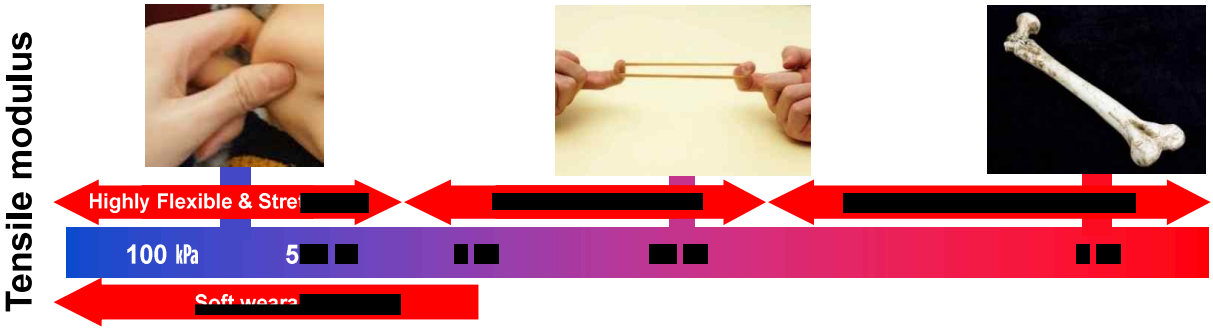

Figure 4.1: Tensile modulus of various materials.

an embedded conductive material. It is important to choose a proper conductive material, because it directly determines the performance of the sensors. Various types of conductive materials have been applied to soft electronics, which can be classified into non-ink and ink type materials (Figure 4.2).

Non-ink type materials include conductive fabric and rubber [160], dielectric elastomer, metal nanowire-based conductors [201], and carbon nanotube-based conductors [200]. Ink type materials include eutectic Gallium-Indium (eGaIn) [131], graphene oxide (GO) ink [202], ionic water [30], and carbon conductive grease (CCG) [119]. For a conductive material for stretchable electronics, properties such as conductivity and reconfigurability are crucial for more delicate sensor performance. From this point of view, the most preferred material is eGaIn due to its metallic conductivity and fluidic reconfigurability. Among the ink type conductive materials, eGaIn has lowest resistivity and viscosity as shown in Figure 4.3.

In addition, eGaIn is commercially available and has many attractive properties [163]. It exists in a liquid phase at room temperature (melting point $= 15.5\,^{\circ}C$) [44] with metallic conductivity ($29.4 \times 10^{-6}\,\Omega \cdot cm$) [212], low viscosity ($1.99 \times 10^{-3}\,Pa \cdot s$, two times higher than water) [167], low toxicity [191], and low vapor pressure (negligible evaporation and mass loss) [109]. Moreover, the gallium at the surface of eGaIn spontaneously forms a very thin oxide skin ($\approx 10\,nm$), reinforcing the adhesive characteristics of eGaIn without significant loss of conductivity [55, 17]. Additionally, the behavior of the oxide skin provides superior moldability of eGaIn, in contrast to mercury [28]. Using the highly flexible and conductive nature of the liquid metal, various types of sensors with superior softness and stretchability have been developed (Figure 4.4), such as strain and pressure gauges [134, 131, 185], tactile arrays [169, 197, 31, 61, 105, 104], and wearable sensors [117, 203, 130, 186, 113, 60, 176].

To develop stretchable sensors using eGaIn, one of the important issues is fabrication,

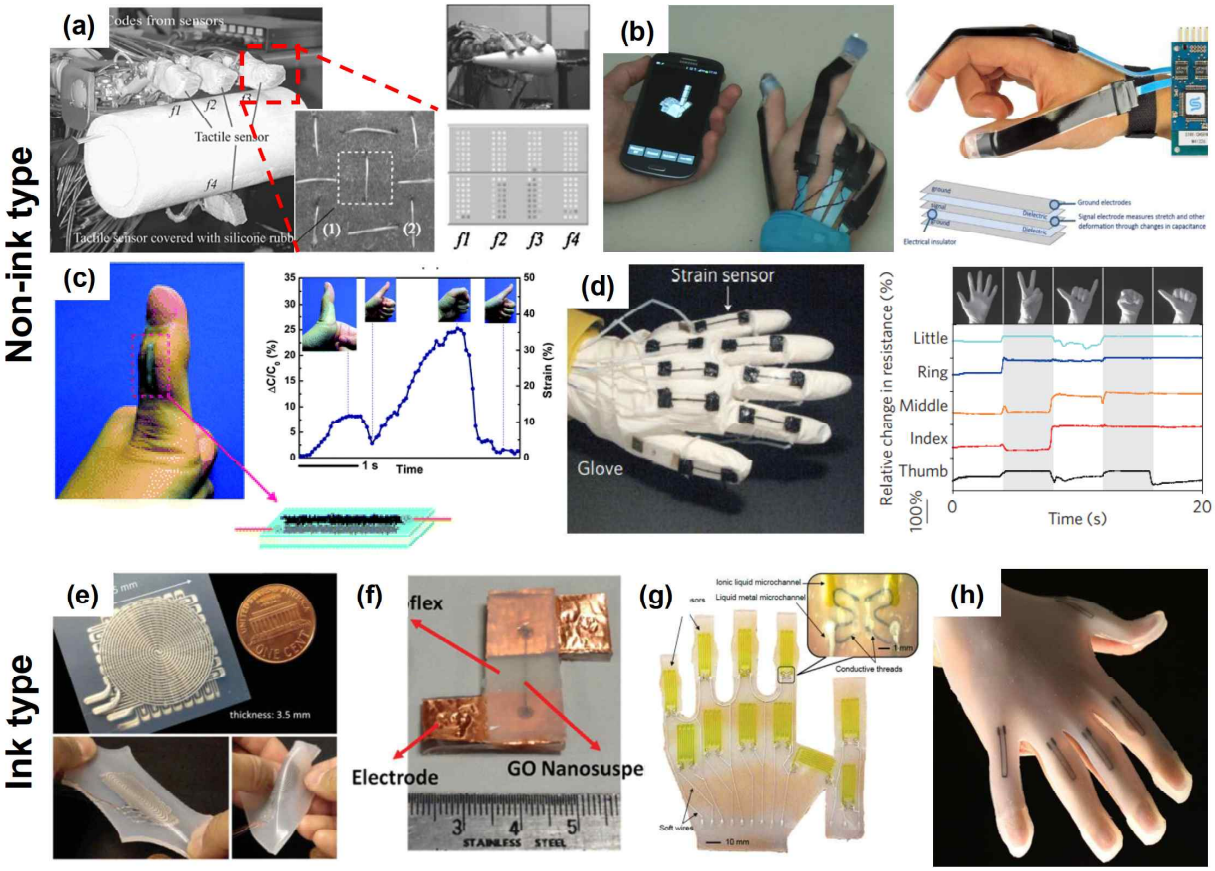

Figure 4.2: Conductive materials for stretchable electronics: (a) conductive fabric and rubber [160], (b) dielectric elastomer, (c) metal nanowire-based conductors [201], (d) carbon nanotube-based conductors [200], (e) eGaIn [131], (f) GO ink [202], (g) ionic water [30], and (h) CCG [119].

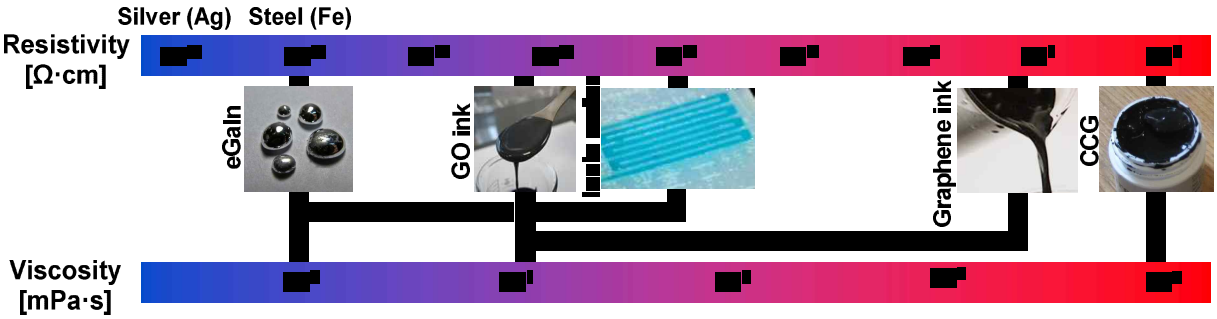

Figure 4.3: Resistivity and viscosity of ink type conductive materials.

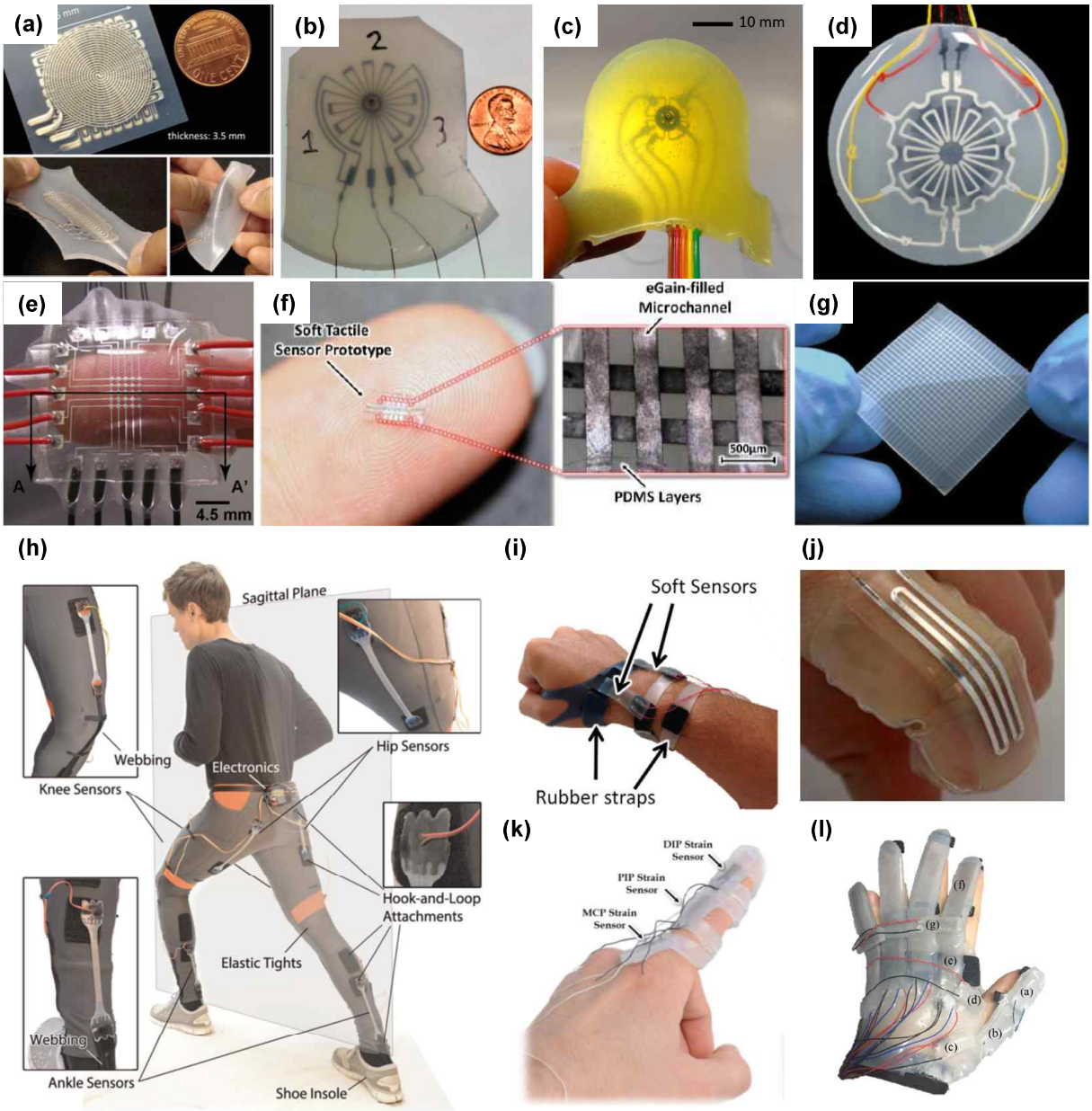

Figure 4.4: eGaIn-based soft sensors: (a) multi-axis strain gauge [131], (b)-(d) multi-axis force sensor [185, 94], (e)-(g) sensor array [197, 62, 105], (h) lower extremity motion sensor [117], (i) wrist motion sensor [186], (j) finger motion sensor [113], (k) finger motion and fingertip pressure sensor [60], and (l) 3D finger motion sensor [176].

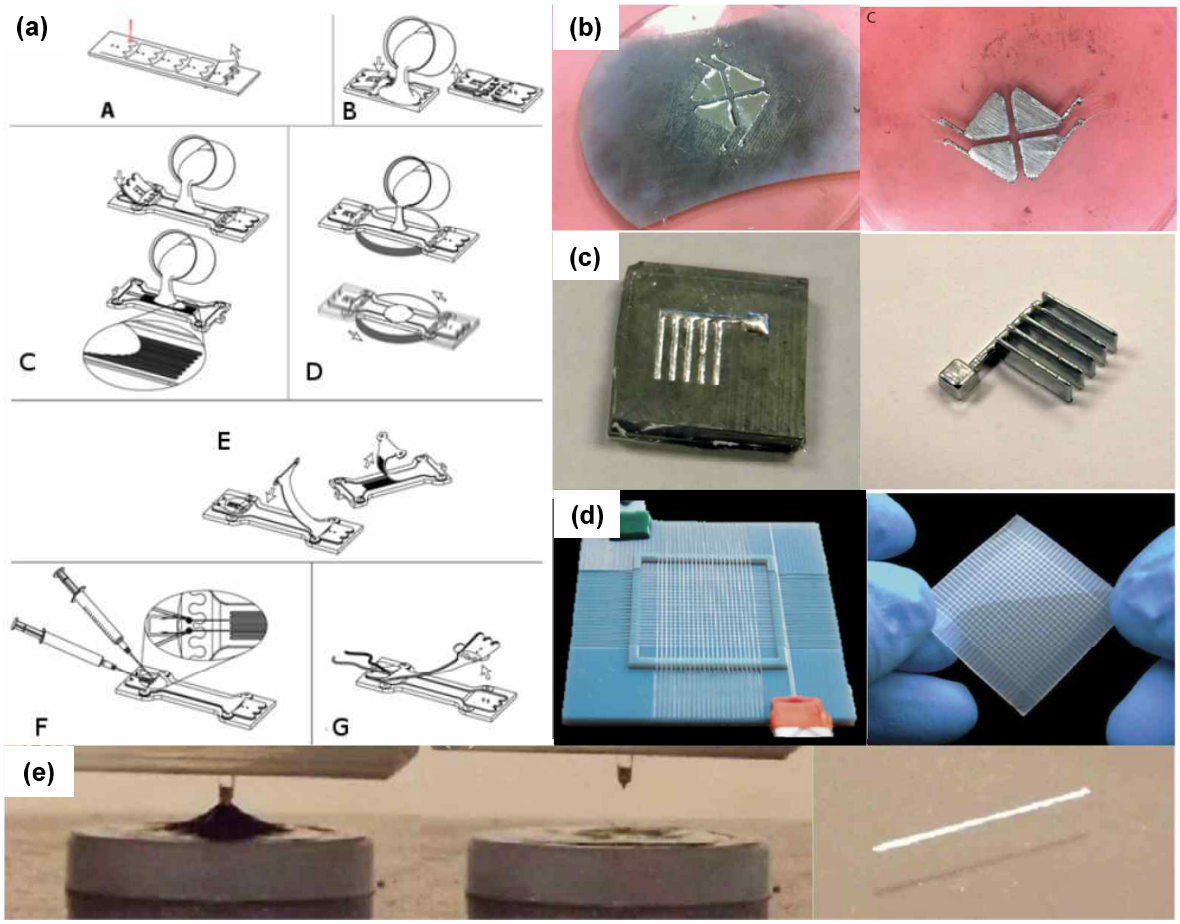

Figure 4.5: Fabrication methods for eGaIn-based soft sensors: (a) casting, bonding, and injection [117], (b) mask deposition [148], (c) freeze casting [52], (d) direct filament casting [105], and (e) microcontact printing [171].

which can determine the accuracy and the feasibility of sensor geometry [84]. Among the various fabrication methods, the most common is casting with a mold, followed by bonding and injection (Figure 4.5 (a)) [44, 131, 185, 113, 169, 197, 31, 117, 203, 130, 29, 135, 161]. Others include mask deposition (Figure 4.5 (b)) [148], freeze casting (Figure 4.5 (c)) [52], direct filament casting (Figure 4.5 (d)) [105, 104], and microcontact printing (Figure 4.5 (e)) [171]. The advantages and disadvantages of each fabrication method are well discussed in detail in [84]. In most fabrication methods, it can be challenging to achieve accurate shapes and configurations of the microchannel, because the fabrication steps require delicate alignment of the workpiece by hand [161, 130]. The accuracy of the fabricated microchannel

has rarely been investigated, even though it can be a source of errors in analysis of sensor performance and the design of a sensor. Some research has demonstrated accurate shapes and spacing of microchannels by direct filament casting through delicate arrangements of fibers [105, 104]. However, this novel fabrication method cannot create a curved microchannel, because it would be difficult to extract the curved fibers within the elastomer without damaging the microchannel. As well as the accuracy of the geometry and configuration of the microchannel, it has been challenging to modify the design of the sensor flexibly for the most fabrication method proposed.

Recently, novel fabrication techniques, which are highly productive, programmable, and scalable with accurate geometry of the microchannel, have been suggested: selective wetting (Figure 4.6 (a) [106]) and direct ink writing (DIW) (Figures 4.6 (b)-(d) [102, 55, 17]. As reported recently, the unique fabrication techniques are attributed to the unique mechanical and rheological behaviors of the liquid metal [44, 199, 102, 106]. In case of the selective wetting, however, a fabrication step, such as sputtering nanoparticles, is necessary, which results in high fabrication costs [106, 127]. In contrast, in case of DIW, liquid metal traces with any configurations can be directly written by a motorized syringe, without special mechanical or chemical treatment of the raw materials, which can allow high programmability and a lower barrier-to-entry of fabrication as well as low production cost [16, 55, 17, 102, 176]. Furthermore, requirement for the hand skills can be minimized, because a motorized syringe can be used to write the microchannel of eGaIn directly [16].

The direct writable property of the liquid metal have been investigated vigorously. As shown in Figure 4.6 (b)-i), even a free standing 3D structure has been printed, achieving values 100 times larger than the Rayleigh stability limit [102, 176]. One study found that eGaIn had writable characteristics on surfaces with different levels of roughness (Figure 4.6 (b)-ii)) [55]. Due to its superior structural stability from the oxide layer, an arbitrary shape of the microchannel can be written directly with eGaIn in a stable manner by adjusting the flow rate of eGaIn and the feed rate of the syringe to fabricate strain gauges (Figure 4.6 (b)-iii)) [16].

As described, the special characteristics of eGaIn have been investigated actively. However, little work have been done to develop the fabrication technique for eGaIn-based soft sensors based on the attractive characteristics. Especially, the following research contents are necessary to widen the applications of the soft sensor technologies: 1) development of a highly productive and programmable fabrication technique, 2) verification of production quality such as consistency and reproducibility, 3) development of fabrication process includ-

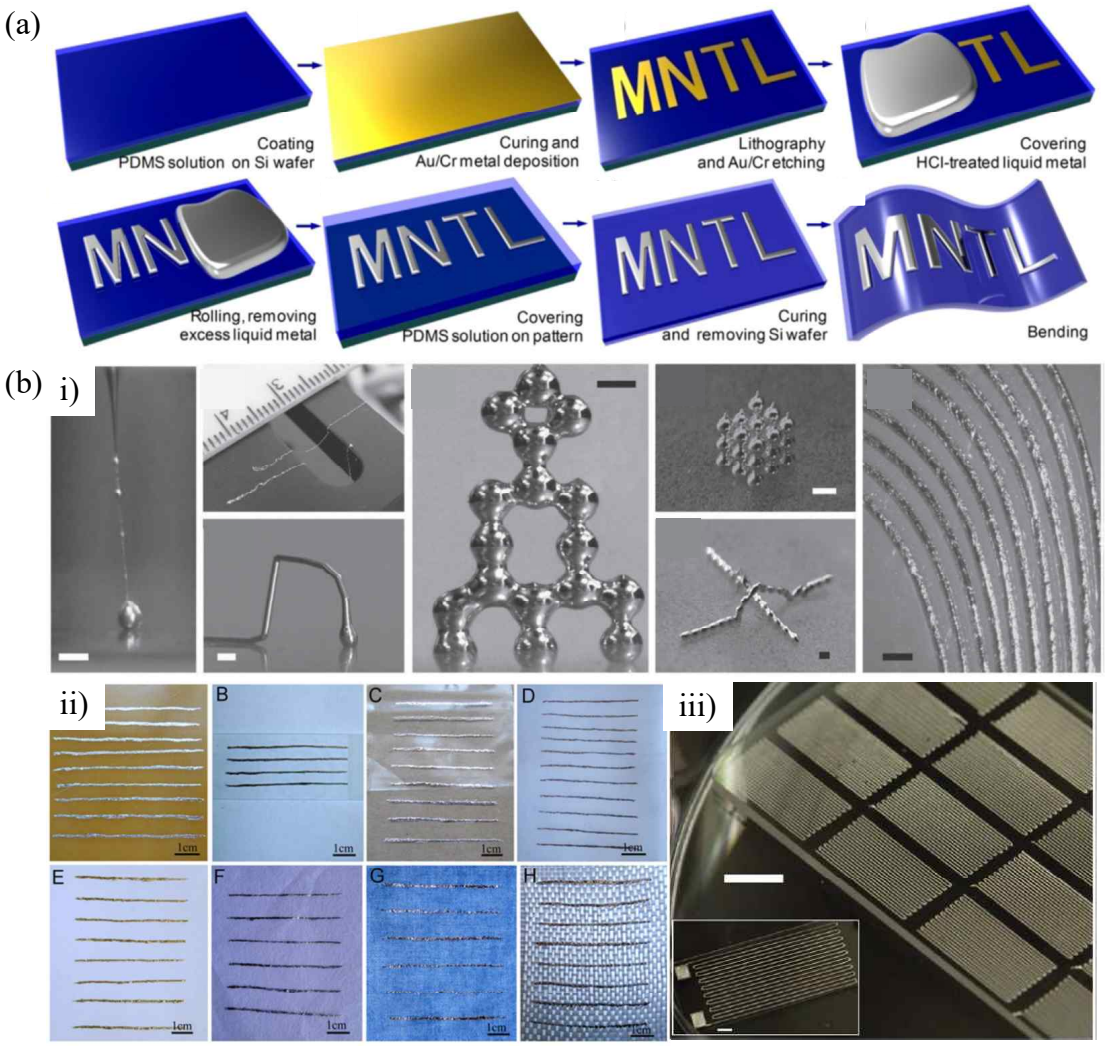

Figure 4.6: Highly programmable fabrication methods for liquid metal-based conductive pathes: (a) selective wetting [106] and (b) direct ink writing (DIW): i) 2D and 3D structures written directly by liquid metal [102], ii) liquid metal written on various substrates [55], and iii) strain gauges based on DIW [17].

ing an electrode part for electrical connection, which is a critical technical gap in the field of soft sensors, and 4) fabrication and demonstration of soft sensor systems (e.g. a wearable sensor system). Therefore, in this study, a DIW-based fabrication technique is proposed to address the issues.

This chapter is organized as follows. In Section 4.2, investigations on manually developed soft sensors are presented, with discussion on its limitation and requirement of highly productive and flexible manufacturing process. In Section 4.3, a fabrication technique based on direct ink writing of eGaIn is suggested and verified. In Section 4.4, a solution for an electrical connection is proposed based on direct writing technique, and reliability of the electrical connection is experimentally verified. In Section 4.5, the suggested fabrication technique is applied to develop a system-level of soft sensor (e.g. glove).

4.2 Application of the Mold-based Fabrication Technique

4.2.1 Fabrication Steps and Measurement Principle

The mold-based fabrication process for soft sensors is well introduced in [131]. The detailed procedures are described in Figure 4.7. First, a mold embossed with channel pattern is prepared based on machining, lithography, laser engraving, or 3D printing (Figure 4.7 (a)). The feasible size and surface quality of the channel depend the fabrication method of the mold. Uncured silicone is poured into the mold and demolded after curing (Figure 4.7 (b)). In this process, the workpiece should be handed with extra cares not to be torn out during the demolding process. The workpiece is bonded onto a flat silicone layer by applying uncured silicone or oxide plasma treatment (Figure 4.7 (c)). The workpiece should remain parallel to the silicone layer not to block the microchannel during bonding process. The edges of the silicone layer is trimmed manually by a knife (Figure 4.7 (d)). eGaIn is injected into the terminal of the microchannel, while air is extracted through the other side simultaneously (Figure 4.7 (e)). This process also requires extra cares to control injection pressure, because bonded surface can burst due to pressure of the injection. The last step is insertion of wires into both terminals and sealing with silicone bonds to prevent leakage (Figure 4.7 (f)).

Figure 4.8 (a) describes how the soft sensor measures mechanical strain. The electrical resistance between a conductive path can be expressed as $R = \rho L/A$, where ρ, L, and A are

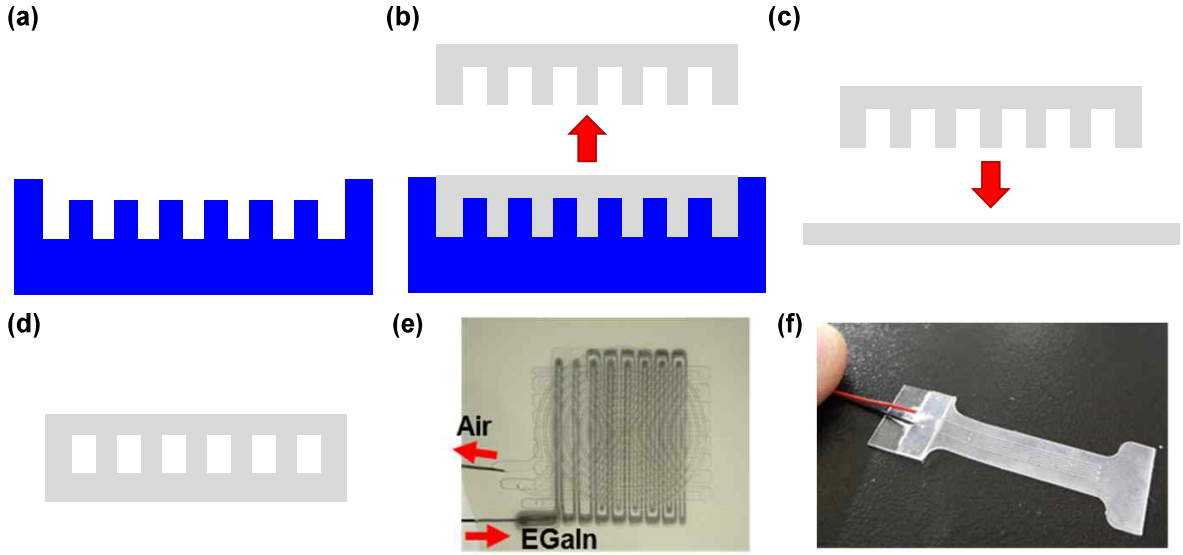

Figure 4.7: Mold-based fabrication steps: (a) preparation of a mold, (b) casting and demolding, (c) bonding, (d) trimming, (e) injection of eGaIn, and (f) insertion of wires and sealing.

resistivity of the conductive material, and length and cross sectional area of the microchannel, respectively. If the elastomeric body is elongated, the length of the microchannel increases with shrunken cross section area, resulting in increase of electrical resistance between the terminals of the microchannel. Serpentine patterns aligned with a target direction are preferred to magnify change of resistance according to the mechanical strain (Figure 4.8). Also, mechanical pressure can be measured similarly, because deformation of the elastomeric body cause resistance change. A circular pattern in origin symmetry is most sensitive to axial deformation (Figure 4.8 (c)).

4.2.2 Application to Measurement of Finger Motions[†]

Based on the mold-based fabrication technique, a strain-sensitive soft sensor was fabricated using EcoFlex 0030 (Smooth On [165]) and its resistance change was measured according to corresponding mechanical strain (Figure 4.9). The resistance change was measured for each 10 % increase in mechanical strain, and the measurements were repeated 10 cycles in total. As shown in the result, the measured resistance change was reproducible (had similar

[†]The contents in this section is based on the published work of the author [130].

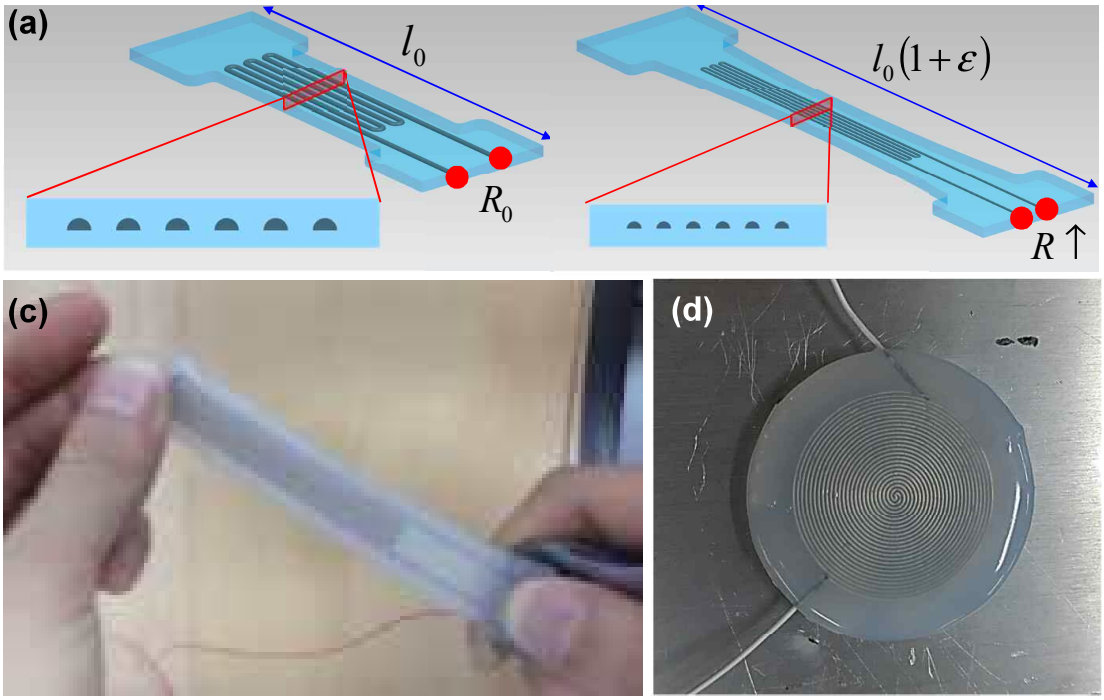

Figure 4.8: Measurement principle and applications of eGaIn-based soft sensors: (a) Measurement principle of a soft strain sensor, (b) A strain-sensitive soft sensor, (c) A pressure-sensitive soft sensor.

values), but the relationship had a nonlinear relationship with large strain ($> 40\,\%$). With relatively smaller strain ($< 40\,\%$), the relationship satisfies a linear trend.

A Glove-type Sensor for 3D Finger Motions

In this application, we tried to measure 3-dimensional finger motions by attaching multiple soft strain sensors. In detail, Figure 4.10 (a) shows the skeletal structures of the fingers, including distal, middle, proximal, and metacarpal bones, connected through distal interphalangeal (DIP), proximal interphalangeal (PIP), and metacarpal (MCP) joints. Four fingers have same structures of bones and joints, while the thumb consists of distal, proximal, and metacarpal bones with interphalangeal (IP), MCP, and carpometacarpal (CMC) joints. Figure 4.10 shows kinematic chains of the fingers with revolute joints, which indicates degrees of freedom (DOF) of each joint. The five fingers were modeled as a kinematic system with 22 DOFs. Figures 4.10 (c)-(g) show the motion of the fingers and location and elongation of the soft sensors. More specifically, Flexion/extension of the MCP, PIP, and CMC joints, which

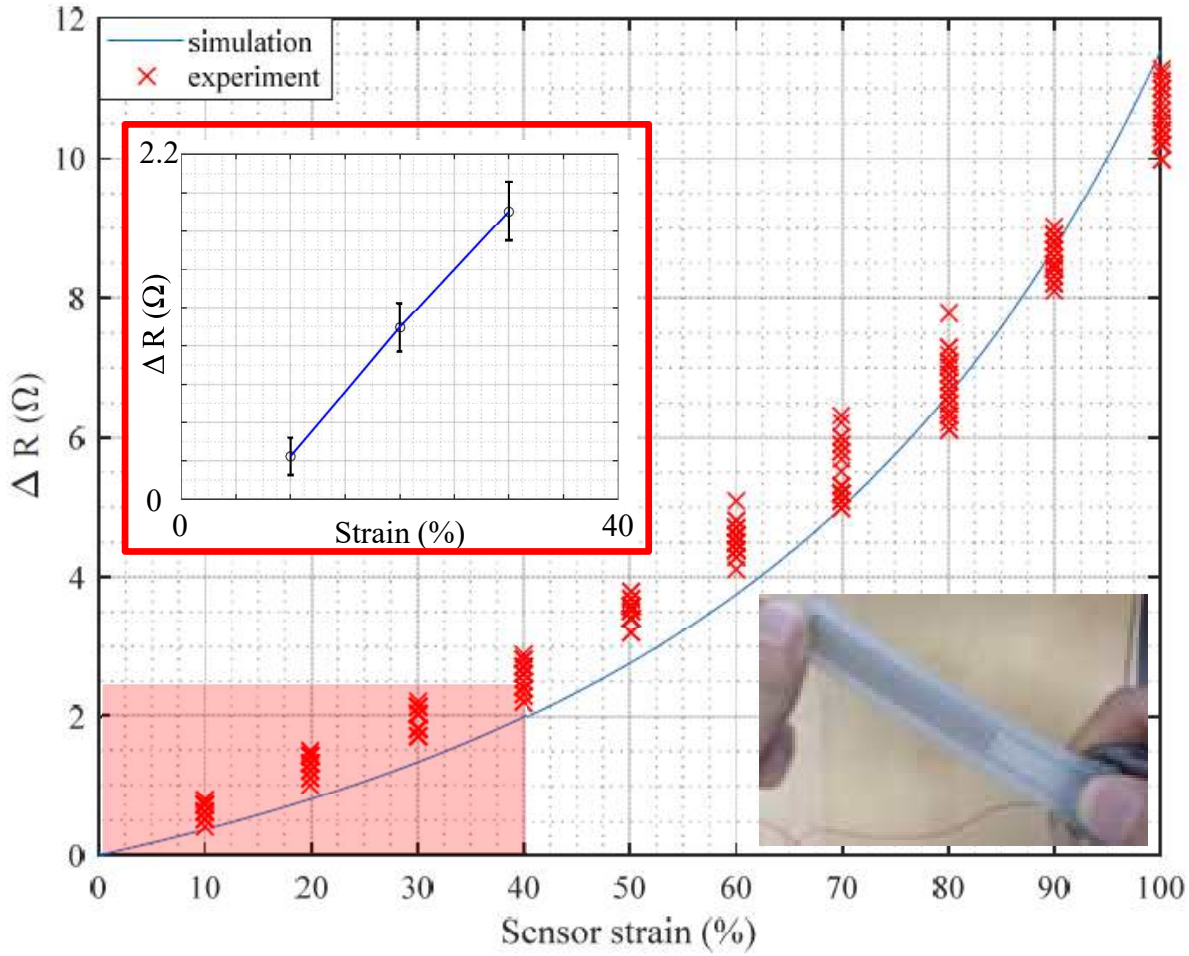

Figure 4.9: Experimental results of a soft strain sensor.

can be measured by attaching a soft sensor on the dorsal side of the joints (Figures 4.10 (c)-(e)). Adduction/abduction of the CMC and MCP (in the four fingers) can be measured by attaching the soft sensor across the fingers (Figures 4.10 (f) and (g)).

Considering the locations of the sensors, two types of strain sensing units were fabricated as shown in Figure 4.11 (a). Type 1 unit consisted of two sensing parts to measure flexion/extension of the PIP and MCP joints, and Type 2 unit consisted of one sensing part to measure adduciton/abduction of the fingers and flexion/extension of the CMC joint. The assembled glove sensor is described in Figure 4.11 (b), composed with 15 sensing units in total.

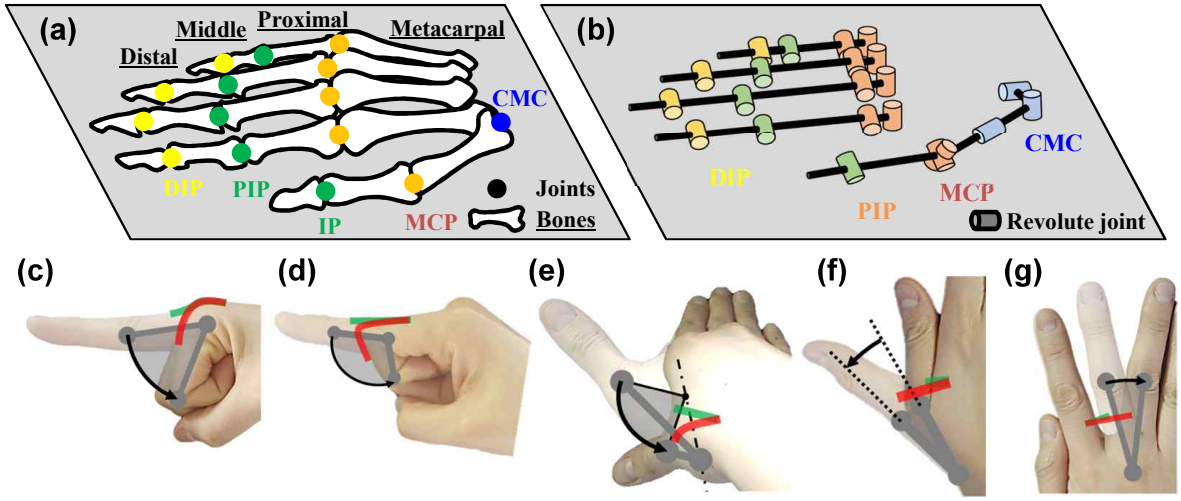

Figure 4.10: Structures and motions of the fingers: (a) skeletal structures of the fingers, (b) kinematic model of the fingers, flexion/extension of the (c) MCP joint, (d) PIP joint, and (e) CMC joints, and adduction/abduction of the (f) CMC and (g) MCP joints.

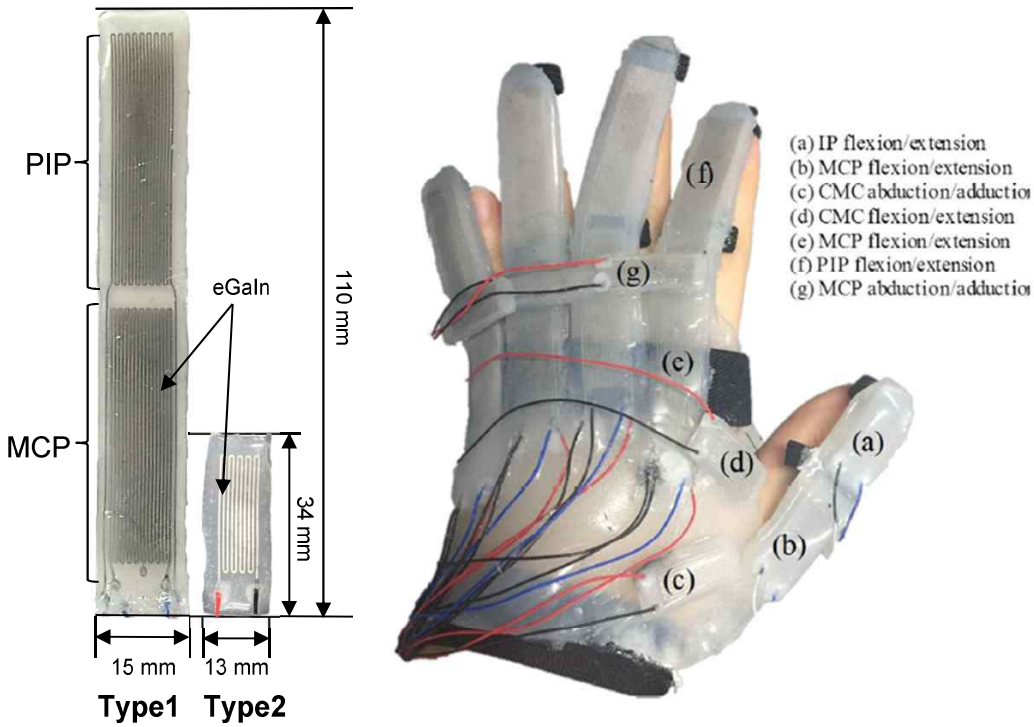

Figure 4.11: A glove-type soft sensor system for 3D finger motions: Two types of strain sensing units (Type 1 for FE of the MCP and PIP joints, Type 2 for AA of the MCP and CMC joints and FE of the CMC joint) and Assembled glove-type sensor system.

A Kinematic Model for Joint Angle Estimation

To estimate joint angles of the four fingers, a kinematic model is required, which converts the sensor signals (proportional to the strain) into joint angle of each DOF. In this model, 22 DOFs in the fingers descried in Figure 4.10 (b) were estimated by 15 soft sensors. First, in case of the flexion/extension (FE) of the MCP and PIP joints, the joint angles were assumed to be linearly proportional to the sensor signal as follows:

$$\begin{aligned} \Delta\theta_{FE,MCP} &= K_{MCP}\Delta L_{FE,MCP} \\ \Delta\theta_{FE,PIP} &= K_{PIP}\Delta L_{FE,PIP} \\ \Delta\theta_{FE,DIP} &= frac23\Delta\theta_{FE,PIP} \end{aligned} \tag{4.1}$$

where θ, L, and K are joint angles, length of the sensor, and proportional constant, respectively. The joint angle of the DIP joint was estimated by a function of the PIP joint angle, because motions of the DIP joint is dependent on that of the PIP joint.

In case of the adduction/abdduction (AA) of the MCP joints in the four fingers (except for the thumb), signal from the Type 2 soft sensor was affected by both FE and AA motion of the MCP joint as shown in Figure 4.12 (a). Thus, a decoupling relationship was introduced as described in Figure 4.12 (b). The PIP joints of the index (I_{PIP}) and the middle (M_{PIP}) finger were projected onto a frontal plane as shown in black solid circles. Based on the projected points, the three segments can be defined, including $L_(horizontal)$ and $L_(vertical)$ parallel to the dorsal and the sagittal plane of the middle finger, and $L_(diagonal)$ which is distance between the two joints. The signal of the Type 1 and Type 2 soft sensors were assumed to be proportional to $L_{vertical}$ and $L_{diagonal}$, respectively. Thus, $L_horizontal$ can be estimated by the following equation.

$$\Delta L_{horizontal} = \sqrt{\Delta L_{diagonal}^2 - \Delta L_{vertical}^2} \tag{4.2}$$

The AA motion of the MCP was estimated by the magnitude proportional to $L_horizontal$.

$$\Delta\theta_{AA,MCP} = K_{AA,MCP}\Delta L_{horizontal} \tag{4.3}$$

Similarly, crosstalk occurred in the Type 1 and Type 2 sensor around the CMC joint of the thumb as shown in Figure 4.13 (a). The length of the Type 2 soft sensor changed under pure flexion of the CMC joint. Therefore, the same strategy was applied as shown in Figure 4.13 (b) with the following equations:

$$\begin{aligned} \Delta L_{horizontal} &= \sqrt{\Delta L_{diagonal}^2 - \Delta L_{vertical}^2} \\ \Delta\theta_{AA,CMC} &= K_{AA,CMC}\Delta L_{horizontal} \end{aligned} \tag{4.4}$$

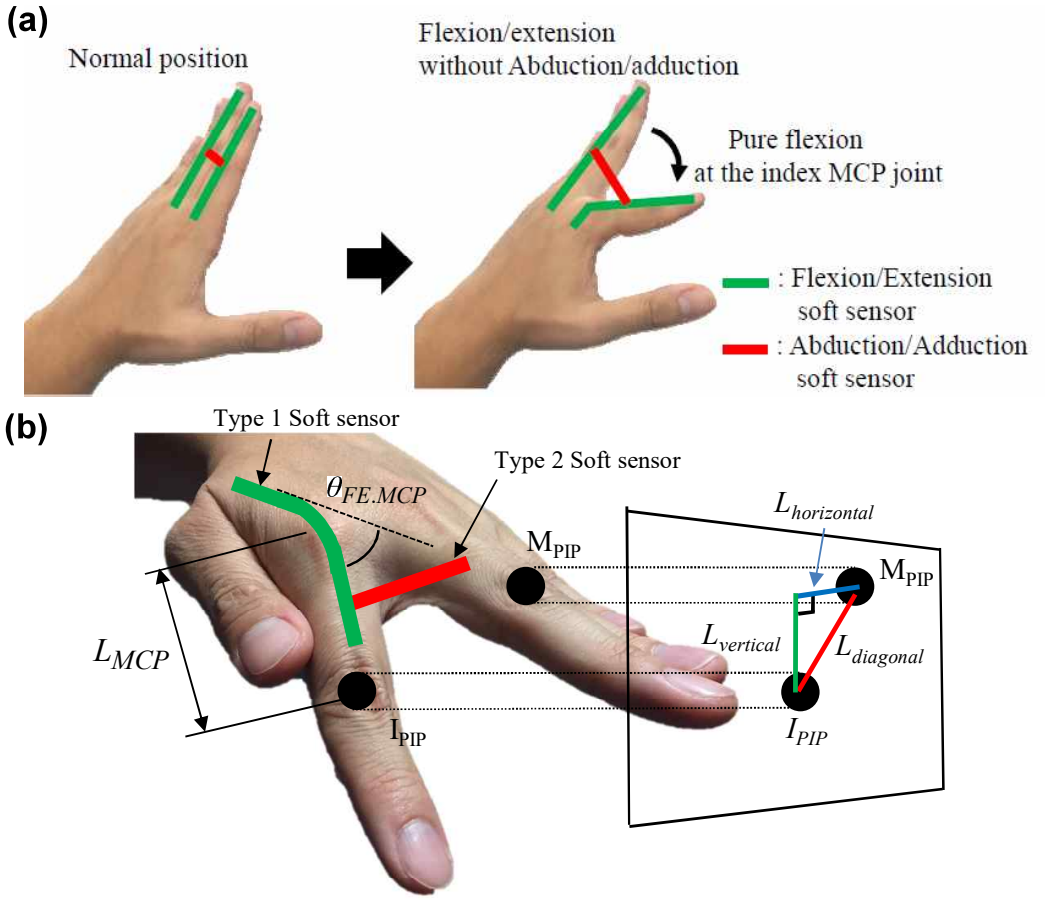

Figure 4.12: Measurement of AA motions of the MCP joint: (a) crosstalk of the AA sensor due to FE of the MCP joint and (b) schematic for a decoupling algorithm for the MCP joint.

where magnitudes of $L_{vertical}$ and $L_{diagonal}$ are estimated by the Type 1 and Type 2 soft sensors, respectively. The AA angle of the thumb MCP joint was estimated by a linear function of the AA angle of the CMC joint, because the linear relationship was identified in our experiment using the motion capture system with reflective markers (Figure 4.14).

Experimental Results

To verify performance of the measurement system with the kinematic model, reflective markers were attached on the fingers. The sensor signals and positions of the markers were recorded simultaneously to compare the results. Figure 4.15 (a) shows the joint angles of the index finger estimated by the motion capture (reference) and the soft sensors (measured),

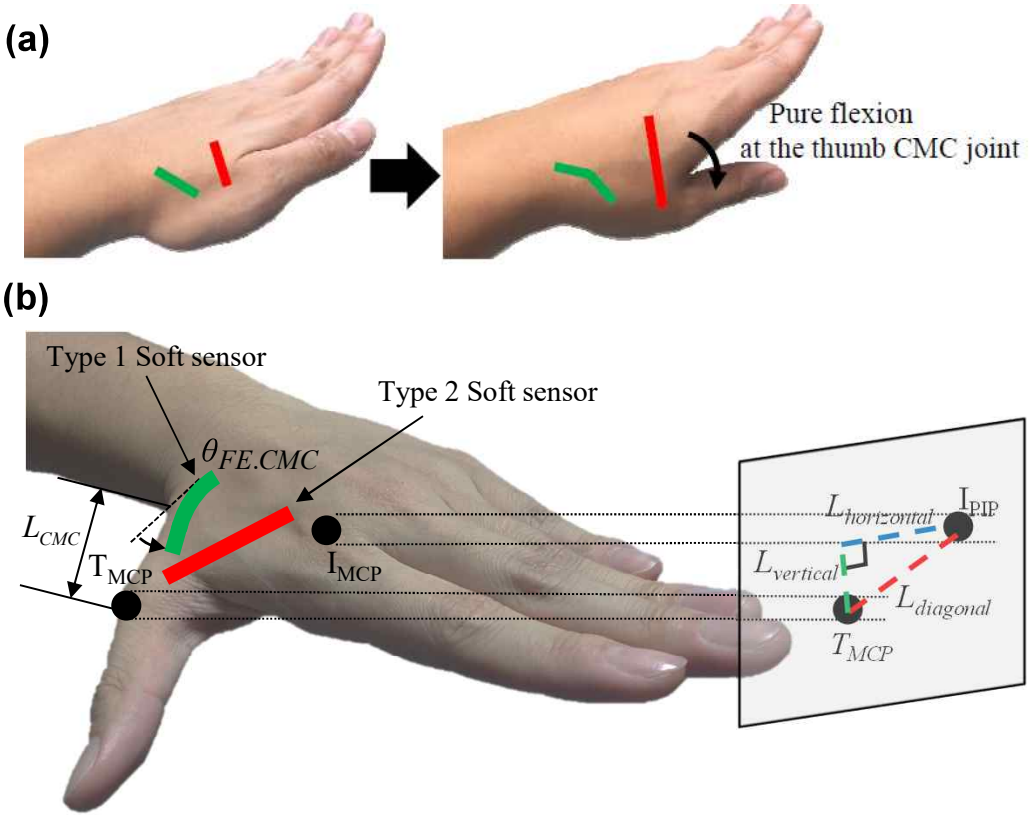

Figure 4.13: Measurement of AA motions of the CMC joint: (a) crosstalk of the AA sensor due to FE of the CMC joint and (b) schematic for a decoupling algorithm for the CMC joint.

respectively. Based on the joint angles estimated by the soft sensor system, motion of the index finger was visualized in the animation as shown in Figure 4.15 (b). Experimental results of the thumb is described in Figure 4.16. In both cases, the maximum error of the estimated joint angles was about 2.55 deg. The error might be caused by misalignment of the soft sensors and slip between the soft sensor and the skin.

Discussion

In this work, 3D finger motions were estimated by multiple soft sensors. Measurement of 3D finger motions without disturbing natural motion of the subject has remained as a challenging task, because limited space on the fingers and multiple DOFs in the joints. Thus, we can claim that this achievement is attributed to superior softness and stretchability of the soft sensors. However, fabrication of the sensors requires long process time due to difficulty in

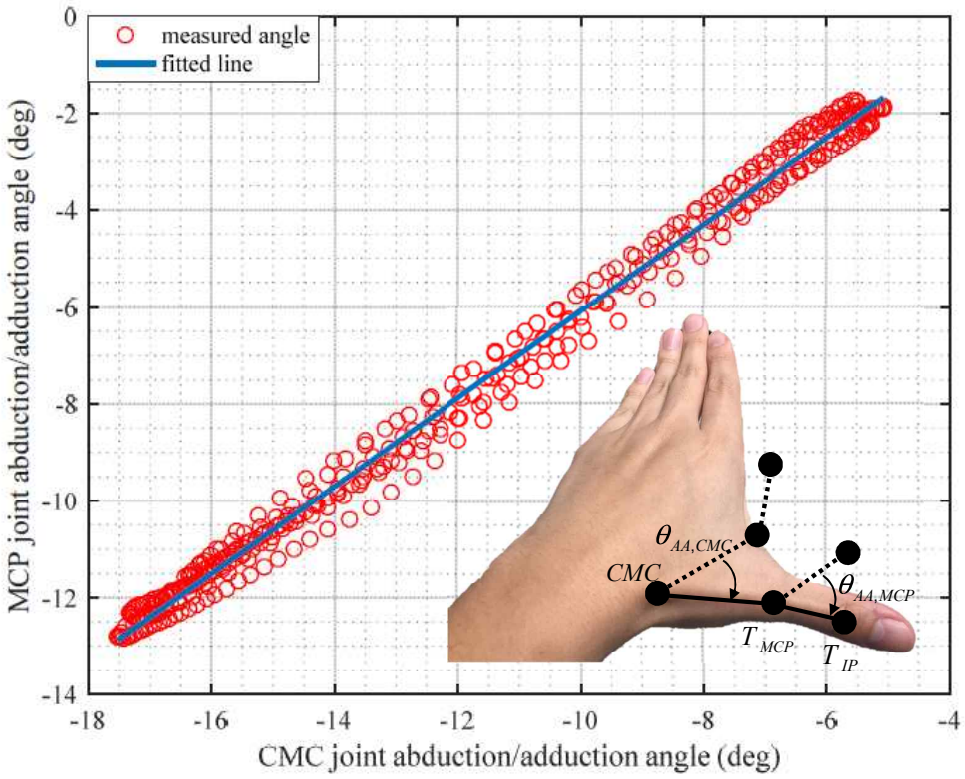

Figure 4.14: Linear relationship between AA motions of the CMC and the MCP joints.

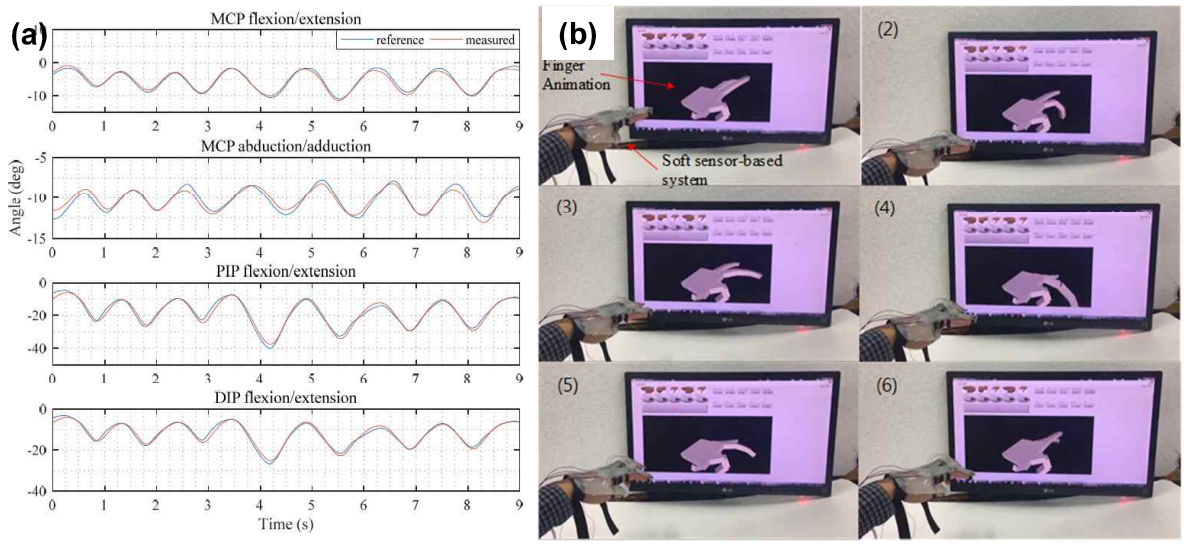

Figure 4.15: Experimental result of the index finger.

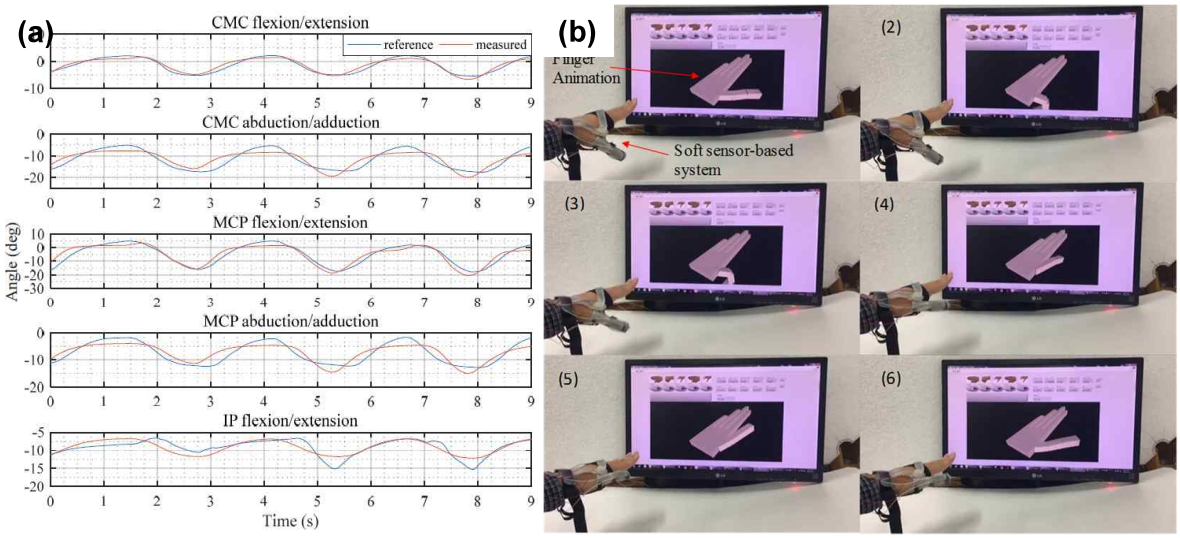

Figure 4.16: Experimental result of the thumb.

fabrication steps and low production rate. The multiple sensing units should be assembled to fabricate a sensor system, which increase volume of the sensor system. Furthermore, the directly inserted wires were mechanically and electrically fragile, resulting in low durability of the system. Thus, a new fabrication technique is required to overcome these technical barriers.

4.2.3 Application to Measurement of Ground Reaction Forces

As an another application, pressure sensitive sensors were fabricated to measure ground reaction forces as an insole sensor (Figure 4.17). Each pressure sensing unit should endure and measure the extreme pressure applied during walking such as hundreds of kPa [112]. To satisfy the target pressure set as 500 kPa, cross sections (square with width 100μm and height 200μm), number of twist (60 times), and elastomer material (Dragon Skin 30, Smooth On [164]) of the pressure sensing units were selected, based on an analytic model based on fracture mechanics (well explained in [134]).

Relaxation in Sensor Signals

To calibrate the pressure sensing unit, the vice was used to apply force to the soft sensor while measuring the applied force by a serially placed loadcell (Figure 4.18 (a)). As shown

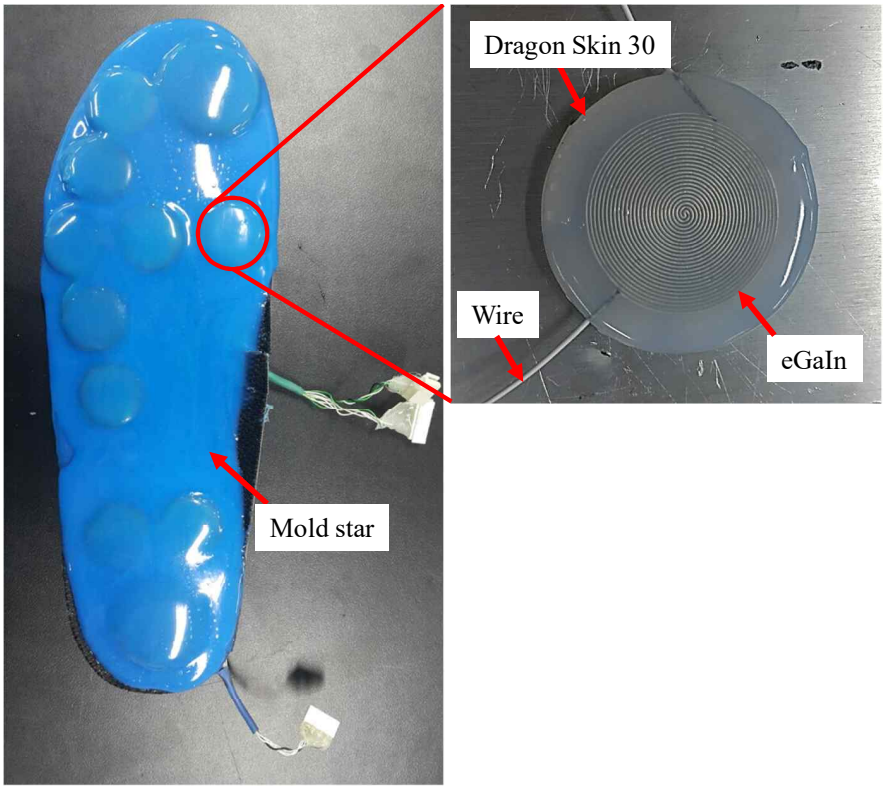

Figure 4.17: Soft insole sensors with 12 pressure sensing units.

in Figure 4.18 (b), although the applied force was converged rapidly as measured by the loadcell, the force estimated by the soft sensor (linearly fitted) had very slow response. To confirm the slowness of the sensor response, normalized step responses were investigated as shown in Figure 4.18 (c). The solid lines shows step response of the soft sensor with $100, 200, 300$ and $350\ N$ loadings. As shown in the results, the response was extremely slow with the loading condition over $350\ N$, even though the target performance ($500\ N$) was larger than the applied load. The actual response of the sensor plotted as red circles in Figure 4.19 (a) was different with the response estimated by the analytic model (Figure 4.19 (b)). In the analytic model, the pressure range was overestimated (estimated pressure limit $>> 350\ kPa$) than the actual performance.

To extend the pressure limit, pressure sensing units were fabricated using elastomer materials with higher hardness as shown in Figure 4.20. The previous pressure sensing unit was made of Dragon Skin 30 with shore hardness 30A, we had three candidates PDMS, Sorta-Clear, and ClearFlex. In case of PDMS, workpieces were easily torn out during demolding

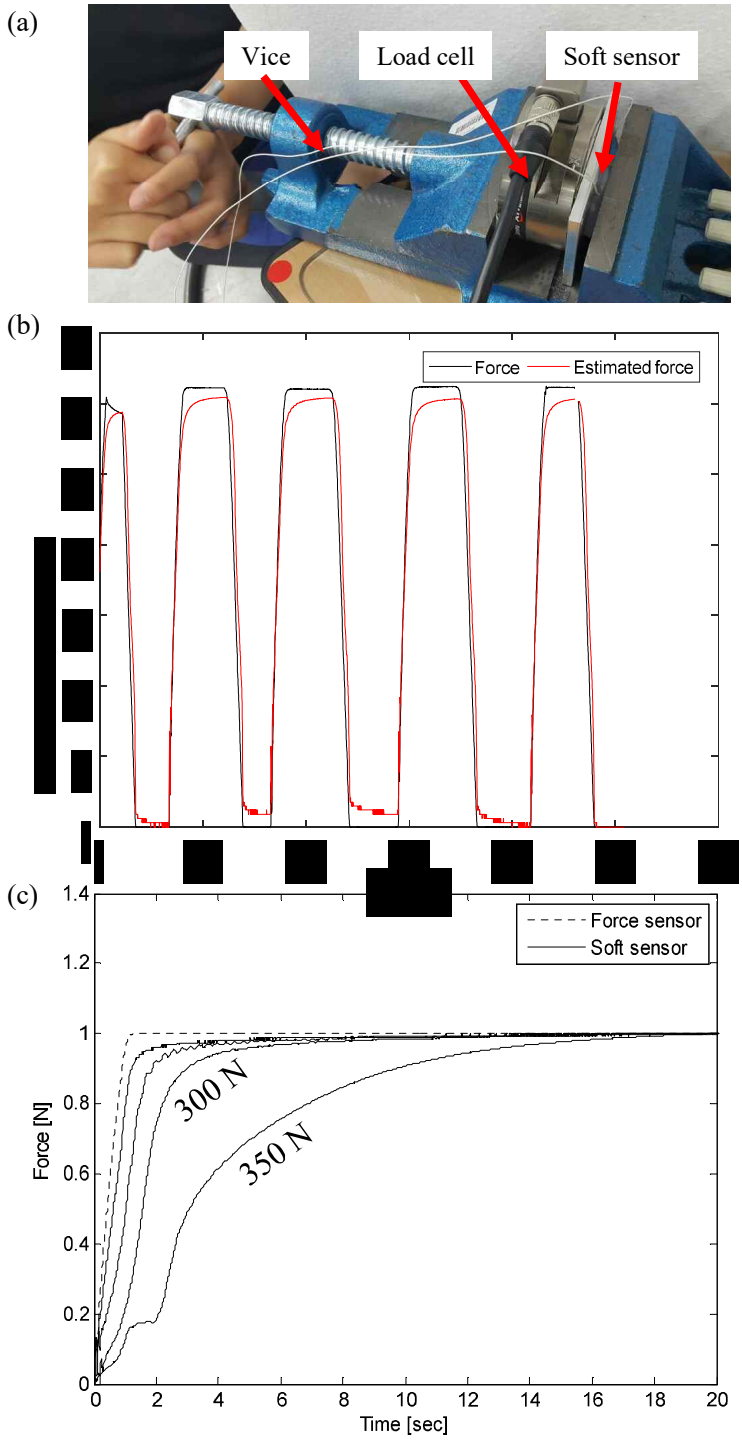

Figure 4.18: Verification of a pressure sensing unit: (a) experimental setup, (b) applied force compared with the estimated force, (c) normalized step responses of the load cell and the soft sensor with various loadings.

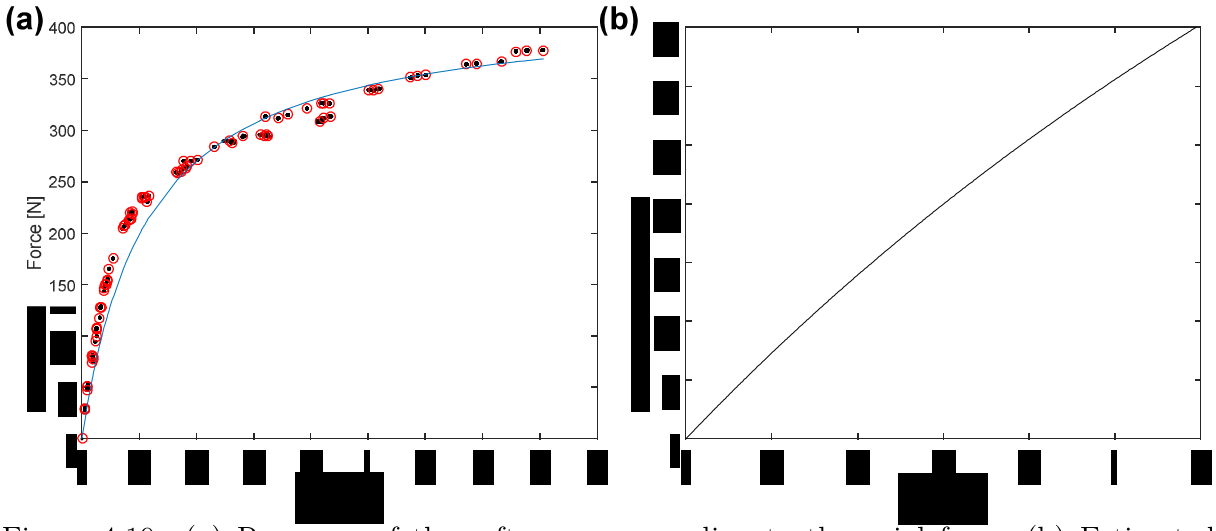

Figure 4.19: (a) Response of the soft sensor according to the axial force, (b) Estimated response of the soft sensor based on the fracture mechanics-based analytic model.

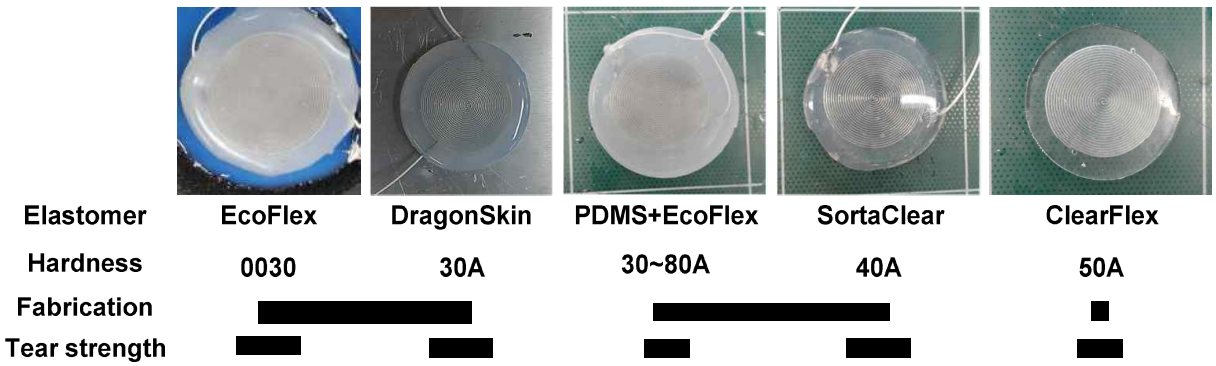

Figure 4.20: Fabrication of pressure sensing units with different elastomers.

process due to low tear strength of the materials and the demolded workpiece would not be bonded on the plain without oxide plasma treatment in the fabrication process. In case of SortaClear, it was extremely difficult to degas air bubbles in the silicone material due to its high viscosity. In case of ClearFlex, the demolded workpiece cannot be bonded.

Derivation of the Analytic Model

Here, the analytic model was modified to elucidate the reason that the limit pressure of the soft sensor was lower than that estimated by the analytic model [134]. In the previously suggested analytic model, the external load was distributed in a straight line and only a

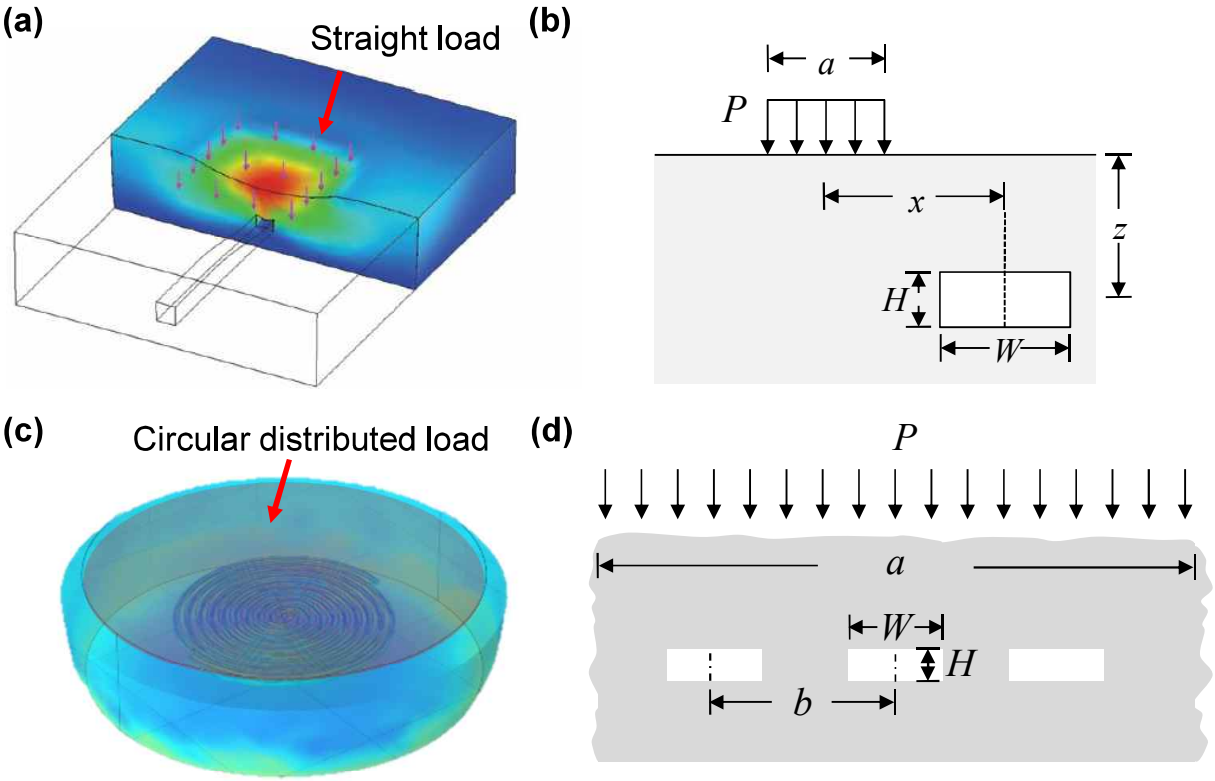

Figure 4.21: Different loading conditions and cross sectional area of the pressure sensing units: (a) Straight external load on the microchannel inside the elastomeric body [134], (b) Cross sectional area of (a) [134], (c) Circular external load on the pressure sensing unit, (d) Cross sectional area of (c).

single channel was considered as shown in Figure 4.21 (a). Under this condition, the cross section of the microchannel can be expressed as in Figure 4.21. However, in case of the pressure sensing units fabricated in this work, the shape of the external load might be a circular shape (Figure 4.21 (c)) rather than a straight line and the neighboring channels might affect the sensor performance (Figure 4.21 (d)).

Considering the different shape of the loading condition and effect of the neighboring microchannels, a modified analytic model was derived. The change of resistance ΔR of the microchannel can be expressed as follows:

$$\Delta R = \rho \frac{L + \Delta L}{(W + \Delta W)(H + \Delta H)} - \rho \frac{L}{WH} \tag{4.5}$$

where ρ, L, W, and H are resistivity of the conductive material inside the microchannel, length, width, and height of the cross sectional area of the mircochannel. We can assume

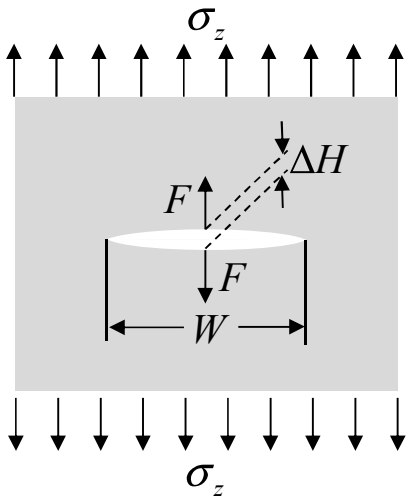

Figure 4.22: A generalized model of a crack under distributed stress.

$\Delta W = 0$ and $\Delta L = 0$, because change of the width and length might be much smaller than that of the channel height under the axial load. Thus, the resistance change of the pressure sensing unit can be expressed as follows:

$$\Delta R = \frac{\rho L}{WH}\left(\frac{\Delta H/H}{1-\Delta H/H}\right)\frac{L}{WH} \tag{4.6}$$

where ΔH can be analytically expressed as crack opening distance (COD) derived by linear elastic fracture mechanics (LEFM). In the previous model, ΔH was expressed as $\Delta H = 2(1-\nu^2)W\sigma_z/E$ (only a single channel was considered as shown in Figure 4.21 (b)), where σ_z is stress applied at the surface and E is Young's modulus of the elastomer. In the actual case, distance between the cross sections of the microchannel, which equals to the width of the microchannel ($a = W$) in the sensor design, might be too close to be neglected (Figure 4.21 (d)). Thus, it may lower the limit pressure for measurement.

Thus, it was necessary to derive a new model considering the effect of the neighboring channels, to elucidate the overestimated sensor performance in the previous model. Figure 4.22 shows a generalized model of a crack under distributed stress σ_z in the vicinity of the crack, the height change ΔH can be derived by applying Paris' equation [172]:

$$\Delta H = \frac{2}{E'}\int_0^{W/2} K_{IP}\frac{\partial K_{IF}}{\partial F}dW \times 2 \tag{4.7}$$

where E' is effective Young's modulus $E' = E/(1=\nu^2)$, K_{IP} and K_{IF} are stress intensity factor with respect to the loads P and F, and W is the crack width. In this equation, F

is a virtual load to calculate displacement at the point where the virtual load F is applied. Thus, after calculating the integral term, the value of F will be substituted with 0; this strategy is so-called Castigliano theorem. By selecting the proper K_{IP} and K_{IP}, the effect of different loading conditions and the number of the neighboring channels can be reflected in the equation. In case of the infinitely many neighboring channels as shown in Figure 4.21 (b), the stress intensity factors are as follows:

$$\begin{aligned} K_{I\sigma_z} =& \sigma_z \sqrt{b \tan \frac{\pi W}{2b}} \\ K_{IF} =& \frac{F}{b} \sqrt{b \tan \frac{\pi W}{2b}} \frac{1}{\sin \pi W/2b} \end{aligned} \tag{4.8}$$

where b is distance between the neighboring channels. By inserting Equation 4.8 into Equation 4.7, the final form of COD can be derived as follows.

$$\Delta H = \frac{4\sigma_z b(1-\nu^2)}{\pi E} \ln |\sec \frac{\pi W}{2b} + \tan \frac{\pi W}{2b}| \tag{4.9}$$

By substituting $b = W$, the resultant COD can be calculated as $\Delta H = 2.245(1-\nu^2)\sigma_z W/E$. Considering the COD in the single crack case was $\Delta H = 2(1-\nu^2)\sigma_z W/E$, the COD of the multiple cracks was only 1.12 times larger than that of the single crack. The increased amount of the COD cannot elucidate the overestimated performance in the analytic model, because the force limit was about 1500 N in the analytic model, about 4 times larger than the actual limit 350 N (Figure 4.19).

The second consideration was shape of the external load; it was a circular shape in the actual case, rather than a straight line in the previous model. The shape of the external load can be reflected by expressing σ_z (distributed stress in the vicinity of the crack) in Equation 4.9 as a function of the external pressure P described in Figures 4.21 (b) and (d), using Boussinesq's method. For example, the loading condition of the previous analytic model (Figure 4.21 (b)) can be expressed as follows:

$$\begin{aligned} \sigma_z =& \int_{-a/2}^{a/2} \int_{-\infty}^{\infty} -\frac{3Pz^3}{2\pi} \{(x-X)^2 + Y^2 + z^2\} dY dX \\ =& -\chi P \end{aligned} \tag{4.10}$$

where χ is correction term, of which specific information can be found in handbooks. The function of χ is different with different shape of the load. However, the factor of the circular load was only 1.154 times larger than that of the straight load, which was not significant

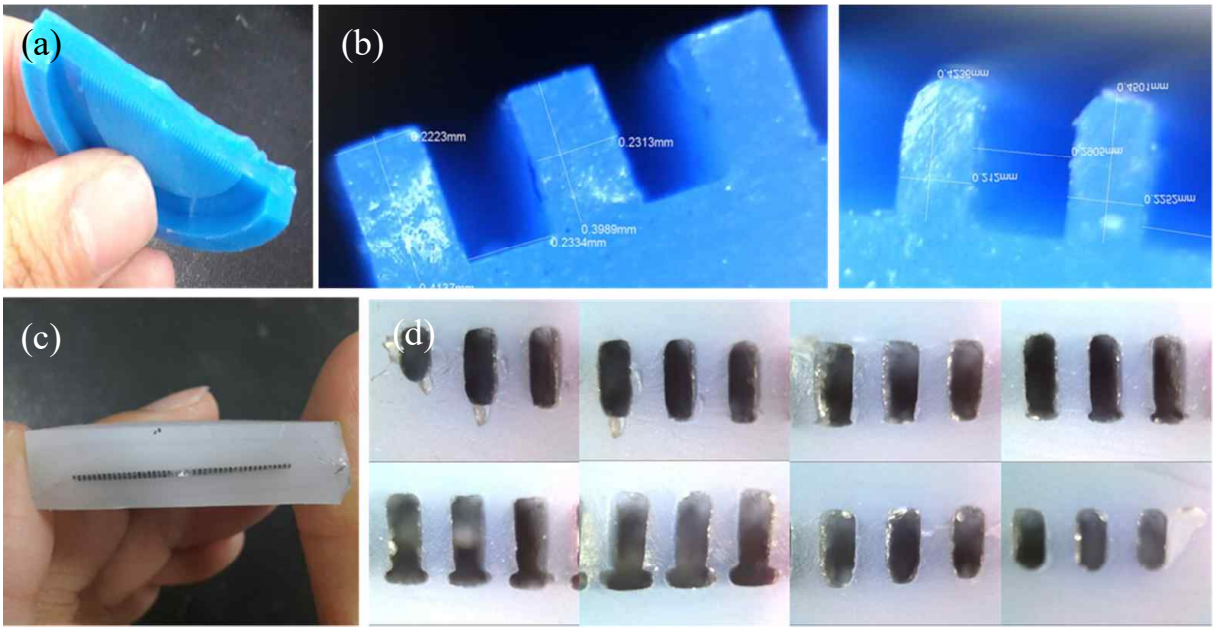

Figure 4.23: Cross sections of the mold and the soft sensor: cross sections of the mold (a) a general view, (b) microscopy images, and the soft sensor (a) a general view, (b) microscopy images.

magnitude compared to the over estimated limit pressure (4 times larger). As a result, the performance of the soft pressure sensing unit (force limit 350 N) cannot be explained even with the newly derived analytic model.

Deformation of the Microchannel under an Axial Load

To observe deformation of the microchannel under the axial load, we cut the sensing units and observe the cross sections of the microchannel 4.23 (a)-(d). As shown in Figure 4.23 (b) and (d), although the shape of the mold had sharp square shape with the predetermined dimension (square with width 100μm and height 200μm), the fabricated microchannel of the soft sensor was inaccurately formed with different shapes and sizes. The inaccurate shape might be caused by tilting of the elastomer during bonding process. In addition, the cross section of the soft sensor was observed, simultaneously pressurizing it (Figure 4.24). The cross sections were fallen down rather than maintaining the square shape, deviated from the assumptions of the analytic model based on LEFM [134].

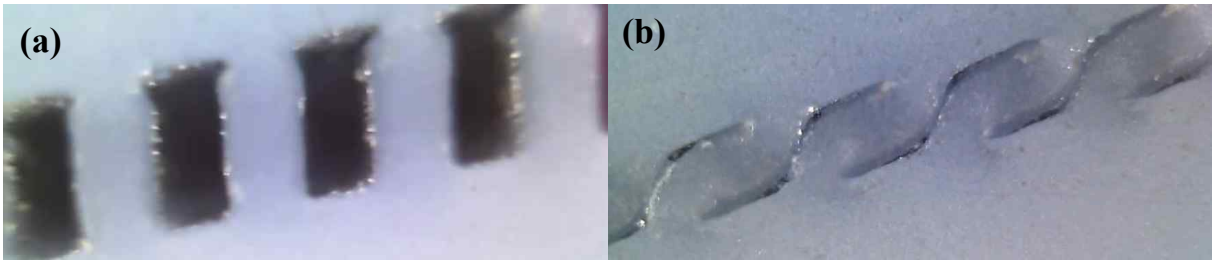

Figure 4.24: Deformation of the microchannel inside the soft sensor: (a) original shape and (b) fully pressurized.

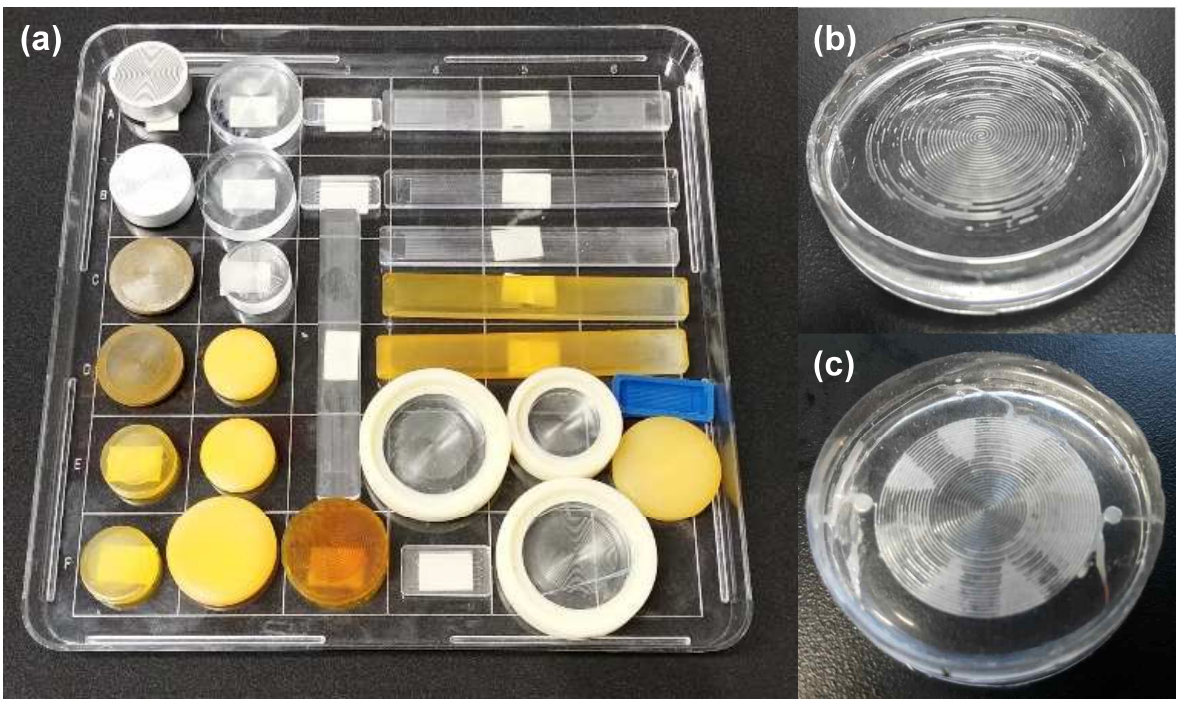

Figure 4.25: Limitations of mold-based fabrication for soft sensors. (a) Single mold should be prepared for a single sensor design, (b) the microchannel is easily clogged during bonding process, (c) the boded wall is burst during injection process.

Discussion on the Mold-based Fabrication Technique

The results indicates that the deformation of microchannel cannot be explained by the analytic model based on LEFM. In addition, if the microchannel is closed as Figure 4.24 (c), the extreme viscoelastic behavior may occur due to hydraulic force caused by eGaIn inside the microchannel and viscoelastic behavior of the elastomer. Due to complexity in such high strain ranges and nonlinear behavior of the elastomer, it is challenging to describe the deformation of the microchannel in an analytic form. Rather than deriving an analytic relation, derivation of an empirical model is more preferable to estimate performance of the soft sensor. Or, highly reliable fabrication is necessary to develop a soft sensor satisfying target performance by modifying the design of the microchannel (such as trajectory, number of twist, density of the microchannel, or etc.). However, the mold-based fabrication technique is very restrictive, because preparation of the mold of this size is very time-consuming (machining time takes a few days.), appropriate machining method is not readily usable, and production rate is very low. More specifically, a single mold should be prepared to modify sensor design (Figure 4.25 (a)), many failures can occur during fabrication process: clogging during bonding (Figure 4.25 (b)) and burst during injection (Figure 4.25 (c)). Therefore, a highly productive and programmable manufacturing technique is strongly required to broaden the application of this highly stretchable soft sensors.

4.3 A Direct Ink Writing-based Fabrication Technique

In this section, to improve productivity and programmability of the fabrication, the direct ink writing (DIW)-based fabrication is introduced.

4.3.1 Experimental Set-up and Process Variables for Direct Ink Writing

Figure 4.26 (a) shows the equipment used to conduct DIW of EGaIn. To manipulate the position of the syringe tip, three stepping motors were used with a CNC controller (CNC1000MDb, Shenzhen Guanhong Automation [158]). The syringe filled with EGaIn can be motorized with a pressure-regulating dispenser (Ultimus V, Nordson [124]), the tip position of which was monitored with a digital microscope (AD4113, Dino-Lite [46]). Figure 4.25

shows the equipment setup. The printed feature was characterized by the width (W) and height (H) of the microchannel (Figure 4.26 (b)), which can be adjusted by the process variables (Figure 4.26 (c)): 1) inner diameter (ID) of the syringe, 2) dispensing pressure (DP), 3) feed rate (FR) of the syringe, and 4) stand-off distance (SOD) between the syringe tip and the substrate. The experimental set-up was similar to that described in [17].

For printing, it was not appropriate to extrude eGaIn by pressurizing the syringe because of its high surface tension. Thus, a droplet of the eGaIn was approximated to the substrate in tens of micrometer to smear the eGaIn on the substrate. In our experiments, frequent failures were observed due to the SOD being too close or too far (Figs. 4.28 (a) and (b)), the major cause of which was the inaccurate calibration of the syringe height. To improve the calibration accuracy, a highly sensitive loadcell (Nano 17, ATI Industrial Automation [7]) was embedded in the syringe holder (Figure 4.26 (a)) to identify contact between the syringe and the substrate. The accuracy of the height calibration was improved significantly with the loadcell ($\pm 3\,\mu m$) versus with the naked eye ($\pm 30\,\mu m$). With accurate height calibration, the value of SOD was set to $20\,\mu m$ in our experiments.

4.3.2 Investigation for Stable Writing of Liquid Metal

Surface Flatness

To prevent writing failures caused by variation of SOD (Figures 4.26 (a) and (b)), the flatness of the equipment stage was quantitatively evaluated by measuring the height of the multiple points on the surface. The area of the working stage (200 mm by 200 mm) was divided into four sections Q1, Q2, Q3, and Q4 as shown in Figure 4.29. On each section, the heights of the 25 points were measured. As a result, the center of the stage was the highest and the height lowered gradually as approaching the edges of the target area. The slope of the surface was larger along X-axis than Y-axis, and the maximum slope was observed in Q1, $-0.58 \mu m/mm$. Considering the workspace, maximum error of SOD might be smaller than $60 \mu m$ from the center to the border of the workspace.

Furthermore, a silicone-coated substrate was placed on the stage and the flatness of the substrate was evaluated using the same method. Figure 4.30 illustrate the surface terrain of the 8 inch wafer spin-coated with silicone material (Dragon Skin 30, Smooth On [164]). Although the shape of the terrain may vary with every substrate, the quantitative quality can be represented as the maximum slope of the substrate. For better flatness, the viscosity of the silicone was reduced by adding $10 wt\%$ thinner (Silicone Thinner, Smooth On), coating

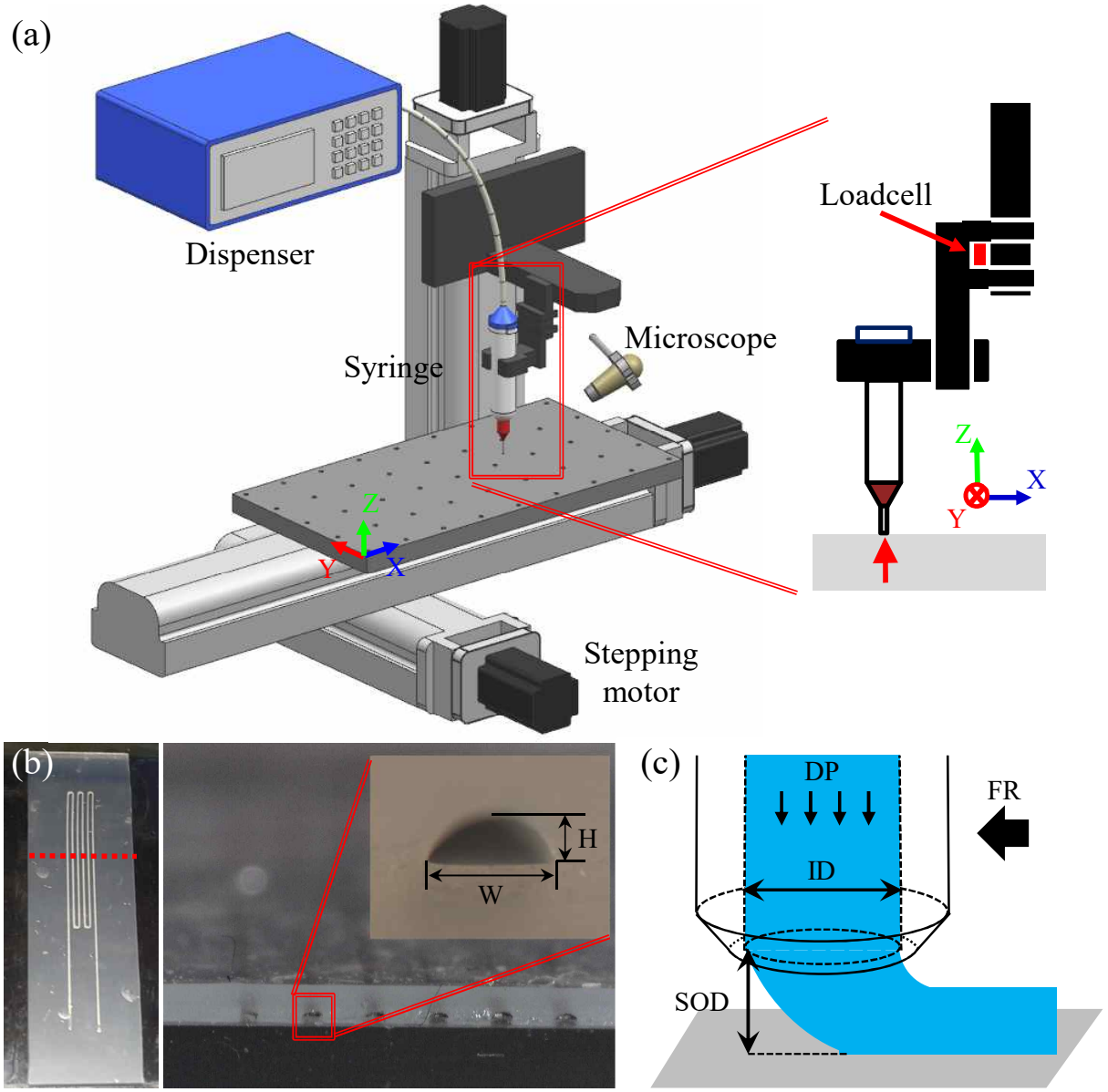

Figure 4.26: Experimental setup for direct writing of eGaIn: (a) configuration of equipment for DIW of eGaIn (b) characterization of a printed trace represented in terms of channel width (W) and height (H), and (c) process variables of inner diameter (ID), dispensing pressure (DP), feed rate (FR), and stand-off distance (SOD).

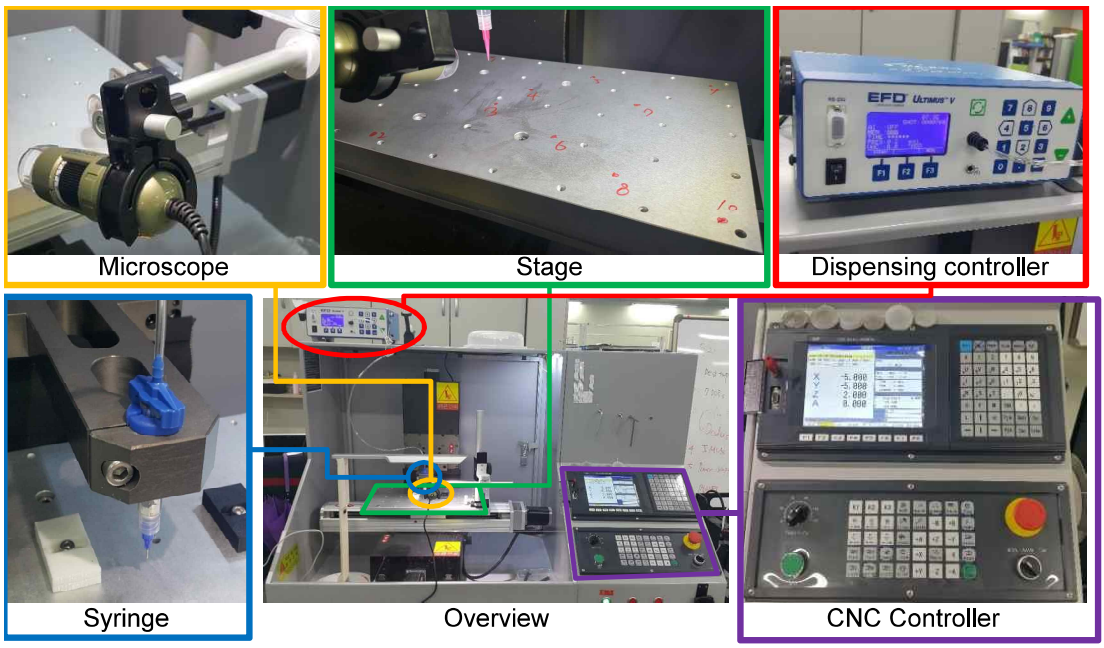

Figure 4.27: Equipment for direct writing of eGaIn.

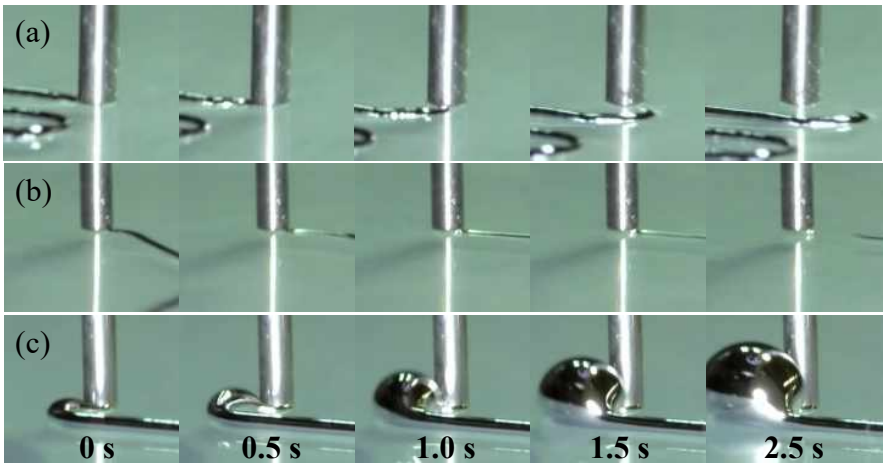

Figure 4.28: Three modes of failures during DIW of eGaIn: (a) a gradually decreasing SOD, (b) a gradually increasing SOD, and (c) the occurrence of a bulge.

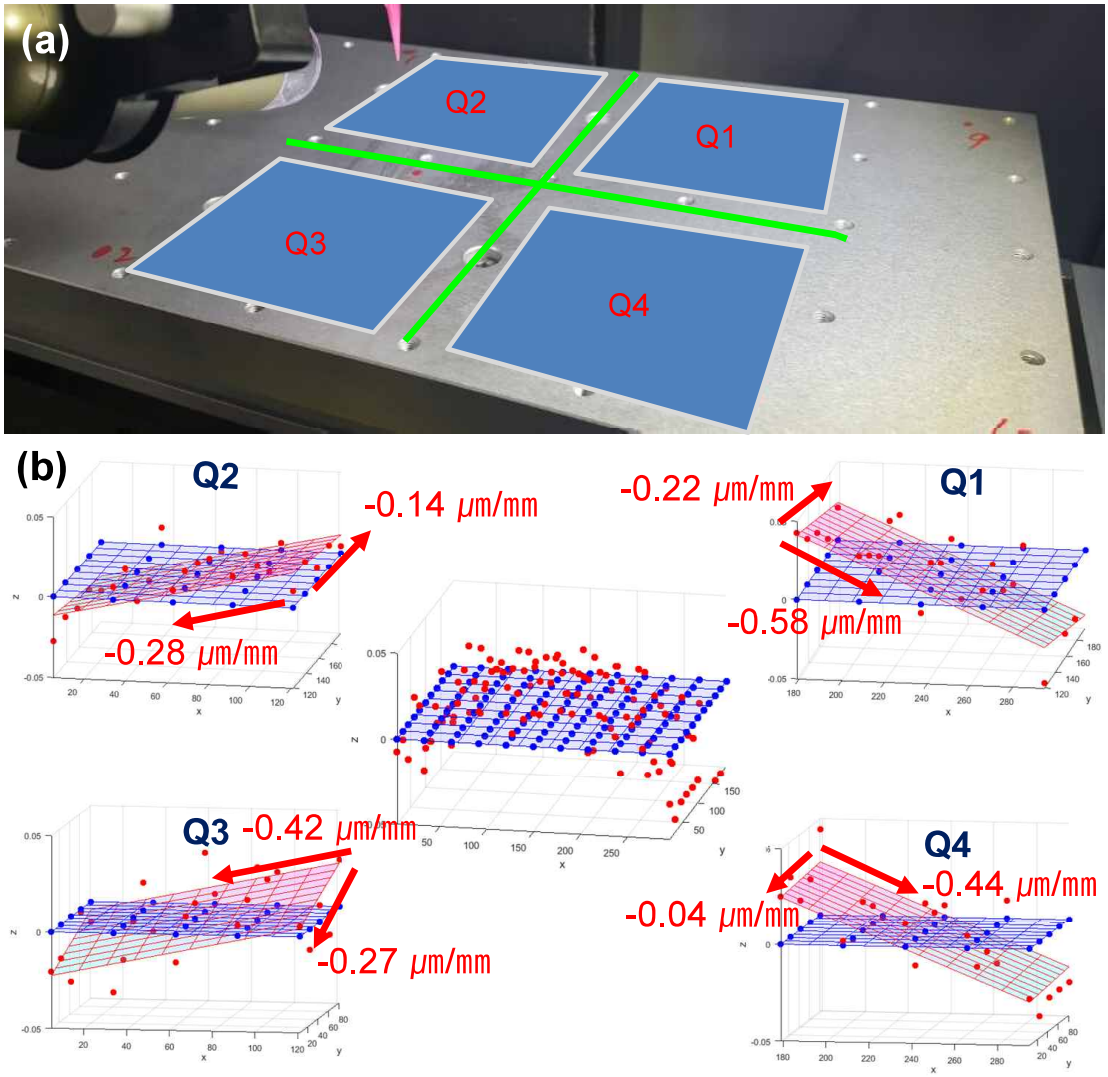

Figure 4.29: Evaluating surface flatness of the working stage: (a) target area and divisions, (b) results.

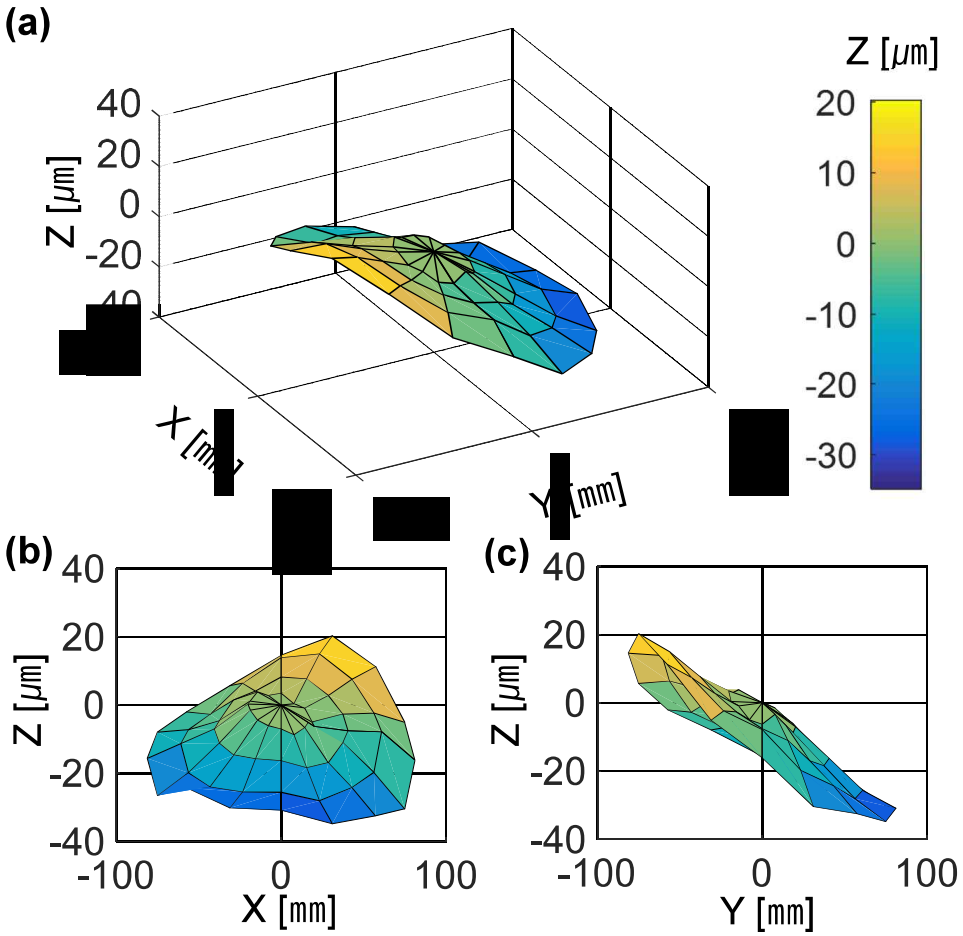

Figure 4.30: Evaluating surface flatness of the silicone-coated substrate located on the working stage: (a) 3D view, (b) XZ plane view, and (c) YZ plane view.

speed was set as 1000 rpm, and the wafer was handled carefully to avoid contamination. As a result, the maximum slope was about 0.3 $\mu m/mm$ along Y-axis (Figure 4.26 (f)). By considering the terrain of the substrate, the two modes of failure (Figures 4.26 (a) and (b)) were prevented by selecting a moderate value of SOD, maintaining the instantaneous SOD as $0 \sim 100\,\mu m$ during writing. The upper limit of SOD, which may vary with ID or FR, was determined empirically for given $ID = 490\,\mu m$ and $FR = 200\,mm/min$ with a moderate margin, because the trace was broken as the instantaneous value of SOD reached 130 μm during printing. In case of a faster FR or a smaller ID, it was necessary to reduce the upper limit. If the designed trace covers a large area on the wafer, an extra care will be required on this discussion.

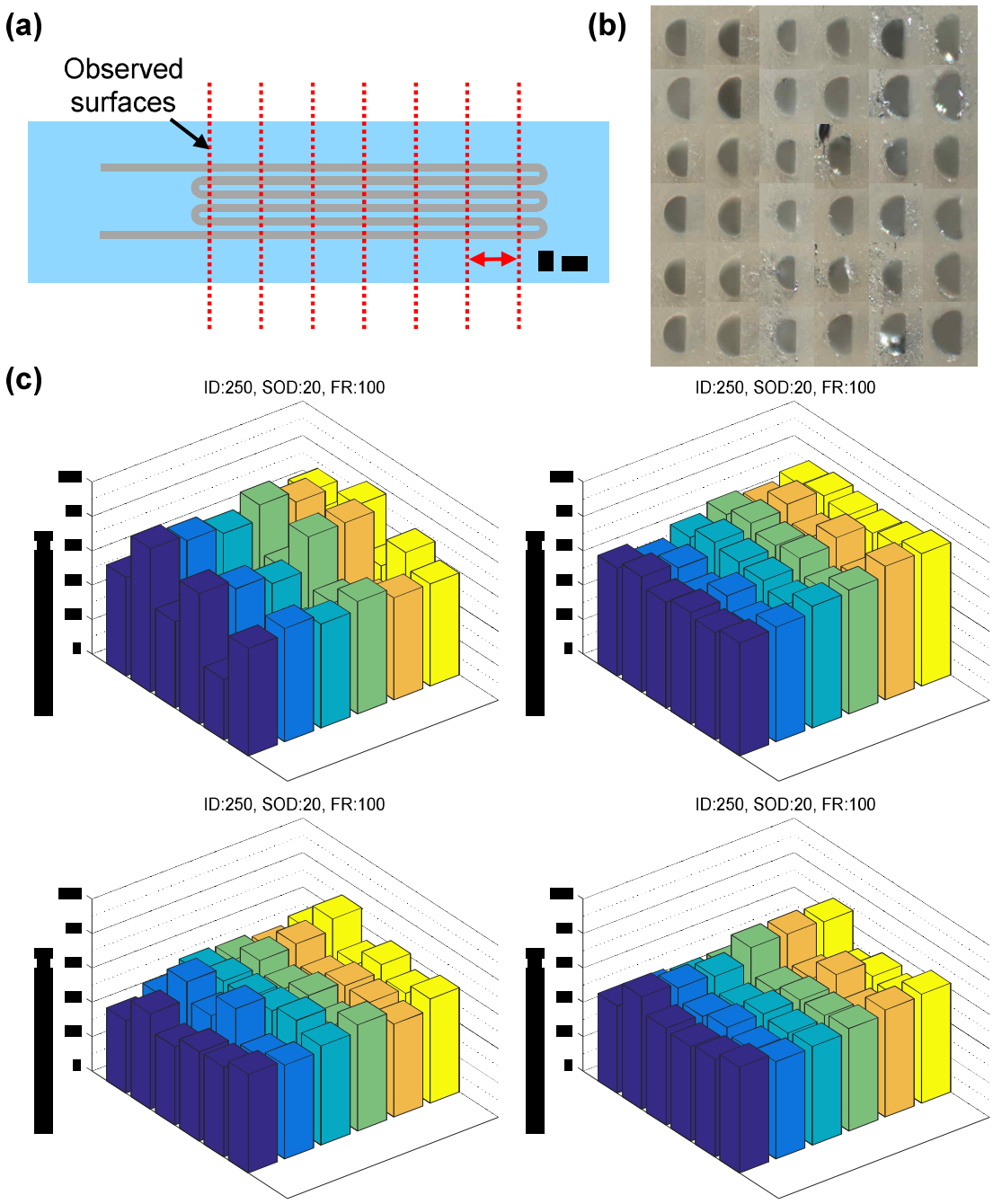

Figure 4.31: Inspection of the cross sectional area of the microchannel: (a) location of observation, (b) observed cross sections of the microchannel, and (c) experimental results: height of the microchannels of the four specimens with same PV ($ID = 250\mu m$, $SOD = 20\mu m$, $FR = 100mm/min$).

Understanding Writing Mechanism

In our experiments, the thickness of the written traces were different despite the same process variables were applied ($ID = 250\mu m$, $SOD = 20\mu m$, $FR = 100mm/min$). For a quantitative clue, the fabricated soft sensors were sliced (Figure 4.31 (a)), and the cross sections were observed (Figure 4.31 (b)). Figure 4.31 (c) shows the measured heights of the cross sections in the four specimens. As mentioned, the heights of the microchannels were inconsistent even with same process variables applied. To control the writing condition more accurately, we investigated three major factors affecting the written traces. First factor is the size of the droplet at the syringe tip (Figure 4.32 (a)). If the droplet is too small, the writing cannot be initiated, but the unstable shape of the trace may generate mode 3 failure (Figure 4.28 (c)), if droplet is too large. Thus, the proper size of the droplet might be crucial for stable writing. In addition, if we determine SOD with respect to the given droplet height, the initial contact width will be determined, which affects resultant thickness of the written traces (Figure 4.32 (b)). Lastly, if the speed of the syringe (FR) is too fast for the given initial width, the oxide skin cannot be filled sufficiently, resulting in lower height of the microchannel (Figure 4.32 (c)). In contrast, if FR is sufficiently slow, the oxide skin can be filled sufficiently, reaching equilibrium state due to balance between the tension of the skin and the inner pressure of the liquid metal.

To investigate the size of the droplet, the experimental setup was prepared as shown in Figure 4.33 (a). The size of the droplet was observed as shown in Figure 4.33 (b) using Microscope 1 (Dino-lite [46]), and the status of eGaIn inside the syringe was observed by Microscope 2 (Supereyes [168]) as shown in Figure 4.33 (c). To form the droplet consistently, it was important to coat eGaIn the insides wall of the syringe to the end. For example, the behavior of the droplet can vary depending on the coated status as shown in Figure 4.33 (d), under the condition that dispensing pressure/vaccum pressure is applied to the syringe by turning on/off the dispensing controller. In this experiment, six different sizes of syringe were used ($ID = 100$, 150, 200, 250, 330, and $410\mu m$), and some of the experimental results are shown in Figure 4.34 and Figure 4.35.

Figure 4.36 (a) shows the width of the droplet with different IDs according to increasing DP. In some cases ($ID = 200$, 250, and $410\,\mu m$), the initial width of the droplet was smaller than ID due to improper initial condition of the syringe as shown in Figure 4.36 (b); the inner wall of the syringe was not fully coated by eGaIn. Thus, the droplet heights of the remained cases ($ID = 100$, 150, and $330\ \mu m$) were considered as plotted in Figure 4.37.

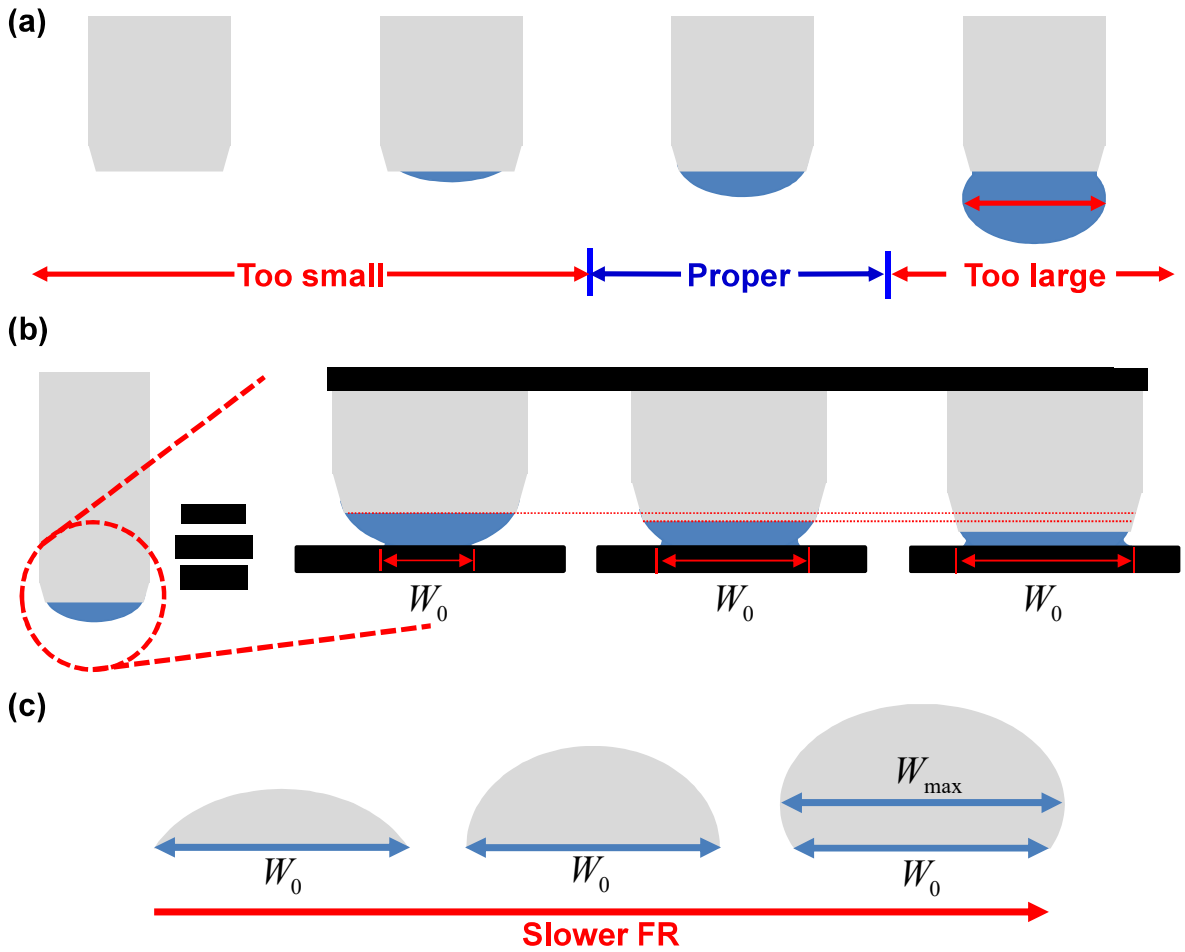

Figure 4.32: Three major factors influencing the written traces of eGaIn: (a) size of the droplet at the syringe tip, (b) initial contact width determined by SOD relative to a given droplet height, and (c) volume of eGaIn filling the oxide skin for a given initial contact width determined by FR.

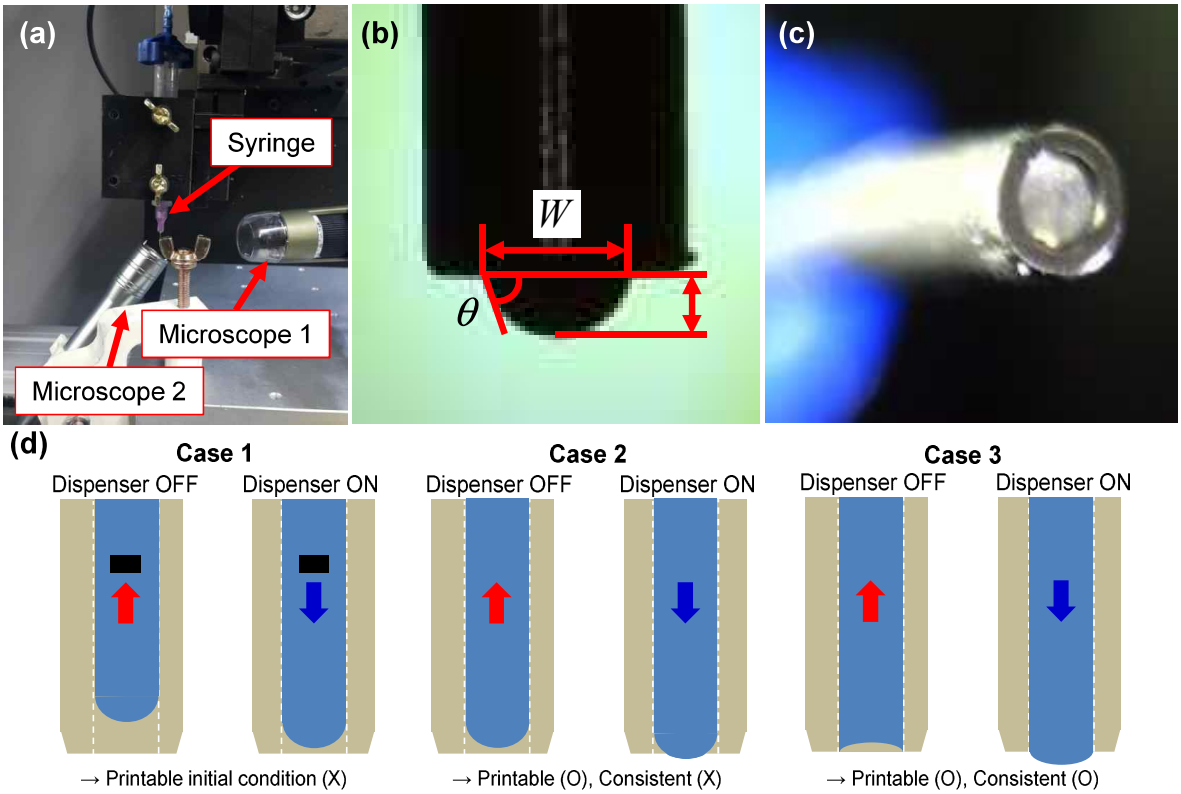

Figure 4.33: Measurement of the droplet size: (a) experimental setup, (b) microscope image 1, (c) microscope image 2, and (d) different behavior of eGaIn according to the different wetting conditions of eGaIn insides the wall.

The size of the droplet was about 45% of ID with small DP and converged to 70% of ID with sufficiently large DP. In our experiments, the larger syringes were also tested such as $ID = 510\,\mu m$, but eGaIn was dripping from the syringe even without application of DP due to weight of eGaIn filled in the syringe. Thus, the syringes smaller than $500\,\mu m$ are appropriate for stable printing. The charged amount of eGaIn increased the size of the droplet as shown in Figure 4.38. Thus, we controlled the charged amount of eGaIn not to exceed $0.45\,ml$ in our experiments.

To determine a proper SOD based on the height of the droplet, equivalent height H_{eq} was calculated as described in Figure 4.39. As shown in Figure 4.39 (a), a given droplet with height H, syringe size ID, and contact angle θ can be represented as an ellipsoid with geometrical factors a, b, and c. As the droplet is approximated to the substrate, the droplet will be deformed into a cylindrical shape with a lower height and a widener width as shown

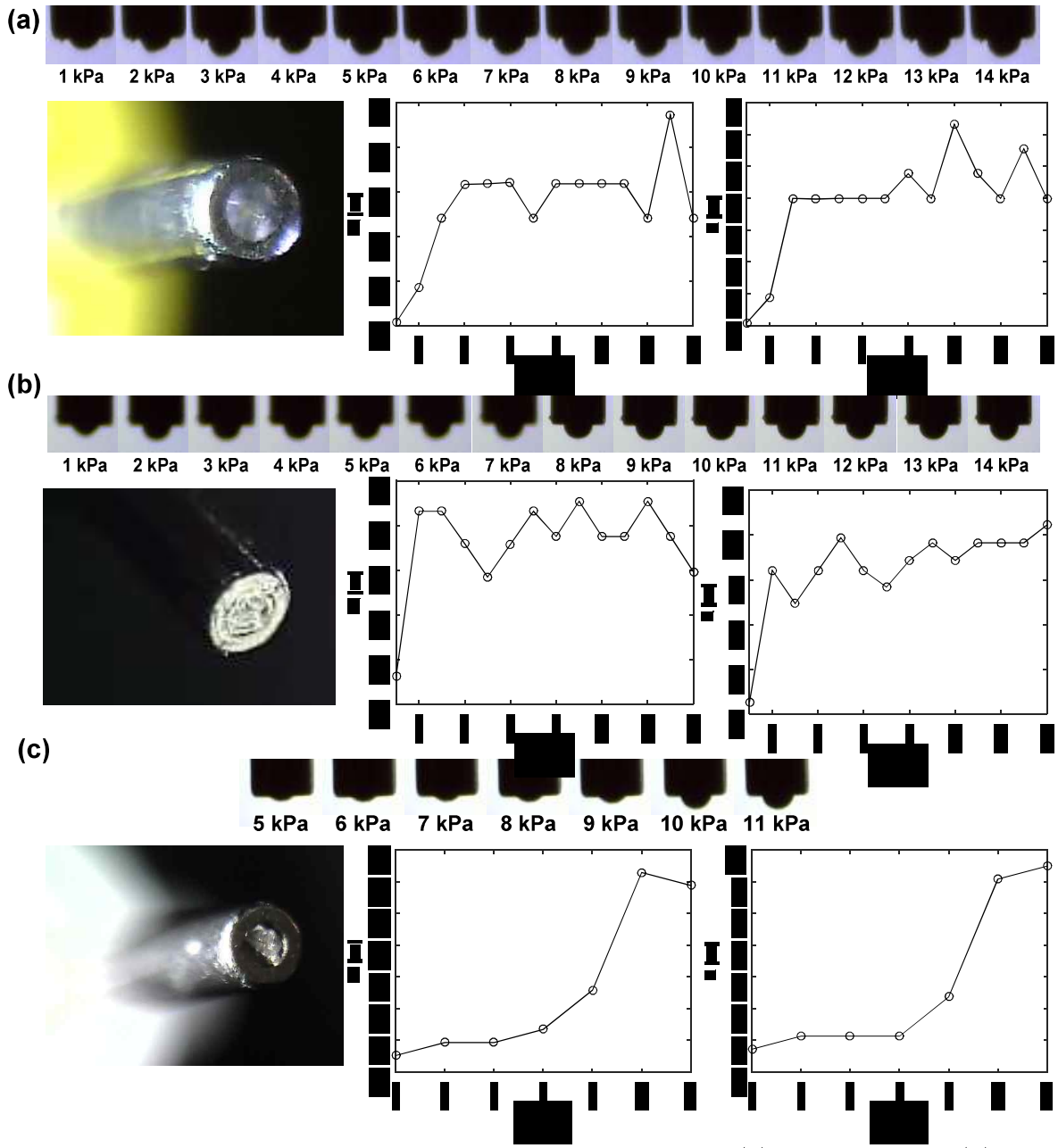

Figure 4.34: Experimental results of measuring droplet sizes: (a) $ID = 100\mu m$, (b) $ID = 150\mu m$, (c) $ID = 200\mu m$.

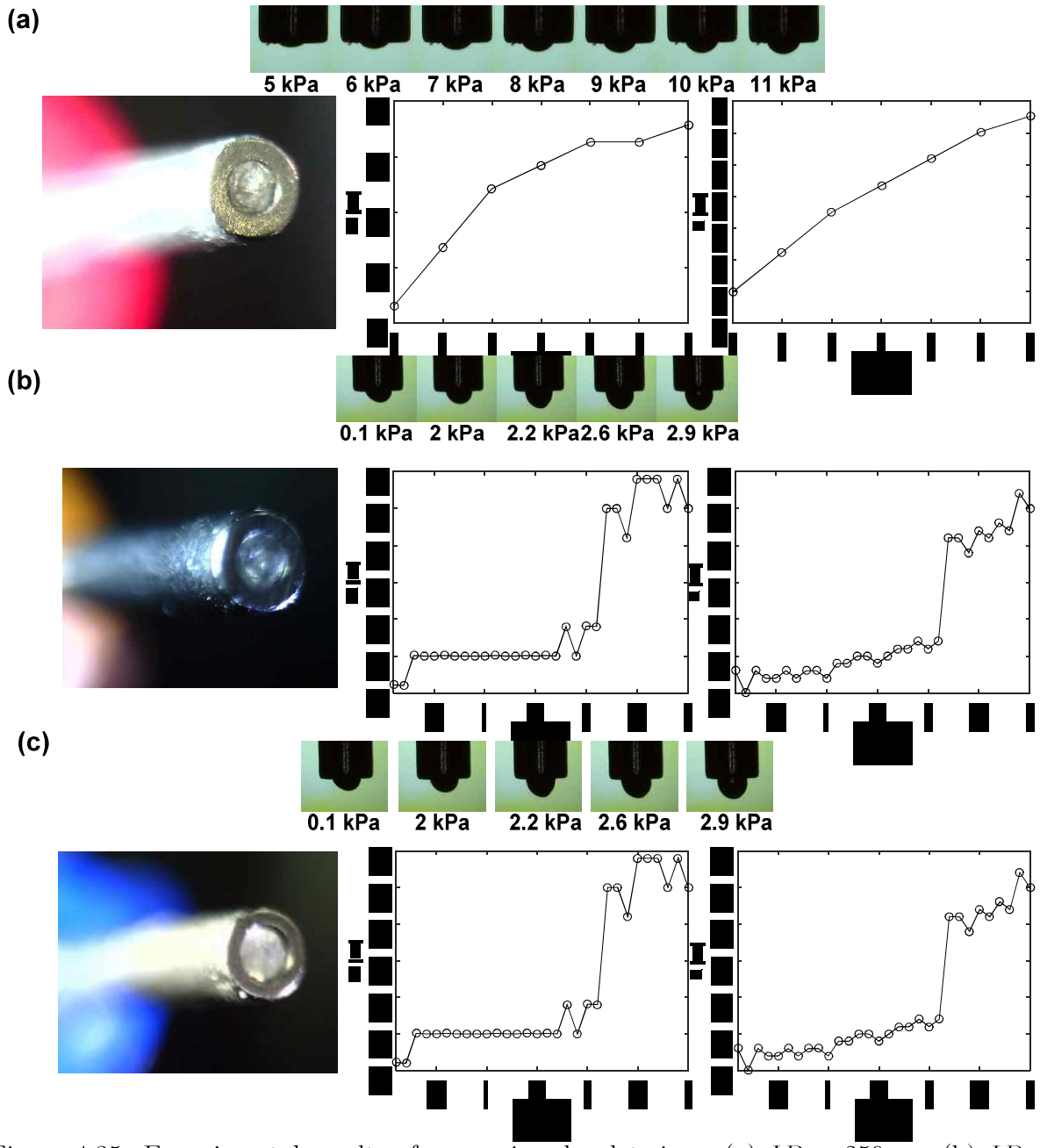

Figure 4.35: Experimental results of measuring droplet sizes: (a) $ID = 250\mu m$, (b) $ID = 330\mu m$, (c) $ID = 440\mu m$.

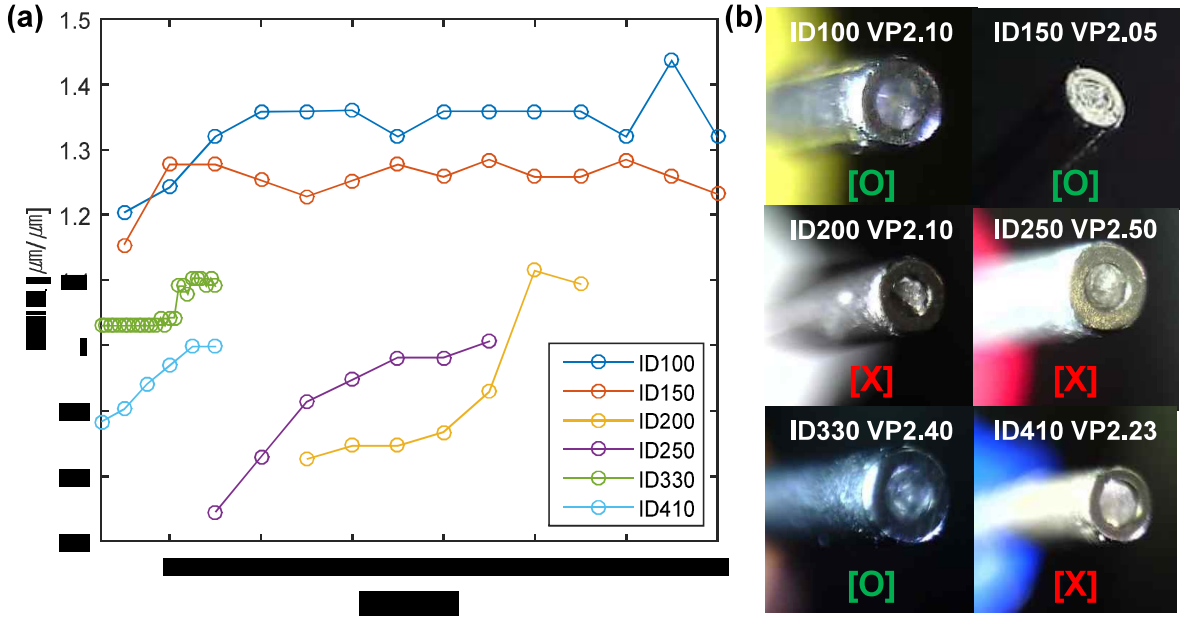

Figure 4.36: Experimental results of measuring droplet widths: (a) W/ID, (b) initial condition of the syringe filled with eGaIn.

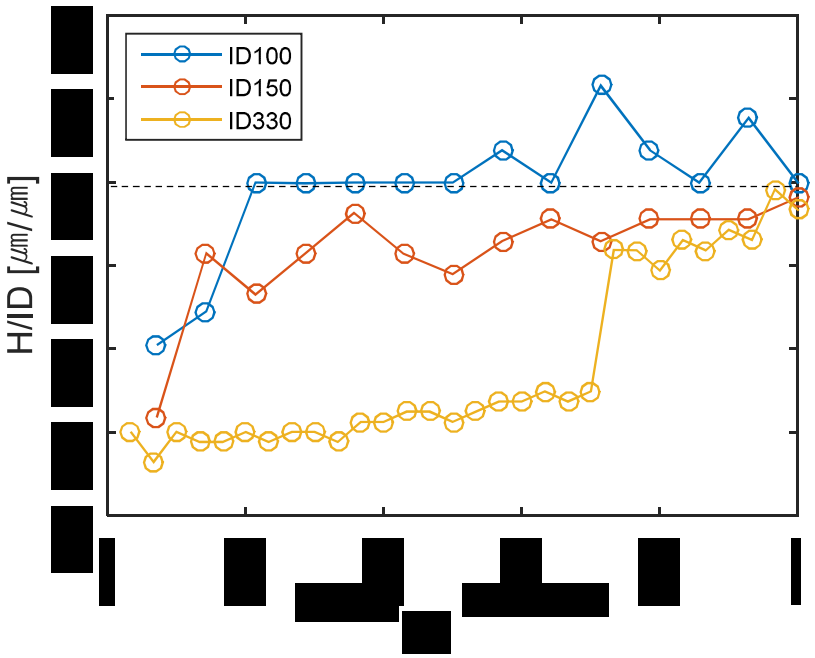

Figure 4.37: Experimental results of measuring droplet heights.

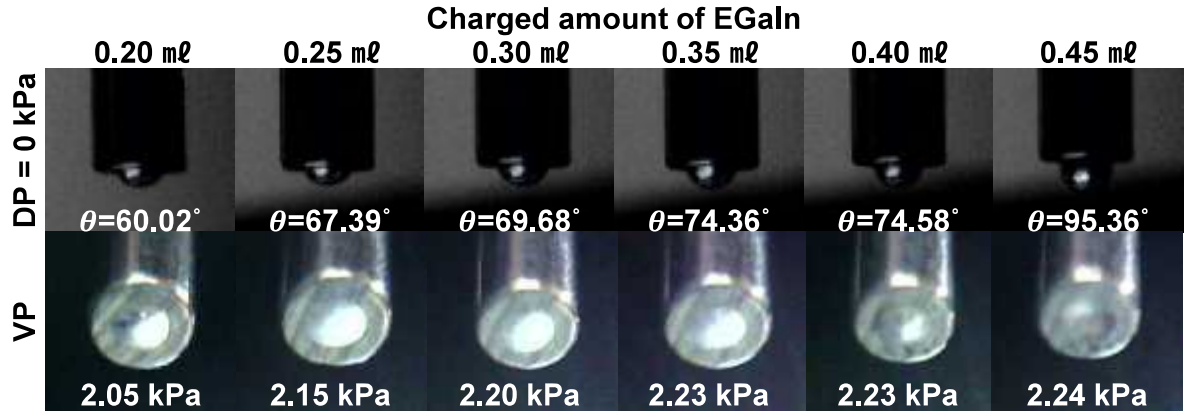

Figure 4.38: Effect of charged eGaIn in the syringe on the droplet size ($ID = 330\,\mu m$).

in Figure 4.39 (c). The cylindrical shape might be feasible under the assumption that eGaIn is perfectly wettable on the given substrate. The equivalent height H_{eq} can be calculated according to the equilibrium that the volume of the droplet remains the same from the ellipsoid (Figure 4.39 (a)) to the cylindrical shape (Figure 4.39 (b)):

$$H_{eq} = \frac{2H^2(3c - H)}{3ID(c - H)\tan\theta} \tag{4.11}$$

where $c = H(2H + ID\tan\theta)/(4H + ID\tan\theta)$.

According to the equation (4.11), the equivalent height was calculated as about 80 μm with give PVs: $ID = 440\,\mu m$, $DP = 2\,kPa$, charged eGaIn $0.2\,ml$ and a give droplet size 130 μm and $theta = 80°$. However, most of trials with $SOD > 30\,\mu m$ were failed in our experiments even with a slow FR (about $200mm/min$). These failures are attributed to poor wettability of eGaIn as shown in Figure 4.40. If wettability of eGaIn for a given substrate is low, the width of the initial contact will be smaller, resulting in insufficient adhesive force to stretch the oxide skin and maintain writing. As reported in [49], wettability of eGaIn without rupturing the preformed oxide skin is usually poor on most of surfaces in regardless of its material types or textures. In other words, it is difficult to from the initial wetted with consistently in spite of consistent size of the droplet. The most important conditions for stable writing are to fill eGaIn insides the wall of the syringe end sufficiently and to smear eGaIn onto a give substrate to form sufficient and consistent initial wetted width.

The another issue affecting writing of eGaIn was speed of the syringe (FR). As shown in Figure 4.41 (a), the written eGaIn traces inflated for a certain period of time after stopping movement of syringe. The inflation terminated after few seconds. This phenomena originates

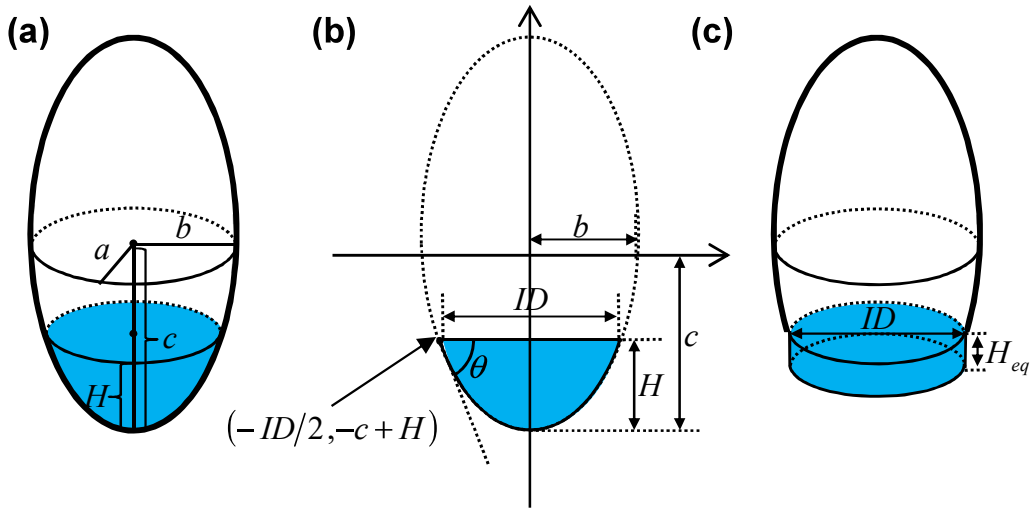

Figure 4.39: Calculation of equivalent height H_{eq} for a given droplet size: (a) geometry of a droplet represented as an ellipsoid, (b) cross sectional area of the ellipsoid, and (c) deformed droplet with $SOD = H_{eq}$ under perfect wettability assumption.

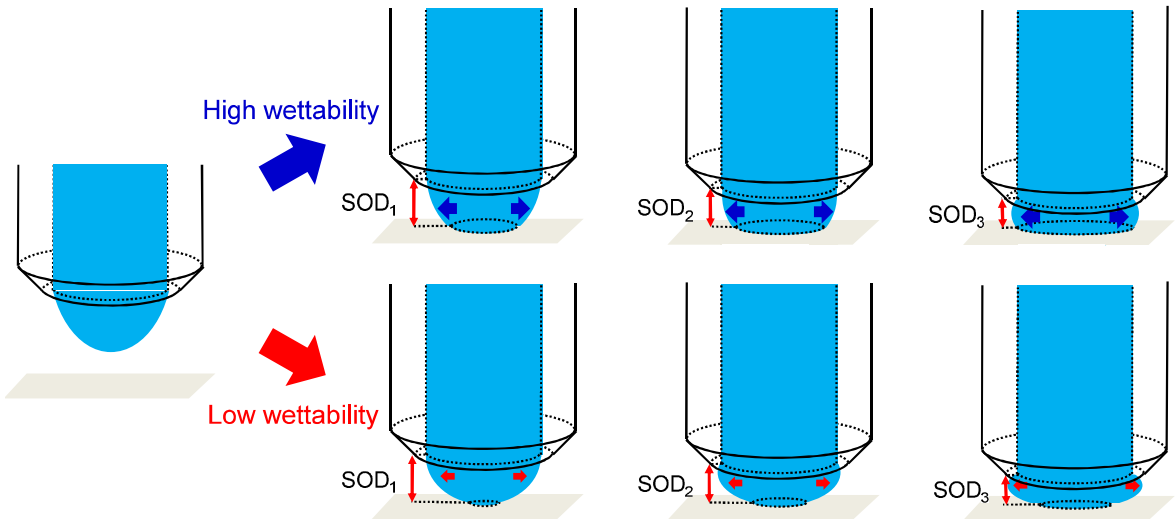

Figure 4.40: Schematic representation of poor wettability of eGaIn.

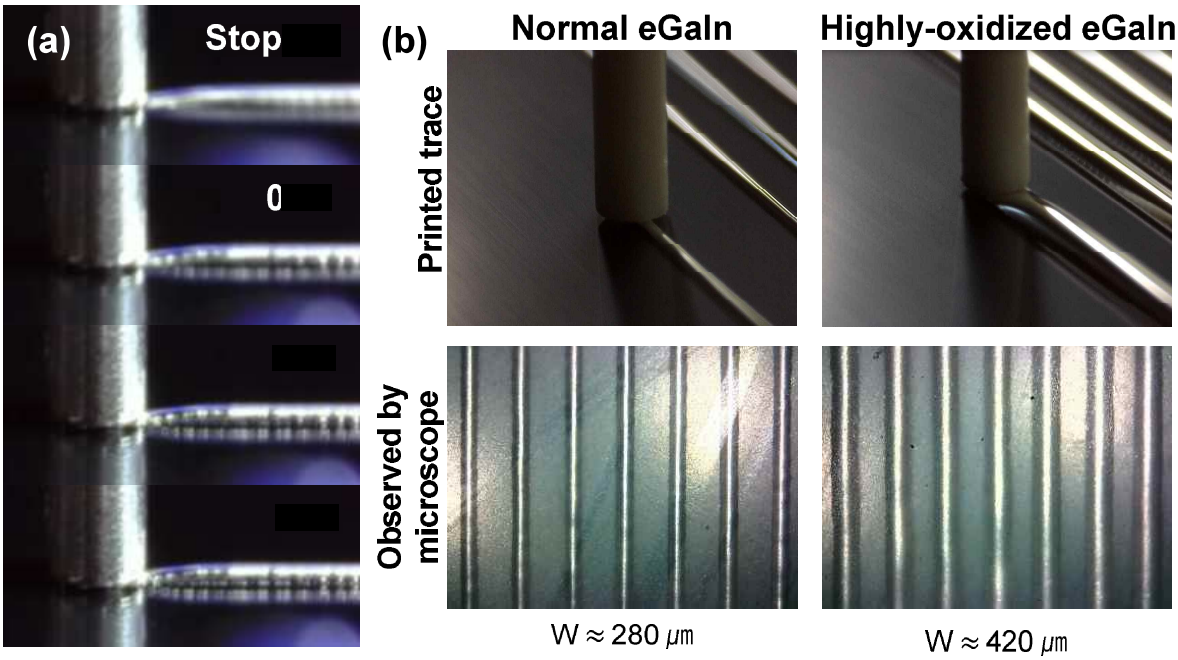

Figure 4.41: Effect of FR and oxidization level of eGaIn on the written traces: (a) Filling response of the written eGaIn trace and (b) Effect of oxidization level of eGaIn on the written traces.

from that a certain amount of time duration is required to fill the oxide ski, which is being formed continuously due to repetitive yielding and reconstruction of the oxide skin during writing, reaching equilibrium between inner pressure and the tension of the oxide skin. It is difficult to control the response quantitatively, sufficiently slow FR is selected for stable and consistent writing to achieve the equilibrium completely.

In our investigations, the thickness of the written trace was highly affected by oxidization level of eGaIn. As shown in Figure 4.41 (b), even under same PVs ($ID = 410\,\mu m$, $FR = 200\,mm/min$, $SOD = 40\,\mu m$, $DP = 0\,kPa$, and charged eGaIn $0.2\,ml$), the thickness of the written trace was about 2 times thicker with highly-oxidized eGaIn. In such a case, the design of the sensor (e.g. interval of the serpentine patterns) should be modified to prevent writing failures caused by a bulge. However, because it is difficult to predict the oxidization level of eGaIn every trial, the oxidization level of eGaIn was lowered sufficiently by applying electrolyte for electrolysis to control the thickness of the written trace consistently. Based on the discussions on this subsection, stable writing of eGaIn was achieved, preventing writing failures and writing the traces consistently.

4.3.3 Direct Ink Writing-based Fabrication Process

The direct writing technique of eGaIn was applied to fabrication of soft sensors, as illustrated in Figure 4.42. First, a thin silicone layer was formed on a wafer by spin coating (TOP-8, Dong Ah Trade Corp [48]) (Figure 4.42 (a)). Dragon Skin 30 [164] was used as a silicone material instead of Ecoflex 0030 [165], because blockage of the microchannel occurred more frequently with Ecoflex in our experiments due to weakness against local deformations caused by its extreme softness and tackiness. On the first silicone layer, desired traces were printed with the motorized syringe filled with the eGaIn (Figure 4.42 (b)). After printing, the written traces can be covered with uncured silicone by spreading the material very gently using a flat inclined surface (Figure 4.42 (c)). This covering method yielded intact printed traces with a very slow feed rate of the rod ($\leq 30mm/min$), but broken traces were readily observed when spin coating was used instead. The thickness of the covered layer can be determined by distance between the rod and the substrate. Additionally, the opposite side should be reinforced (Figure 4.42 (d)), because the first layer, for improved surface flatness, was usually very thin ($\approx 50\mu m$). The total thickness of the sensor can be determined by the three silicone layers, which can be united in a monolithic structure without any special treatment. To form the desired shape of a sensor with smooth edges, the completed work piece was trimmed with a laser cutter (VLS6.60, Universal Laser Systems [179]) (Figure 4.42 (e)). Finally, wires were inserted directly into the both ends of the microchannel and fixed firmly by silicone bonds with an inextensible film (Figure 4.42 (f)). The suggested fabrication procedures allow any arbitrary shape of a soft sensor without preparation of a mold or intensive intervention by skilled hands.

4.3.4 Confirmation of Consistency and Reproducibility

Consistent Writing Using a Non-metallic Syringe

After the process variables were adjusted as discussed in the previous section, the failure rate of writing was significantly decreased. However, as shown in Figures 4.43 (a) and (b), differences in thicknesses were observed in the serpentine traces written by a metallic syringe (stainless steel, $ID = 430\mu m$, Nordson Corporation [123]), whereas the printed traces using a non-metallic syringe (polypropylene, $ID = 490\,\mu m$, Nordson Corporation [122]) had relatively consistent thickness. For detailed inspection, each fabricated sensor was cut into pieces and clear images of the cross-sections were acquired at X423 magnification using a

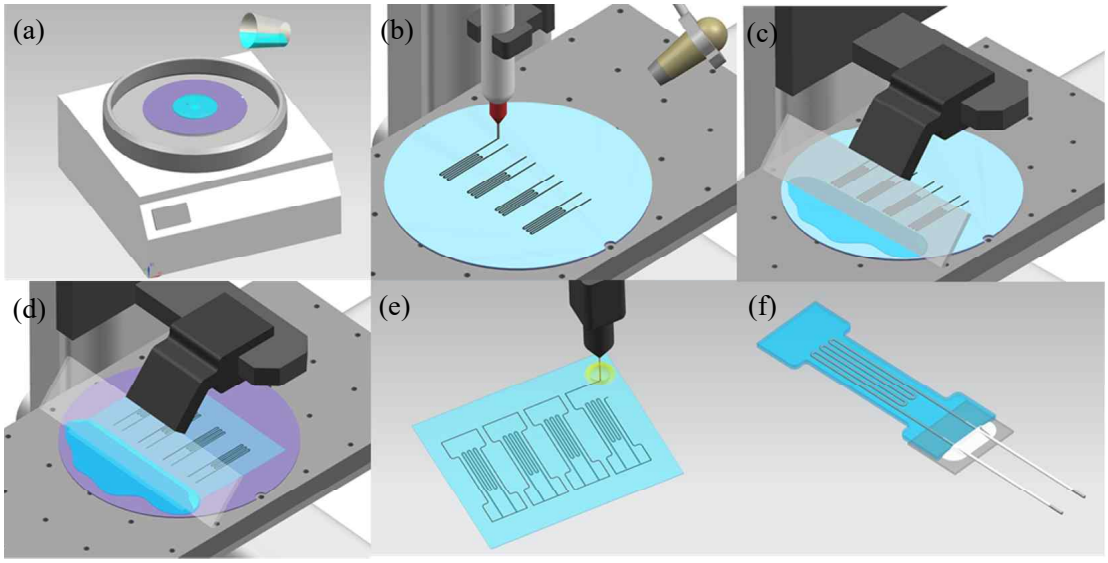

Figure 4.42: Fabrication procedures for an eGaIn DIW-based soft sensor: (a) preparation of a silicone layer on a wafer by spin coating, (b) writing EGaIn on the silicone layer, (c) spreading uncured silicone material on the printed trace by rod coating, (d) coating the opposite side for reinforcement, (e) trimming the silicone body into a desired shape by laser cutting, and (f) direct insertion and fixation of electrodes.

stereo zoom microscope (Axio Zoom V16, Zeiss [208]). As shown in in Figure 4.43 (c), the images of cross sections were arranged according to relative locations within the microchannel along the transverse and longitudinal axes, and the height of each cross-section was measured (Figure 4.43 (d)).

In the case of the metallic syringe, the printed trace displayed an obvious pattern: the trace became thicker right after passing through the turning point due to the lumped liquid (Figure 4.43 (b)). Because of the phenomenon inducing the critical degradation of channel consistency, the standard deviation of 36 cross-sections was much larger with the metallic syringe (39.34 μm) than with non-metallic syringe (5.18 μm) despite their similar sizes. The major cause of this phenomenon was a strong attractive force between the metallic syringe and eGaIn, which could be seen clearly by dipping each syringe into eGaIn (shown in Figure 4.43 (e)). An empty syringe was immersed into eGaIn with a depth of 10 mm and lifted up at a speed of $3 mm/s$. As shown in the snapshots, attraction to the metallic syringe was much stronger than to the non-metallic syringe.

Thus, the consistency of printed traces can be improved using a non-metallic syringe even with a small radius of turning section, because the non-metallic syringe was hardly

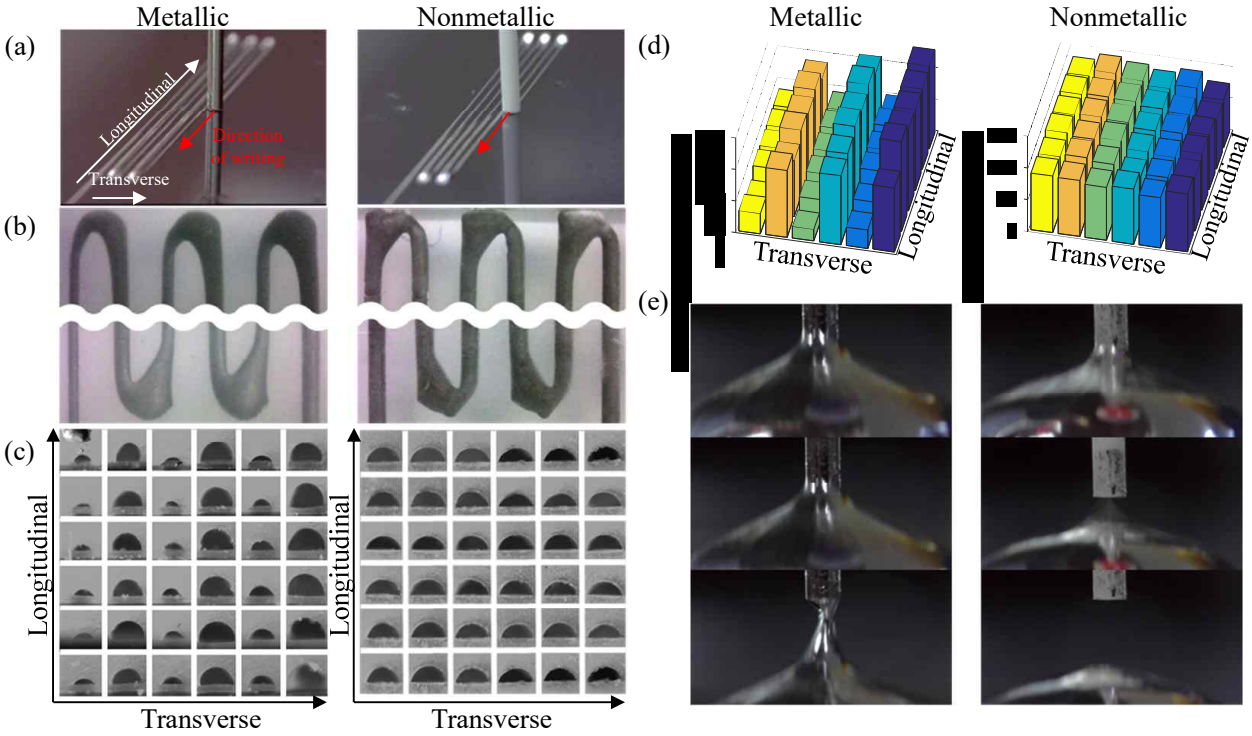

Figure 4.43: Comparison of printed traces using a metallic (stainless steel, $ID = 430\,\mu m$) and a non-metallic (polypropylene, $ID = 490\,\mu m$) syringe tip: (a) snapshot of traces during writing for each syringe material, (b) printed traces at turning sections (scale bar = $200\,\mu m$), (c) multiple cross-sections with respect to the transverse and longitudinal axes (scale bar = $100\,\mu m$), (d) height of the cross sections, and (e) dipping experiment to investigate attraction force between a syringe and eGaIn.

affected by the lumped liquid metal because of its modest attraction force. In addition to the consistency issue, broken traces were observed more frequently when using a metallic syringe, because it was more difficult for the liquid metal to be extruded from the syringe. The problem could be prevented by increasing DP, but it might still incur a bulge during writing.

Reproducible Fabrication of Soft Sensors

Compared with the typical fabrication technique, using a mold, a great advantage of the suggested technique is that it needs minimal intervention by skilled hands in building a microchannel inside a sensor, allowing for reproducible fabrication of sensors. To show this advantage, multiple sensors were manufactured based on the conventional technique (see [131])

using a mold (square microchannel, $300\,\mu m \times 300\,\mu m$) and the suggested technique using the three types of syringe tips (ID=490, 430, and $340\,\mu m$). Because the quality of the fabricated sensors can be evaluated based on the consistency of their performance, represented as a strain-resistance relationship, the experimental set-up was prepared as shown in Figure 4.44 (a).

A sensor was fixed by two clips, of which one could move in the longitudinal direction of the sensor. The sensor was connected serially by a $1\,k\Omega$ resistance and a $5\,V$ voltage source, the signal of which was amplified about 200 times by a non-inverting amplifier and recorded with a data acquisition board (USB-6216, National Instruments [121]). The resistance values of the sensor were calculated by the inverse relation of the circuits. During the experiment, each sensor was extended up to 100 % strain 20 times at a rate of $25\,mm/s$, simultaneously measuring the displacement and required force with a linear potentiometer and a loadcell, respectively.

As shown in Figure 4.44 (b)-(d), the experimental results are expressed in strain-resistance relationships and normalized resistance changes, $\Delta R/R_0$, against strain, ϵ, where each slope $(\Delta R/R_0)/\epsilon$ represents a gauge factor (GF), for 9 manually developed sensors, 21 ($ID_1 = 490\,\mu m$), 11 ($ID_2 = 430\,\mu m$), and 10 ($ID_3 = 340\,\mu m$) printed sensors. Reproducibility of the fabrication technique can be evaluated in terms of consistency in initial resistance (R_0) at zero strain and GF: the consistent R_0 indicates the fabrication procedure can form identical microchannels repeatedly, whereas the consistent GF indicates that sensors have similar performance. The specific values are presented in Table 4.1, where μ is mean, σ is standard deviation, σ/μ is coefficient of variation (CV), and *p-values* are the results of the *Kolmogorov-Smirnov test* to confirm normality; normality of a distribution is rejected if *p-value* < 0.05) [114]. The printed groups had 8.7 and 4.5 times smaller values of CV for R_0 and GF, respectively; the dispersion levels of sensors were smaller in the printed groups.

To visualize the differences more clearly, R_0 and GF were normalized by the corresponding means, $\overline{R_0}$ and $\overline{GF}$, and illustrated using a normal distribution function (Figs. 4.44 (e) and (f)). The number of samples in the printed group was matched with the manual group by selecting nine samples randomly. The bold lines represent a probability density function, and the actual data values are represented as circles. The standard deviations were compared in statistical terms using the $F - test$ ($\alpha = 0.025$), which confirmed the negligible distinction between the printed groups, whereas the dispersions of the manual group were significantly larger than the other groups in both of R_0 and GF (Figs. 4.44 (e) and (f)).

In the experimental results, the manual sensors had the higher GFs, the two main causes

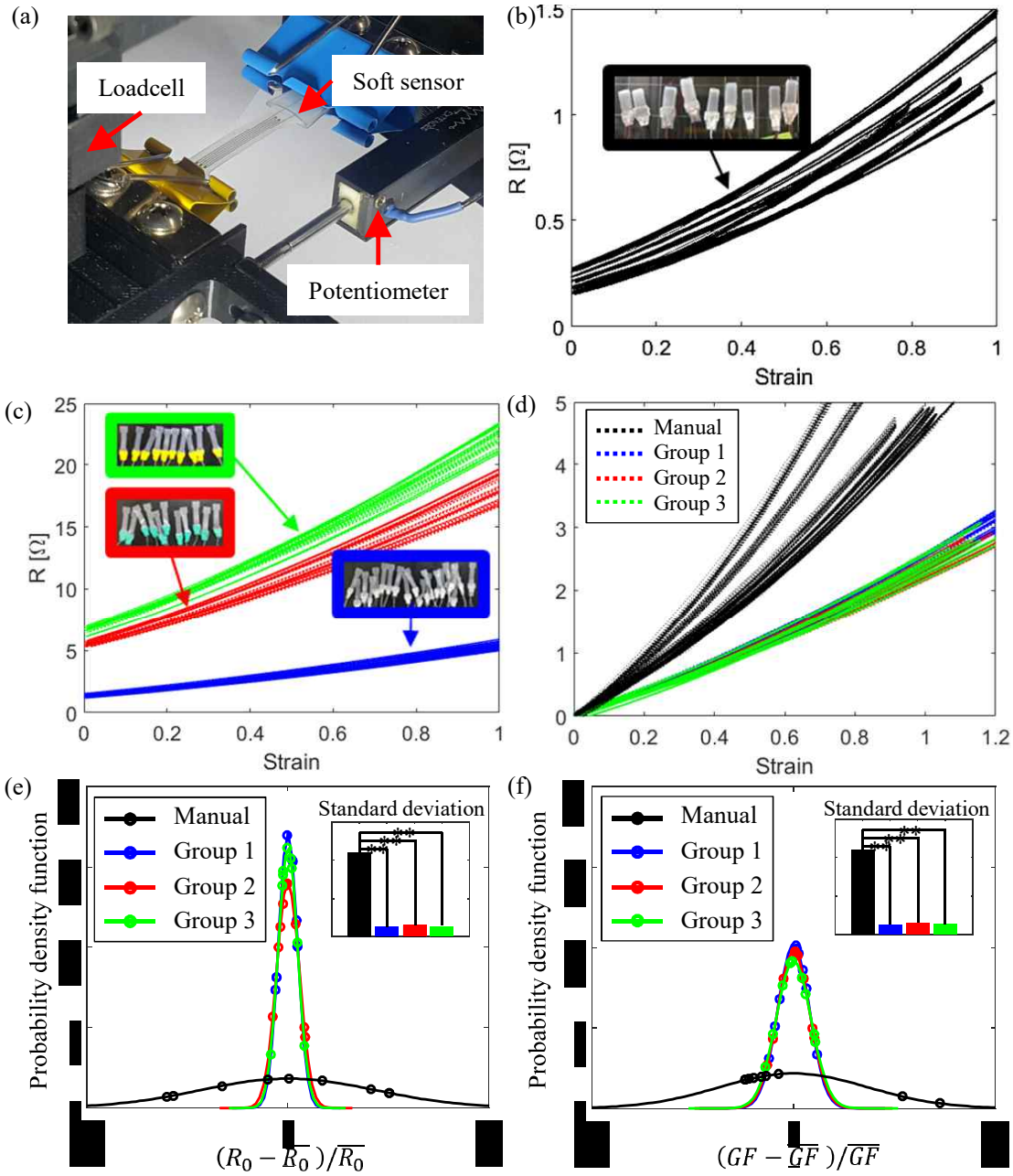

Figure 4.44: Verification of reproducibility of DIW-base fabrication: (a) experimental set-up for tensile tests, (b) strain-resistance curves of manually developed sensors (square cross section, $300\mu m \times 300\mu m$), (c) strain-resistance curves of printed sensors (blue : ID=490 μm, red : ID=430 μm, green : ID=340 μm), (d) strain-resistance change normalized by initial resistance, (e) probability density function (normal distribution) and its standard deviation (with F-test results, $\alpha = 0.025$) in terms of normalized initial resistance $(R_0 - \overline{R_0})/\overline{R_0}$, and (f) in terms of normalized gauge factors (GF) $(GF - \overline{GF})/\overline{GF}$.

Table 4.1: Experimental results for confirming reproducibility of sensor fabrication

		Manual	Printed		
			1	2	3
Initial resistance (R_0 [Ω])	$\mu \pm \sigma$	0.215±0.047	1.33±0.031	5.412±0.153	6.567 ± 0.161
	σ/μ	0.218	0.023	0.028	0.025
	p-value	0.941	0.644	0.728	0.911
Gauge factor (GF)	$\mu \pm \sigma$	5.183±0.950	2.602±0.102	2.402±0.098	2.476±0.108
	σ/μ	0.183	0.039	0.041	0.044
	p-value	0.656	0.728	0.911	0.941
Number of sensors		9	21	11	10

of which were overestimation of the stretchable body length and difference in elastomer material. Specifically, the body thickness of the manually developed sensor was about $3.8mm$ 10 times thicker than the printed sensors ($0.35\,mm$), which could shorten the actual stretchable length for a given loading condition due to a larger Saint-Venant effect [175]. Additionally, the manually developed sensors were made of Ecoflex 0030, with a larger Poisson's ratio than Dragon Skin 30, which was a source of the larger GFs [29]. The GF values of the printed sensors ($GF \approx 2.5$) were reasonable, compared with those of the previously reported sensors ($GF \approx 2.37$ [117]). Due to proficient manual skill, the manually developed sensors had quite consistent GFs, but considerably different GFs were observed in the two samples. That is, the reproducibility can be degraded severely with a larger number of sensors. As shown in the results, the DIW-based fabrication exhibited superior reproducibility to manual fabrication because the performances of multiple sensors were more consistent in terms of R_0 and GFs.

4.3.5 Application to Soft Sensors

Performance Evaluation of a Strain Gauge

In the suggested fabrication process, the dimensions of the microchannel cross-section and thickness of the elastomer body can be adjusted by applying different syringe sizes and covering thicknesses, respectively. As shown in Figure 4.45 (a), the fabricated sensor had $350\,\mu m$ thickness in total, the microchannel of which had $200\,\mu m$ width and 0.5 aspect ratio (height/width); the elastomer body should be at least two times thicker than the channel height to prevent damage.

To test its performance, the sensor was stretched up to 110 % ($\approx 35\,mm$) strain with

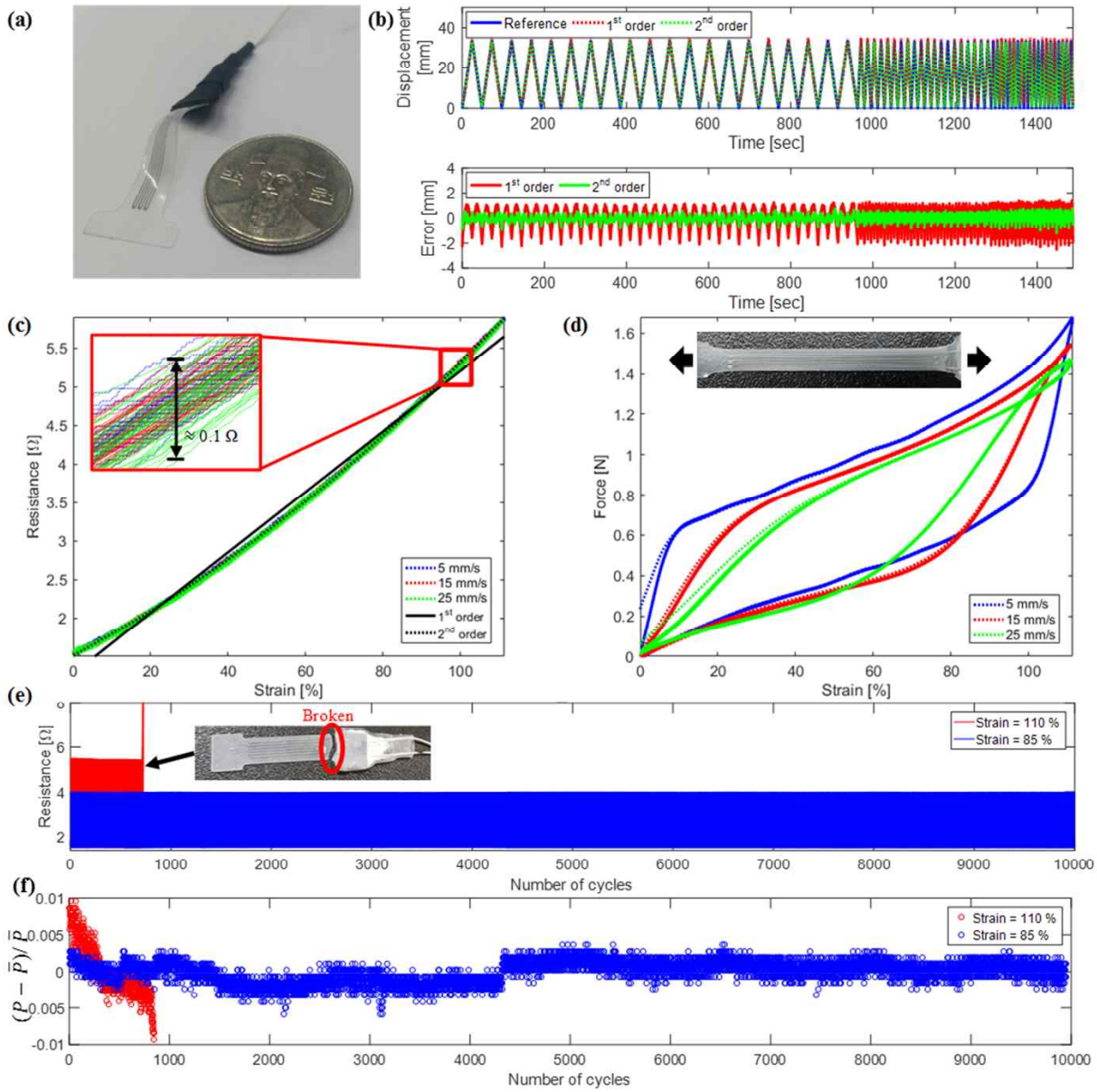

Figure 4.45: Performance evaluation of the DIW-based soft sensors: (a) Displacement measured with a linear potentiometer (blue solid line) and estimated by a first (red dotted line) and a second (green dotted line) polynomial based on sensor signals, (b) strain-resistance curve with respect to loading speeds of $5 mm/s$ (blue dotted line), $15 mm/s$ (red dotted line), and $25\ mm/s$ (green dotted line), (c) strain-tensile force curve, (d) duty cycle test: 80 % strain (blue solid line), 110 % strain at the speed of $25\ mm/s$ (red solid line), and (e) peak values of the duty cycle tests with 80 % strain (blue circles) and 110 % strain (red dots).

different loading speeds, 5, 15, and 25 mm/s, 15 times each by using the same experimental set-up (Figure 4.44 (a)). As shown in Figure 4.45 (b), the displacement was measured with the linear potentiometer as a reference (blue solid line), which was estimated with the sensor signal combined with a first-order (red dotted line) and a second-order (green dotted line) polynomial model fitted by the least-square method, and the corresponding estimation errors are illustrated in the graph below. The reason for using a second-order polynomial was that the previously suggested theoretical model was based on a higher order polynomial than a linear model [131, 117, 130, 29]. In the experimental results, the sensor signals were consistent against repeated loads with different speeds and the accuracy of the estimation was about $\pm 2\,mm$ and $\pm 1\,mm$ for each polynomial model.

As shown in Figure 4.45 (c), the sensor had a very little hysteresis effect about a 0.1 Ω difference−without apparent disparities between loading speeds. In a linear regression analysis, the coefficient of determination (R^2) was 0.996, and the fitted line is shown by the black solid line. For more accurate estimation, a second polynomial could be a better alternative (black dotted line), resulting in 10 times smaller RMS error than the linear model. In the experimental results of the reaction force (Figure 4.45 (d)), an abrupt increase in the force was observed after 100 % strain. Despite the abrupt increase, the observed reaction force at 50 % strain (on average 0.4 N) was comparable with that of the soft sensor made by Ecoflex (with 8.6 times smaller modulus) based on a manual fabrication technique reported in a previous of study [126], because the sensor developed in this study was six times thinner.

The sensor was stretched at 25 mm/s with 85 % and 110 % strain repeatedly to test its duty cycle (Figure 4.45 (e)). In the case of 85 % strain, the sensor performance was consistent up to 10,000 cycles without a significant change in the normalized peak values $(P - \bar{P})/\bar{P}$ (blue dots in Figure 4.45 (f)), where P is resistance value at the peak strain whose average is $\bar{P}$. In contrast, the sensor was broken after about 800 cycles with 110 % strain with gradually decreasing peak values (red dots in Figure 4.45 (f)). As shown in Figure 4.45 (d), because a strain level above 100 % was an extreme condition for the sensor, the result can be interpreted as a damaged sensor, attributed to repeated load over the extreme loading condition, which demonstrated as a sudden increase in the required tensile force. Without an extreme loading condition, the sensor had very stable signals in our experiments ($\sigma/\mu = 0.15\%$ for $10,000\,cycles$), although it has been reported previously that the long-term stability of the eGaIn-based sensor is questionable [58].

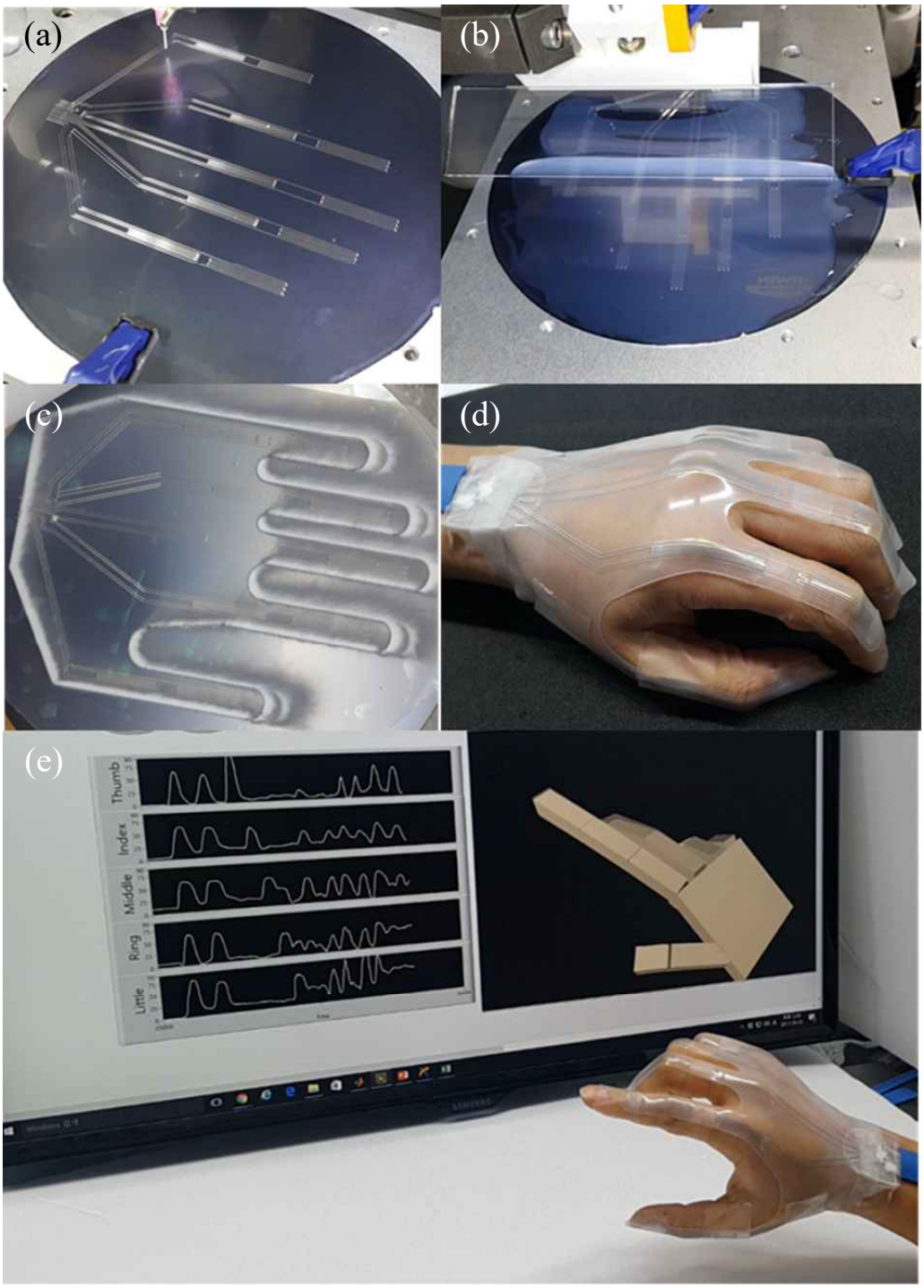

Figure 4.46: Application to a glove-type sensor measuring flexion/extension of 10 joints, the metacarpal and proximal interphalangeal joints of the five fingers: (a) printing, (b) covering, (c) laser cutting, (d) wearing a glove with medical tapes, (e) real-time measurement of joint angles.

A Glove-type Sensor

In addition to a strain gauge, various types of sensors can be developed based on the suggested fabrication technique by modifying the trace to be printed. A glove-type system was fabricated for one of the applications (Figure 4.46). Each sensing module was located on a target joint [130, 30] and printed on the silicone-coated wafer in one 15-min process (Figure 4.46 (a)). After printing, both sides of the printed feature were covered gently by the silicone material (Figure 4.46 (b)). The external shape of the sensor was trimmed with a laser cutter (Figure 4.46 (c)). The sensor system can be worn by simply attaching a medical tape (Figure 4.46 (d)). The glove-type sensor can measure finger motions in real-time for the 10 joints−including metacarpal (MCP) joints and proximal interphalangeal (PIP) joints−of the five fingers. Figure 4.46 (e) presents the joint angles of each finger as a real-time plot and the posture of the fingers is visualized as an animation. The total thickness of the sensor was about 600 μm, and the entire sensor had a monolithic body. The glove is more compact than previously developed glove sensors, and the proposed fabrication process is also superior [30, 60, 130].

4.3.6 Predicting Sensor Performance using an Isovolumetric Model

In previously reported studies, the performance of the sensor has been predicted by a mathematical model under the assumption that the cross-section of the microchannel will shrink with a constant Poisson's ratio according to elongation [131, 126, 117, 130]. However, in case of silicone material where Poisson's ratio, ν, is about 0.49, the total volume of the microchannel should be decreased to satisfy the decrease in cross-sections according to the Poisson's ratio, which is not feasible for a sensor where the microchannel is filled with liquid due to its incompressibility. Thus, it can be assumed that the microchannel filled with EGaIn will satisfy an isovolumetric condition during elongation, regardless of its cross-sectional shape.

The equivalent volumes of the microchannel were estimated by the different methods with respect to elongation, under the assumption that the cross section shape was consistent along the channel. First, the volume of the channel was calculated based on the experimental results (V_{exp}):

$$V_{exp} = \rho \frac{[l_0(1+\epsilon)]^2}{R} \tag{4.12}$$

where ρ is resistivity of the EGaIn ($\rho = 29.4 \times 10^{-6}\,\Omega \cdot cm$), l_0 is the initial length of the microchannel, ϵ is strain, and R is the resistance between both ends of the microchannel, measured during the experiment. The equation was derived based on the definition of a resistance, $R = \rho(A/l)$, where A and l are the area and length of the microchannel, respectively. Secondly, the volume was estimated by a theoretical model based on Poisson's ratio (V_ν):

$$V_\nu = A(w, h) \cdot l_0(1 + \epsilon) \tag{4.13}$$

where $A(w, h)$ is the cross-sectional area of the circular segment as a function of channel width, $w = w_0(1 - \nu\epsilon)$, and height, $h = h_0(1 - \nu\epsilon)$.

Another way to estimate channel volume is to measure the area of cross-sections directly, by inspecting mircochannels in a non-destructive way. Figure 4.47 (a) presents an actual image of a microchannel (green cylindrical shape) captured by a multi-photon confocal microscopy (LSM780NLO, Zeiss [209]), which focalizes particles of fluorescent material (Fluorescein, Sigma-Aldrich [162]) layer by layer using a so-called z-stacking function. The stacked 3D image was rendered with image-processing software (Imaris 9, Bitplane [15]) to improve visibility by adjusting the rendering parameters in the software without distorting the channel size at zero strain.

To prepare a specimen, the liquid metal inside the sensor was extracted by injecting a strong acid ($35\ wt\%\ HCl$), and the microchannel was filled with the fluorescent material solution ($1\,M$ Fluorescein, Sigma-Aldrich [162]) after washing the remaining acid sufficiently with distilled water (Figure 4.47 (b)) (Supplementary Video 5). The EGaIn inside the microchannel can clearly be replaced with different liquid substances due to the inherent properties of EGaIn [83, 129]. With different strain levels, the microchannel of the specimen was captured correspondingly, the transverse area of which was measured with an image measurement software (Image Measurement 8.49, Bersoft [14]) on a mm^2 scale. As shown in Figure 4.47 (c), the area decreased gradually as the microchannel was elongated. Using the measured values, the equivalent volume based on the non-destructive inspection, V_{fluo}, was estimated as follows:

$$V_{fluo} = A_m \cdot l_0(1 + \epsilon) \tag{4.14}$$

where A_m is the measured cross-sectional areas.

The equivalent volumes with respect to strain are presented in Figure 4.47 (d); V_{exp} (blue dotted line) agreed V_{iso} (green solid line) rather than the Poisson's ratio-based model V_ν

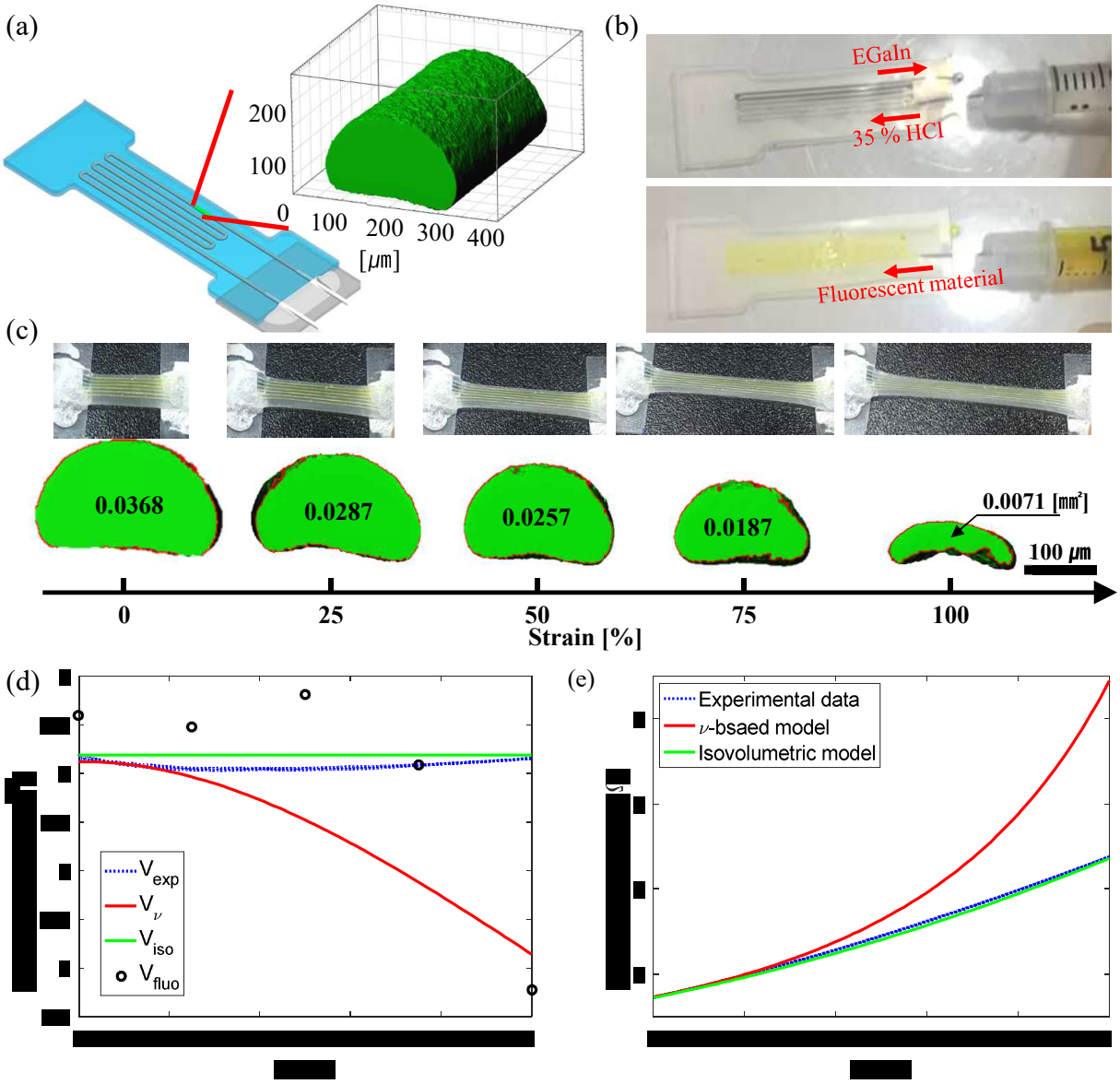

Figure 4.47: Investigation on the isovolumeric deformation of the microchannel: (a) Non-destructive inspection for the three dimensional shape of microchannel, (b) extraction of EGaIn using a strong acid ($35wt\%HCl$) and injection of a fluorescent material ($1\ M$ Fluorescein [162]), (c) transverse cross-sectional area of the microchannel with respect to strain, (d) equivalent volume of the microchannel estimated by the experimental data V_{exp} (blue-dotted line), the Poisson's ratio-based model V_{ν} (red solid line), the isovolumetric condition V_{iso} (green solid line), and the cross section area from the non-destructive inspection V_{fluo} (black dots), (e) resistance-strain curve of the experimental results (blue dotted line), estimated by the previously suggested analytic model based on Poisson's ratio $\nu = 0.499$ (red solid line), and the isovolumetric model (green solid line).

(red solid line), where V_{iso} is constant. Additionally, the values of V_{fluo} (black dots) also supported the isovolumetric condition, up to $\epsilon = 0.75$. At $\epsilon = 1$, the volume was appeared to be decreased by half, which was attributable to the loss of isovolumetric conditions caused by a combination of the locally emptied space within the microchannel from vaporization and heavy shrinkage of the cross-section due to the extreme load. Although the fluorescent solution can be vaporized in this experiment, the EGaIn in the sensor was hardly affected, because of its low vapor pressure, maintaining the isovolumetric condition. As shown in Figures 4.45 (e) and (f), the sensor had consistent performance during $10,000$ *cycles* (for about 400 *min*), indicating that the amount of EGaIn inside the microchannel remained constant.

The performance of the sensor can also be estimated using a simulated cross-section area from each model (Figure 4.47 (e)). The experimental data (blue dotted line) were successfully described by an isovolumetric model (green solid line), while the Poisson's ratio-based model overestimated the resistance change due to the excessive shrinkage of the cross sections without considering the incompressible liquid inside the channel, especially over the range of strain > 0.2. The change in the cross-section filled with incompressible liquid can be explained solely based on the isovolumetric condition, regardless of its cross-sectional shape, predicting the sensor performance more accurately even over a range of large deformation (strain > 0.2).

This study was able to validate the feasibility of the theoretical model because of the accurate geometry of the microchannel, realized by the suggested fabrication technique. Additionally, a sensor design based on modeled predictions, such as the desired configuration and dimensions of the microchannel, can be achieved more accurately using the suggested fabrication technique, illustrating the potential applications of the theoretical model.

4.4 Direct Wiring of Liquid Metal to Metal Electrodes

In the experimental results in the previous section, the sensor signals were acquired through the directly inserted wires. A stable and compact electrode part is necessary to acquire stable sensor signals from the soft sensors and not to impede free movement of the user in the wearable applications. Thus, in this section, a solution for electrical connection from the microchannel is proposed based on direct writing of liquid metal.

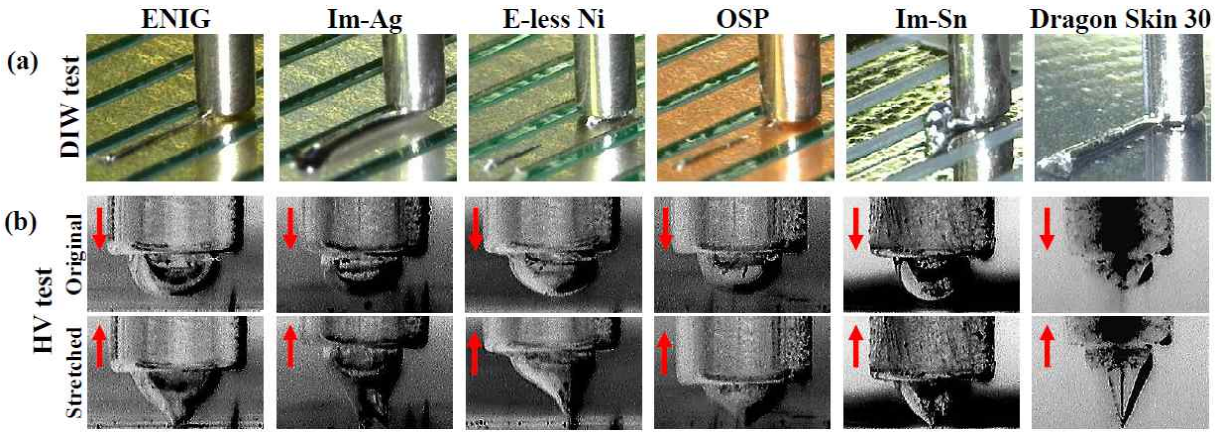

Figure 4.48: Wettability test of eGaIn onto metal electrodes: (a) direct writing test and (b) height variation (HV) test

4.4.1 Direct Writing of eGaIn on Metal Electrodes

For electrode materials, the surface finished metal electrodes were prepared, most frequently used in the printed circuit board (PCB) industry [189, 152]: 1) electroless nickel immersion gold (ENIG), 2) immersion silver (Im-Ag), 3) electroless nickel (E-less Ni), 4) organic soldability preservative (OSP), and 5) immersion tin (Im-Sn). We prepared 6 specimens including customized boards treated with ENIG, Im-Ag, E-less Ni, OSP (custom made by order), and flexible flat cable (FFC) treated with Im-Sn and ENIG (commercial products). The customized board was 25 mm by 20 mm rectangular with 20 plated traces at the intervals of 1 mm. The FFC had 1 mm pitch and 50 mm length.

First, direct writing of eGaIn was tested on each surface. eGaIn cannot be directly written on most of the metal surfaces except for the Im-Ag as shown in Figure 4.48 (a). In case of the silicone substrate, Dragon Skin 30 (Smooth On [164]), eGaIn was successfully written. The results can be explained based on the previously reported wetting behaviors of eGaIn [49]. Direct writing of eGaIn can be realized by continuous yielding and spontaneous and rapid reconstruction of the oxide skin at the syringe tip. To initiate the writing, it is important to wet the droplet of eGaIn on the surface. However, as the oxide skin already formed makes contact with a surface without rupturing the skin, minimal adhesion occurs between the eGaIn and most solids, regardless of material or texture [49]. It is mainly due to nano-scale texture of the oxide skin.

The phenomenon can be observed easily by height variation (HV) wettability test [101].

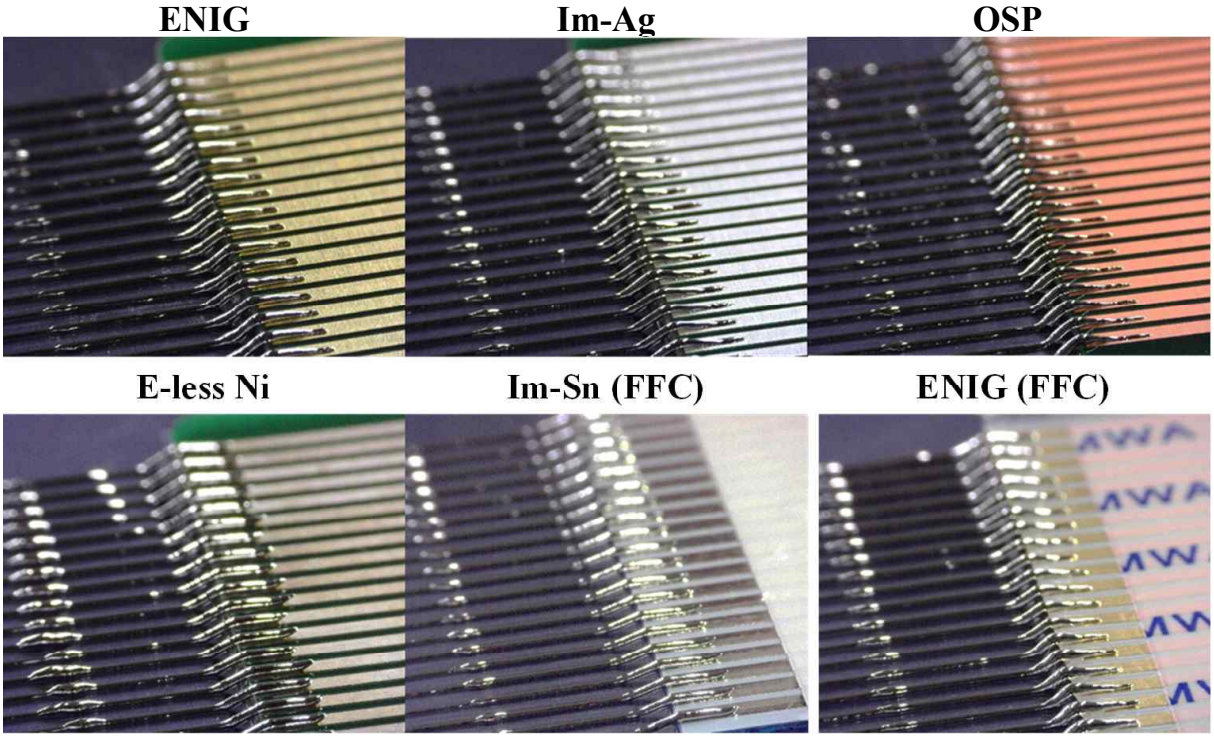

Figure 4.49: Directly wired eGaIn onto metal electrodes

A syringe tip with a droplet of eGaIn was prepared, moved closely to the substrate until the syringe reached the surface completely, and removed from the surface in the vertical direction. The experimental results on each substrate is shown in Figure 4.48, with snapshots of the original droplets and the stretched droplet shortly before detached from the substrate. The ratios of the stretched droplet length to the original were roughly calculated from the snapshots for each substrate. The ratios were smaller than 1.5 for the metal electrodes, except for the Im-Ag ($\approx$ 2) and the Dragon Skin 30 ($\approx$ 2.5) substrates. This result corresponds to direct writing test (Figure 4.48 (a)). The successful writing on the Im-Ag and the silicone substrates can be explained by the adhesive property of eGaIn in the previous reports [49, 74, 155]. The wettability on Im-Ag can be understood by the characteristics of eGaIn rapidly alloying with most metals [155]; which is more vigorous with silver [211]. In case of silicone materials, the air permeable and viscoelastic properties enable increased adhesive property even with the texture of the skin [74].

Except the two cases, eGaIn cannot be connected to most of the metal electrodes by writing eGaIn directly onto the metallic surfaces. As an alternative, in this study, the trace

of eGaIn was extended from the silicone substrate, raised up in the vertical direction around the electrode (building a vertical pillar of eGaIn), and stretched on the metal electrode to form mechanical contacts between eGaIn and the metal electrode. By adjusting the location, height, and amount of stretch of the pillar, eGaIn pillars were successfully connected to the metal electrodes in a reproducible manner (Figure 4.49). This unique process can be feasible due to superior structural stability of eGaIn from the oxide shell, which allows even a free standing 3D structures, achieving values 100 times larger than the Rayleigh stability limit [102, 176].

4.4.2 Verification of Electrical Stability

Reproducibility of Contact Resistance

To verify stability of the contact resistance between the eGaIn and the metal electrodes, the resistance between the two ends of the metal electrode was measured, which was connected through the eGaIn wire (50 mm length). As shown in Figure 4.50 (a), Each specimen contained 10 eGaIn wires to the 20 metal traces, two metal electrodes were connected with a eGaIn wire. To probe the other side of the metal electrode, contact connector assembly was used, which was composed with a compression connector (made by Samtec [153]), a FFC connector, and a FFC. The FFC from the connector assembly was connected to the amplifier circuit containing a voltage divider and a non-inverting amplifier circuit to convert the resistance from the specimen into analog voltage signal. The FFCs finished with Im-Sn and ENIG were directly connected to the amplifier. The analog voltages were recorded by a data acquisition (DAQ) system (USB-6217, National Instruments [121]).

For each material, resistances from the 30 wires (3 specimen for each material) were measured, and their mean and standard deviation were calculated for each material (Table 4.2). To remove outliers, the wires with resistance higher than 100 Ω were excluded, treated as connect failures. As shown in the number of sires (N) in Table 4.2, 2 3 failures were observed in E-less Ni, OSP, and Im-Sn, while no failures were observed in the other three cases, ENIG, Im-Ag, and ENIG (FFC). As shown in Figure 4.50 (b), the resistance values can be visualized with a normal probability density function (PDF), fitted with the mean and standard deviation values from the experimental results, to compare the mean values and distribution of each case. The x-axis of the plot shows the resistance value, and the y-axis shows the probability that the resistance values can be observed. The circular plots show the actual resistance value of each wire, the solid line shows a fitted PDF. The more the peak of the

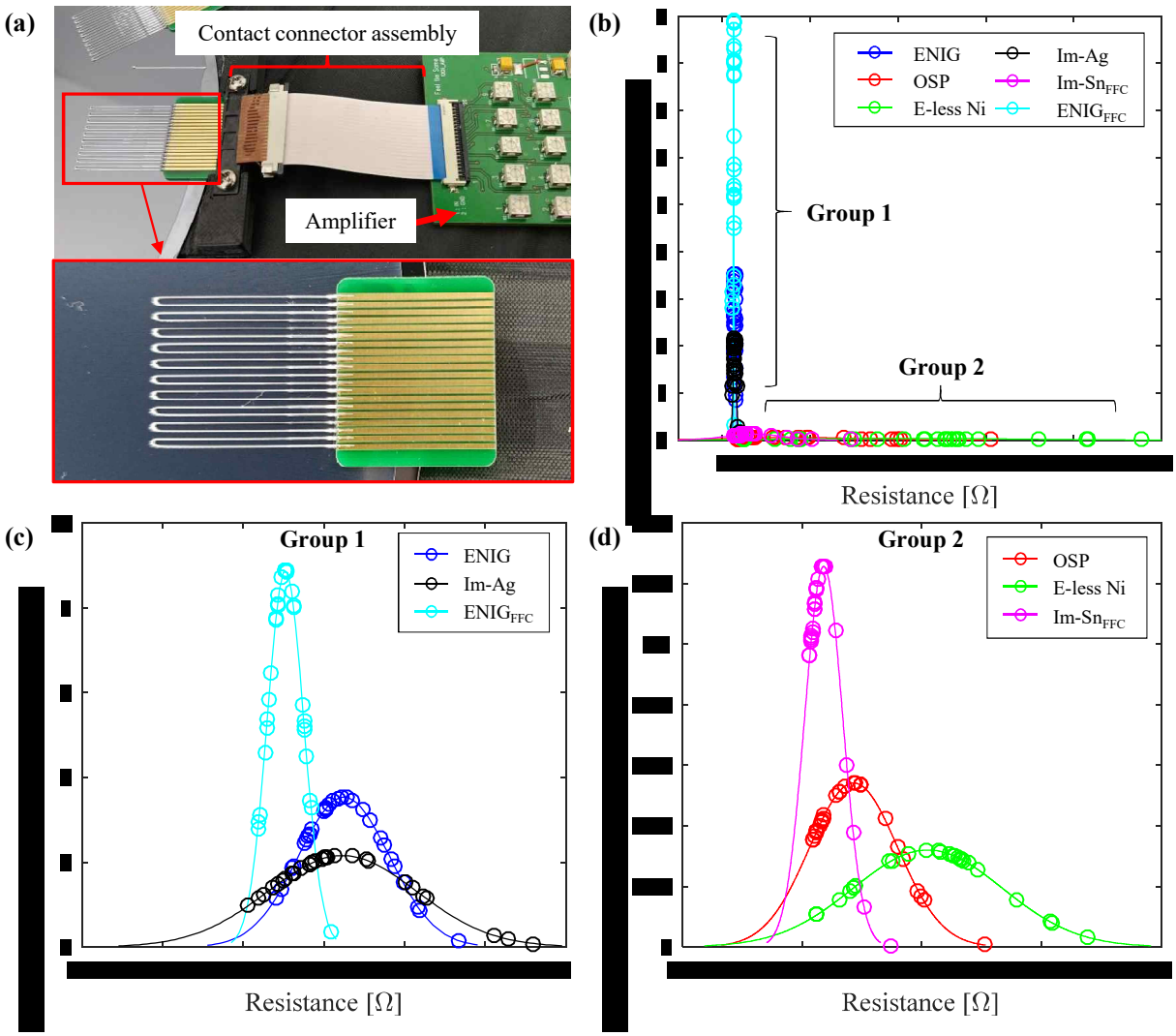

Figure 4.50: Verification of reproducibility of contact resistance between eGaIn and the metal electrodes: (a) experimental setup, (b) visualized results with a normal probability density function (PDF), (c) detailed plot for Group 1, and (d) for Group 2.

PDF is located on the left, the metal electrode has lower contact resistance. The narrower and higher peak of the PDF indicates that the resistance values are highly reproducible.

Table 4.2: Resistance between the metal electrodes connected through an eGaIn wire

	ENIG	Im-Ag	E-less Ni	OSP	Im-Sn	ENIG (FFC)
$\mu[\Omega]$	1.449	1.445	20.99	8.595	3.592	1.304
$\sigma[\Omega]$	0.1129	0.1849	12.460	7.3649	3.1735	0.0449
σ/μ	0.0779	0.1279	0.5936	0.8569	0.8835	0.0334
N	30	30	27	28	27	30

The experimental results were classified into two groups as shown in Figure 4.50. Group 1 (ENIG and Im-Ag) had lower value of resistance with higher reproducibility (narrower distribution) while Group 2 (E-less Ni, OSP, and Im-Sn) had higher resistance values with wider distribution (higher uncertainty). In other words, it is more advantageous to choose materials in Group 1 as an electrode material to be connected with eGaIn wires, because of lower contact resistance and lower uncertainty in the contact resistance. This results can be explained with the amount of mechanical contact area between eGaIn and the metallic surface. In a previous report, uncertain contact resistances with higher resistance values between eGaIn and metal electrode were observed, attributed to small amount of contact area [127]. In other words, the contact area between eGaIn and the metal might not be formed sufficiently for the materials in Group 2, based on the proposed method, stretching and placing eGaIn wires on the metal electrode. On the other hand, the same amount of mechanical contact areas were enough for Group 1 materials due to their higher conductivity. The gold and silver have higher conductivity than tin and nickel. In case of the OSP, although the conductivity of the copper is comparable with that of the silver, organic component may degrade the conductivity on the surface. The difference of resistance value between the ENIG (FFC) and the others in Group 1 resulted from the resistance from the contact connector assembly ($\approx 0.15\,\Omega$).

Time-dependent Stability of Contact Resistance

In this test, 10 eGaIn wires were connected to each specimen and the resistance values were measured for 8 hours to observe time-dependent variation of the resistance values. In this experiment, the failed wires with resistance values larger than $100\,\Omega$ was included

in the plot, and their values were assumed to be 100 Ω to observe tendency in resistance change rather than their exact values. The experimental results are plotted as a box plot as shown in Figure 4.51. In Group 1 materials, time-dependent variations were rarely observed. However, In Group 2 materials, the specimen finished with OSP and Im-Sn had vigorous time-dependent variation of the resistance values.

More specifically, nine of ten wires connected to the OSP-finished electrodes had initial resistances larger than 50 Ω, which was reduced to lower than 5 Ω for the six of them within 3 hours. The other three wires had resistances larger than 100 Ω, two of which recovered ($< 5\Omega$) in 5 hours, and the other had not recovered. In case of the Im-Sn, six of ten wires had relatively low resistance values ($\approx 2.5\Omega$), but the other four wires had higher values ($> 20\Omega$). Resistance change was not observed in the six wires with the low resistance values. In case of the four wires with high resistance value, one of them maintained its initial resistance for 8 hours, while the increment of resistance was observed in the other three for 3 hours. One of the three recovered its resistance value ($\approx 2.5\,\Omega$), and the other two had not recovered.

This time-dependent variation is attributed to variation in mechanical contact area due to alloying behavior of eGaIn [101, 127]. In case of the materials in Group 1, the initial mechanical contact area was sufficient enough to form low contact resistance. The stable resistance values with little variation might be attributed to no decrement in mechanical contact area. For the Group 2 materials, because the initial contact area was usually not enough to acquire sufficiently low contact resistance, time-dependent wetting of eGaIn onto the surface might decrease the contact resistance. In case of the Im-Sn, the increasing tendency in resistance was observed also, which might be caused by delamination between the eGaIn wire and lump of eGaIn wet on the surface with decreased contact area between them. Our observations can support the situation. Vigorous alloying behaviors were observed between eGaIn and tin, the eGaIn wires lost their original shape with burst of the oxide skin. The plated tin surfaces were even delaminated from the copper layer, allowing direct contact between eGaIn and the copper traces, which greatly decreased the contact resistance. However, in the wires with higher resistance or increased resistance over time, the eGaIn wires on the electrode maintained their original shape without burst. That means only small amount of alloying occurred between the eGaIn and the tin surface, and the reaction was terminated due to the decreased contact area. In case of E-less Ni, no significant time-dependent variations were observed due to severe nonwetting properties between eGaIn and Ni [127].

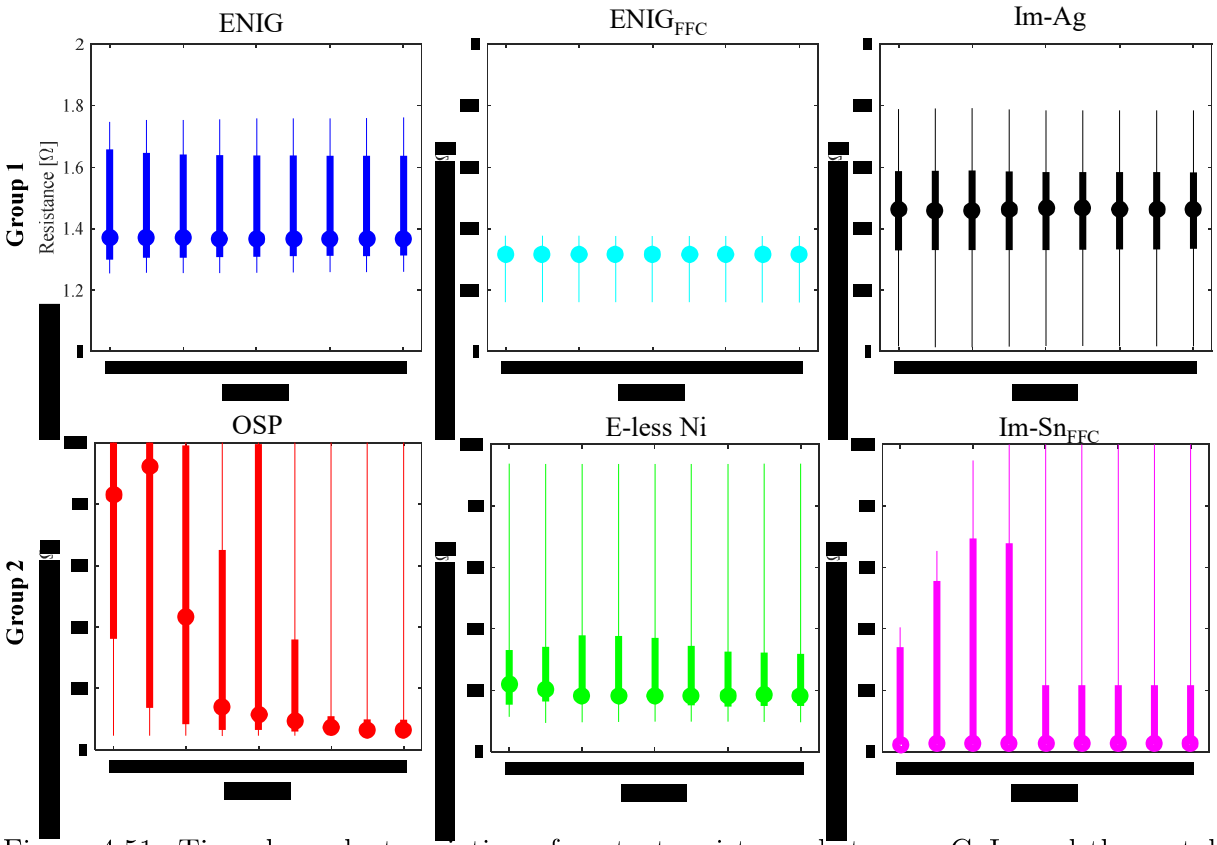

Figure 4.51: Time-dependent variation of contact resistance between eGaIn and the metal electrodes (circular points, bold lines, and solid lines indicate median values, from 25 to 75 percentile values, and from minimum to maximum values, respectively.)

Measurement of Contact Resistance

In the experimental results, ENIG and Im-Ag had low resistance values reproducibly, and time-dependent variation was not observed. However, in a previously reported study, it was found that strong alloying behavior of the silver with Ga resulted in unstable connection between them [155]. Therefore, it is most favorable to use the ENIG surface finish for a stable electrical connection with eGaIn. In addition, the interfacial resistance can be reduced by 0.15 Ω. Using the FFC finished with ENIG, contact resistance between the eGaIn and the metal electrode was evaluated by transmission line method (TLM) [147]. The experimental results is shown in Figure 4.52. The resistance increased linearly with increasing the length of the eGaIn wire due to stable contact resistance, which is the half of the y-intercept (0.2702Ω). The measured contact resistance in this study is comparable with the

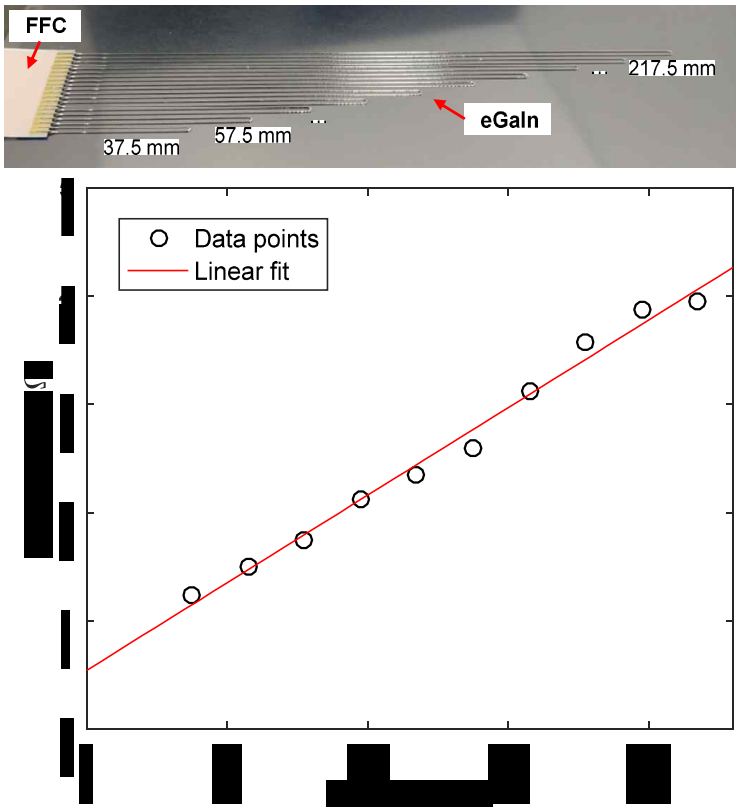

Figure 4.52: Contact resistance between eGaIn and the metal electrode (ENIG)

previously reported values: contact resistance between 1) eGaIn/PEDOT:PSS/Au interface (contact resistance$\approx$ 0.25 Ω considering the y-intercept$\approx$ 0.5 Ω in the TLM result) [86] and 2) eGaIn/Graphene/Ag (contact resistance=0.263 $\Omega \cdot mm$, which is approximately 0.877 Ω considering width of the eGaIn wire in this study, 300 μm) [155].

4.4.3 Mechanical and Thermal Durability

Durability against Mechanical Strain

The written eGaIn wires on the base silicone layer can be shielded by pouring a second silicone layer. The related fabrication process is well organized in [92]. The Dragon Skin 30 was used for the silicone layers, which has little adhesive properties to the solids. Therefore, the boundary surfaces between eGaIn, silicone, and the electrode surface were filled with an adhesive silicone material (Sil-Poxy, Smooth On [166]) for higher durability against leakage.

To test durability against mechanical strain, the specimen and the experimental setup were prepared as shown in Figure 4.53 (a). The specimen was stretched as shown in Figure 4.53 (b), with strain up to 100% and 150%. The mean values ($\overline{R}$) of the ten wires within the specimen was observed during 1000 cycles of stretch. The normalized resistance change $\Delta\overline{R}/\overline{R}_0$ is plotted in Figure 4.53 (c). In case of the 100 % strain, none of the wires was broken even after 1000 cycles, but at least one wire was broken after tens of cycles with 150 % strain. Figure 4.53 (d) shows the low peak values of Figure 4.53 (c), which maintained its value very stably (¡0.5% change) along the 1000 cycles.

Durability against Mechanical Pressure

To test durability against external pressure, the specimen and the experimental setup was prepared as shown in Figure 4.54 (a). The square area (20 mm by 10 mm) on the electrode was pressurized by a stamp, while the applied force was simultaneously measured by a loadcell. Applied pressure can be calculated by the area of the square and the force measured by the loadcell. As shown in Figure 4.54, all of the ten wires were not broken after 1000 cycles under the pressure 600 kPa ($\approx 12\,N$), but at least one wire was broken within tens of cycles under the pressure 800 kPa ($\approx 16\,N$). The low peaks of Figure 4.54 (b) is plotted in Figure 4.54 (c), showing very stable values ($< 0.5\%$ change) along the 1000 cycles.

Durability against Heating

To test thermal durability of the electrical connection, the experimental setup was prepared as shown in Figure 4.55 (a). The specimen was heated locally by a heat gun, and the temperature was observed in real-time using a infrared camera (FLIR C-Series, FLIR [53]). The resistance values of the 10 wires were measured and averaged ($\overline{R}$). Figure 4.55 shows the experimental results, where the circular points indicate mean value of $\overline{R}$ and the solid lines shows the range of a standard deviation of $\overline{R}$ from the mean value. The black symbols show the measured values as temperature increases, and the red symbols show that as temperature decreases.

As shown in the results, the resistance values increased linearly with increasing temperature linearly, which was lower than 5 % up to $150\,^{\circ}C$ without significant difference in their distribution. In case of metals, resistivity of materials increase with higher temperature, and the increasing trend is observed in liquid gallium also [47]. At $180\,^{\circ}C$, the distribution of the wire resistances increased significantly, which might not be attributed to increased resistivity

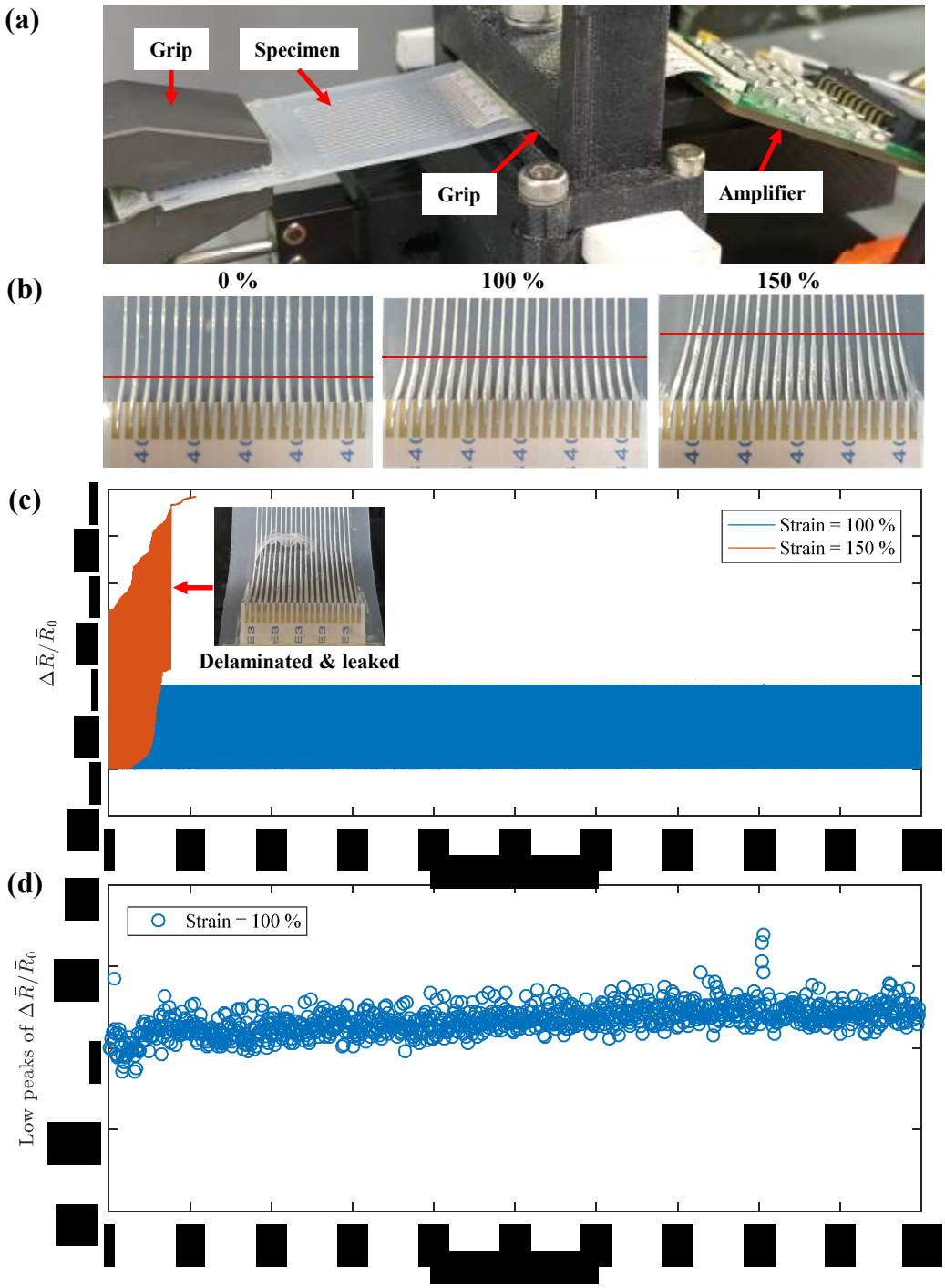

Figure 4.53: Durability test against strain of directly wired eGaIn to the metal electrode: (a) experimental setup, (b) electrode parts with strain applied, (c) normalized resistance change of the average resistance of the 10 wires ($\Delta\overline{R}/\overline{R}_0$) over 1000 stretching cycles, and (d) low peaks of $\Delta\overline{R}/\overline{R}_0$ over 1000 stretching cycles.

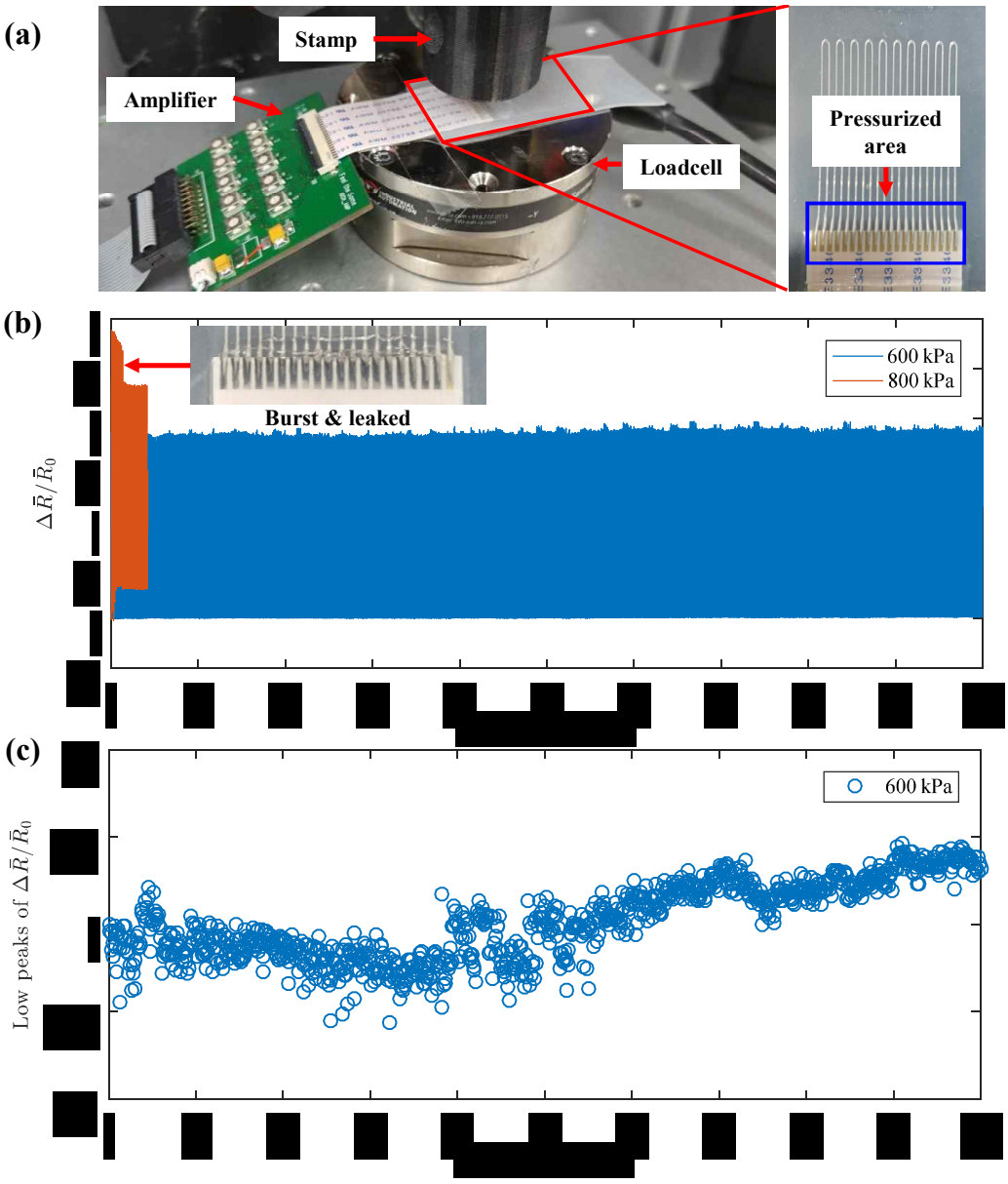

Figure 4.54: Durability test against pressure of directly wired eGaIn to the metal electrode: (a) experimental setup, (b) normalized resistance change of the average resistance of the 10 wires ($\Delta\overline{R}/\overline{R}_0$) over 1000 pressurizing cycles, and (c) low peaks of $\Delta\overline{R}/\overline{R}_0$ over 1000 pressurizing cycles.

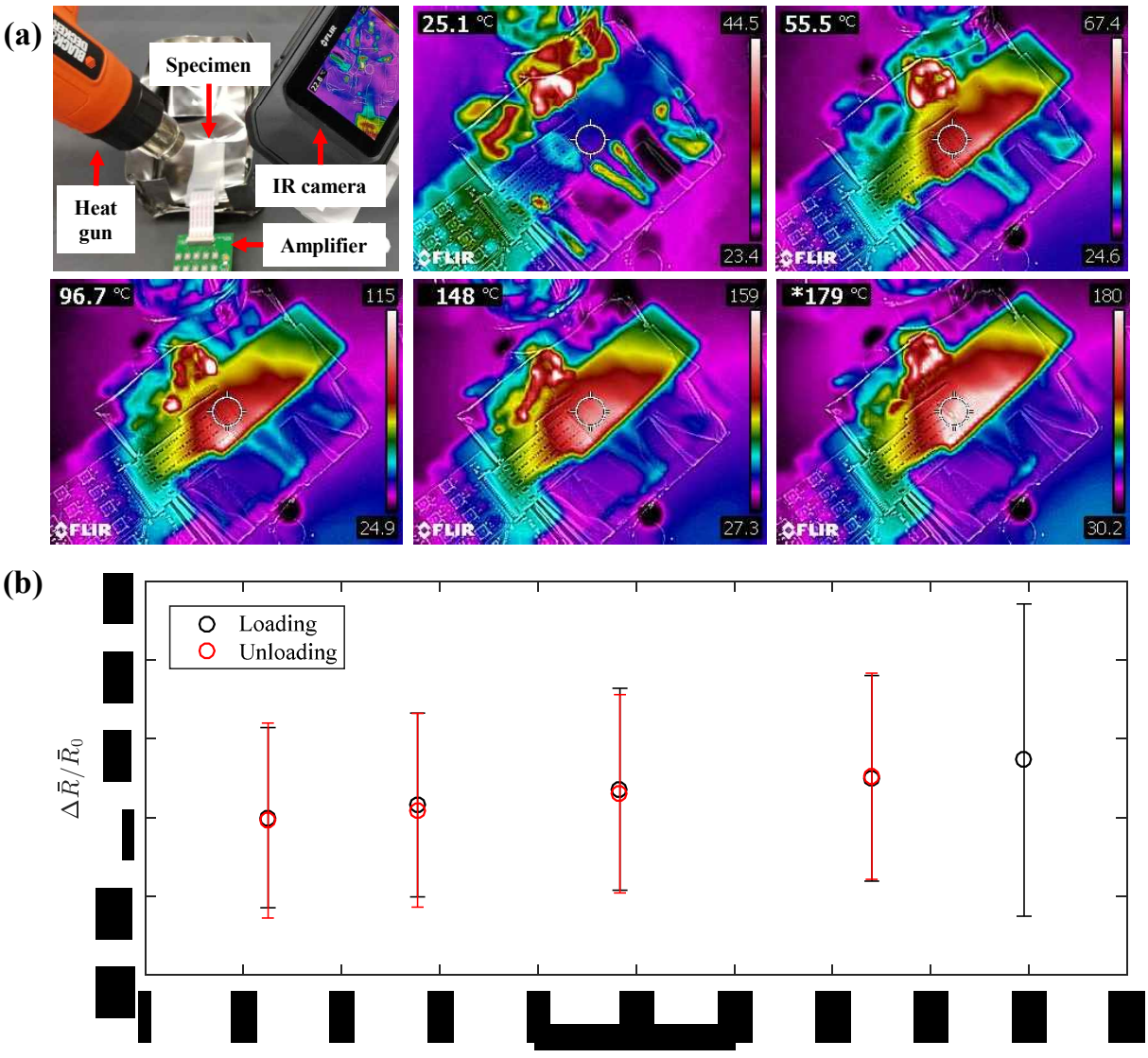

Figure 4.55: Durability test against heating of directly wired eGaIn to the metal electrode: (a) experimental setup, (b) normalized resistance change following heating.

of the material. Over 180 $°C$, the electrical connection of wires were observed, which was caused by the locally disconnected eGaIn wires due to expansion of the air inside the microchannel. The disconnected wires were not recovered even after lowering the temperature. If the temperature was lower than 180 $°C$, the increased resistances were recovered to their original values as shown in red plots. Based on the experimental results, the electrode part made by the proposed method is workable at the temperature lower than 180 $°C$ with slight increment in its resistance.

4.4.4 Application to a Soft Sensor System

A Sensing Skin Measuring Finger Flexion/Extension

To measure flexion/extension of the fingers, the 10 sensing units with serpentine shapes were located onto the metacarpal (MCP) and the proximal interphalangeal (PIP) joints of the five fingers. The sensor sheet embedded with 10 sensing units was fabricated with a ENIG finished FFC as shown in Figure 4.56 (a). The thickness of the sheet was 700 μm and highly stretchable. The sensor sheet was directly attached onto the dorsal side of the fingers with medical tapes, which can act as a sensing skin. The sensor signals were acquired by a customized PCB composed with the amplifier, main control unit (MCU), and bluetooth module for wireless communication. A lithium-polymer battery was used to supply power to the PCB.

As shown in Figure 4.56 (c), the sensing skin measured motions of the fingers successfully. In detail, all of the sensing units were activated with flexion of all the joints, the sensors with the even numbers were activated with flexion of the PIP joints, and distinguishable sensors signals were observed in the other three gestures. No significant relaxation was observed in sensor signals, which means the sensor signal converged fast enough. Slightly decreased sensor signal in Sensor 2 was observed in the second gesture. It was originated from the hyperextension of the MCP joint in the index finger, which was more extended posture than the initial posture at the beginning of this experiment. The sensor signals were not recovered after the last gesture. It might be caused by difference in the final posture with the initial posture, which was not strictly controlled in this experiment.

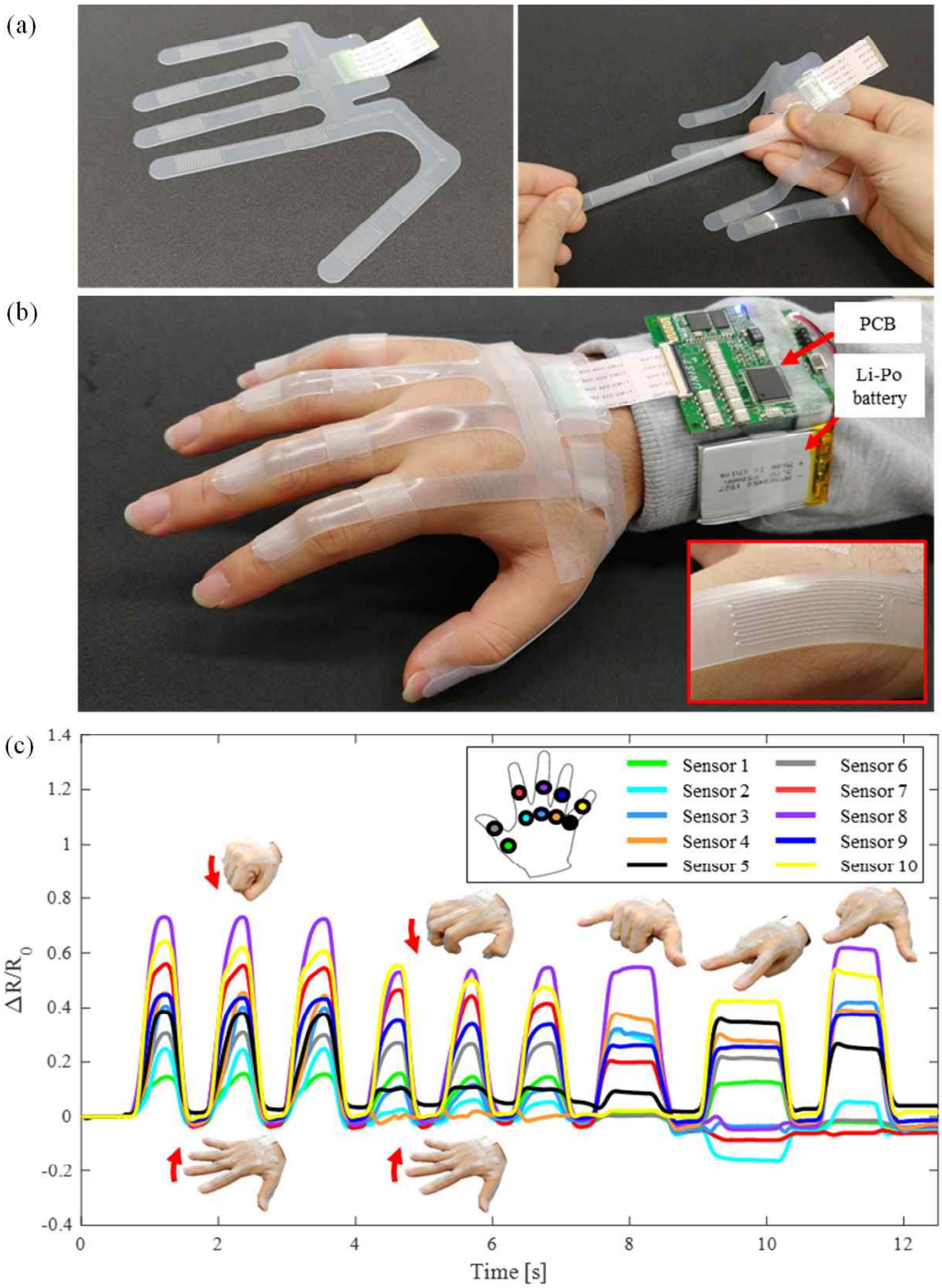

Figure 4.56: A soft sensing skin measuring finger flexion/extension: (a) fabricated sensing skin with 10 serpentine sensing units, (b) sensing skin attached on the fingers with medical tapes and connected to the customized PCB, (c) experimental results (flexion/extension of all the joints and the PIP joints only, three times for each, and the three gestures).

A Sensing Skin Measuring Ground Reaction Forces

As another application, 10 circular sensing units were located under the foot to measure ground reaction force during walking as shown in Figure 4.57. The sensing skin was attached below the foot with medical tapes (Figure 4.57), and the signals from the sensors were acquired similarly with the sensing skin for finger motions, using the customized PCB and a lithium-polymer battery. Figure 4.57 (c) shows the sensor signals during 3 walking cycles, and one of the cycles is magnified as shown in Figure 4.57 (d). The intensity of the sensor signal was visualized with a gradation plot.

As shown in the results, only six sensors (sensor 2, 3, 5, 8, 9, and 10) out of the ten had significant change in sensor signal during walking. As the heel touched the ground, the three sensors in the heel were activated in the order from the rear side of the heel. As the center of pressure moved from the rear to the front side of the foot, the other three sensors were activated with higher magnitude in resistance change. The higher resistance change is attributed to concentrated loads generated from the bone structure of the foot. These results originate from the fact that such type of soft sensor is not sensitive distributed pressure, while quite sensitive against concentrated load. Some of the sensors (sensor 1, 4, 6, 7) were not activated, because they were attached on the locations with more flesh or higher distance from the ground due to the shape of the palm, resulting in insufficient pressure applied. Therefore, to improve the design of the sensor system, the inactivated sensor should be removed or relocated.

4.5 All-in-one Manufacturing Process For a Soft Sensor System

In this section, based on the fabrication technique suggested in the previous sections, the system-level application to a sensing glove is highlighted. First, a novel fabrication process for a soft sensor system is introduced, which produces a monolithic structure including all the required items from sensing units to the electrode parts. The signals from the fabricated sensor system can be acquired through commercialized connectors and flexible flat cables (FFC) with the compact and stable structure of the electrode. In addition, the fabrication process minimally requires intervention of the skilled hands, provides extreme flexibility to modify the sensor design, and enables manufacturing a large-area sensor system. In

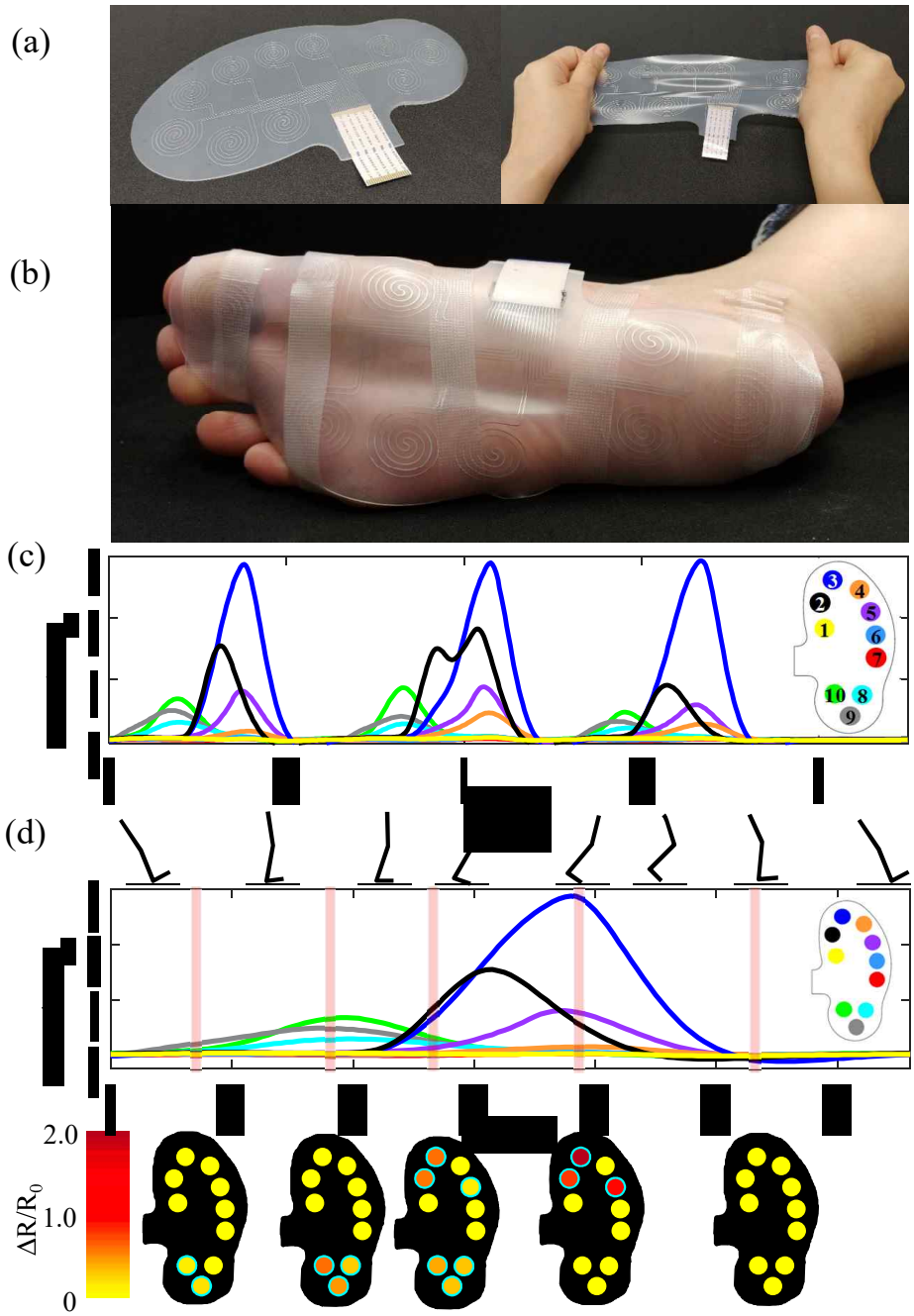

Figure 4.57: A soft sensing skin for measuring ground reaction force: (a) fabricated sensing skin with 10 twisted sensing units, (b) sensing skin attached on the palmar side of the foot, (c) experimental results during 3 walking cycles, (d) magnified plot of the first walking cycle with gradation plots for visualizing intensity of the sensor signal.

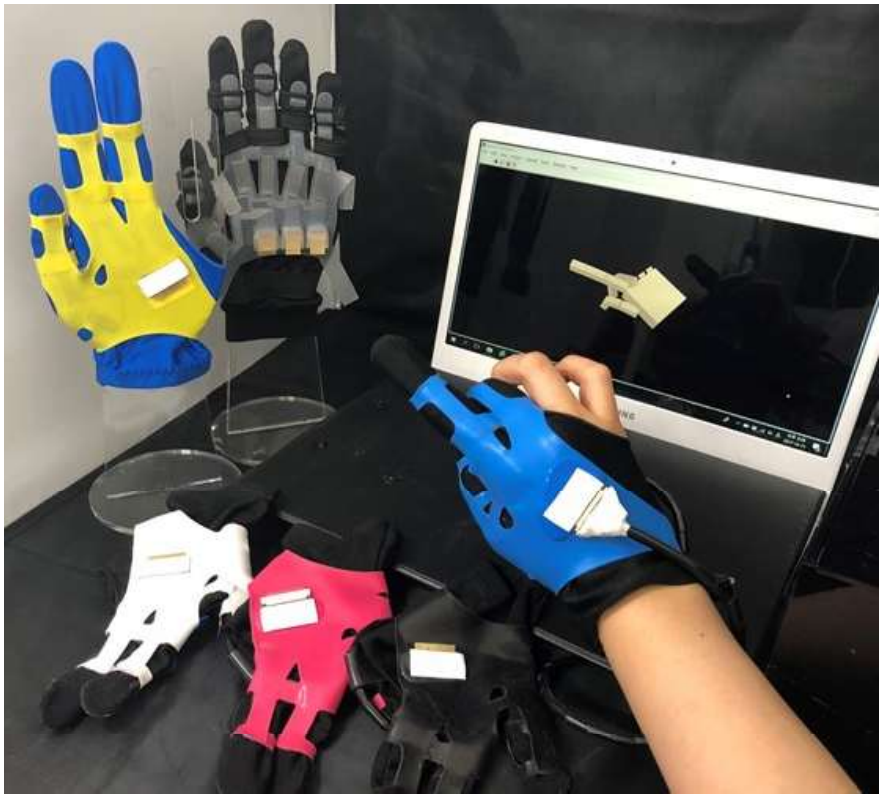

Figure 4.58: Soft sensing gloves with various forms and colors fabricated by DIW of EGaIn

other words, the proposed fabrication technique is highly productive, programmable, and scalable, which allows fabrication of sensing gloves in various forms and colors (Figure 4.58). Based on the suggested fabrication technique, a soft sensing glove was manufactured and its performance was tested in terms of linearity, step and relaxation response, and accuracy.

4.5.1 Fabrication Steps for a Soft Sensing Glove

Figure 4.59 illustrates detailed steps to manufacture a soft sensing glove through DIW of eGaIn. First, a silicone layer was coated onto a flat circular wafer through spin-coating process (Figure 4.59 (a)). Dragon Skin 30 was used as a elastomer matrix [164]. The desired pattern of sensing units and wirings were directly written by eGaIn (Figure 4.59 (b)). The custom board was placed at the end of the wiring parts, and the electrode parts were connected by writing eGaIn (Figure 4.59 (c)). The written traces were covered by uncured silicone material through squeezing (Figure 4.59 (d)). The cured part was trimmed

by a laser cutter (Figure 4.59 (e)). The workpiece was bonded onto a fabric glove by applying uncured silicone material (Figure 4.59 (f)). The electrodes within the custom board were connected by a assembling the contact-type connector module, which was combination of a contact connector and a FFC connector (Figure 4.59 (g)). Finally, the sensing glove can be used by connecting a commercial FFC.

4.5.2 Direct Ink Writing of Sensing Units and Electrodes

As shown in Figure 4.60 (a), the sensing glove was successfully written along a large area (200 mm diameter circular wafer), including sensing units, wirings, and the electrode part. The custom board (thickness=0.3 mm) was designed to widen the pitches between the wires from 1 mm to 2.54 mm. All the items were written within 15 minutes. The written eGaIn traces of the electrode part were highly consistent as shown in Figure 4.60 (b), (c). The detailed steps to form the electrode part, connecting the eGaIn traces to the custom board, are as follows: 1) locating the syringe on the target trace, 2) reconnecting, (iii) extending, 3) building a pillar of eGaIn, 4) throwing the pillar down onto the custom board, 5) stretching and cutting the trace. In this process, it was important to adjust the height of the pillar, feed rate, and application timing and intensity of vacuum pressure with respect to the residual quantity of eGaIn inside the syringe barrel. By adjusting the factors, the electrode parts were formed stably and efficiently (within 3 minutes for 20 pins).

4.5.3 Design of a Sensing Glove based on a Kinematic Model of the Fingers

Attached on the epidermal side of the hand, a soft sensing unit estimates the joint angle by measuring strain generated on the skin (Figure 4.61 (a), (b)). For this, it is important to understand anatomical structure of the fingers (Figure 4.61 (c)), define its kinematic model (Figure 4.61 (d)), select target joints and degrees of freedom, and place the sensors on an appropriate location and orientation (Figure 4.61 (e)). Specifically, as shown in Figure 4.61 (c), the four fingers are composed with the four bones respectively, including the distal, middle, proximal phalanges, and metacarpals, and the thumb consists of the distal and proximal phalanges, and metacarpals. The bones are interconnected through the joints such as the distal interphalangeal (DIP), proximal interphalangeal (PIP), and metacarpophalangeal (MCP)

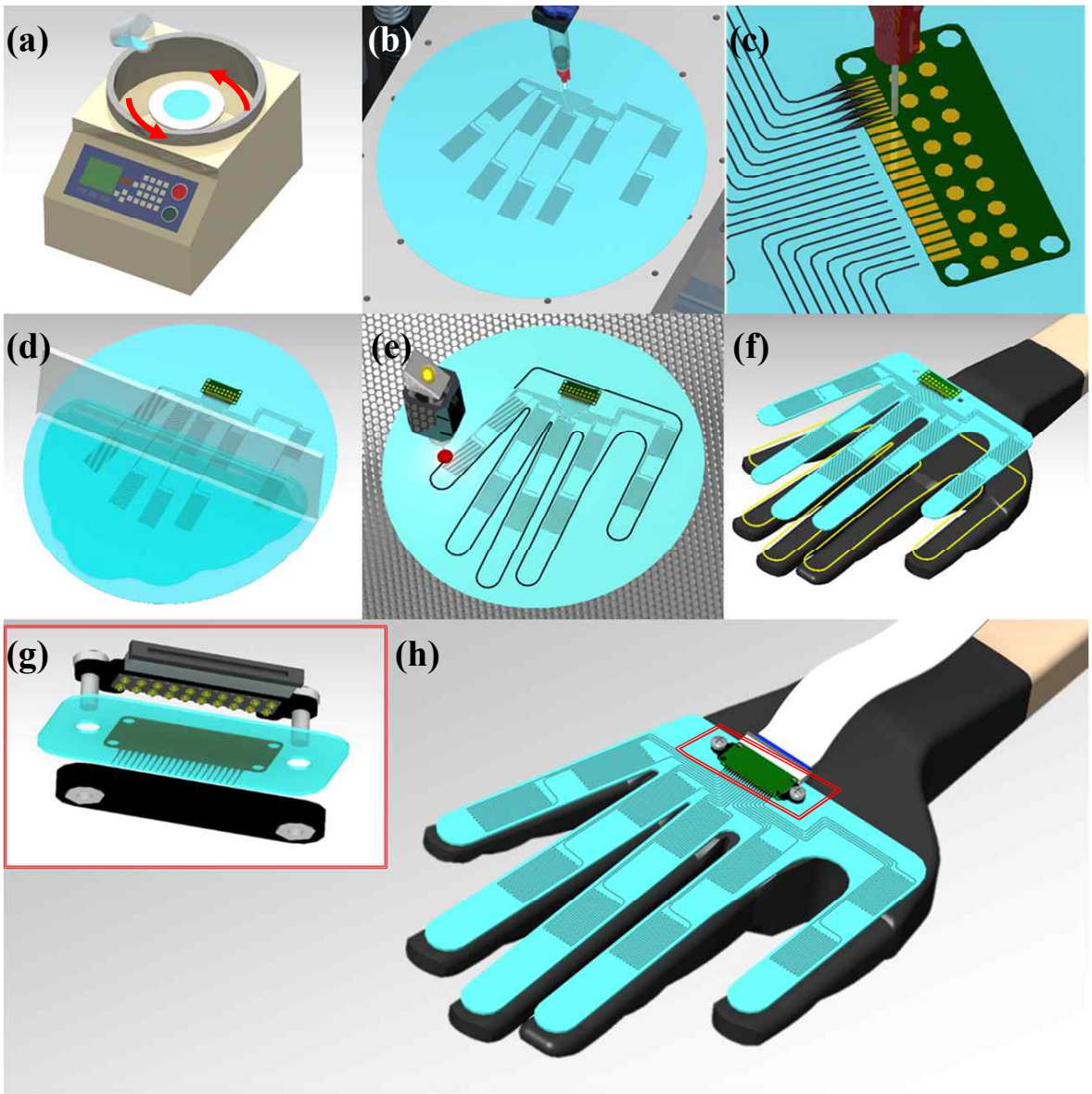

Figure 4.59: DIW-based fabrication for a soft sensing glove: (a) spin-coating, (b) DIW of eGaIn, (c) writing the electrode part, (d) silicone squeezing, (e) laser cutting, (f) bonding, (g) a completed sensing glove connected with a FFC with the contact connector module assembled.

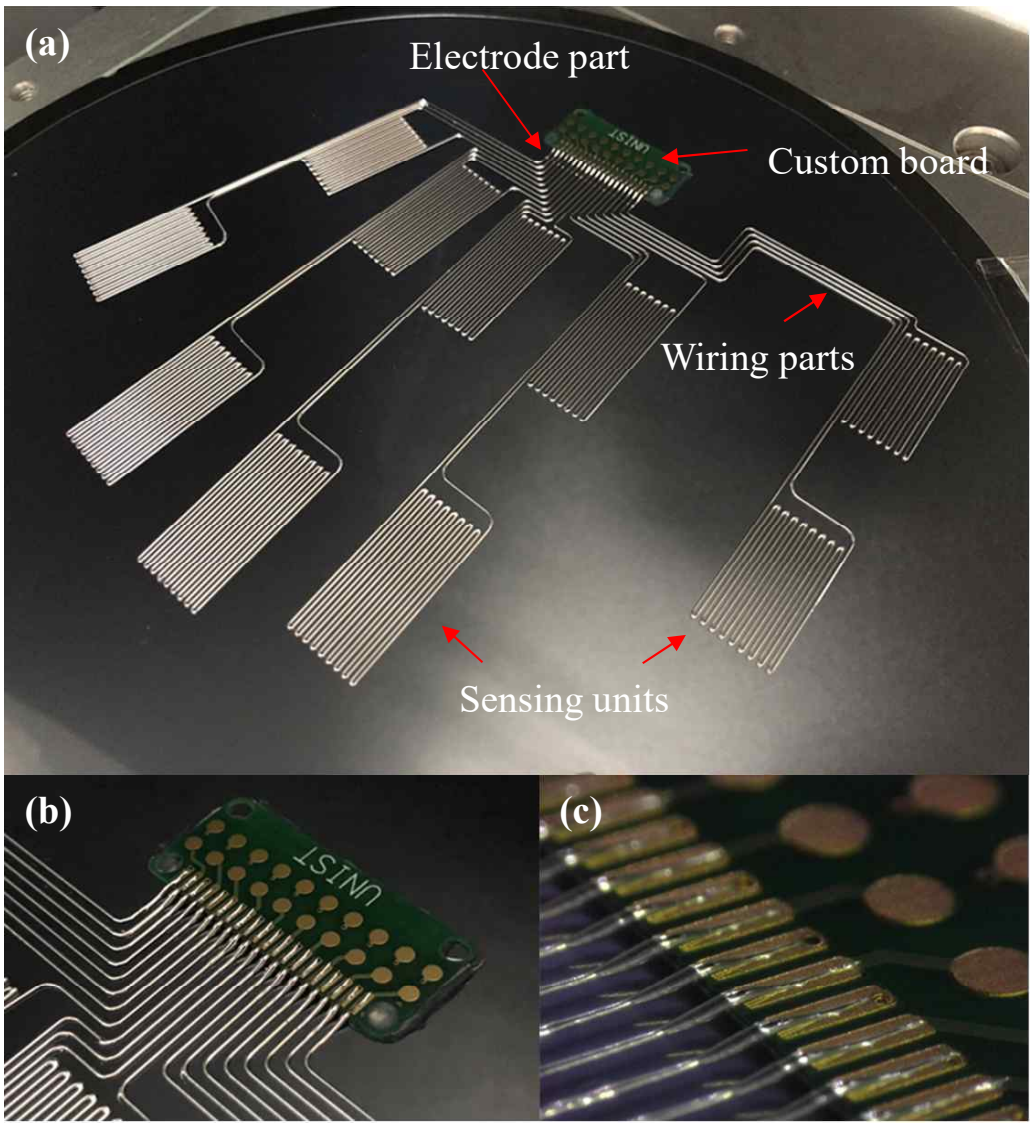

Figure 4.60: Direct writing of sensing gloves: (a) written traces of eGaIn for a sensing glove, (b) a detailed snapshot of the electrode part, (c) a microscope image of the electrode part.

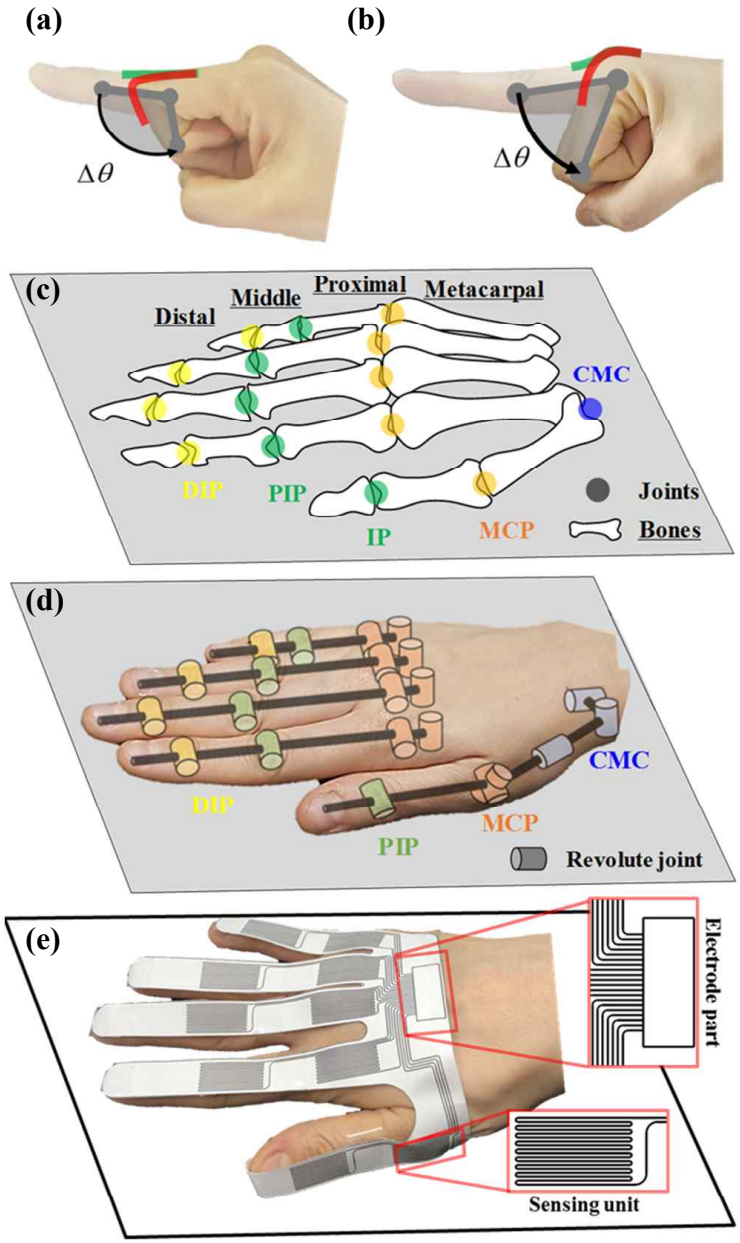

Figure 4.61: Design process of a sensing glove: (a) measuring FE of the PIP joint and (b) the MCP joint, (c) anatomical structure of the fingers, (d) kinematic model, and (e) design of a sensing glove for 2D finger motions.

Figure 4.62: A soft sensing glove: (a) soft sensing glove worn by a user, (b) rotary potentiometer attached on the lateral surface of the MCP joint.

joints for the four fingers, and the interphalangeal (IP) and metacarpophalangeal (MCP), and carpometacarpal (CMC) joints for the thumb.

4.5.4 Performance Verification of a Soft Sensing Glove

Figure 4.62 (a) shows the developed soft sensing glove worn by a user with a FFC connected. The sensing glove can be worn and removed within 15 seconds, providing the same feeling of a fabric glove. To verify performance of the soft sensing units, a rotary potentiometer was placed on a target joint with rigid links attached on each phalanx (Figure 4.62 (b)). In this experiment, the MCP and PIP joints of the index fingers were selected, which can be easily accessed through the lateral surface of the hand. The experimental results are shown in Figure 4.63.

Relationships between the joint angles estimated by the rotary potentiometer and sensor

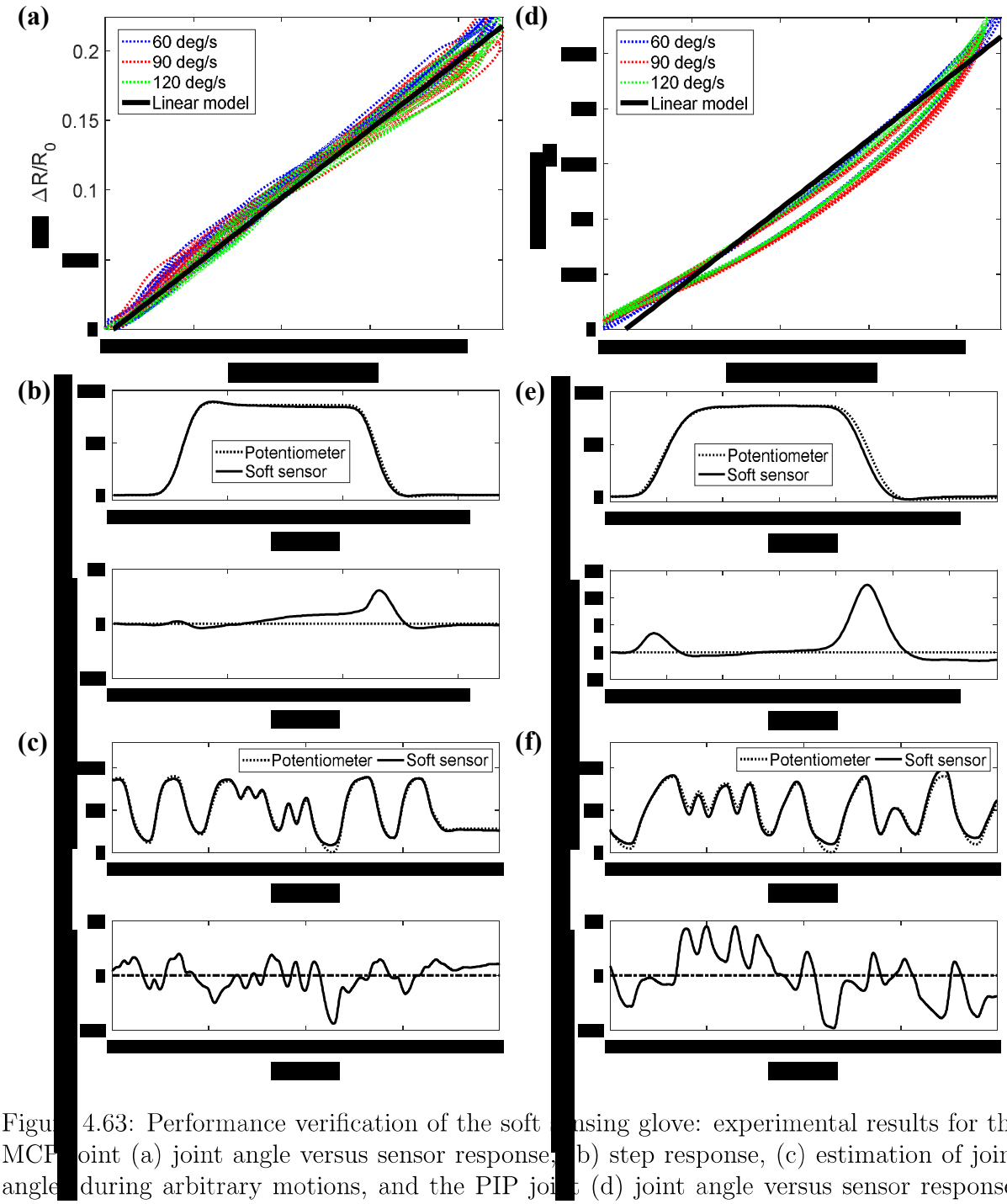

Figure 4.63: Performance verification of the soft sensing glove: experimental results for the MCP joint (a) joint angle versus sensor response, (b) step response, (c) estimation of joint angles during arbitrary motions, and the PIP joint (d) joint angle versus sensor response, (e) step response, (f) estimation of joint angles during arbitrary motions.

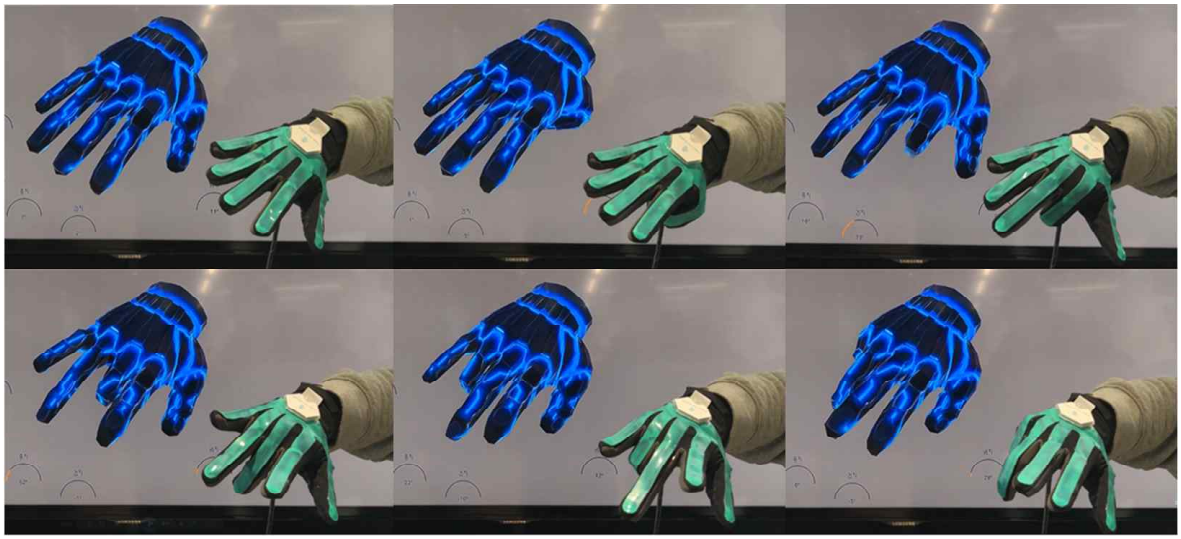

Figure 4.64: The soft sensing glove and synchronized animation.

signal were acquired with different angular speeds, 60 deg/s, 90 deg/s and 120 deg/s (Figure 4.63 (a), (d)). As shown in the results, the sensor response hardly varied with loading speeds. Slight hysteresis was observed in the both joints, which was attributed to viscoelastic property of the silicone material and fabric. The R^2 values of each linear model were 0.985 and 0.982 for the MCP and PIP joints, respectively.

To test step and relaxation of the sensor, the subjects were instructed to flex and extend their finger as fast as possible. The experimental results are presented in Figure 4.63 (b), (e). In the previous reports, severe time-dependent responses were occasionally observed in soft sensors [130, 113]. Using the highly homogeneous, conductive, and flowable EGaIn, the sensor signals were settled in 0.4 s for both step and relaxation interval, without a time-dependent response. Thus, it can be claimed that the suggested sensor system is appropriate to measure dynamic motions of the fingers.

The arbitrary finger motions were estimated by soft sensors and compared with the joint angles measured by the potentiometer (Figure 4.63 (c), (f)). As shown in the results, the errors were within ± 5 deg and ± 10 deg and the root-mean-square errors were 4 deg and 2.5 deg for the MCP and PIP joints, respectively. The captured finger motions can be simultaneously reconstructed by the 3D animation (Figure 4.64) using a gaming interface (Unity [178]). Verified in the experiments, the soft sensors successfully estimated both static and dynamic motions of the fingers.

Figure 4.65: Prototype of a soft sensor system with sensor locations engraved by laser.

4.5.5 Application to Measurement of 3D Finger Motions

In this work, a glove-type soft sensor system is developed based on the direct writing technique to measure 3D finger motions, similar with the work introduced in the previous sections using mold-based fabrication-based soft sensors. Based on the DIW-based fabrication technique, a sensor system can be manufactured in one piece, without assembling multiple sensing units. First, the locations of the sensing units were determined based on the prototyping process, because the sensor locations varied after the sensor system was worn by a user due to pretension of the system. Rather than fabricating the actual sensor system, the locations of the sensing units were engraved on the silicone sheet to examine a given design, as shown in Figure 4.65. Repeating prototyping, the sensor locations were modified 50 times in total as shown in Figure 4.66.

To ensure performance of the sensor system, the both ends of the sensor should be firmly fixed on the fingers. Thus, it is important to design the wearing parts, and we considered three options (Figure 4.67). The first option was attaching the sensor sheet onto the dorsal side of the hand using medical tapes (Figure 4.67 (a)). The location of the sensors can be

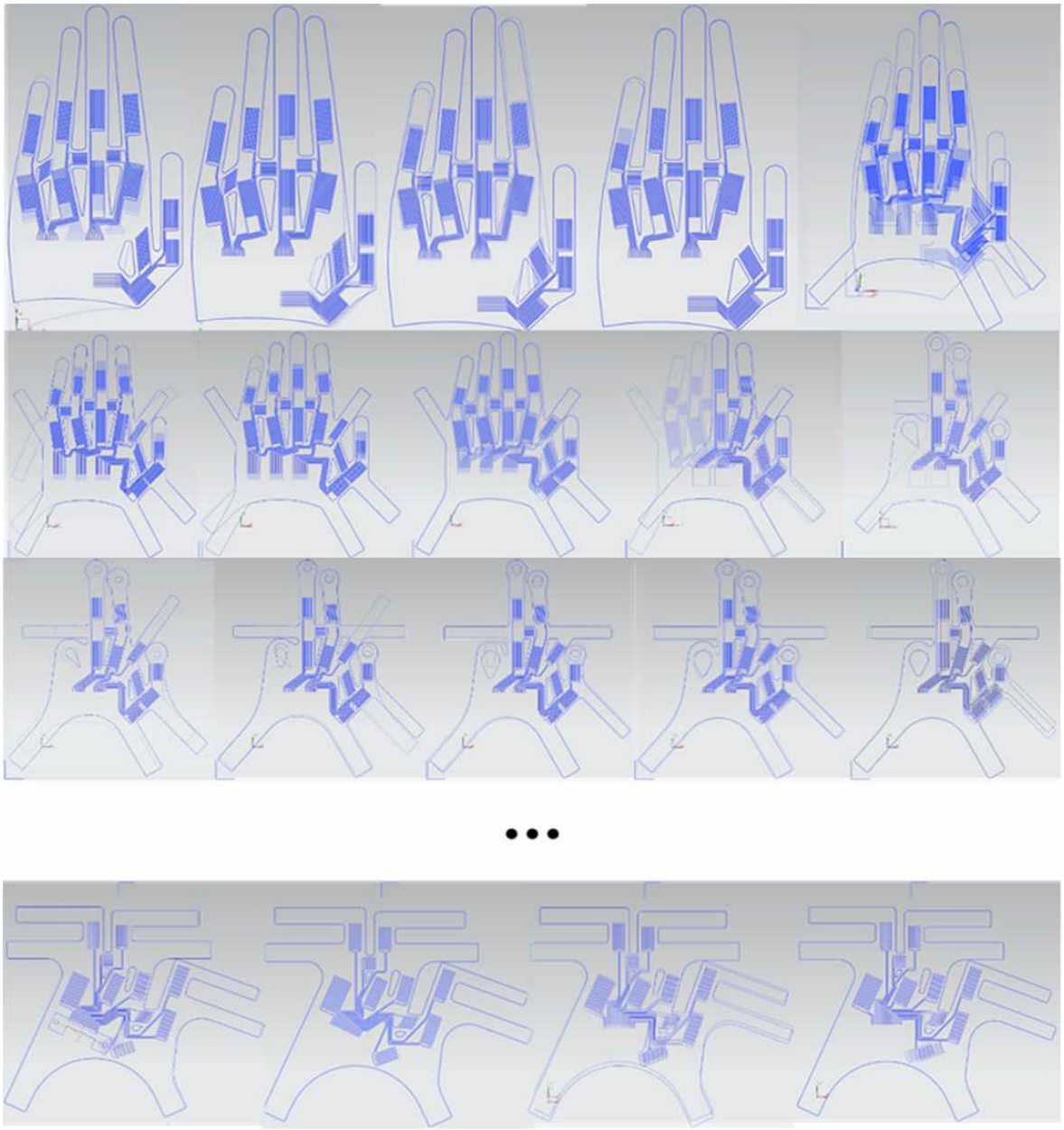

Figure 4.66: Modification of sensor locations for a soft sensing glove for 3D finger motions.

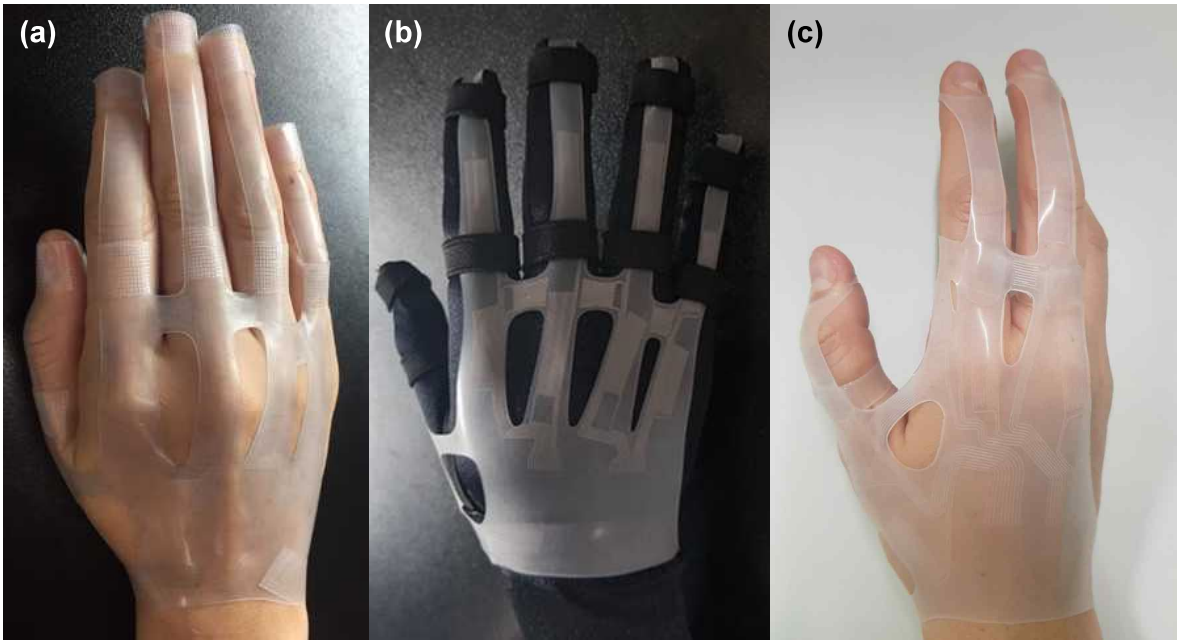

Figure 4.67: Different wearing methods of the soft sensing glove: (a) attaching directly onto the skin using medical tapes, (b) a glove with rubber ring, and (c) silicone ring.

modified easily, but the process is time-consuming and the users cannot wear it themselves. The second option was inserting the soft sensor sheet through rubber rings attached to a fabric glove (Figure 4.67 (b)). Using the glove, the user can wear the system more easily, but the rubber ring pressurizes the fingers, restricting natural range of motion. The last option was silicon rings extended from the sensor sheet (Figure 4.67 (c)). High stretchability and softness of the silicone material allows natural motion of the users. In addition, the sensors can be placed firmly as designed due to little slip between the sensor sheet and the skin. However, it was difficult to wear the system and the sensor sheet can be torn out easily during wearing it due to randomly applied shear stress. To prevent the random shear loads, the sensor sheet was bonded to a fabric glove as shown in Figure 4.68. The wearing method allows easy wearing by the user with the sensing units firmly fixed in place.

The 3D motion of the fingers (thumb, index, and middle fingers) were estimated by sensor signals and visualized as an animation as shown in Figure 4.69. For more delicate measurement, a more advanced decoupling strategy is required, because the proposed system generates crosstalk between the sensors due to its integrated structure.

Figure 4.68: Soft sensing gloves with different colors.

4.6 Summary

In this chapter, the mold-based manual fabrication method was implemented and discussed. Due to its inherent limitation, the DIW-based fabrication technique for eGaIn-based soft sensor was proposed and verified. First, the writing stability was discussed, considering critical factors influencing the writing process. After that, consistency of the microchannel was improve by selecting a non-metallic syringe. Based on the stable and consistent writing, the soft sensors were fabricated reproducibly. In addition, the electrical connection was also resolved by DIW-based technique without special chemical and mechanical treatment. To verify performance of the electrode part fabricated by the proposed method, various experiments were conducted such as reproducibility and time-dependent stability of the contact resistance, mechanical durability, and thermal durability. Based on the fabrication technique, various soft sensor systems were fabricated and tested.

The DIW-based fabrication process rarely requires the intervention of the skilled hands, because the important parts, such as the sensing units, wiring, and electrode parts, can be directly written by eGaIn using the automated equipment. That is, the suggested fabrication process is highly productive (with minimal intervention of the hand skills) and programmable (easy to modify the designs), and efficient (all the writing was done in 15 minutes, from printing the sensing units to connecting the electrode parts). Therefore, a system-level of eGaIn-based soft sensors can be easily and simply fabricated based on the proposed method, which will greatly widen the application of the soft sensors.

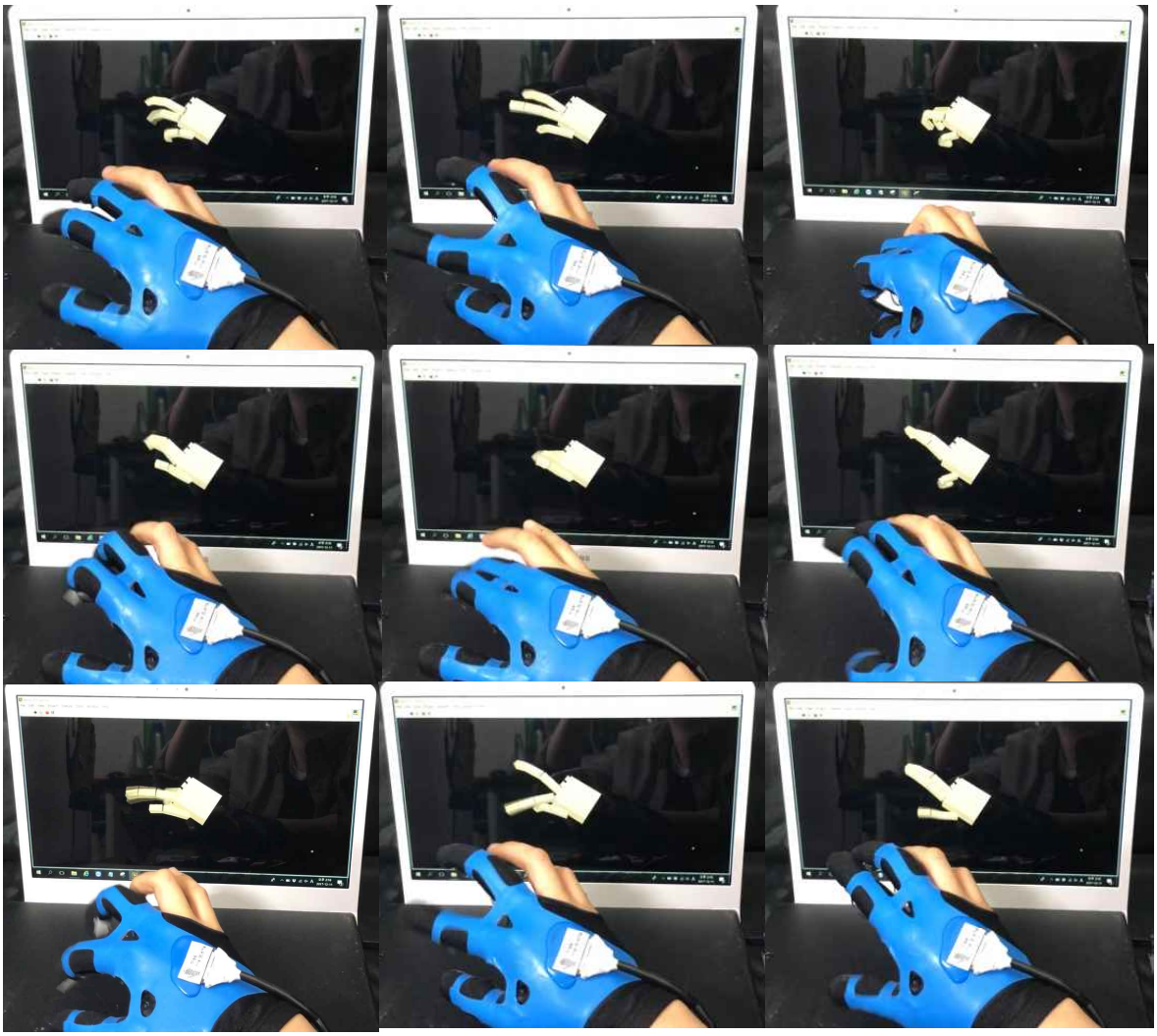

Figure 4.69: Measurement of 3D finger motions using a soft sensor system.

Chapter 5

Concluding Remarks and Open Issues

In this thesis, technological issues were discussed to implement wearable systems in a more practical manner in the transition from the rigid robotics to the soft robotics, including (1) development and implementation of a rigid exoskeleton, (2) estimation of muscular forces for motion intention, and (3) direct writing of liquid metal for soft sensors.

5.1 Concluding Remarks

5.1.1 Development and Implementation of a Rigid Exoskeleton

The wearable system for physical human-robot interaction has been implemented as a form of the exoskeleton. For the exoskeleton systems, it is important to control the interaction force accurately not to impede the user's motion and assist the user by providing proper assistance force in an appropriate timing. However, it is difficult to control the force accurately due to uncertain interaction with the user. In Chapter 2, a rigid exoskeleton was developed and implemented with the series elastic actuator module controlled by model-inverse time delay control (MiTDC) to deal with the challenge. The proposed controller successfully adjusted the output force from the actuator module in the presence of interactions with the user. Thus, the force-controllable system can be used as actuator modules for various applications requiring robust force-control performance in uncertain environment as well as physical human-robot interaction system.

5.1.2 Estimation of Muscular Forces for Determining a Desired Force Trajectory

By introducing a high level controller to determine desired force profile delivered to the user, the force-controllable platform proposed in Chapter 2 can be implemented as a gait assistance system. Because the muscular forces are the sources of the movements in the human body, human motion intention can be estimated by estimating the muscular forces. Thus, estimation of muscular forces were conducted by implementing the inverse dynamics-based static optimization in Chapter 3. The motion information required for the algorithm were measured by wearable systems. Using the wearable sensor system, the muscular forces in the lower extremity were estimated during walking. Using the hand exoskeleton system, the muscular forces in the fingers were estimated during extension of the fingers. The movement in each experiment was physically explainable based on the estimated muscular forces in each case. The combination of the wearable sensors and the estimation algorithm can be implemented as a mobile system for analyzing the muscular forces or a high level controller for the exoskeleton.

5.1.3 Direct Writing of Liquid Metal for Soft Sensors

By combining the exoskeleton platform developed in Chapter 2 and the estimation algorithm developed in Chapter 3, it is possible to develop an exoskeleton providing assistance for the human theoretically. However, it is doubtful that the system can be helpful for the user practically due to discomfort and heavy weight of the rigid robotic parts. To overcome such limitations, soft wearable system was considered in Chapter 4. For soft wearable systems, highly stretchable electrical path is necessary to maintain its function even under the extreme mechanical strain. Intuitively, the stretchable electrical path can be used as soft sensors, and the fabrication technique for liquid metal-based soft sensors were studied in Chapter 4. Direct ink writing (DIW) was a key technology to greatly improve fabrication of soft sensors, resolving the issues of productivity, programmability, reproducibility, and electrical connection. Based on the suggested fabrication technique, soft sensor systems can be manufactured in various configurations with high productivity. This technology can greatly widen the application of liquid metal-based soft sensors and stretchable electronics.

5.2 Open Issues

Various technological issues for wearable systems have been discussed in this thesis, but there still remains much room for developing the suggested technologies further. The open issues are as follows.

5.2.1 Application of the Force-controllable Platform

In Chapter 2, the series elastic actuator modules under MiTDC realized force-mode control in a robust manner. As future work, based on the accurate force control platform, a high-level decision making algorithm can be developed and implemented to realize a highly functional interactive control in wearable robots. In addition, by modifying the actuator modules, the proposed platform can be implemented to various mechatronic systems, such as robot arms.

5.2.2 Extension of the Muscle Force Estimation Algorithm for 3D Motions

In Chapter 3, the muscular forces were estimated based on biomechanics algorithm. In this investigation, only two dimensional movements in the sagittal plane were considered in both the lower extremity and the fingers, because the muscular forces in the sagittal plane are usually larger than that in the other planes. However, movements in the frontal and transverse plane should be considered also to express more complicated motions in the human body, introducing additional factors and constraints in the algorithm.

5.2.3 Fusion of the Exoskeleton and the Muscle Force Estimation Algorithm

The force-mode controller developed in Chapter 2 can be combined with the estimation algorithm in Chapter 3 as a low level and a high level controller, respectively. Based on the estimated muscular forces, assistance force required at the moment can be transmitted to the force-mode controller, which delivers the force to the users. To verify the efficacy of the combined control system, further investigations are required to monitor variation in fatigue of the muscles or metabolic cost while the user is walking with and without assistance of the exoskeleton.

5.2.4 Development of a Full Body Motion Capture System based on Soft Sensors

Based on the fabrication process discussed in Chapter 4, various types of soft sensor systems can be fabricated. In this thesis, only the glove-type sensor system were fabricated and tested, but the soft sensor system can be fabricated for diverse body parts, such as the wrist, shoulder, leg, and etc. Thus, a full body motion capture system can be developed, attaching the soft sensors to the body parts and analyzing the sensor signals in future study.

5.2.5 Full Automation of Soft Sensor Fabrication

In Chapter 4, direct ink writing-based fabrication for soft sensors were suggested as a series of multiple steps: 1) spin coating, 2) direct writing of eGaIn, 3) blade coating, and 4) cutting. In future work, the fabrication steps can be fully automated by replacing the fabrication steps with the following steps: 1) silicone printing (first silicone layer), 2) pick and place for attaching the electrode (e.g. FFC), 3) direct writing of eGaIn, and 4) silicone printing (second silicone layer). To implement this automated fabrication system, development of a silicone printing technique is required to reduce the thickness of the printed layer and ensure the flatness of it. In addition, a customized equipment is required with a software to operate the system.

5.2.6 Application of Liquid Metal-based Conductive Pathes

Microchannels with various forms filled with eGaIn can be built inside an elastomeric body based on the fabrication technique proposed in Chapter 4. Therefore, in future study, the conductive channel can be employed in a variety of applications, such as lab on a chip, stretchable heater, and stretchable circuit, as well as soft sensors.

Bibliography

[1] S. L. *Delp, A. E. Grierson, and T. S. Buchanan. "Maximum isometric moments generated by the wrist muscles in flexion-extension and radial-ulnar deviation". In: *Journal of biomechanics* 29 (1996), pp. 1371–1375.

[2] O. Amft *et al.* "Sensing muscle activities with body-worn sensors". In: *International Workshop on Wearable and Implantable Body Sensor Networks*. 2006, pp. 4–141.

[3] M. Amjadi *et al.* "Stretchable, skin-mountable, and wearable strain sensors and their potential applications a review". In: *Advanced Functional Materials* 26 (11 2016), pp. 1678–1698.

[4] K. N. An *et al.* "Normative model of human hand for biomechanical analysis." In: *Journal of biomechanics* 12 (1979), pp. 775–788.

[5] E.M. Arnold *et al.* "A model of the lower limb for analysis of human movement". In: *Annals of biomedical engineering* 38 (2010), pp. 269–279.

[6] A.T. Asbeck *et al.* "Biologically-inspired soft exosuit". In: *Proc. of 2013 IEEE international conference on Rehabilitation robotics (ICORR)*. 2013, pp. 1–8.

[7] ATI Industrial Automation. *Nano 17 F/T sensor*. 2017. URL: `http://www.ati-ia.com/products/ft/ft_models.aspx?id=Nano17`.

[8] J. Bae, K. Kong, and M. Tomizuka. "Real-time estimation of lower extremity joint torques in normal gait". In: *Robot Control* 9 (2009), pp. 443–448.

[9] J. Bae, K. Kong, and M. Tomizukma. "A Gait Rehabilitation Strategy Inspired by an Iterative Learning Algorithm." In: *Mechatronics* 22 (2 2012), pp. 213–221.

[10] J. Bae, K. Kong, and M. Tomizukma. "Gait Phase-Based Control for a Rotary Series Elastic Actuator Assisting the Knee Joint". In: *ASME Journal of Medical Devices* 5 (3 2011), pp. 031010–031015.

[11] J. Bae and M. Tomizuka. "A tele-monitoring system for gait rehabilitation with an inertial measurement unit and a shoe-type ground reaction force sensor". In: *Mechatronics* 23 (2013), pp. 646–651.

[12] J. Bae *et al.* "A mobile gait monitoring system for abnormal gait diagnosis and rehabilitation: A pilot study for parkinson disease patients". In: *Journal of biomechanical engineering* 133 (2011), p. 041005.

[13] J.C. Bean, D.B. Chaffin, and A.B. Schultz. "Biomechanical model calculation of muscle contraction forces: A double linear programming method". In: *Journal of biomechanics* 21 (1988), pp. 59–66.

[14] Bersoft. *Image Measurement 8.49*. 2017. URL: `http://bersoft.com/bimagem/index.htm`.

[15] Bitplane. *Imaris 9*. 2017. URL: `http://www.bitplane.com/newrelease`.

[16] J. W. Boley *et al.* "Direct writing of gallium indium alloy for stretchable electronics". In: *Advanced Functional Materials* 24 (23 2014), pp. 3501–3507.

[17] J. W. Boley *et al.* "Direct writing of gallium-indium alloy for stretchable electronics". In: *Advanced Functional Materials* 24 (23 2014), pp. 3501–3507.

[18] Y. Bouteraa and I. B. Abdallah. "Exoskeleton robots for upper-limb rehabilitation". In: *13th International Multi-Conference on Systems, Signals & Devices (SSD)*. 2016, pp. 1–6.

[19] R.A. Brand *et al.* "A model of lower extremity muscular anatomy". In: *Journal of biomechanical engineering* 104 (1982), pp. 304–310.

[20] B. Bresler and J. Frankel. "The forces and moments in the leg during level walking". In: *Trans. Asme* 72 (1950), pp. 25–35.

[21] N. Brook *et al.* "A biomechanical model of index finger dynamics". In: *Medical engineering & physics* 17 (1995), pp. 54–63.

[22] S.H. Brown and J.R. Potvin. "Constraining spine stability levels in an optimization model leads to the prediction of trunk muscle cocontraction and improved spine compression force estimates". In: *Journal of biomechanics* 38 (2005), pp. 745–754.

[23] A. Cappozzo, T. Leo, and A. Pedotti. "A general computing method for the analysis of human locomotion". In: *Journal of Biomechanics* 8 (1975), pp. 307–320.

[24] C. R. Carignan and K. R. Cleary. "Closed-loop force control for haptic simulation of virtual environments." In: *Haptics-e: The Electronic Journal of Haptics Research* 1 (2 2000), pp. 1–14.

[25] C. Carignan, J. Tang, and S. Roderick. "Development of an exoskeleton haptic interface for virtual task training". In: *2009 IEEE/RSJ International Conference on Intelligent Robots and Systems*. 2009, pp. 3697–3702.

[26] Pyung H. Chang and Jeong W Lee. "An observer design for time-delay control and its application to dc servo motor". In: *American Control Conference*. 1993, pp. 1032–1036.

[27] E. Y. Chao and K. N. An. "Graphical interpretation of the solution to the redundant problem in biomechanics". In: *Journal of Biomechanical Engineering* 100 (1978), pp. 159–167.

[28] R. C. Chiechi *et al.* "Eutectic Gallium-Indium (EGaIn): A Moldable Liquid Metal for Electrical Characterization of Self-Assembled Monolayers". In: *Angewandte Chemie* 120 (1 2008), pp. 148–150.

[29] J. B. Chossat *et al.* "A soft strain sensor based on ionic and metal liquids". In: *IEEE Sensors Journal* 13 (9 2013), pp. 3405–3414.

[30] J. B. Chossat *et al.* "Wearable soft artificial skin for hand motion detection with embedded microfluidic strain sensing". In: *In 2015 IEEE International Conference on Robotics and Automation (ICRA)*. 2015, pp. 2568–2573.

[31] P. J. Codd *et al.* "Novel pressure-sensing skin for detecting impending tissue damage during neuroendoscopy: Laboratory investigation". In: *Journal of Neurosurgery: Pediatrics* 13 (1 2014), pp. 114–121.

[32] J. Collins. "The redundant nature of locomotor optimization laws". In: *Journal of biomechanics* 28 (1995), pp. 251–267.

[33] J. Collins. "The redundant nature of locomotor optimization laws". In: *Journal of Biomechanics* 28 (1995), pp. 251–267.

[34] G. Colombo *et al.* "Treadmill training of paraplegic patients using a robotic orthosis". In: *Journal of rehabilitation research and development* 37 (6 2000), pp. 693–700.

[35] L. Columbus. *Roundup of internet of things forecasts and market estimates*. Forbes, 2015, p. 27.

[36] N.J. Cronin and G. Lichtwark. "The use of ultrasound to study muscle-tendon function in human posture and locomotion". In: *Gait & posture* 37 (2013), pp. 305–312.

[37] R.D. Crowninshield and R.A. Brand. "A physiologically based criterion of muscle force prediction in locomotion". In: *Journal of biomechanics* 14 (1981), pp. 793–801.

[38] R. Crowninshield *et al.* "A biomechanical investigation of the human hip". In: *Journal of biomechanics* 11 (1978), pp. 75–85.

[39] C.J. De Luca. "The use of surface electromyography in biomechanics". In: *Journal of applied biomechanics* 13 (1997), pp. 135–163.

[40] S.L. Delp *et al.* "Opensim: Open-source software to create and analyze dynamic simulations of movement". In: *IEEE Transactions on Biomedical Engineering* 54 (2007), pp. 1940–1950.

[41] Dempster. *Patterns of Human Motion.* Prentice-Hall, Inc., 1971.

[42] Dempster, Miller, and Nelson. *Biomechanics of Sprots.* Lea and Febiger, 1973.

[43] M. D. Dickey. "Stretchable and soft electronics using liquid metals". In: *Advanced Materials* 29 (27 2017), p. 1606425.

[44] M. D. Dickey *et al.* "Eutectic gallium-indium (EGaIn): a liquid metal alloy for the formation of stable structures in microchannels at room temperature". In: *Advanced Functional Materials* 18 (7 2008), pp. 1097–1104.

[45] Y. Ding *et al.* "IMU-based iterative control for hip extension assistance with a soft exosuit". In: *Proc. of 2016 IEEE International Conference on Robotics and Automation (ICRA).* 2016, pp. 3501–3508.

[46] Dino-Lite. *AD4113TL-MA1.* 2017. URL: `http://www.dino-lite.com/products_detail.php?index_m1_id=0&index_m2_id=0&index_id=91`.

[47] C Dodd. "The electrical resistance of liquid gallium in the neighbourhood of its melting point". In: *Proceedings of the Physical Society. Section B.* Vol. 63. 1950, p. 662.

[48] Dong Ah Trade Corp. *TOP-8.* 2017. URL: `http://www.spincoater.net/eng/spincoater/spincoater.php?str_gubun=2&int_gubun=2&str_no=2`.

[49] K. Doudrick *et al.* "Different shades of oxide: From nanoscale wetting mechanisms to contact printing of gallium-based liquid metals". In: *Langmuir* 30 (23 2018), pp. 6867–6877.

[50] S. van Drongelen *et al.* "Glenohumeral contact forces and muscle forces evaluated in wheelchair-related activities of daily living in able-bodied subjects versus subjects with paraplegia and tetraplegia". In: *Archives of physical medicine and rehabilitation* 86 (2005), pp. 1434–1440.

[51] H.D. Eberhart, V.T. Inman, and B. Bresler. *Human limbs and their substitutes*. Hafner Pub. Co., 1954.

[52] A. Fassler and C. Majidi. "3D structures of liquid-phase GaIn alloy embedded in PDMS with freeze casting". In: *Lab on a Chip* 13 (22 2013), pp. 4442–4450.

[53] FLIR. *FLIR C-Series*. 2018. URL: `http://ww4.flir.com/instruments/c-series/`.

[54] J. A. Galvez *et al.* "Measuring human trainers' skill for the design of better robot control algorithms for gait training after spinal cord injury". In: *9th International Conference on Rehabilitation Robotics*. 2005, pp. 231–234.

[55] Y. Gao, H. Li, and J. Liu. "Direct writing of flexible electronics through room temperature liquid metal ink". In: *PLoS One* 7 (9 2012), e45485.

[56] U. Glitsch and W. Baumann. "The three-dimensional determination of internal loads in the lower extremity". In: *Journal of biomechanics* 30 (1997), pp. 1123–1131.

[57] R. V. Gonzalez, T. S. Buchanan, and S. L. Delp. "How muscle architecture and moment arms affect wrist flexion-extension moments". In: *Journal of biomechanics* 30 (1997), pp. 705–712.

[58] B. A. Gozen *et al.* "High-Density Soft-Matter Electronics with Micron?Scale Line Width". In: *Advanced materials* 26 (30 2014), pp. 5211–5216.

[59] A. Gupta *et al.* "Design, control and performance of RiceWrist: A force feedback wrist exoskeleton for rehabilitation and training". In: *The International Journal of Robotics Research* 27 (2 2008), pp. 223–251.

[60] F. L. Hammond, Y. Menguc, and R. J. Wood. "Toward a modular soft sensor-embedded glove for human hand motion and tactile pressure measurement". In: *In 2014 IEEE/RSJ International Conference on Intelligent Robots and Systems (IROS 2014)*. 2014, pp. 4000–4007.

[61] F. L. Hammond *et al.* "Soft tactile sensor arrays for force feedback in micromanipulation". In: *IEEE Sensors Journal* 14 (5 2014), pp. 1443–1452.

[62] F. L. Hammond *et al.* "Soft tactile sensor arrays for micromanipulation". In: *In Proceedings of IEEE/RSJ International Conference on Intelligent Robots and Systems (IROS)*. 2012, pp. 25–32.

[63] T. C. Hara and L. S. Gao. "Robot manipulator control using decentralized time invariant time-delayed controller". In: *Proc. of IEEE Int. Conf. on Robotics and Automation*. 1990, pp. 2070–2075.

[64] S. Heintz. *Muscular forces from static optimization*. 2006.

[65] Herr, H.M. and Kornbluh, R.D. "In New horizons for orthotic and prosthetic technology: Artificial muscle for ambulation". In: *Smart structures and materials* (2004), pp. 1–9.

[66] S. Hiremath, G. Yang, and K Mankodiya. "Wearable Internet of Things: Concept, architectural components and promises for person-centered healthcare". In: *In EAI 4th International Conference on Wireless Mobile Communication and Healthcare*. 2014, pp. 304–307.

[67] K. R. Holzbaur, W. M. Murray, and S. L. Delp. "A model of the upper extremity for simulating musculoskeletal surgery and analyzing neuromuscular control". In: *Annals of biomedical engineering,* 33 (2005), pp. 829–840.

[68] M.G. Hoy, F.E. Zajac, and M.E. Gordon. "A musculoskeletal model of the human lower extremity: The effect of muscle, tendon, and moment arm on the moment-angle relationship of musculotendon actuators at the hip, knee, and ankle". In: *Journal of biomechanics* 23 (1990), pp. 157–169.

[69] TC Steve Hsia. "A new technique for robust control of servo systems". In: *IEEE Transactions on Industrial Electronics* 36 (1989), pp. 1–7.

[70] R. E. Hughes, M. G. Rock, and K. N. An. "Identification of optimal strategies for increasing whole arm strength using karush-kuhn-tucker multipliers". In: *Clinical Biomechanics* 14 (1999), pp. 628–634.

[71] R.E. Hughes *et al.* "Evaluation of muscle force prediction models of the lumbar trunk using surface electromyography". In: *Journal of Orthopaedic Research* 12 (1994), pp. 689–698.

[72] F. Ilievski *et al.* "Soft robotics for chemists". In: *Angewandte Chemie* 123 (8 2011), pp. 1930–1935.

[73] H. In *et al.* "Exo-Glove: a wearable robot for the hand with a soft tendon routing system". In: *IEEE Robotics & Automation Magazine* 22 (1 2015), pp. 97–105.

[74] J. N. Israelachvili. *Intermolecular and surface forces*. Academic press, 2011.

[75] M. D. Jacobson *et al.* "Architectural design of the human intrinsic hand muscles". In: *The Journal of Hand Surgery* 17 (1992), pp. 804–809.

[76] S.P. Jenkins. *Sports science handbook*. Sunningdale Publications, 2001.

[77] S. Jezernik *et al.* "Robotic orthosis lokomat: A rehabilitation and research tool". In: *Neuromodulation: Technology at the neural interface* 6 (2003), pp. 108–115.

[78] R. Jimenez-Fabian and O. Verlinden. "Review of control algorithms for robotic ankle systems in lower-limb orthoses, prostheses, and exoskeletons". In: *Medical engineering & physics* 34 (2012), pp. 397–408.

[79] Y. Jung and J. Bae. "Kinematic analysis of a 5-dof upper-limb exoskeleton with a tilted and vertically translating shoulder joint". In: *IEEE/ASME transactions on mechatronics* 20 (3 2015), pp. 1428–1439.

[80] H. Kazerooni. "Exoskeletons for human power augmentation". In: *IEEE/RSJ International Conference on Intelligent Robots and Systems (IROS)*. 2005, pp. 3459–3464.

[81] H. Kazerooni *et al.* "On the control of the berkeley lower extremity exoskeleton (BLEEX)". In: *Proceedings of the 2005 IEEE International Conference on Robotics and Automation*. 2005, pp. 4353–4360.

[82] L. D. Ketchum *et al.* "A clinical study of forces generated by the intrinsic muscles of the index finger and the extrinsic flexor and extensor muscles of the hand". In: *The Journal of Hand Surgery* 3 (1978), pp. 571–578.

[83] M. R. Khan, C. Trlica, and M. D. Dickey. "Recapillarity: electrochemically controlled capillary withdrawal of a liquid metal alloy from microchannels". In: *Advanced Functional Materials* 25 (5 2015), pp. 671–678.

[84] M. A. H. Khondoker and D. Sameoto. "Fabrication methods and applications of microstructured gallium based liquid metal alloys". In: *Smart Materials and Structures* 25 (9 2016), p. 093001.

[85] K. Kiguchi and Y. Hayashi. "An EMG-based control for an upper-limb power-assist exoskeleton robot". In: *IEEE Transactions on Systems, Man, and Cybernetics, Part B (Cybernetics)* 42 (2012), pp. 1061–1071.

[86] B. Kim *et al.* "Interfacing liquid metals with stretchable metal conductors". In: *ACS applied materials & interfaces* 7 (15 2015), pp. 7920–7926.

[87] D. H. Kim and J. A. Rogers. "Stretchable electronics: materials strategies and devices". In: *Advanced Materials* 20 (24 2014), pp. 4887–4892.

[88] S. Kim and J. Bae. "Development of a lower extremity exoskeleton system for human-robot interaction". In: *International Conference on Ubiquitous Robots and Ambient Intelligence (URAI)*. 2014, pp. 132–135.

[89] S. Kim and J. Bae. "Force-Mode Control of Rotary Series Elastic Actuators in a Lower Extremity Exoskeleton Using Model-Inverse Time Delay Control". In: *IEEE/ASME Transactions on Mechatronics* 22 (3 2017), pp. 1392–1400.

[90] S. Kim, J. Lee, and J. Bae. "Analysis of Finger Muscular Forces using a Wearable Hand Exoskeleton System". In: *Journal of Bionic Engineering* 14 (4 2017), pp. 680–691.

[91] S. Kim, K. Ro, and J. Bae. "Estimation of individual muscular forces of the lower limb during walking using a wearable sensor system". In: *Journal of Sensors* (2017).

[92] S. Kim *et al.* "A Novel All-In-One Manufacturing Process for a Soft Sensor System and Its Application to a Soft Sensing Glove". In: *In Proceedings of IEEE/RSJ International Conference on Intelligent Robots and Systems (IROS)*. 2018, pp. 7004–7009.

[93] S. Kim *et al.* "Consistent and Reproducible Direct Ink Writing of Eutectic Gallium-Indium for High-Quality Soft Sensors". In: *Soft Robotics* (2018).

[94] T. Kim and Y.-L. Park. "A soft 3-axis load cell using liquid-filled 3-D microchannels in a highly deformable elastomer". In: *IEEE Robot. Autom. Lett.* 3 (2 2018), pp. 881–887.

[95] Kistler. *Multicomponent force plate*. 2017. URL: `https://www.kistler.com/?type=669&fid=60693&model=document&callee=frontend`.

[96] K. Kong, J. Bae, and M. Tomizuka. "A compact rotary series elastic actuator for human assistive systems". In: *IEEE/ASME Transactions on Mechatronics* 17 (2012), pp. 288–297.

[97] K. Kong, J. Bae, and M. Tomizuka. "Control of rotary series elastic actuator for ideal force-mode actuation in human-robot interaction applications". In: *IEEE/ASME Transactions on Mechatronics* 14 (2009), pp. 105–118.

[98] K. Kong and M. Tomizuka. "Sensor-embedded shoes based gait monitoring system for rehabilitation". In: *IEEE/ASME Trans. Mechatron* 14 (2009), pp. 358–370.

[99] W. Kong, V. Goel, and L. Gilbertson. "Prediction of biomechanical parameters in the lumbar spine during static sagittal plane lifting". In: *Journal of biomechanical engineering* 120 (1998), pp. 273–280.

[100] R. K. Kramer, C. Majidi, and R. J. Wood. "Wearable tactile keypad with stretchable artificial skin". In: *In IEEE International Conference on Robotics and Automation (ICRA)*. 2011, pp. 1103–1107.

[101] R. K. Kramer *et al.* "Effect of microtextured surface topography on the wetting behavior of eutectic gallium?indium alloys". In: *Langmuir* 30 (2 2014), pp. 533–539.

[102] C. Ladd *et al.* "3D printing of free standing liquid metal microstructures". In: *Advanced Materials* 25 (36 2013), pp. 5081–5085.

[103] J. Lee and J. Bae. "Design of a hand exoskeleton for biomechanical analysis of the stroke hand". In: *IEEE International Conference on Rehabilitation Robotics(ICORR)*. 2015, pp. 484–489.

[104] B. Li *et al.* "Assemblies of Microfluidic Channels and Micropillars Facilitate Sensitive and Compliant Tactile Sensing". In: *IEEE Sensors Journal* 16 (24 2016), pp. 8908–8915.

[105] B. Li *et al.* "Soft capacitive tactile sensing arrays fabricated via direct filament casting". In: *Smart Materials and Structures* 25 (7 2016), p. 075009.

[106] G. Li, X. Wu, and D. W. Lee. "Selectively plated stretchable liquid metal wires for transparent electronics". In: *Sensors and Actuators B: Chemical* 221 (2015), pp. 1114–1119.

[107] G. Li *et al.* "Wearable gait analysis system for ambulatory measurement of kinematics and kinetics". In: *Sensors* (2014), pp. 1316–1319.

[108] H.-T. Lin *et al.* "Muscle forces analysis in the shoulder mechanism during wheelchair propulsion". In: *Journal of Engineering in Medicine* 218 (2004), pp. 213–221.

[109] T. Liu, P. Sen, and C. J. Kim. "Characterization of nontoxic liquid-metal alloy galinstan for applications in microdevices". In: *Journal of Microelectromechanical Systems* 21 (2 2012), pp. 443–450.

[110] S. D. Loren G. J.and Shoemaker *et al.* "Human wrist motors: biomechanical design and application to tendon transfers". In: *Journal of biomechanics* 29 (1996), pp. 331–342.

[111] N. Lu and D. H. Kim. "Flexible and stretchable electronics paving the way for soft robotics". In: *Soft Robotics* 1 (1 2014), pp. 53–62.

[112] Z. P. Luo, L. J. Berglund, and K. N. An. "Validation of F-Scan pressure sensor system: a technical note". In: *Journal of rehabilitation research and development* 35 (1998), p. 186.

[113] C. Majidi, R. Kramer, and R. J. Wood. "A non-differential elastomer curvature sensor for softer-than-skin electronics". In: *Smart Materials and Structures* 20 (10 2011), p. 105017.

[114] F. J. Massey. "The Kolmogorov-Smirnov Test for Goodness of Fit". In: *Journal of the American Statistical Association* 46 (253 1951), pp. 68–78.

[115] R. Maughan, J. Watson, and J. Weir. "Strength and cross-sectional area of human skeletal muscle". In: *The Journal of physiology* 338 (1983), pp. 37–49.

[116] Maxon Motor. *Maxon Motor*. 2016. URL: `http://www.maxonmotor.com`.

[117] Y. Menguc *et al.* "Wearable soft sensing suit for human gait measurement". In: *The International Journal of Robotics Research* 33 (14 2014), pp. 1748–1764.

[118] Motion analysis corp. *Kestrel digital realtime system*. 2017. URL: `http://www.motionanalysis.com/html/movement/kestrel.html`.

[119] J. T. Muth *et al.* "Embedded 3D printing of strain sensors within highly stretchable elastomers". In: *Advanced Materials* 26 (36 2014), pp. 6307–6312.

[120] National Instruments. *NI cRIO*. 2016. URL: `http://www.ni.com`.

[121] National Instruments. *USB-6216*. 2017. URL: `http://sine.ni.com/nips/cds/view/p/lang/ko/nid/207099`.

[122] Nordson. *Flexible Tips*. 2017. URL: `http://www.nordson.com/en/divisions/efd/products/dispense-tips/flexible-tips`.

[123] Nordson. *General Purpose Tips*. 2017. URL: http://www.nordson.com/en/divisions/efd/products/dispense-tips/general-purpose-tips.

[124] Nordson EFD. *Ultimus V High Precision Dispenser*. 2017. URL: http://www.nordson.com/en/divisions/efd/products/fluid-dispensing-systems/ultimus-v-high-precision-dispenser.

[125] M.A. Nussbaum and D.B. Chaffin. "Lumbar muscle force estimation using a subject-invariant 5-parameter emg-based model." In: *Journal of biomechanics* 31 (1988), pp. 667–672.

[126] J. T. Overvelde *et al.* "Mechanical and electrical numerical analysis of soft liquid-embedded deformation sensors analysis". In: *Extreme Mechanics Le tters* 1 (2014), pp. 42–46.

[127] K. B. Ozutemiz *et al.* "EGaIn-metal interfacing for liquid metal circuitry and microelectronics integration". In: *Advanced Materials Interfaces* 5 (10 2018), p. 1701596.

[128] Panasonic. *Rotary potentiometer*. 2016. URL: https://na.industrial.panasonic.com.

[129] D. P. Parekh *et al.* "3D printing of liquid metals as fugitive inks for fabrication of 3D microfluidic channels". In: *Lab on a Chip* 16 (10 2016), pp. 1812–1820.

[130] W. Park *et al.* "A Soft Sensor-Based Three-Dimensional (3-D) Finger Motion Measurement System". In: *Sensors* 17 (2 2017), p. 420.

[131] Y. L. Park, B. R. Chen, and R. J. Wood. "Design and fabrication of soft artificial skin using embedded microchannels and liquid conductors". In: *IEEE Sensors Journal* 12 (8 2012), pp. 2711–2718.

[132] Y. L. Park *et al.* "Bio-inspired active soft orthotic device for ankle foot pathologies". In: *Proc. of 2011 IEEE/RSJ International Conference on Intelligent Robots and Systems (IROS)*. 2011, pp. 4488–4495.

[133] Y. L. Park *et al.* "Design and control of a bio-inspired soft wearable robotic device for ankle-foot rehabilitation". In: *Bioinspiration & biomimetics* 9 (1 2014), p. 016007.

[134] Y. L. Park *et al.* "Hyperelastic pressure sensing with a liquid-embedded elastomer". In: *Journal of Micromechanics and Microengineering* 20 (12 2010), p. 125029.

[135] Y. L. Park *et al.* "Influence of cross-sectional geometry on the sensitivity and hysteresis of liquid-phase electronic pressure sensors". In: *Applied Physics Letters* 101 (19 2012), p. 191904.

[136] A. Patriarco *et al.* "An evaluation of the approaches of optimization models in the prediction of muscle forces during human gait". In: *Journal of biomechanics* 14 (1981), pp. 513–525.

[137] D.R. Pedersen, R.A. Brand, and D.T. Davy. "Pelvic muscle and acetabular contact forces during gait". In: *Journal of biomechanics* 30 (1997), pp. 959–965.

[138] D. Penrod, D. Davy, and D. Singh. "An optimization approach to tendon force analysis". In: *Journal of Biomechanics* 7 (1974), pp. 123–129.

[139] J. C. Perry, J. Rosen, and S. Burns. "Upper-limb powered exoskeleton design". In: *IEEE/ASME transactions on mechatronics* 12 (4 2007), pp. 408–417.

[140] J. Perry and J.R. Davids. "Gait analysis: Normal and pathological function". In: *Journal of Pediatric Orthopaedics* 12 (1992), p. 815.

[141] J.E. Pierce and G. Li. "Muscle forces predicted using optimization methods are coordinate system dependent". In: *Journal of biomechanics* 38 (2005), pp. 695–702.

[142] J. L. Pons. *Wearable robots: biomechatronic exoskeletons*. John Wiley & Sons, 2008.

[143] Jerry Pratt, Ben Krupp, and Chris Morse. "Series elastic actuator for high fidelity force control". In: *Industrial Robot: An International Journal* 29 (2002), pp. 234–241.

[144] V. R. Preedy. *Handbook of anthropometry: physical measures of human form in health and disease*. Springer Science & Business Media, 2012.

[145] B. T. Quinlivan *et al.* "Assistance magnitude versus metabolic cost reductions for a tethered multiarticular soft exosuit". In: *Sci. Robot* 2 (2 2017).

[146] R. Raikova and H. Aladjov. "The influence of the way the muscle force is modeled on the predicted results obtained by solving indeterminate problems for a fast elbow flexion". In: *Computer methods in biomechanics and biomedical engineering* 6 (2003), pp. 181–196.

[147] G. K. Reeves and H. B. Harrison. "Obtaining the specific contact resistance from transmission line model measurements". In: *IEEE Electron device letters* 3 (5 1982), pp. 111–113.

[148] P. Roberts *et al.* "Soft-matter capacitive sensor for measuring shear and pressure deformation". In: *In 2013 IEEE International Conference on Robotics and Automation (ICRA)*. 2013, pp. 3529–3534.

[149] E. Rocon *et al.* "Design and validation of a rehabilitation robotic exoskeleton for tremor assessment and suppression". In: *IEEE Transactions on Neural Systems and Rehabilitation Engineering* 15 (2007), pp. 367–378.

[150] H. Rohrle *et al.* "Joint forces in the human pelvis-leg skeleton during walking". In: *Journal of biomechanics* 17 (1984), pp. 409–424.

[151] D. Rus and M. T. Tolley. "Design, fabrication and control of soft robots". In: *Nature* 521 (7553 2015), p. 467.

[152] P. Sahoo and S. K. Das. "Tribology of electroless nickel coatings-a review". In: *Materials & Design* 32 (4 2009), pp. 1760–1775.

[153] Samtec. *Compression micro pitch one-piece interfaces*. 2018. URL: `https://www.samtec.com/`.

[154] A. Schultz *et al.* "Use of lumbar trunk muscles in isometric performance of mechanically complex standing tasks". In: *Journal of Orthopaedic Research* 1 (1983), pp. 77–91.

[155] E. B. Secor *et al.* "Wiring up Liquid Metal: Stable and Robust Electrical Contacts Enabled by Printable Graphene Inks". In: *Advanced Electronic Materials* 4 (1 2018), p. 1700483.

[156] A. Seireg and R. Arvikar. "The prediction of muscular load sharing and joint forces in the lower extremities during walking". In: *Journal of biomechanics* 8 (1975), pp. 89–102.

[157] S. Seok *et al.* "Meshworm: a peristaltic soft robot with antagonistic nickel titanium coil actuator". In: *IEEE/ASME Transactions on mechatronics* 18 (5 2013), pp. 1485–1497.

[158] Shenzhen Guan Hong Automation Co., LTD. *SZGH-CNC1000MDb-5*. 2017. URL: `http://www.szghauto.com/index.php?c=product&id=145`.

[159] R. F. Shepherd *et al.* "Multigait soft robot". In: *Proceedings of the national academy of sciences* 108 (51 2011), pp. 20400–20403.

[160] M. Shimojo *et al.* "A tactile sensor sheet using pressure conductive rubber with electrical-wires stitched method". In: *IEEE Sensors journal* 4 (5 2004), pp. 589–596.

[161] H. S. Shin *et al.* "Enhanced performance of microfluidic soft pressure sensors with embedded solid microspheres". In: *Journal of Micromechanics and Microengineering* 26 (2 2016), p. 025011.

[162] Sigma-Aldrich. *Fluorescein*. 2017. URL: http://www.sigmaaldrich.com/catalog/product/mm/fx0325?lang=en&region=US.

[163] Sigma-Aldrich. *Gallium-Indium eutectic*. 2017. URL: http://www.sigmaaldrich.com/catalog/product/aldrich/495425?lang=en&region=US.

[164] Smooth-On. *Dragon Skin 30*. 2017. URL: https://www.smooth-on.com/products/dragon-skin-30/.

[165] Smooth-On. *Ecoflex 00-30*. 2017. URL: https://www.smooth-on.com/products/ecoflex-00-30/.

[166] Smooth-On. *Sil-Poxy*. 2017. URL: https://www.smooth-on.com/product-line/sil-poxy/.

[167] K. E. Spells. "The determination of the viscosity of liquid gallium over an extended nrange of temperature". In: *Proceedings of the Physical Society*. Vol. 48. 1936, p. 299.

[168] Supereyes. *B011 5MP 500X*. 2018. URL: https://www.supereyes-store.com/.

[169] R. Surapaneni *et al.* "Microfabrication of flexible self-repairing ground reaction sensor with liquid metal electrodes". In: *Procedia Engineering* 25 (2011), pp. 124–127.

[170] K. Suzuki *et al.* "Intention-based walking support for paraplegia patients with Robot Suit HAL". In: *Advanced Robotics* 21 (12 2007), pp. 1441–1469.

[171] A. Tabatabai *et al.* "Liquid-phase gallium-indium alloy electronics with microcontact printing". In: *Langmuir* 29 (20 2013), pp. 6194–6200.

[172] H. Tada, P. C. Paris, and G. R. Irwin. *The stress analysis of cracks*. Del Research Corporation, 1973.

[173] Teasell, R. "Stroke recovery and rehabilitation". In: *Stroke* 34 (2003), pp. 365–366.

[174] D.G. Thelen, F.C. Anderson, and S.L. Delp. "Generating dynamic simulations of movement using computed muscle control". In: *Journal of biomechanics* 36 (2003), pp. 321–328.

[175] R. A. Toupin. "Saint-Venant's principle". In: *Archive for Rational Mechanics and Analysis* 18 (2 1965), pp. 83–96.

[176] C. Trlica *et al.* "3-D printing of liquid metals for stretchable and flexible conductors". In: *In SPIE Defense+ Security International Society for Optics and Photonics*. 2014, pp. 90831D–90831D.

[177] A. Tsukahara, Y. Hasegawa, and Y. Sankai. "Gait support for complete spinal cord injury patient by synchronized leg-swing with HAL". In: *2011 IEEE/RSJ International Conference on Intelligent Robots and Systems*. 2011, pp. 1737–1742.

[178] Unity. *Unity*. 2018. URL: `https://unity3d.com/`.

[179] Universal Laser Systems. *VLS6.60*. 2017. URL: `https://www.ulsinc.com/products/platforms/vls660`.

[180] O. Unluhisarcikli *et al.* "Design and control of a robotic lower extremity exoskeleton for gait rehabilitation". In: *2011 IEEE/RSJ International Conference on Intelligent Robots and Systems*. 2011, pp. 4893–4898.

[181] A. D. Valentine *et al.* "Hybrid 3D printing of soft electronics". In: *Advanced Materials* 29 (40 2017), p. 1703817.

[182] H. Vallery *et al.* "Compliant actuation of rehabilitation robots." In: *IEEE Robotics & Automation Magazine* 15 (3 2008), pp. 60–69.

[183] H. Vallery *et al.* "Passive and accurate torque control of series elastic actuators". In: *2007 IEEE/RSJ International Conference on Intelligent Robots and Systems*. 2008, pp. 3534–3538.

[184] J. F. Veneman *et al.* "Design of a series elastic-and Bowden cable-based actuation system for use as torque-actuator in exoskeleton-type training." In: *9th International Conference on Rehabilitation Robotics*. 2005, pp. 496–499.

[185] D. M. Vogt, Y. L. Park, and R. J. Wood. "Design and characterization of a soft multi-axis force sensor using embedded microfluidic channels". In: *IEEE Sensors Journal* 13 (10 2013), pp. 4056–4064.

[186] D. M. Vogt and R. J. Wood. "Wrist angle measurements using soft sensors". In: *In Proceedings of IEEE SENSORS*. 2014, pp. 1631–1634.

[187] C. J. Walsh, K. Endo, and H. Herr. "A quasi-passive leg exoskeleton for load-carrying augmentation". In: *International Journal of Humanoid Robotics* 4 (03 2007), pp. 487–506.

[188] S. Wang *et al.* "Design and Control of the MINDWALKER Exoskeleton." In: *IEEE Transactions on Neural Systems and Rehabilitation Engineering* 23 (2015), pp. 277–286.

[189] W. Wang *et al.* "An assessment of immersion silver surface finish for lead-free electronics". In: *Journal of electronic materials* 38 (6 2009), pp. 815–827.

[190] V. Wank *et al.* "Accelerated contractile function and improved fatigue resistance of calf muscles in newborn piglets with iugr". In: *American Journal of Physiology-Regulatory* 278 (2000), R304–R310.

[191] R. C. Weast, M. J. Astle, and W. H. Beyer. *CRC handbook of chemistry and physics.* Boca Raton, FL: CRC press, 1988.

[192] A. Wege and G. Hommel. "Development and control of a hand exoskeleton for rehabilitation of hand injuries". In: *Proc. of 2005 IEEE/RSJ International Conference on Intelligent Robots and Systems (IROS).* 2005, pp. 3046–3051.

[193] Wehner, M. and Quinlivan, B. and Aubin, P.M.and Martinez-Villalpando, E. and Baumann, M. and Stirling, L. and Holt, K. and Wood, R. and Walsh, C. "A lightweight soft exosuit for gait assistance". In: *Proc. of 2013 IEEE International Conference on Robotics and Automation (ICRA).* 2013, pp. 3362–3369.

[194] D. A. Winter. *Biomechanics and motor control of human movement.* John Wiley & Sons, 2009.

[195] Withrobot. *myahrs+.* 2017. URL: `http://www.withrobot.com/myahrs_en/`.

[196] E. T. Wolbrecht, D. J. Reinkensmeyer, and J. E. Bobrow. "Pneumatic control of robots for rehabilitation". In: *The International Journal of Robotics Research* 29 (1 2009).

[197] R. D. P. Wong, J. D. Posner, and V. J. Santos. "Flexible microfluidic normal force sensor skin for tactile feedback". In: *Sensors and Actuators A: Physical* 179 (2012), pp. 62–69.

[198] F. Xia *et al.* "Internet of things". In: *International Journal of Communication Systems* 25 (9 2012), pp. 1101–1102.

[199] Q. Xu *et al.* "Effect of oxidation on the mechanical properties of liquid gallium and eutectic gallium-indium". In: *Physics of Fluids* 24 (6 2012), p. 063101.

[200] T. Yamada *et al.* "A stretchable carbon nanotube strain sensor for human-motion detection". In: *Nature nanotechnology* 6 (5 2011), pp. 296–301.

[201] S. Yao and Y. Zhu. "Wearable multifunctional sensors using printed stretchable conductors made of silver nanowires". In: *Nanoscale* 6 (4 2014), pp. 2345–2352.

[202] J. C. Yeo *et al.* "Highly Flexible Graphene Oxide Nanosuspension Liquid?Based Microfluidic Tactile Sensor". In: *Small* 12 (12 2016), pp. 1593–1604.

[203] J. C. Yeo *et al.* "Wearable tactile sensor based on flexible microfluidics". In: *Lab on a Chip* 16 (17 2016), pp. 3244–3250.

[204] I. Youcef-Toumi and C. C. Shortlidge. "Control of robot manipulators using time delay". In: *Proceedings., International Conference on Robotics and Automation.* 1991, pp. 2391–2398.

[205] K. Youcef-Toumi and T. A. Fuhlbrigge. "Application of decentralized time-delay controller to robot manipulators". In: *IEEE International Conference on Robotics and Automation.* 1989, pp. 1–7.

[206] Youcef-Toumi, Kamal, and Osamu Ito. "A time delay controller for systems with unknown dynamics". In: *Journal of dynamic systems, measurement, and control* 112 (1990), pp. 133–142.

[207] V.M. Zatsiorsky. *Kinetics of human motion.* Human Kinetics, 2002.

[208] Zeiss. *Axio Zoom.V16.* 2017. URL: `https://www.zeiss.com/microscopy/int/products/stereo-zoom-microscopes/axio-zoom-v16.html`.

[209] Zeiss. *Zeiss LSM 780.* 2017. URL: `https://www.zeiss.com/microscopy/int/products/confocal-microscopes/lsm-800-with-airyscan.html`.

[210] W. J. Zhang, Q. Li, and L. S. Guo. "Integrated Design of Mechanical Structure and Control Algorithm for a Programmable Four-Bar Linkage". In: *Mechatronics, IEEE/ASME Transactions on* 4.4 (1999), pp. 354–362.

[211] J. Y. Zhu *et al.* "An integrated liquid cooling system based on galinstan liquid metal droplets". In: *ACS applied materials & interfaces* 8 (3 2016), pp. 2173–2180.

[212] D. Zrnic and D. S. Swatik. "Resistivity and surface tension of the eutectic alloy of gallium and indium". In: *Journal of the less common metals* 18 (1 1969), pp. 67–68.